

---

# X-ray and neutron scattering study of organic-organic heterolayers for organic electronics and biointerfaces

Martin Huth

---



München 2010



---

# **X-ray and neutron scattering study of organic-organic heterolayers for organic electronics and biointerfaces**

**Martin Huth**

---

Dissertation  
an der Fakultät für Physik  
der Ludwig-Maximilians-Universität  
München

vorgelegt von  
Martin Huth  
aus München

München, den 28.10.2010

Erstgutachter: PD. Dr. B.Nickel

Zweitgutachter: Prof. Dr. W.W.Schmahl

Tag der mündlichen Prüfung: 23.12.2010

# Contents

Contents	v
Zusammenfassung	vii
Summary	viii
<b>1 Introduction and Motivation</b>	<b>1</b>
<b>2 Anisotropic Aggregation of Molecules on Surfaces</b>	<b>5</b>
2.1 Introduction . . . . .	5
2.2 Basics of van der Waals Interactions . . . . .	7
2.3 Analysis of Different Growth Scenarios . . . . .	13
2.4 Long, Thin Molecules (Alkanes) . . . . .	17
2.5 Simulation of Pentacene Molecules . . . . .	18
2.6 Molecule - Molecule Interaction . . . . .	23
<b>3 Growth of Pentacene Thin Films on Technically Relevant Surfaces</b>	<b>31</b>
3.1 Experimental – Organic Molecular Beam Epitaxy . . . . .	31
3.2 Pentacene . . . . .	34
3.3 Pentacene on Gate Dielectrics . . . . .	35
3.4 Pentacene on Modified Diamond Surfaces . . . . .	39
<b>4 Organic-organic Bilayer for Encapsulation</b>	<b>47</b>
4.1 Spincoating of Thermoplasts . . . . .	47
4.2 Sputter Oxides . . . . .	52
4.3 Vacuum Deposition of Alkanes . . . . .	53
<b>5 Lipid Membranes on hydrophobic surfaces</b>	<b>61</b>
5.1 Membrane on Pentacene . . . . .	61
5.2 Membrane on an Alkane Layer . . . . .	64
<b>6 An Artificial Biomimetic Binding Surface</b>	<b>69</b>
6.1 Trilayer Structure . . . . .	72
6.2 Cell Adhesion . . . . .	77

---

6.3 Preparation Details . . . . .	78
<b>7 Conclusions and Outlook</b>	<b>81</b>
<b>Bibliography</b>	<b>85</b>
<b>A Publications</b>	<b>95</b>
A.1 Full text of Ref. [1] . . . . .	97
A.2 Full text of Ref. [2] . . . . .	111
A.3 Full text of Ref. [3] . . . . .	117
A.4 Full text of Ref. [4] . . . . .	125
A.5 Full text of Ref. [5] . . . . .	133
A.6 Full text of Ref. [6] . . . . .	143
A.7 Full text of Ref. [7] . . . . .	149
<b>B Performing Reflectometry Experiments</b>	<b>153</b>
B.1 Preparing the sample . . . . .	153
B.2 Mounting the sample . . . . .	154
B.3 Possible errors during alignment/measurement . . . . .	155
<b>C MATLAB custom tools</b>	<b>163</b>
C.1 Unit Cell Solver . . . . .	164
C.2 File Merger . . . . .	168
<b>D Photos</b>	<b>171</b>
<b>List of Figures</b>	<b>177</b>
<b>List of Tables</b>	<b>181</b>
<b>Acknowledgements</b>	<b>183</b>

# Zusammenfassung

Die biologische und medizinische Forschung stellt immer mehr Informationen über die Funktion des Lebens bereit. Dem voraus geht eine hochpräzise und spezifische Diagnostik. Allerdings gibt es noch keine überzeugenden Lösungen für die Lebend-Überwachung von Substanzen, die möglicherweise an Demenzkrankheiten oder Alterserscheinungen beteiligt sind. Die vorliegende Arbeit beschäftigt sich mit Grundlagenforschung zur Entwicklung eines Sensors, der in der Lage ist, Änderungen des elektrischen Potentials, z.B. neuronale Aktivität, in biologisch relevanter Umgebung zu detektieren.

In dem hier behandelten Ansatz wird eine Sensorfläche eingesetzt, welche vollständig aus organischen Materialien aufgebaut ist. Die effektive Schnittstelle zwischen dem Sensor und den Zellen ist eine künstliche Zellmembran, die mit einer Bindungseinheit ausgestattet ist, deren Aufbau dem Vorbild der Natur nachempfunden ist. Der Sensor selbst ist ein organischer Dünnschichttransistor, der seine Sensitivität aus den elektronischen Eigenschaften des organischen Halbleiters erhält. Zudem hat die aktive Schicht eine Dicke von nur 50nm.

Entscheidend im Umgang mit organischen Molekülen ist die enge Beziehung zwischen Struktur und Funktion. Die starke Anisotropie der Struktur spiegelt sich in den elektronischen Eigenschaften wider. Die molekulare Anordnung wiederum hängt sensibel von den verwendeten Prozessparametern bei der Herstellung der Schichten ab. Wichtig sind z.B. die Rate, die Temperatur oder die physikalischen Eigenschaften der Oberfläche (polar, nicht-polar, rau etc.). Die so gewonnenen organischen Multischichtsysteme wurden mit Hilfe von Röntgen- und Neutronenstreuung an Großgeräten (Synchrotron, Reaktor) charakterisiert.

Ein Schwerpunkt der vorliegenden Arbeit ist das Auffinden und Beeinflussen der Struktur der verwendeten Materialien auf molekularer Ebene. Zunächst werden Konzepte und Aggregationsmechanismen von Molekülen auf Oberflächen vorgestellt. Der experimentelle Teil widmet sich der Herstellung der organischen Halbleiterschicht aus Pentacen ( $C_{22}H_{14}$ ) auf unterschiedlichen Oberflächen. Durch chemische Modifikation von Diamantoberflächen konnten Pentacen-Filme kontrolliert in stehender oder liegender Phase gewachsen werden. Ferner wurde die Verkapselung organischer Filme mit verschiedensten Techniken und Materialien untersucht. Die Verwendung der Vakuumsublimations-Technik ermöglichte die Konservierung der "Dünnschichtphase" von Pentacen durch Verkapseln mit dem Alkan Tetrat-

tracontan (TTC, C<sub>44</sub>H<sub>90</sub>). Somit konnte der stabile Betrieb eines organischen Transistors in ionischer wässriger Umgebung ermöglicht werden, was den entscheidenden Schritt in Richtung Sensorik darstellt.

Des Weiteren gelang der Aufbau einer vielseitig funktionalen Beschichtung, welche von Zellen als ihre natürliche Umgebung akzeptiert wird. Basierend auf substratgestützten Lipid-Doppelschichten wurde mit Hilfe der Biotinbindung ein synthetischer Peptid-Komplex über eine Protein-Zwischenschicht an die Oberfläche gebunden. Dieser Komplex enthält mehrfach die RGD Sequenz, eine Aminosäure-Sequenz, die für die Bindung von Proteinen an ihre Zellrezeptoren verantwortlich ist. Die Struktur der Beschichtung wurde mit Röntgen- und Neutronenbeugung mit einer Auflösung von 5 Å bestimmt. Es zeigt sich eine mehrlagige Schichtung beginnend mit einer 36 Å Lipidmembran, darüber eine stark hydrierte Zwischenschicht (26 Å), gefolgt von einer 38 Å dicken Streptavidinschicht und abschließend eine 30 Å Schicht aus dicht gepackten, seitlich liegenden Bindungskomplexen. Neuronale Stammzellen wurden auf dieser Beschichtung kultiviert und zeigten rasche Anlagerung sowie eine Ausbreitung auf der angebotenen Oberfläche.

Die Kompatibilität der Beschichtung mit dem verkapselten Transistor wurde durch das Ausbilden einer Lipidschicht auf der Sensoroberfläche bestätigt. In Zukunft sollen die Möglichkeiten mit dieser Anordnung Änderungen des elektrischen Potentials zu messen erforscht werden. Dazu detektiert man zunächst Referenzsignale die im Elektrolyten über eine Platin- oder eine Ag/AgCl-Elektrode angelegt werden. Aufgrund der vielfältigen Oberflächen die sich mit Lipidmembranen beschichten lassen, ist diese Methode auch für die Gewebeentwicklung oder als Implantatsbeschichtung interessant.

# Summary

Biological and medical research provides more and more information about the functioning of life. The basis therefor are high accurate and specific diagnostics. However, no satisfying solution has been found for the *in vivo* monitoring of substances, being possibly involved in dementia or old-age diseases. The presented work deals with fundamental research to develop an all-organic sensor device capable of detecting changes of the electrical potential, e.g. neural activity, in a biologically relevant environment.

In this approach the active area of the sensor is built from organic materials only. The effective interface between the sensor and the cells is an artificial cell membrane decorated with a synthetic binding unit, which has been constructed adopting the methods found in nature. The sensor itself is an organic thin film transistor (OTFT), obtaining its sensitivity from the properties of the organic semiconductor and from having an active layer with a thickness of only 50nm.

The crucial issue when working with organic molecules is the strong relation between the structure and the function. The strong anisotropy of the structure is also found in the electronic properties. On the other hand the structure is highly influenced by processing parameters like deposition rate, temperature or the surface properties (polar, non polar, rough etc.) The fabricated multilayer systems were characterized with X-ray and neutron diffraction using giant equipment (synchrotron, reactor).

A major focus of the presented thesis lies on discovering and manipulating the structure of the involved materials on the molecular scale. At first, an overview on aggregation mechanism and molecular interaction with surfaces depending on the shape of the molecules is given. The experimental part deals with the growth of the organic semiconductor, pentacene (C<sub>22</sub>H<sub>14</sub>) on various surfaces. By chemically modifying diamond surfaces, controlled pentacene film growth in a standing or lying configuration was achieved. Furthermore, the encapsulation with an alkane, tetratetracontane (TTC, C<sub>44</sub>H<sub>90</sub>), which has been achieved using vacuum deposition. Applying the correct process parameters, the electronically best suited "thin film phase" of pentacene could be conserved. Coating of the pentacene film with a TTC layer was possible in a way that a transducer device showed stable operation in ionic aqueous environment, which is the essential step towards sensor technology.

On the other hand we succeeded in constructing a versatile functional coating, providing a surface which cells accept as their "natural" environment. On the basis of a supported lipid bilayer, a synthetic peptide conjugate is bound to the surface with the help of biotin linking via a streptavidin interlayer. This conjugate contains multiples of the RGD sequence (amino acid sequence responsible for binding of proteins to their receptors on the cell surface). The structure of the coating has been determined with a resolution of 9 Å with X-ray and neutron scattering. It has been found to form a layered stacking with a 36 Å lipid bilayer, above a highly hydrated interlayer (26 Å) followed by a 38 Å streptavidin layer and a 30 Å film of lying binding units on top. Neural stem cells have been grown on the coated surface. They have been found to attach rapidly and spread on the surface.

The compatibility of the coating with the encapsulated transducer device has been demonstrated by confirming lipid layer formation. In the near future the capabilities of this system to measure changes of the electrical potential will be further explored by detecting reference signals induced with a platinum and a Ag/AgCl counter electrode. Due to the large variety of surfaces that can be coated by lipid layers, this membrane based method to bind cells is of general interest, also for tissue engineering or coating implants.

# Chapter 1

## Introduction and Motivation

The aggregation of organic molecules is a complex phenomenon due to their anisotropic shape and the various interactions that have to be considered. In combination with a specific surface, one has to account for the molecule – surface and the molecule – molecule interaction. Furthermore the surrounding medium, like water or air, has a strong influence on the aggregation. Contrary to metals, e.g. gold, where the type of aggregation has a limited scope, many different stable polymorphs can be found in organic crystallites. The metallic bonds responsible for the crystal structure of metals are noticeable stronger than the weak forces (van der Waals) arising from the presence of a surface. Hence the metallic aggregation is quite independent from the surface and its properties. Most hydrocarbons are electrically neutral, thus the van der Waals forces are responsible for the aggregation of the molecules, which leads to a situation where the forces between a surface close by and the molecules are in the same order of magnitude than the forces between the molecules themselves. Besides the shape of the molecules, the fabrication parameters and the properties of the surface on which the molecules aggregate play an important role in determining the formed crystal structure. On different surfaces, the same organic molecules could either arrange e.g. in a standing configuration having a herringbone structure, or lie flat on the surface. Chapter 2 presents a detailed calculation about the aggregation of neutral molecules having cylindrical shape close to a surface. A complex behavior is found, even if rather simple conditions are considered.

The aggregation is an even more complex topic if larger conjugates like proteins are involved. In addition to their complicated shape, proteins are flexible and can have charged residues, thus a deterministic prediction of its aggregation behavior even on a well defined surface is often not possible, which already indicates the challenge to understand protein aggregation to a cell surface. This problem manifests e.g. in the still not satisfying understanding of the correlation between the aggregation and fibrillation of the protein beta amyloid in the human brain and the Alzheimer disease. Although a first non invasive diagnostic tool for the Alzheimer disease has been demonstrated recently from Pittsburgh University [8] in which they use positron emission tomography to detect a benzothiazole salt (thioflavin T) that binds to fibrille like aggregates of beta amyloid proteins, yet is not

clarified to what extent the protein aggregation is responsible for the dementia, or if it is just a byproduct. A correlation supporting the "amyloid hypothesis" is that people suffering from trisomy 21 (they have an extra copy of the 21st chromosome) almost universally exhibit Alzheimer disease by 40 years of age [9, 10]. The gene expressing the amyloid precursor protein (APP) is found on chromosome 21. Besides the large scale over expression and aggregation of amyloid (plaques), also smaller amyloid aggregates have been proposed to cause Alzheimer disease. Their receptors are the prion proteins, which have been linked to the Creutzfeldt-Jakob disease. However, only limited diagnostic tools are available and they can only detect late stages of the disease.

Here we present an approach envisioning the controlled investigation of cultivated neurons in a defined environment on a cellular scale. A great advantage would be the ability to study the influence of specific substances on the neural function at very low concentrations. In order to provide an experimental platform to facilitate such investigations, an all-organic sensor device combined with a functional cell adhesive coating has been developed. The sensor is an organic field effect transistor (OFET) which has to be encapsulated to be operated in liquid environment. E.g. the action potential of a neuron attached to the sensor surface would change the effective potential inside the transistor channel, which could be measured.

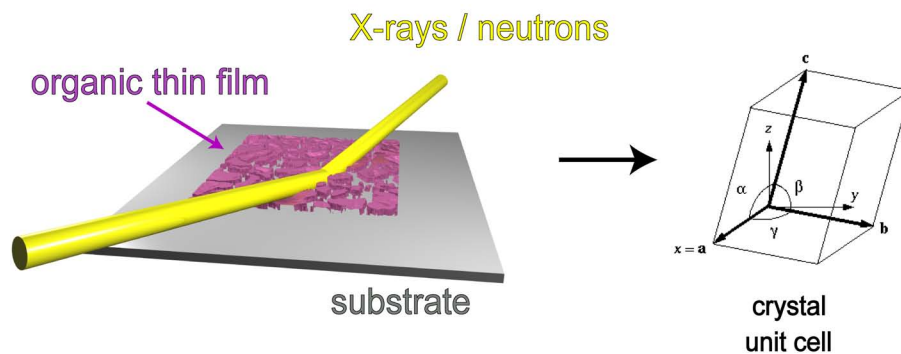


Figure 1.1: Illustration of scattering techniques used to determine the molecular structure of organic thin films.

The challenge is to fabricate a functional organic multilayer system with a specific function of each layer. Due to the strong interdependence of function and structure of organic films, X-ray and neutron scattering techniques are essential to determine the molecular arrangement (Fig. 1.1) with a resolution in the Å regime. The possibility to use synchrotron and reactor sources enables the measurement of organic heterolayers in aqueous environment with a high signal to noise ratio. Furthermore a deterministic thin film fabrication technology is needed to create reproducible films. The introduction of fluidic cells allows for the combination with fluorescence microscopy techniques.

The first task is to fabricate an organic field effect transistor. Pentacene ( $C_{22}H_{14}$ ) is an aromatic hydrocarbon which forms layered crystals on smooth inert surfaces. The highly anisotropic intermolecular coupling leads to field effect mobilities as high as amorphous silicon, if the pentacene crystallites form the so-called "thin film phase", a polymorph found e.g. on silicon oxide. Even a slightly different molecular packing decreases the charge transport drastically. Besides the crystal packing, also the film morphology is important in terms of grain size, grain boundaries and conducting pathways. Pentacene growth on different technical relevant surfaces is investigated in chapter 3. An appropriate gate dielectric has to be identified to provide the desired characteristics. Section 3.4 shows how to switch the growth mode of pentacene in a controlled way on chemically modified diamond surfaces.

Because of the sensitivity of the FET device to water, a proper encapsulation is needed to provide stable operation in physiological conditions. To encapsulate the FET, an organic film has to be deposited on top of the pentacene film without changing the crystal structure of pentacene or damaging the film. Conservation of the crystal structure can be confirmed by X-ray reflectometry measurements. A further challenge is the rough pentacene surface. Molecular aggregation on such a surface is not predictable, and has to be improved by trial and error. Structure determination using AFM and scattering techniques help to reveal the properties of the heterolayer. Several coating techniques are discussed and evaluated in chapter 4.

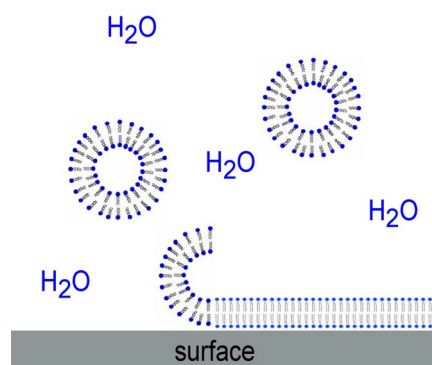


Figure 1.2: Schematic of lipid vesicles rupturing at a surface and forming a lipid bilayer.

After successfully capping the OFET, biocompatibility needs to be implemented. A substantial toolkit for coating almost every surface are supported lipid bilayers (SLB). Phospholipids are a component of the natural cell membrane and can be extracted and are commercially available. In liquid, they self assemble to micelles or vesicles due to their amphiphilic nature. When brought to a surface, the vesicles or micelles may rupture and form a monolayer or bilayer (Fig. 1.2) on top of the surface, depending on the hydrophobicity of the surface. A discussion of membrane formation on the capped OFET surface under fluorescent microscopic control is shown in chapter 5.

The last step is to provide a surface on which cells readily attach and survive. On most non toxic surfaces, cells may attach loosely. Because of the cells metabolism proteins will cover the surface after a while. This enlarges the distance of the cells to the surface and screen electrical activity from the surface, which is obstructive for sensing applications. Only a proper attachment could keep the cells in close contact with the sensor surface. An amino acid sequence found in nature that is responsible for the binding of proteins to their receptors on the cell surface is the RGD sequence (arginyl-glycyl-aspartic acid). In chapter 6 we report on a cell adhesive coating based on supported lipid bilayers (SLB) where a synthetic peptide conjugate carrying multiples of the RGD sequence is bound via a protein interlayer (Fig. 1.3). The layering and ordering of the coating as well as the hydration level has been determined by a combination of X-ray and neutron scattering experiments. The functionality was tested by growing neural stem cells on the coating.

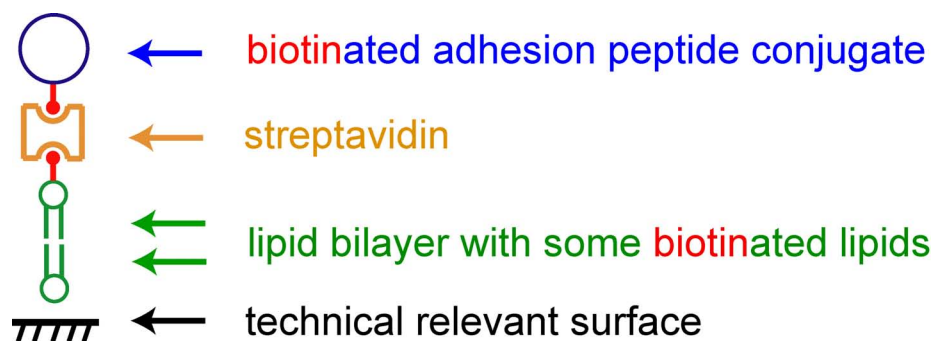


Figure 1.3: Schematic of the architecture of the binding surface. Using biotin binding, a synthetic adhesion peptide conjugate is bound to a substrate supported lipid bilayer via a streptavidin interlayer.

This thesis is structured as follows: Theoretical calculations concerning the aggregation mechanism of organic molecules on surfaces are presented in chapter 2. Chapter 3 examines organic thin film growth. After a short description of the experimental realization, the organic molecule pentacene is introduced and thin film growth of pentacene on various surfaces is discussed. Chapter 4 covers the encapsulation of a crystalline pentacene thin film by considering different surface coating methods, i.e. spincoating, sputtering and vacuum deposition. Chapter 5 reports on the compatibility of the encapsulated organic thin film transistor and the cell adhesive coating. Chapter 6 deals with the versatile biomimetic coating and its function. After discussing the structure and cell growth experiments, a preparation protocol is given.

## Chapter 2

# Anisotropic Aggregation of Molecules on Surfaces

### 2.1 Introduction

The anisotropic nature of organic molecules leads to different possible equilibrium states (inter-molecular orientations) of organic crystals, depending on the stoichiometry of the crystal and the growth parameters such as temperature or deposition rate. To gain insight into the aggregation mechanism of small rod like molecules on a substrate, a simulation is presented to estimate the interaction between molecules and a smooth inert surface.

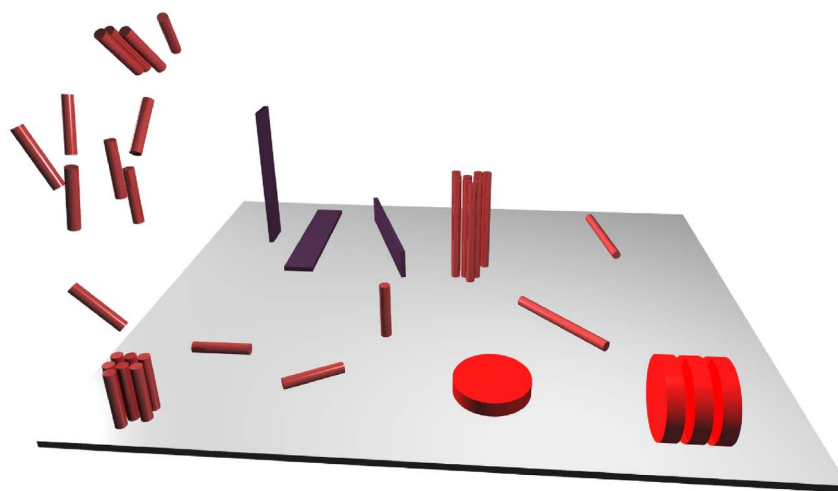


Figure 2.1: A schematic showing possible scenarios of differently shaped molecules interacting and aggregating on a smooth inert surface.

A selection of possibilities how anisotropic shaped molecules may aggregate on a surface is depicted in Fig.2.1. The schematic shows different scenarios, where single molecules

attach to the surface in a lying or standing configuration, or clusters of molecules arrange on the surface in different ways.

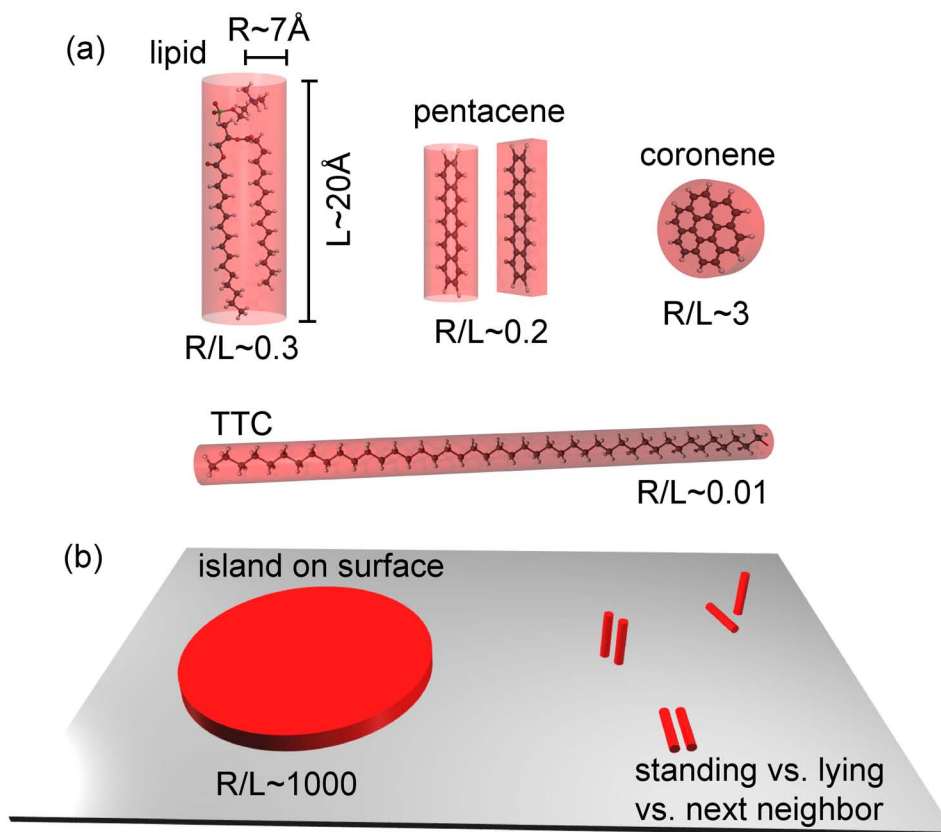


Figure 2.2: a) Organic molecules are approximated by geometric shapes in order to estimate their aggregation behavior. b) A larger cluster is treated as flat cylinder with radius  $R$  and length  $L$ . The ratio  $R/L$  of the considered structures is given. The final crystal structure will depend on the balance between the molecule - molecule and the molecule - surface interactions.

The materials used in this thesis are mostly non polar organic molecules, which can be approximated by simple geometrical shapes, including the volumes of the van der Waals spheres of all atoms, as illustrated in Fig. 2.2a. For all the materials used here, a cylindrical shape is appropriate. As the calculation will show, the ratio  $R/L$  between the radius  $R$  and the length  $L$  of the cylinder will influence the aggregation behavior. In the case of pentacene, also a box shape is used later on to simulate its properties. The case where many molecules aggregated to a larger island on a smooth surface can also be seen as a cylindrical shaped cluster interacting with the surface. To learn about the preferred structure of an aggregate, we quantitatively compare the molecule - molecule interactions with the molecule - surface interactions (Fig. 2.2b)

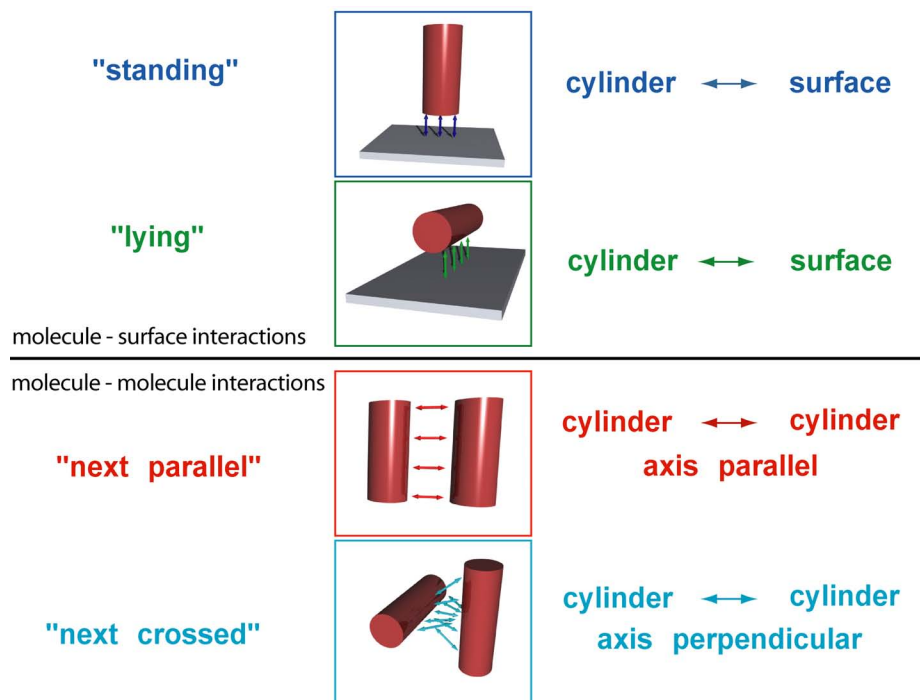


Figure 2.3: Illustration of the different interactions that are compared as a function of the distance. Equations 2.8,2.12,2.13,2.14 respectively are used for the simulations. The colors are in accordance with the colors of the curves in Fig. 2.7.

Four distinct situations have been calculated, the respective schematics are shown in Fig. 2.3. The molecule - surface interaction is considered in a standing and a lying configuration. The molecule - molecule interaction contributes in parallel or perpendicular geometry.

## 2.2 Basics of van der Waals Interactions

If organic thin films are grown in high vacuum, a model corresponding to the Hamaker summation method [11] can be used to estimate the interaction potentials and forces between molecules and a solid substrate. For this purpose the attractive van der Waals forces between the constituents of the molecules are considered. Here we assume that the molecules are non polar, thus the van der Waals forces are dominated by the contributions from the induced dipole interactions (London component), whereas the Keesom component (permanent dipole - permanent dipole) and Debye component (permanent dipole - induced dipole) are negligible. The presented model describes the attractive interaction potentials and forces at distances greater than  $\approx 4\text{\AA}$ , where repulsive forces are very small, and thus are neglected. Therefore, the aggregation mechanism of molecules approaching a surface is examined. Due to the lack of repulsive forces, equilibrium states are not considered.

From quantum mechanical perturbation theory of the interaction between electrons and nuclei [12], and after applying the Unsöld approximation, the interaction energy can be expressed in terms of polarizability and ionization potentials [13]. These material properties are combined in the London constant  $C$ , which is given by

$$C = \frac{3}{4} \cdot \frac{h\nu\alpha_A\alpha_B}{(4\pi\epsilon_0)^2} \quad (2.1)$$

where  $(\alpha_{A/B}/4\pi\epsilon_0)$  is the polarizability and  $h\nu = \frac{I_A I_B}{I_A + I_B}$  is the effective ionization potential. We now assume an interaction pair potential

$$w(\Delta r) = -\frac{C}{\Delta r^n} \quad (2.2)$$

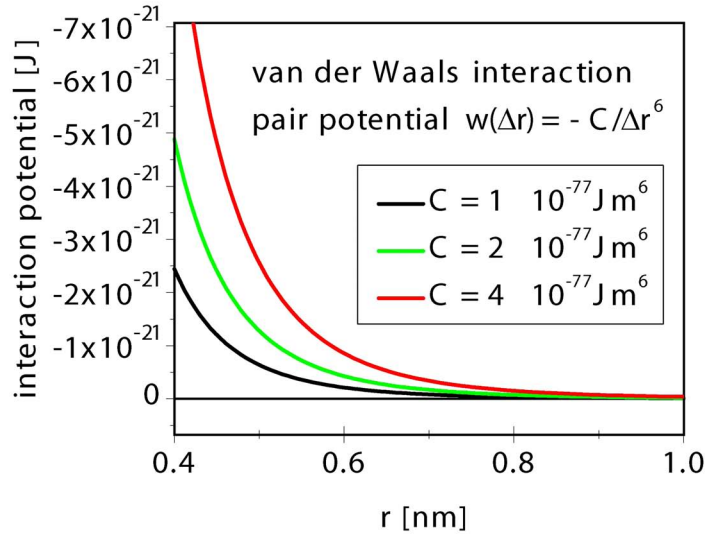


Figure 2.4: Illustration of the interaction pair potential (Eq. 2.2) using van der Waals like forces ( $n = 6$ ) and different values for the dispersion interaction ( $C$ , London constant) between point particles.

which allows to calculate the net interaction energy  $w_{par}$  between a point particle and a semi-infinite solid surface (with particle density  $\rho$ ) as a function of its distance  $D$  via integration to

$$w_{par}(D) = -\frac{2\pi C\rho}{(n-2)(n-3)D^{n-3}} \quad (2.3)$$

The complete calculation can be found in [13]. The distance  $D$  describes the distance between the solid surface and the point particle. If van der Waals forces with an exponent  $n = 6$  are assumed in Eq. 2.2, the interaction energy becomes

$$w_{par}(D) = -\frac{\pi C\rho}{6D^3} \quad (2.4)$$

Integrating over the volume of a sphere, Israelachvili [13] calculates the attractive interaction energy between a surface and a sphere shaped particle (colloid) to  $W(D) = -\pi^2 C\rho^2 R/6D$ .

Here, a different geometry is of larger interest. The rod like molecules pentacene ( $C_{22}H_{14}$ ) and tetratetracontane ( $C_{44}H_{90}$ , TTC) can be approximated by a cylinder with length  $L$  and radius  $R$ . Now, we calculate the interaction energy of a cylinder, being separated from the surface by a distance  $D$ , in a standing configuration, i.e. with its long axis perpendicular to the surface (Fig. 2.5). We consider a volume increment of the cylinder of  $2\pi r dr dz$ . Adding a density of particles in the cylinder of  $\rho_{cyl}$  yields  $\rho_{cyl} 2\pi r dr dz$  as the number of particles inside the volume increment interacting with the surface.  $\rho_{sur}$  is the particle density of the surface. To calculate the whole interaction energy of the cylinder shaped molecule with the solid surface, we have to integrate Eq. 2.3 over the cylinder volume.

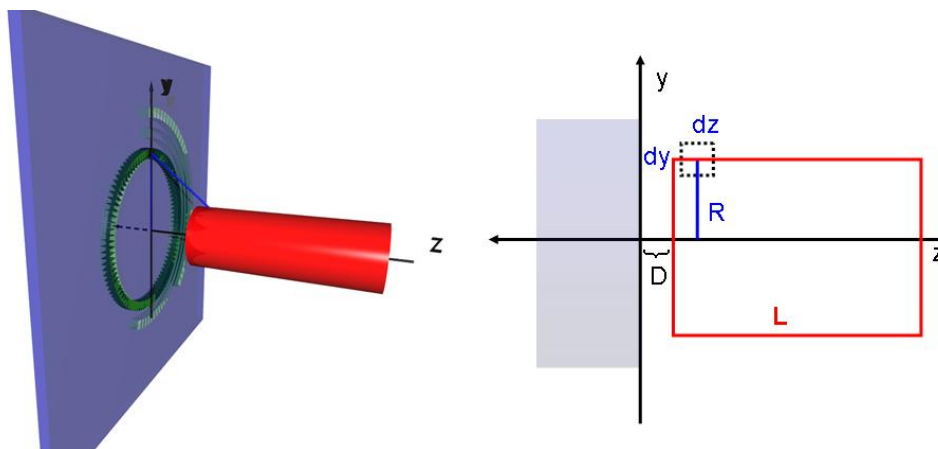


Figure 2.5: Geometry of a cylinder with length  $L$  and radius  $R$ , orienting along the surface normal at a distance  $D$  from the surface. The ring of green segments in the surface denotes the integration over small volume increments.

$$\begin{aligned}
W_{cyl\_stand}(D) &= -\rho_{cyl} \int_0^R 2\pi r dr \int_0^L w_{par}(D) dz \\
&= -\frac{\rho_{cyl}\rho_{sur}2\pi^2CR^2}{(n-2)(n-3)} \int_0^L \frac{1}{(D+z)^{n-3}} dz \\
&= -\frac{\rho_{cyl}\rho_{sur}2\pi^2CR^2}{(n-2)(n-3)} \int_D^{L+D} \frac{1}{z^{n-3}} dz \\
&= -\frac{\rho_{cyl}\rho_{sur}2\pi^2CR^2}{(n-2)(n-3)(n-4)} [z^{-(n-4)}]_D^{L+D} \\
&= -\frac{\rho_{cyl}\rho_{sur}2\pi^2CR^2}{(n-2)(n-3)(n-4)} \left[ \frac{1}{D^{n-4}} - \frac{1}{(D+L)^{n-4}} \right]
\end{aligned} \tag{2.5}$$

Introducing the conventional Hamaker constant [11]

$$\boxed{A = \pi^2 C \rho_A \rho_B} \tag{2.6}$$

where  $\rho_A$  and  $\rho_B$  are the particle densities of two interacting objects A and B (e.g. a cylinder, representing a molecule, or a surface), Eq. 2.5 simplifies to

$$W_{cyl\_stand}(D) = -\frac{2AR^2}{(n-2)(n-3)(n-4)} \left[ \frac{1}{D^{n-4}} - \frac{1}{(D+L)^{n-4}} \right] \tag{2.7}$$

which is in the case of van der Waals forces ( $n = 6$ ) further reduces to

$$\boxed{W_{cyl\_stand}(D) = -\frac{AR^2}{12} \left[ \frac{1}{D^2} - \frac{1}{(D+L)^2} \right]} \tag{2.8}$$

Now we can calculate the interaction potential of a cylinder shaped molecule in a distance  $D$  from a solid surface in standing configuration (Fig. 2.3 "standing"). To be able to compare this situation with a lying configuration (Fig. 2.3 "lying"), we calculate a cylinder shaped molecule having its long molecular axis oriented parallel to the surface. Again, its shape is approximated by a cylinder with radius  $R$  and length  $L$ . Starting from the interaction of

a single particle with a surface (Eq. 2.3), the net interaction of a cylinder in the distance  $D$  is

$$W_{cyl\_lying}(D) = -\frac{\rho_{cyl}\rho_{sur}2\pi CL}{(n-2)(n-3)} \int_{z=0}^{2R} \frac{\sqrt{(2R-z)z}}{(D+z)^{n-3}} dz \quad (2.9)$$

The integral in Eq. 2.9 is solved by

$$\int_{z=0}^{2R} \frac{\sqrt{(2R-z)z}}{(D+z)^{n-3}} dz = \frac{R^2\pi}{2D^{n-3}} \text{hypergeom}([3/2, n-3]; [3]; [-2R/D]) \quad (2.10)$$

where  $\text{hypergeom}(a, b; c; d)$  is the Gauss hypergeometric function  ${}_2F_1$ . For the specific case of  $n = 6$  and assuming that  $R \geq 0$  and  $D \geq 0$ , the hypergeometric function simplifies to

$$\int_{z=0}^{2R} \frac{\sqrt{(2R-z)z}}{(D+z)^3} dz = \frac{\pi R^2}{2D^{\frac{3}{2}}(2R+D)^{\frac{3}{2}}} \quad (2.11)$$

Using this solution (Eq. 2.11) and substituting the Hamaker constant (Eq. 2.6), the interaction energy of a lying cylinder (Eq. 2.9) becomes

$$W_{cyl\_lying}(D) = -\frac{ALR^2}{6\pi D^{\frac{3}{2}}(2R+D)^{\frac{3}{2}}} \quad (2.12)$$

Now we have calculated the two competing cases of the surface - molecule interactions (standing vs. lying), and we can compare the aggregation behavior of different shaped cylinders, which also includes disc like islands (cylinder with small length and large radius). Without the presence of a surface, the molecule - molecule interactions dominate. Next, two cylinders close-by and with their axis parallel or perpendicular are considered. Both scenarios have been calculated by Israelachvili (Ref. [13]). Here, just the results are given:

$$W_{cyl\_parallel}(D) = -\frac{AL\sqrt{R}}{24D^{\frac{3}{2}}} \quad (2.13)$$

$$W_{cyl\_crossed}(D) = -\frac{AR}{6D} \quad (2.14)$$

To get additional information on the behavior of these model molecules, we also take a look at the forces between the interacting objects. The force is defined as

$$F(D) = \frac{\partial W(D)}{\partial D} \quad (2.15)$$

type	interaction potential $W(D)$	force $F(D)$
"standing"	$-\frac{AR^2}{12} \left[ \frac{1}{D^2} - \frac{1}{(D+L)^2} \right]$	$\frac{AR^2}{6} \left[ \frac{1}{D^3} - \frac{1}{(D+L)^3} \right]$
"lying" <span style="border: 1px solid black; padding: 2px;"><i>mol. - surf.int.</i></span>	$-\frac{ALR^2}{6\pi D^{\frac{3}{2}}(2R+D)^{\frac{3}{2}}}$	$\frac{ALR^2(R+D)}{2\pi D^{\frac{5}{2}}(2R+D)^{\frac{5}{2}}}$
<span style="border: 1px solid black; padding: 2px;"><i>mol. - mol.int.</i></span> "next parallel"	$-\frac{AL\sqrt{R}}{24D^{\frac{3}{2}}}$	$\frac{AL\sqrt{R}}{16D^{\frac{5}{2}}}$
"next crossed"	$-\frac{AR}{6D}$	$\frac{AR}{6D^2}$

Table 2.1: Summary of the interaction potentials and forces used in the simulations.

Table 2.1 summarizes the molecule - surface (upper rows) and the molecule - molecule (lower rows) interaction potentials and forces that are used for the calculations. In the following section, the aggregation behavior of cylinder shaped molecules with varied aspect ratios (ratio R/L) is analyzed.

## 2.3 Analysis of Different Growth Scenarios

The interaction energies of cylinder shaped molecules in different orientations are compared as a function of the distance  $D$  and the ratio of the radius  $R$  and the length  $L$  ( $R/L$ ). The compared scenarios, summarized in Fig. 2.3, are calculated using a cylinder of length  $L = 5nm$  and respective radii, using the relations summarized in table 2.1. For two explicit regions, the interaction potentials  $W(D)$  and the forces  $F(D)$  have been calculated. Distances  $D$  from 0.4nm to 5nm are shown in the left column of Fig. 2.7, while distances from 5nm to 50nm are shown in the right column. For the simulations a Hamaker constant of  $A = 1 \cdot 10^{-19} J$  was used. According to Eq. 2.6, this implies volume densities of  $1/\pi \cdot 10^{29} m^{-3}$ , if a London constant of  $1 \cdot 10^{-77} Jm^6$  is assumed (for comparison, the value for silicon is:  $0.5 \cdot 10^{29} m^{-3}$ ). Values were taken from [13].

Interesting results can be derived from these simulations. In general, the interaction potentials between the molecules themselves (see Fig. 2.7, red and cyan curves) are dominant at distances larger than 5nm (Fig. 2.7, right column). That means a molecule which is 5nm apart from the surface would rather feel a neighboring molecule at a distance of 5nm than the surface. Closer than 3nm, we find that the surface – molecule interactions (Fig. 2.7, blue and green curves) become larger than the intermolecular potentials if the ratio  $R/L$  exceeds  $\approx 0.4$ , while the "next parallel" intermolecular potential is still dominant at a ratio  $R/L \leq 0.1$ .

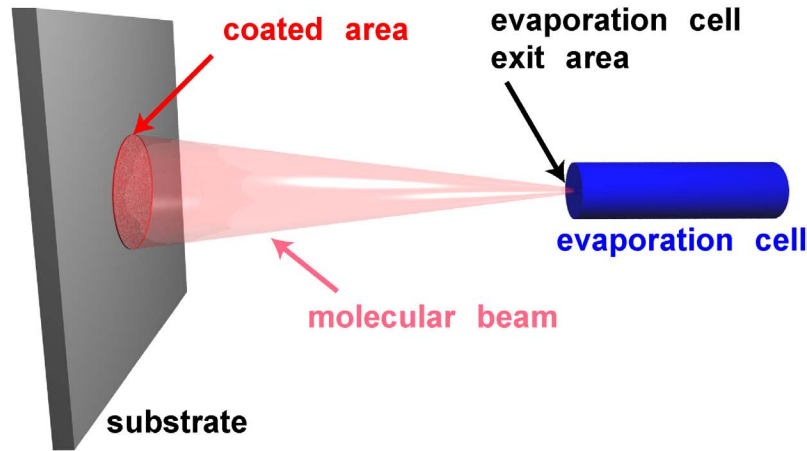


Figure 2.6: Sketch of a thin film grown with molecular beam epitaxy.

The calculated forces between different objects in varied orientations (simulated as a function of the distance  $D$ , using the relations summarized in Tab. 2.1) are shown in Fig. 2.8. In agreement with the findings from the interaction potential calculations, also the forces between two neighboring molecules are dominant over the molecule – surface forces in the region at distances greater than 5nm. For a geometry of  $R/L = 0.2$  or smaller, this is also

true for the region close to the simulated limit ( $0.4nm$ ), supporting a picture where the molecules might form aggregates before they finally attach to the surface.

To compare these results to experimentally grown thin films (using molecular beam epitaxy), we estimate the particle density inside the molecular beam in the following section. We consider an area of  $A = 1cm^2$  to be coated with 1 monolayer pentacene (Fig. 2.6).  $1cm^2 = 1 \cdot 10^{16} \text{\AA}^2$  has enough space for  $\approx 10^{16} \text{\AA}^2 / 22.61 \text{\AA}^2 \approx 4.4 \cdot 10^{14}$  (pentacene unit cell parameter  $a = 5.95 \text{\AA}$  and  $b = 7.60 \text{\AA}$ ,  $a \cdot b = 45.22 \text{\AA}^2$ , with 2 molecules per unit cell) pentacene molecules. At a deposition rate of  $0.1 \text{\AA}/s$ , it takes  $\approx 150s$  to form 1 ML. Thus,  $N \approx 4.4 \cdot 10^{14} / 150 \approx 2.9 \cdot 10^{12}$  molecules arrive at the surface per second. Their average speed, if evaporated with  $180^\circ C$ , is estimated from kinetic theory of gases to  $\langle v \rangle \approx 1.596 \sqrt{\frac{kT}{m}} \approx 174.5m/s$ . Here,  $k$  is the Boltzmann constant,  $T$  the temperature in K and  $m$  the molecular mass. Inside the molecular beam, we obtain a volume per molecule of

$$\frac{\text{Vol}}{\text{Mol}} \approx \frac{A \cdot v \cdot t}{N} \approx \frac{1 \cdot 10^{16} \text{\AA}^2 \cdot 1.74 \cdot 10^{12} \text{\AA}/s \cdot 1s}{2.9 \cdot 10^{12} \text{Mol}} \approx 0.6 \cdot 10^{16} \frac{\text{\AA}^3}{\text{Mol}}$$

Close to the surface, the mean distance between 2 molecules is  $\sqrt[3]{0.6 \cdot 10^{16} \text{\AA}^3} = 1.82 \cdot 10^5 \text{\AA} = 18.2 \mu m$ , which is too large to allow for preclustering of molecules before they arrive at the surface.

The fact that a standing phase is often observed on smooth inert surfaces, can be explained by a considerable diffusion of molecules on the surface, which enables close contact of the molecules and cluster formation. Because the molecular diffusion on a surface is constrained by dirt particles or surface defects, this also explains the nucleation of bulky structures at these positions.

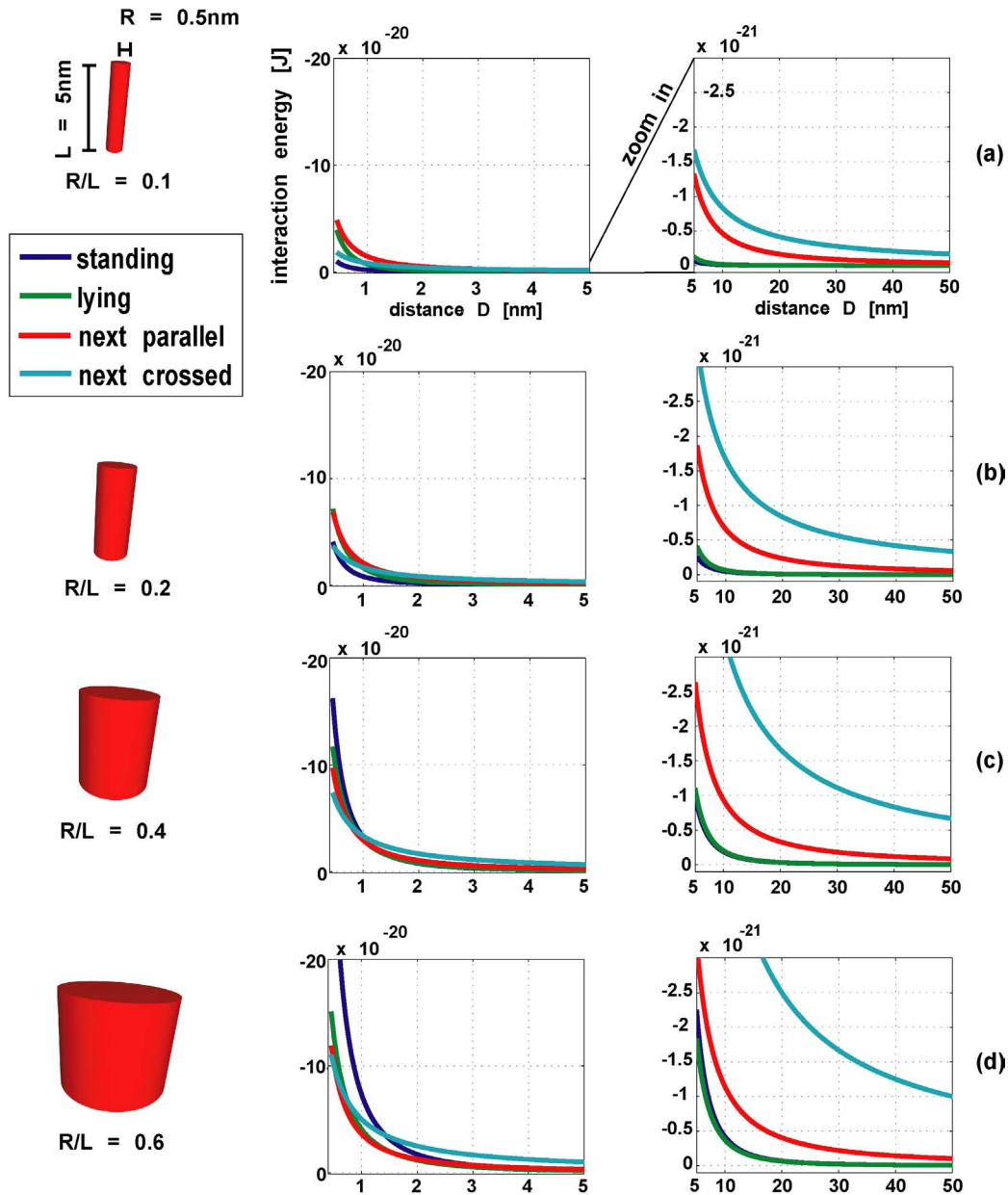


Figure 2.7: Comparison of the interaction energies of the different orientations (see Fig. 2.3) as a function of the distance  $D$  and the cylinder geometry (ratio  $R/L$ ).

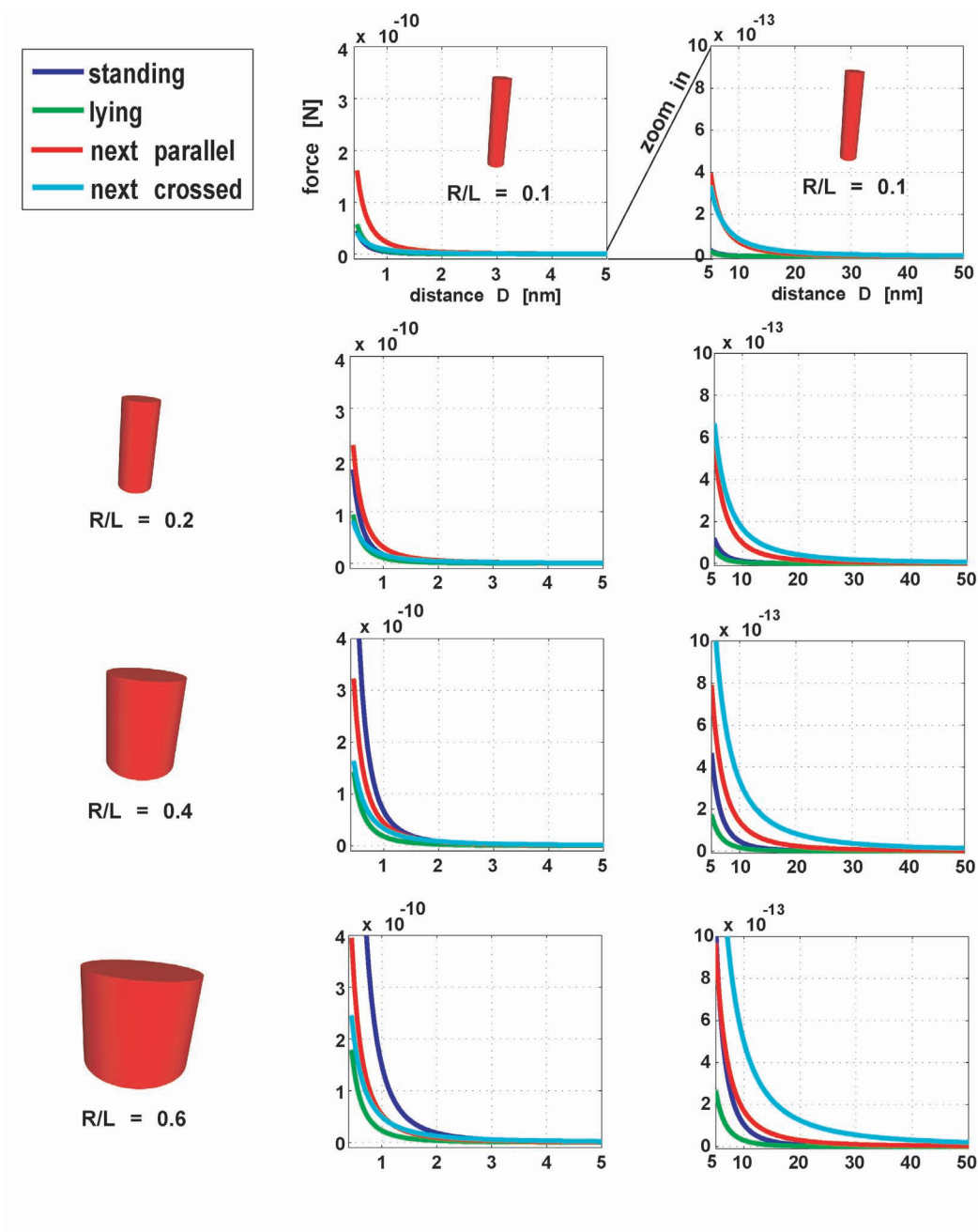


Figure 2.8: Plots of the simulated forces between interacting objects at different situations according to Fig. 2.3

The picture of aggregation of diffusing molecules to clusters before they attach to the surface is also supported by the comparison of the forces  $F(D)$  between a surface and a molecule (Fig. 2.8). Considering cylinders of a ratio  $R/L = 0.1$  (graphs in the first row), the force acting on a molecule with its long axis parallel to the surface is almost equal to the force acting on a molecule in standing configuration, but both are around a factor  $\approx 3$  lower than the "next parallel" force. For increasing values of  $R/L$ , the force on a molecule standing on the surface becomes more important, and is even bigger than the force between molecules themselves if the ratio exceeds 0.4. Thus, molecules diffusing on the surface with high velocity possibly meet other molecules and form clusters, before they finally attach to the surface.

## 2.4 Long, Thin Molecules (Alkanes)

Alkanes are linear chains of carbon atoms saturated with hydrogen. Using long, thin cylinders with different length  $L$  as model molecules, we describe the growth of alkanes on smooth, inert substrates. As an example, cylinders with a radius of  $3\text{\AA}$  and a length of  $5\text{nm}$ ,  $20\text{nm}$  and  $40\text{nm}$  respectively are simulated.

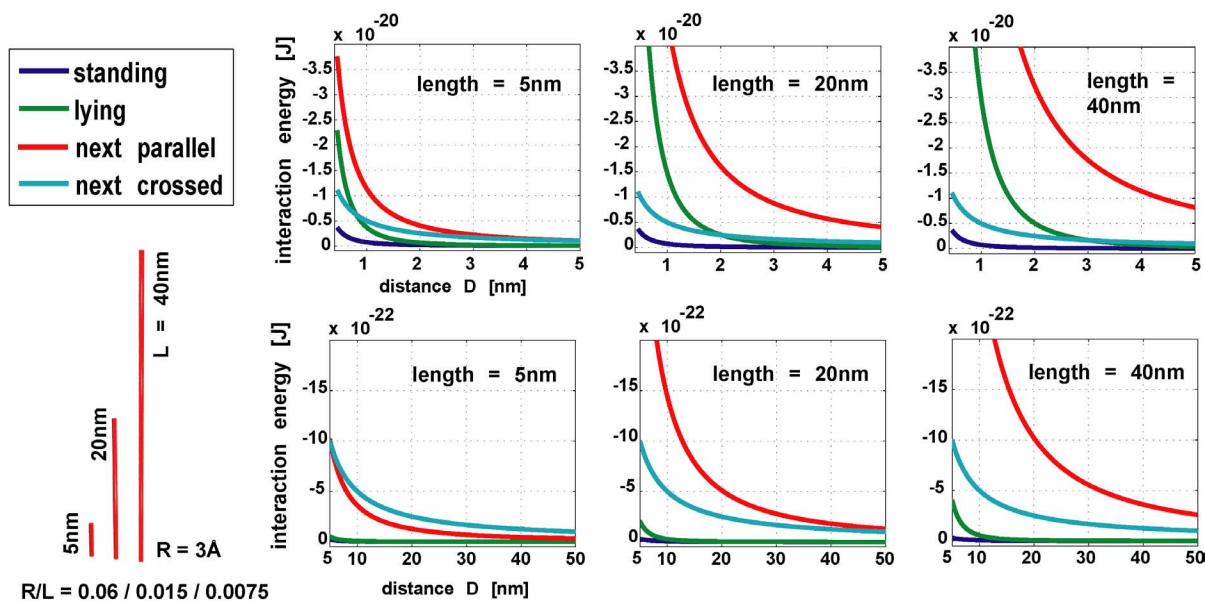


Figure 2.9: Influence of the cylinder length  $L$  on the four interaction types (see Fig. 2.3) as a function of the distance  $D$ .

Each curve shown in Fig. 2.9 shows the calculated interaction potential as a function of the distance  $D$  between the molecules and the surface (in the case of standing or lying configuration, blue and green curve), or between two neighboring molecules (next parallel

or next crossed, red and cyan curve). The region where two interacting objects are very close, from  $0.4\text{nm}$  to  $5\text{nm}$ , is shown in the upper row, while the more distant region from  $5\text{nm}$  to  $50\text{nm}$  is shown in the three lower graphs. Please note the different scales.

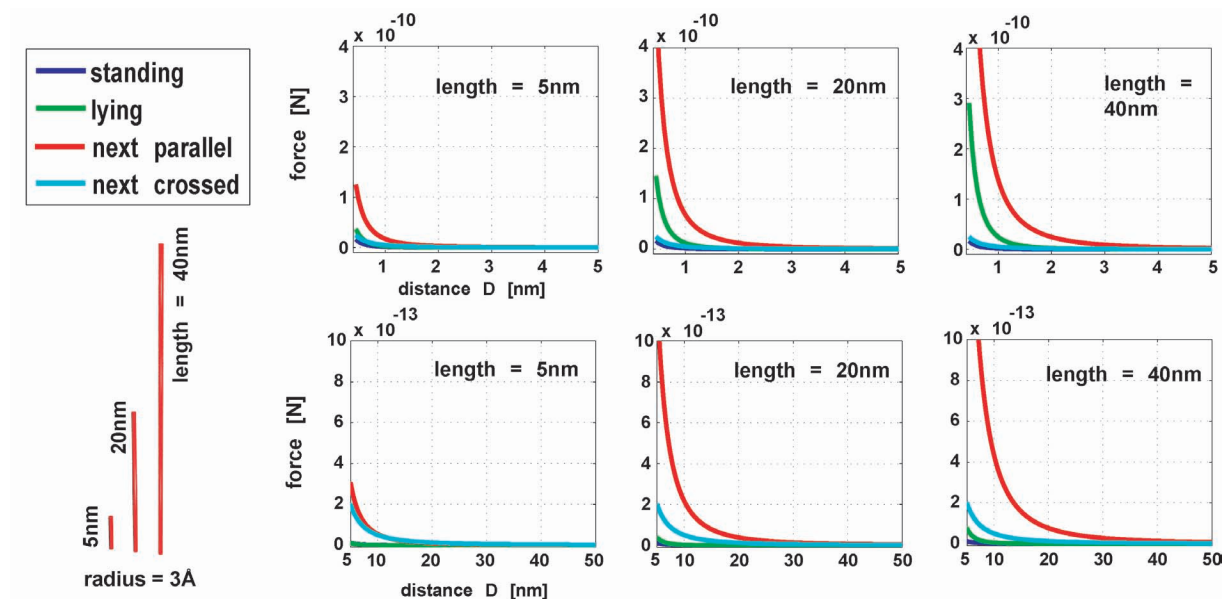


Figure 2.10: Force between cylinders with length  $L$  as a function of the distance  $D$ , considering various orientations (see Fig. 2.3).

In analogy to the section above, we also consider the forces between the molecules and/or the surface (see Tab.2.1). Fig. 2.10 shows the forces between thin cylinders of different length in varied orientations. Noticeable is that the "next parallel" force is dominant in all regions and at all the three different length, while additionally increasing strongly with the length  $L$  of the cylinder. On the other hand, the "next crossed" and the "standing" configuration contribute only weak to the net force on a random oriented molecule. Comparison to the experimental observations of a fast growing standing phase of e.g. TTC ( $C_{44}$ , Fig. 2.2) on  $\text{SiO}_2$  leads to the conclusion that even long alkyl chains diffuse on the surface and form clusters before they finally attach to the surface.

## 2.5 Simulation of Pentacene Molecules

Pentacene molecules can be considered as boxes with a length  $L = 15\text{\AA}$ , width  $B = 3.2\text{\AA}$  and height of  $H = 1\text{\AA}$ . The interaction with a solid surface is calculate in the same way as described above, assuming that the box shaped molecule is either standing on the surface (see Fig. 2.11, left, (a)), lying flat on the surface (b) or is standing on the side (c). The interaction potentials as a function of the distance  $D$  between the molecule and the

surface are calculated using Eq. 2.3 and integrating over the box volume in the direction perpendicular to the surface. The interaction potential of a box standing on the surface is

$$\begin{aligned} W_{box\_stand}(D) &= -\frac{2AHB}{\pi(n-2)(n-3)} \int_0^L \frac{1}{(D+z)^{n-3}} dz \\ &= -\frac{2AHB}{\pi(n-2)(n-3)(n-4)} \left[ \frac{1}{D^{n-4}} - \frac{1}{(D+L)^{n-4}} \right] \end{aligned} \quad (2.16)$$

In the case of  $n = 6$  we find

$$W_{box\_stand}(D) = -\frac{AHB}{12\pi} \left[ \frac{1}{D^2} - \frac{1}{(D+L)^2} \right] \quad (2.17)$$

$$W_{box\_lying}(D) = -\frac{ALB}{12\pi} \left[ \frac{1}{D^2} - \frac{1}{(D+H)^2} \right] \quad (2.18)$$

$$W_{cyl\_side}(D) = -\frac{AHL}{12\pi} \left[ \frac{1}{D^2} - \frac{1}{(D+B)^2} \right] \quad (2.19)$$

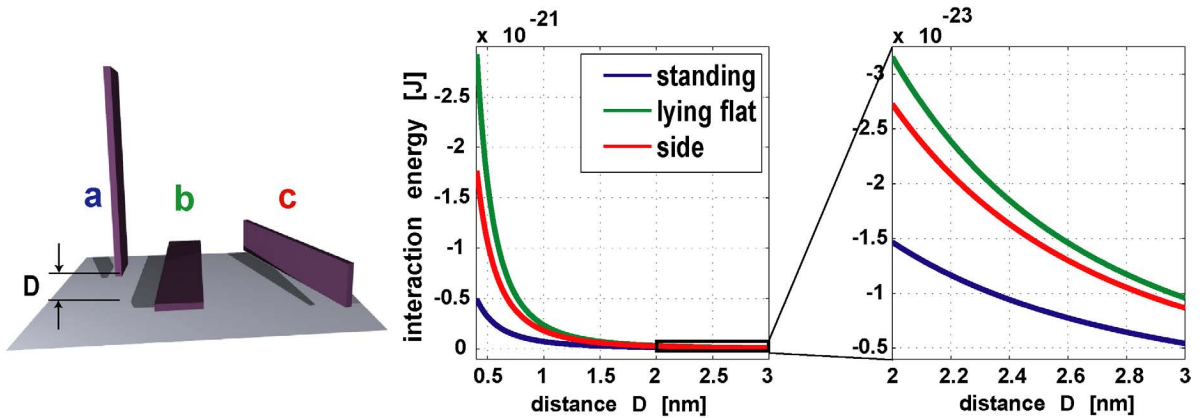


Figure 2.11: Estimated interaction energies of box shaped molecules close to a solid surface in different conformations. (a) in the left scheme shows the molecule standing on the surface, (b) lying flat and (c) standing on the side.

The interaction energies as a function of the distance  $D$  are shown in the graph in the middle of Fig. 2.11. The graph on the right side zooms into the region where  $2 \text{ nm} < D < 3 \text{ nm}$ ,

as indicated by the black box. Please note that even in a distance of  $3nm$ , which is multiple times the size of the molecule, the differences of the interaction energy of the standing configuration is considerable lower than the at the lying or side conformation.

The forces between box shaped molecules and a solid surface is calculated using Eq. 2.15. The force on a molecule in standing configuration is

$$F_{box\_stand}(D) = \frac{AHB}{6\pi} \left[ \frac{1}{D^3} - \frac{1}{(D+L)^3} \right] \quad (2.20)$$

In the same way the forces of the "lying" or "side" configurations can be calculated. A comparison of the forces as a function of the distance is shown in Fig. 2.12. Note the different scale when the distance between the box and the surface increases.

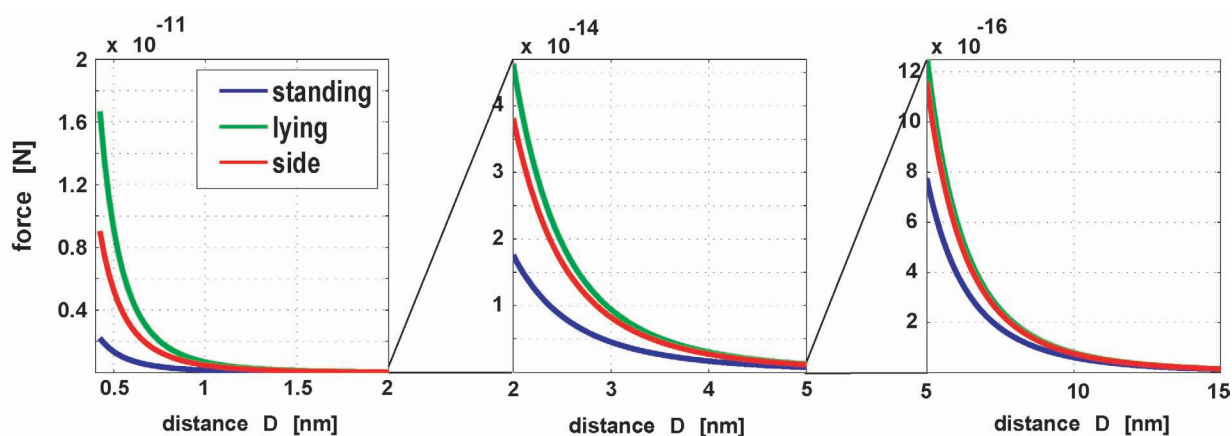


Figure 2.12: Calculated forces on box shaped molecules from a solid surface. In different proximity ranges, the molecules are compared in various conformations, according to the left sketch in Fig. 2.11

As expected, the force on a lying molecule is dominant compared to the forces on molecules in standing configuration or on the side, due to the larger area which is in close contact with the surface. Contrary to the case of cylinder shaped molecules, the box shaped molecules would then rather form a lying phase than a standing phase, if no other forces as van der Waals forces are considered. To get an idea of the stability of single molecules or clusters attaching to a surface, a cylinder model using the dimensions of a pentacene molecule (Fig. 2.13) and an estimation of the thermal energy is presented next.

The thermal energy of a pentacene molecule which is evaporated at  $180^{\circ}\text{C}$  can be estimated to  $E_{\text{therm}} = \frac{f}{2}kT = 2.2 \cdot 10^{-20}\text{J}$  and to  $1.4 \cdot 10^{-20}\text{J}$  at room temperature. Here,  $f$  is the

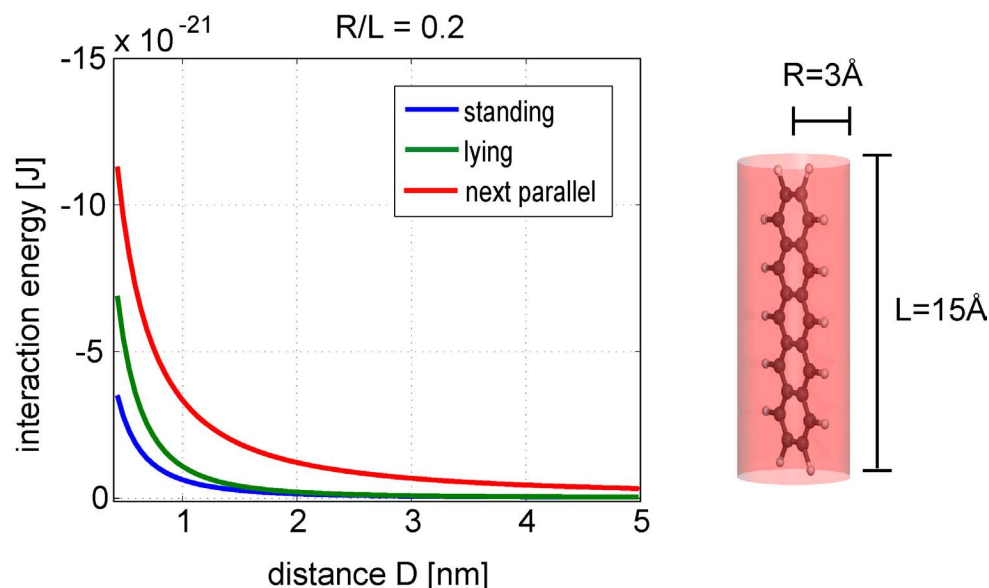


Figure 2.13: Calculation of the interaction energies of a cylinder with the geometry corresponding to the dimensions of a pentacene molecule.

number of degrees of freedom (7, 3 translation, 3 rotation, 1 vibration),  $k$  is the Boltzmann constant and  $T$  the temperature in K. Using the equations summarized in Tab. 2.1, the interaction energies of a cylinder, having a geometry corresponding to the dimensions of a pentacene molecule (radius  $R = 3\text{\AA}$  and length  $L = 15\text{\AA}$ ), in different orientations are calculated. Fig. 2.13 shows a sketch of the cylinder model and the calculated interaction energies in standing or lying conformation on a surface, and the next parallel interaction energy. The next crossed interaction energy is omitted because the approximation used for the calculate is only valid for long thin cylinders. Closer than  $0.4\text{nm}$ , the repulsive forces are getting dominant, thus we use the interaction energy value calculated for a distance  $D = 0.4\text{nm}$  as a measure of the stability of an attached molecule or cluster.

The interaction energies of single molecules and small aggregates of seven molecules in hexagonal packing are evaluated as illustrated in Fig. 2.14. Comparing the estimated thermal energy of  $\approx 2 \cdot 10^{-20}\text{J}$  to the interaction energy of a single cylinder shaped molecule on a surface, which is  $\approx 0.65 \cdot 10^{-20}\text{J}$  in a lying conformation or  $\approx 0.4 \cdot 10^{-20}\text{J}$  in a standing conformation, we find that the thermal energy is considerable higher. Hence an attachment of single molecules without other attractive forces than the London component of the van der Waals forces is very unlikely. This is also true if comparing the thermal energy to the values obtained from the box model (Fig. 2.11).

An aggregate of seven cylinder shaped molecules in a hexagonal packing in a lying phase (Fig. 2.14d) is estimated to be stabilized on the surface by two times the interaction energy of a lying molecule (white double sided arrows) to  $\approx 1.3 \cdot 10^{-20}\text{J}$ , which is slightly below the

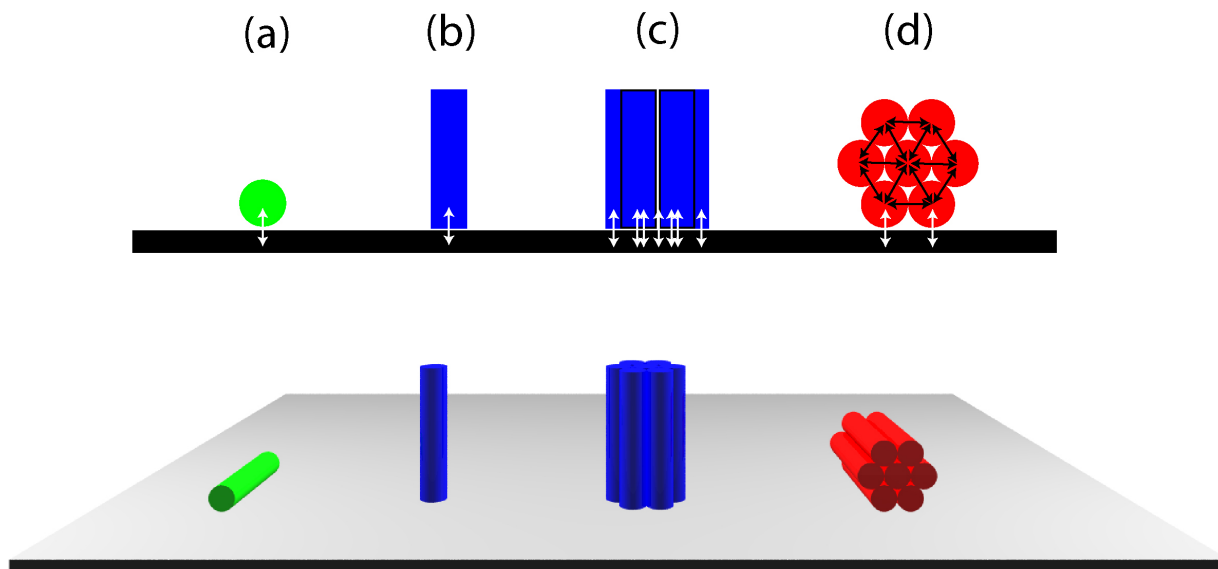


Figure 2.14: Illustration of how the interaction energies of different molecular orientations as single molecules or aggregates are estimated.

thermal energy and thus unstable. The molecule - molecule interaction energy stabilizing the cluster can be approximated by eleven times the next parallel interaction (black double sided arrows in Fig. 2.14d) to  $\approx 12 \cdot 10^{-20}\text{J}$ , which is  $\approx 6$  times the thermal energy. At room temperature, a cluster of three molecules or more would already have an interaction energy higher than the thermal energy and most likely be stable and tend to grow.

In a standing configuration, the interaction energy between the aggregate of seven cylinder shaped molecules and the surface is estimated by seven times the interaction potential of one molecule in a standing configuration (white double sided arrows in Fig. 2.14 b, c) to  $\approx 2.1 \cdot 10^{-20}\text{J}$ , which is slightly higher than the thermal energy at room temperature. According to the calculation, clusters with a size of more than  $\approx 7$  molecules are stable in a standing phase.

## 2.6 Molecule - Molecule Interaction

Now we look at the molecule - molecule interaction using the box model. First, the interaction of a point particle with a box shaped object (length  $L$ , width  $B$  and height  $H$ ) is calculated as illustrated in Fig. 2.15. A particle is considered to be placed in the origin. The box is located at a distance  $D$  in the  $z$ -direction, oriented in a way that the  $L$  is defined along the  $y$ -axis,  $B$  along the  $x$ -axis and  $H$  along the  $z$ -axis. The distance from the particle to a volume increment  $dx dy dz$  is  $r = \sqrt{x^2 + y^2 + z^2}$ . Assuming an attractive pair potential as described in Eq. 2.2 and applying the cartesian coordinate system, the interaction potential of the particle and the box is

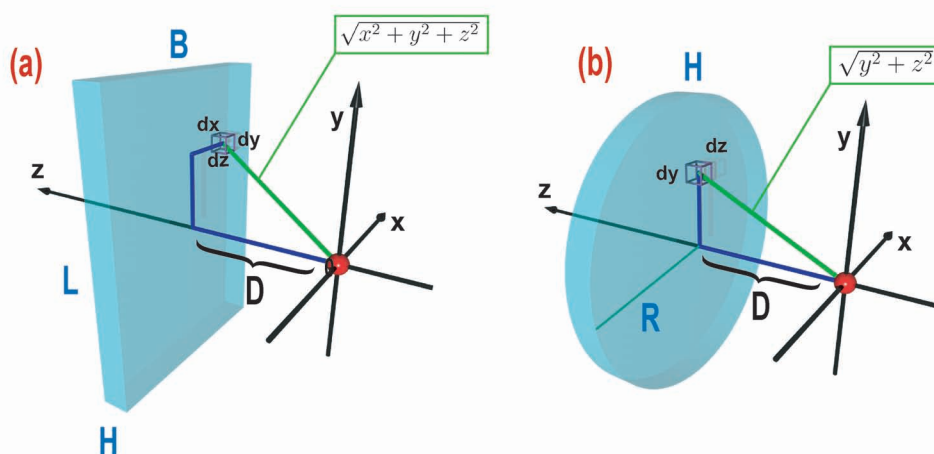


Figure 2.15: (a) The volume increment  $dx dy dz$  of a box is considered to interact with the particle at the distance  $r = \sqrt{x^2 + y^2 + z^2}$ . The net interaction is obtained by integrating over the box volume. (b) Disc shaped molecule interacts with a particle.

$$w_{\text{box}}(D) = -C \rho_{\text{box}} \int_{z=D}^{D+H} \int_{y=-L/2}^{L/2} \int_{x=-B/2}^{B/2} \frac{1}{(x^2 + y^2 + z^2)^{\frac{n}{2}}} dx dy dz \quad (2.21)$$

An analytical solution of this integral is not known and as a numerical solution needs extensive calculation effort and is found to induce large errors due to the use of simplifications, and given that this is an experimental work, this approach is not further pursued. Thus the box - box interaction is approximated by two opposing discs, having the same volume as the boxes. This reduces the dimension of the problem by 1 because of radial symmetry. The radius of the discs is  $R_{\text{disc}} = \sqrt{\frac{L \cdot B}{\pi}}$ . In the example shown above, the radius would be  $4.037 \text{ \AA}$ . To calculate the interaction between a particle and the disc, a volume increment of  $2\pi r \rho_{\text{disc}} dr dz$  (Fig. 2.15b) is integrated over the volume of the disc, multiplied by the

London constant  $C$ .

The specific case of  $n = 6$  (van der Waals like forces) is considered. With the assumptions that  $R > 0$  and  $z \geq 0$ , the interaction energy is

$$\begin{aligned}
 w_{disc}(D) &= -2\pi C \rho_{disc} \int_{z=D}^{D+H} \int_{r=0}^R \frac{r}{(z^2 + r^2)^3} dr dz \\
 &= -2\pi C \rho_{disc} \int_{z=D}^{D+H} 1/4 \frac{R^2 (R^2 + 2z^2)}{z^4 (R^2 + z^2)^2} dz
 \end{aligned} \tag{2.22}$$

The integration is done with *Maple*. An abstract of the worksheet is shown in Fig. 2.16

$I := \frac{y}{(y^2 + z^2)^{\left(\frac{6}{2}\right)}}$	<i>Maple worksheet</i>
$\frac{y}{(y^2 + z^2)^3}$	(3)
$B := \text{int}(I, [y=0..R]) \text{ assuming } R > 0, z \geq 0$	
$\frac{1}{4} \frac{R^2 (R^2 + 2z^2)}{z^4 (R^2 + z^2)^2}$	(4)
$C := \text{int}(B, [z=D..(D+H)], \text{AllSolutions}) \text{ assuming } D \geq 0, H > 0, R \geq 0$	
$  \begin{aligned}  & - \frac{1}{24} \left( 9 D^4 \arctan\left(\frac{D+H}{R}\right) H^2 R^4 + 3 D^6 \arctan\left(\frac{D+H}{R}\right) R^4 + 30 D^7 \arctan\left(\frac{D+H}{R}\right) H^3 \right. \\  & \quad - 30 \arctan\left(\frac{D}{R}\right) D^8 H^2 - 3 \arctan\left(\frac{D}{R}\right) D^6 R^4 + 6 D^8 \arctan\left(\frac{D+H}{R}\right) R^2 \\  & \quad - 15 \arctan\left(\frac{D}{R}\right) D^9 H - 6 \arctan\left(\frac{D}{R}\right) D^8 R^2 + 15 D^9 \arctan\left(\frac{D+H}{R}\right) H \\  & \quad \left. + 15 D^6 \arctan\left(\frac{D+H}{R}\right) H^4 - 15 \arctan\left(\frac{D}{R}\right) D^6 H^4 - 12 D^5 R H^4 - 3 R D^4 H^5 \right)  \end{aligned}  $	(5)

Figure 2.16: Abstract of the *Maple* worksheet calculating the integral in Eq. 2.22. Shown here is a simplified version of the result, obtained by applying the *Maple* function "simplify()". In the calculations, the original result is used.

If the radius  $R$  of the disc and its thickness  $H$  goes to infinity, the solution matches Eq. 2.4, the interaction of a point particle and a solid surface. In Fig. 2.17 the force (as defined in Eq. 2.15) on a particle in front of a disc in different geometries (thickness  $H = 2nm$  and radii  $R = 0.5nm, 5nm$  and  $10nm$ , green curves) is compared to the the force on a particle in front of a surface (blue curves). As expected, at distances larger than  $10nm$ , the force

acting on a particle in front of a surface is considerably higher than in front of a disc. However, the difference between the forces on a particle is decreasing clearly at smaller distances. Even when a very small disc with a radius of only  $0.5\text{nm}$  is considered, the force on a particle in a distance  $< 1\text{nm}$  is less than a factor  $\approx 2$  lower than in front of a surface.

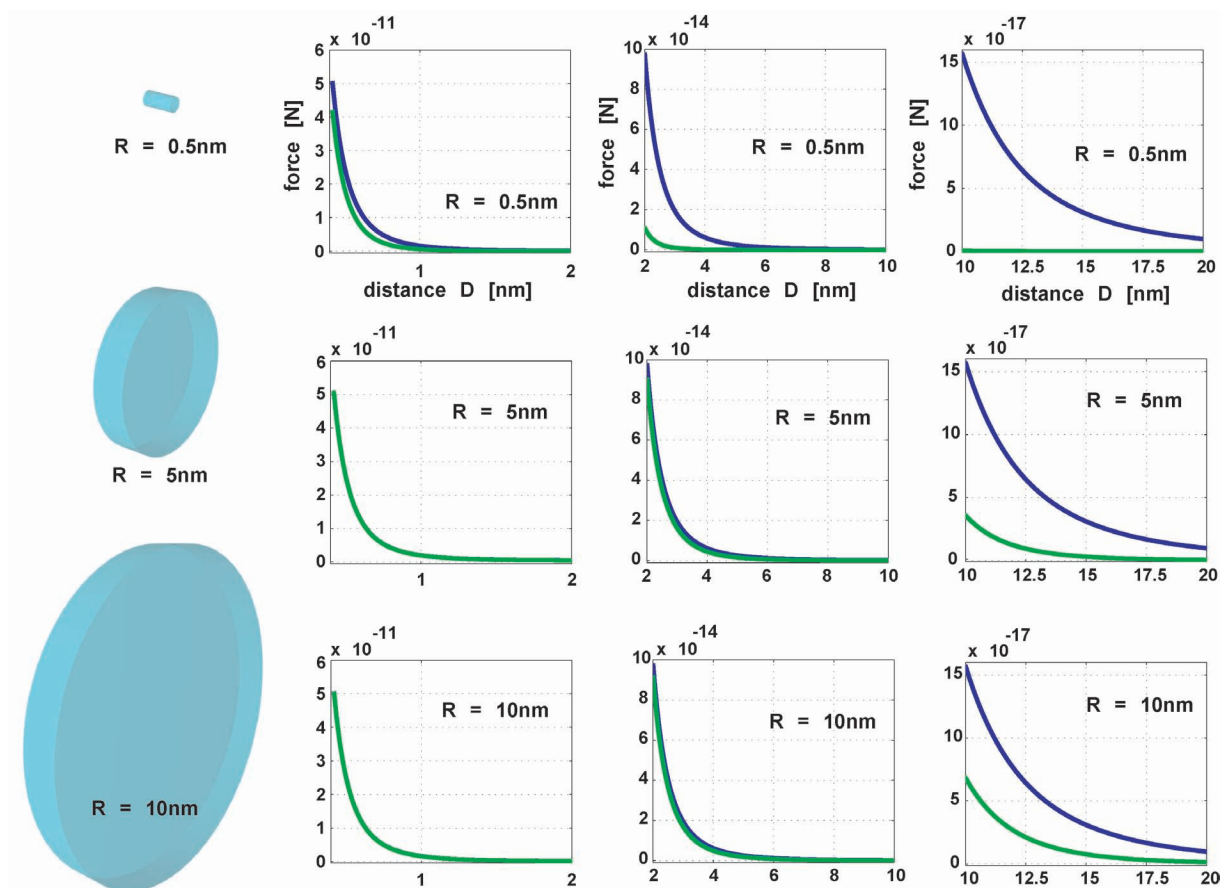


Figure 2.17: Comparison of the force on a particle in a distance  $D$  in front of a disc (green curves) with radius  $R$  and thickness  $H = 2\text{nm}$  (see Fig. 2.15) and the force on a particle close to a semi-infinite surface (blue curves)

Concerning the aggregation of molecules on a surface, this tells us that once the molecule is close to the surface, only the nanoenvironment of the surface is contributing to the forces on the molecule. In the region closer than  $2\text{nm}$  we find no considerable difference of the force on a point particle between a disc with radius  $5\text{nm}$  and thickness  $2\text{nm}$  and a semi-infinite surface (Fig. 2.17, middle left graph). Thus, chemical or physical defects of the size of a few nanometer may completely determine the growth in this area, possibly leading to different crystal structures.

The next step towards a calculation of discs in a face to face geometry is to consider a point

particle which is considered to be positioned in a distance  $D$  away from the disc shaped molecule and having a distance  $S$  from the rotation axis of the disc. As shown in Fig. 2.18, the integration splits up in two parts. To calculate the interaction potential, at first the volume of the disc with radius  $(R - S)$  is calculated using Eq. 2.22. In a second step, we consider all volume increments with the same distance to the particle, as indicated by the outer dashed circle. The fraction ( $\equiv A$ ) of volume increments inside the disc (green part of dashed circle) is calculated using the relation  $\gamma = \arccos\left(-\frac{R^2 - S^2 - r'^2}{2Sr'}\right)$  to

$$A = \frac{\gamma}{\pi} = \frac{1}{\pi} \arccos\left(-\frac{R^2 - S^2 - r'^2}{2Sr'}\right) \quad (2.23)$$

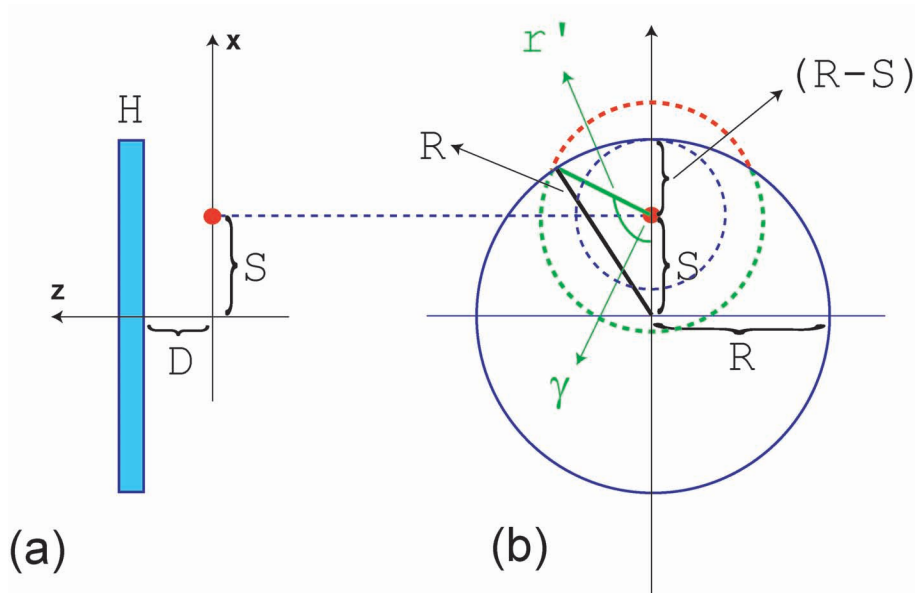


Figure 2.18: (a) Side view of a particle close to a disc in a distance  $D$  from the surface and  $S$  from the center. (b) Front view to illustrate the integration method. For each position of the particle ( $S$ ), the interaction is a sum of the quasi disc below the particle (black dashed circle, calculated using Eq. (5) in Fig. 2.16) and an integration from  $R - S$  to  $R + S$  over the outer circles, taking into account that only a fraction (green dashed part of the circle, defined as  $A$ ) attributes to the interaction.

Combining both parts, the interaction of a particle being asymmetric in front of a disc is

$$w_{disc,asym}(D, S) = w_{disc}(D)_{R=(R-S)} - 2\pi C \rho_{disc} \int_{z=D}^{D+H} \int_{r'=R-S}^{R+S} A \frac{r'}{(r'^2 + z^2)^3} dr' dz \quad (2.24)$$

*Maple worksheet*

```

restart;
Digits := 100;
const := 1E-77;
results := Array();
I :=  $\frac{y}{(y^2 + z^2)^3}$ ;
B := int(I, [y=0..r]) assuming r :: real, r ≥ 0, z :: real, z > 0, y :: real, y > 0;
D := 4E-10;
H := 1E-10;
rhodisc :=  $\frac{1}{\pi} \cdot 1E29$ ;
C := int(B, [z=D..D+H]) assuming z :: real, R :: real, R ≥ 0;
w := -2·π·const·rhodisc·C;
A :=  $\frac{1}{\pi} \arccos\left(-\frac{R^2 - S^2 - a^2}{2 \cdot R \cdot a}\right)$ ;
R := 4.037E-10;
steps := 100;
for i from 1 to steps do
  S :=  $\frac{R}{steps} \cdot i$ ;
  wdisc := eval(w, r = R - S);
  F := int( $\frac{A \cdot a}{(a^2 + z^2)^3}$ , [a = R - S..R + S]) assuming z :: real, a :: real;
  Final := int(F, [z = D..D + H]);
  results(1, i) := S;
  results(2, i) := wdisc - 2·π·const·rhodisc·Final;
end do;
results;
VecX := results(1, 1..steps);
VX := convert(VecX, Vector);
VecY := results(2, 1..steps);
VY := convert(VecY, Vector);
plot(VX, VY, style = point, color = blue);
save results, "resultsfull100steps100digits.txt";

```

Figure 2.19: Implementation of the integration loop in *Maple*. Calculation time about 80 min on a Intel Core 2 Quad Q9550 2.83GHz/6144KB with 8GB DDR2-800 RAM.

As an example, the specific case where a particle is in front of a disc with the dimensions  $R = 4.037 \text{ \AA}$  and  $H = 1 \text{ \AA}$  in a distance of  $D = 4 \text{ \AA}$  is calculated (see Fig. 2.19). The solution was implemented in *Maple* as a loop which evaluates the full interaction of a particle at a given distance  $S$  from the symmetry axis in 100 steps from  $0 \text{ \AA}$  to  $4.037 \text{ \AA}$ .

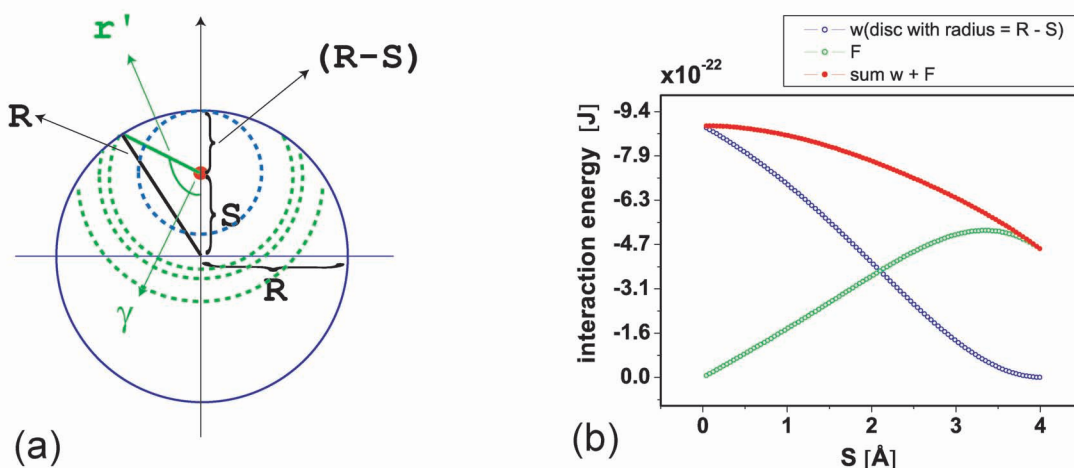


Figure 2.20: (a) Schematic representing the different integration regimes (b) plot of the calculated interaction energy of a particle being  $4 \text{ \AA}$  away from of disc with  $H = 1 \text{ \AA}$  and  $R = 4 \text{ \AA}$  as a function of the displacement  $S$  (distance from the rotation axis).

In Fig. 2.20 (b) the calculated values are plotted as a function of  $S$ . The green curve in (b) shows the contribution of the second term in Eq. 2.24 and refers to the segments of the green circle in (a), while the blue curves represent the first term, referring to the blue dashed circle in the schematic in (a). The red curve is the sum of the blue and the green curve and represents the full interaction of a particle in a distance  $S$  from the symmetry axis, using the parameters given above.

To visualize the results, a polynomial function of 6th degree was fitted to the calculated points using the fitting toolbox of *MatLab*. The function found is  $w = 6.3025 \cdot 10^{33} \cdot S^6 + 2.5818 \cdot 10^{25} \cdot S^5 + -1.8616 \cdot 10^{16} \cdot S^4 + 1.3472 \cdot 10^6 \cdot S^3 + 0.0033312 \cdot S^2 + 1.0314 \cdot 10^{-14} \cdot S - 8.9262 \cdot 10^{-22}$ . In Fig. 2.21 (a) the upper graph shows the data (blue points) and the fitted curves (blue and purple lines, 6th degree and cubic polynomial). The lower graphs plots the residuals of the fits. The norm of the residuals is  $2.9263 \cdot 10^{-25}$  in the case of the 6th degree polynomial. (b) demonstrates the interaction energy of an infinitesimal thin disc in front of the disc shaped model calculated above. Because of the finite size of the disc, the interaction energy of a particle and a disc shaped molecule is considerably larger in the center than in the outer region of the disc (see Fig. 2.21,(b)). This supports the self assembling character of organic molecules, because in order to minimize their interaction energy, two opposing discs would have to align their rotation axis. This approximation is limited to the case of two isolated molecules interacting. In an organic crystals of e.g.

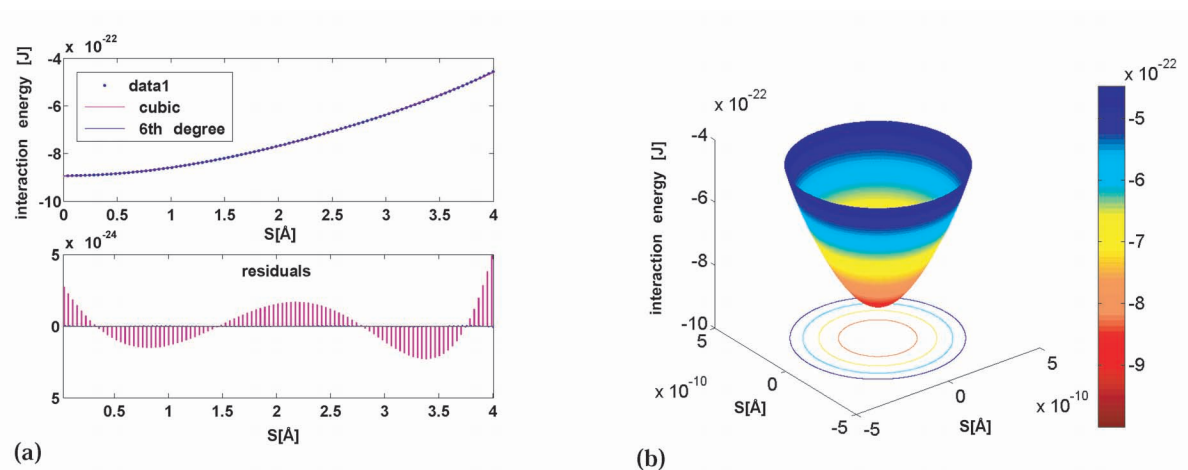


Figure 2.21: (a) Polynomial fits and residuals of the calculated interaction potential of a particle at position  $S$  away from the center in front of a disc (see Fig. 2.20a) (b) 3D visualization of the situation corresponding to the interaction of a disc in front of a disc.

coronene (Fig. 2.2a), a herringbone structure turns out to minimize the interaction energy, in which the rotation axis of the molecules are not aligned.

## Conclusion

In conclusion we can understand why rod like molecules arrange in a standing phase on smooth inert substrates. At distances a few times the size of a molecule or larger, the attractive forces between the molecules are considerable higher than the forces between the molecules and the surface. This leads to an aggregation of molecules to larger clusters, provided that enough molecules are available. As a consequence of the clustering, the aspect ratio ( $R/L$ ) changes towards a configuration which prefers a standing orientation on the surface. Once the first clusters have nucleated at the surface, incoming molecules find their way to an existing island and aggregate, a concept which is already established for point particles and called diffusion limited aggregation (DLA).

This effect is found to be even stronger when considering long and thin cylinder shaped molecules, thus we can also understand how those molecules form a standing phase on a smooth inert surface, which is quite counterintuitive at first thought. The observed lying phase in thicker films or on top of other organic films can be explained by the high roughness of these surfaces. Here, it is possible for molecules to attach to sites where the molecule is in contact with a larger area of the surface, which leads to enhanced attractive forces.

The intrinsic defects found in organic crystals, especially at grain boundaries, can be explained by taking into account the anisotropic forces acting on the molecules. If we assume

the molecules to be flexible, it is possible that a molecule and consequently the whole crystal deforms under the influence of the forces (like it has been shown for some organic molecules already [14]). This topic is especially interesting if we consider an organic crystal with grain boundaries and regions where the layers are incomplete. In the middle of a crystal grain, the molecules have many neighboring molecules in every direction. Assuming symmetric molecules, this leads to an averaging of the forces, and a symmetric crystal structure should be the most stable configuration. At the boundary of a grain, a molecule is missing neighbors in one or two directions. As a result, a slightly deformed crystal structure might be the most stable configuration. This picture is also in good agreement with the observation that the diffuse scattering intensity measured from organic films is not a function of the temperature. As concluding remark it is mentioned that of course also the repulsive forces should be taken into account to gain a more detailed picture of the situation. The purpose of the proceeding was to develop an intuitive understanding of the main effect.

In the following chapter, the organic semiconductor used in this thesis, pentacene ( $C_{22}H_{14}$ ), is introduced and experimental data of the film growth on various substrates is presented.

# Chapter 3

## Growth of Pentacene Thin Films on Technically Relevant Surfaces

### 3.1 Experimental – Organic Molecular Beam Epitaxy

The organic thin films in this thesis are grown in high vacuum with a base pressure  $< 1 \cdot 10^{-7}$  mbar. A custom designed evaporation gun is mounted in a vacuum chamber and contains the material of choice (Fig. 3.1). The design is chosen to provide reproducible deposition rates (ranging from  $0.05 \text{ \AA}/s$  to  $\approx 10 \text{ \AA}/s$ ) by controlling the temperature at the exit of the gun with a temperature sensor (PT100) and a halogen bulb (20W) heating. Temperatures from room temperature to  $500^\circ\text{C}$  can be realized.

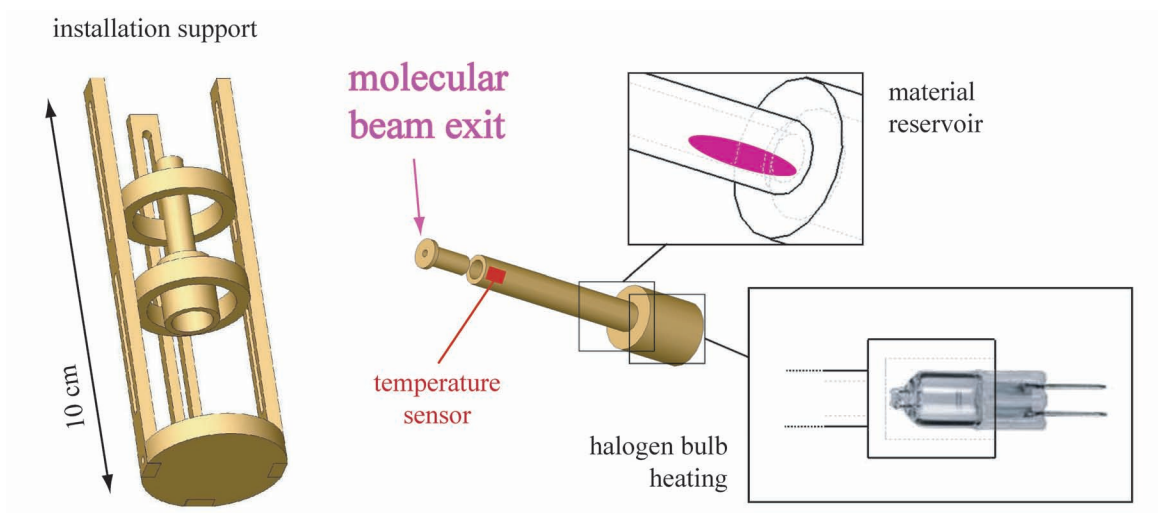


Figure 3.1: Design of the evaporation cell used to grow organic thin films in high vacuum.

For each material, a separate evaporation gun is mounted inside the vacuum chamber. The guns are made of ultra pure aluminum or high-grade steel and are positioned pointing

slightly upwards to avoid loss of material. The tube containing the gun can be closed with a shutter at the frontend. To be able to set a deposition rate of interest, the shutter is equipped with a quartz crystal microbalance. A second thickness monitor is located next to the sample holder at the same distance to the evaporation gun as the samples. The whole setup is controlled with a *LabView*® program (see Fig. 3.3) which collects, handles and saves all the important deposition parameters.

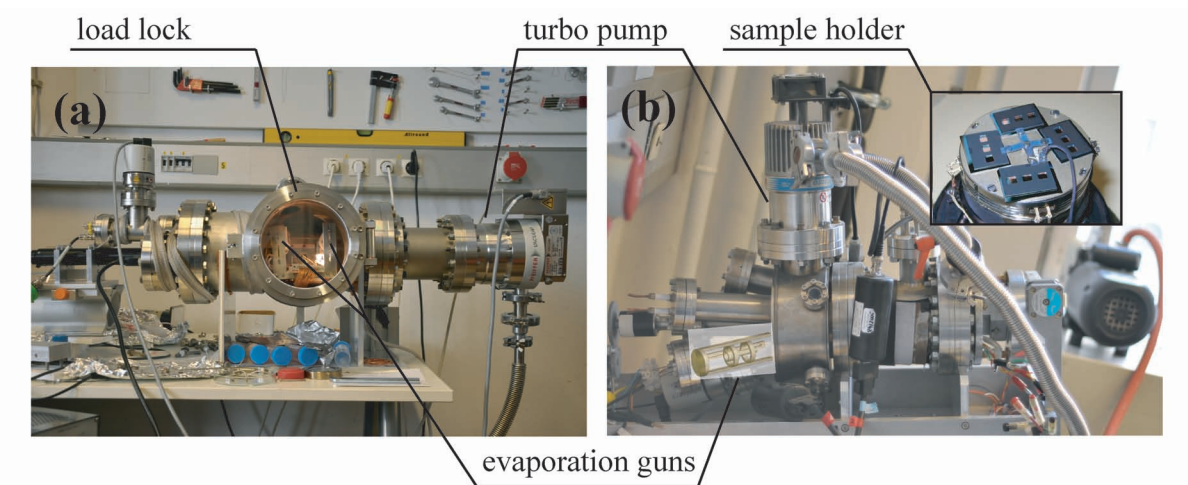


Figure 3.2: Photographs of the vacuum deposition chambers. (a) the larger chamber to produce the large size samples for the neutron measurements. (b) mobile UHV chamber capable of producing four samples at once (inset shows the sample holder).

As a substrate we use doped silicon wafers as purchased from *SiMat*® with thermal silicon oxide as a top layer. The thickness of the oxide layer was in the order of 500nm. Before the organic thin films are grown, the samples are cleaned chemically using a standard silicon wafer cleaning method [15], and are annealed at 180°C for 20 min. Depending on the surface treatment prior to deposition, the annealing step has sometimes to be done at lower temperatures or even omitted. Fig. 3.3 shows a screenshot of the control software while annealing samples. Pictures of the vacuum chambers are shown in Fig. 3.2. These chambers are custom made to match the specific requirements for organic thin film deposition. Crucial parameters are the purity of the organic material, the deposition rate, the sample temperature and the base pressure. Furthermore the sample surface chemistry highly influences the thin film growth.

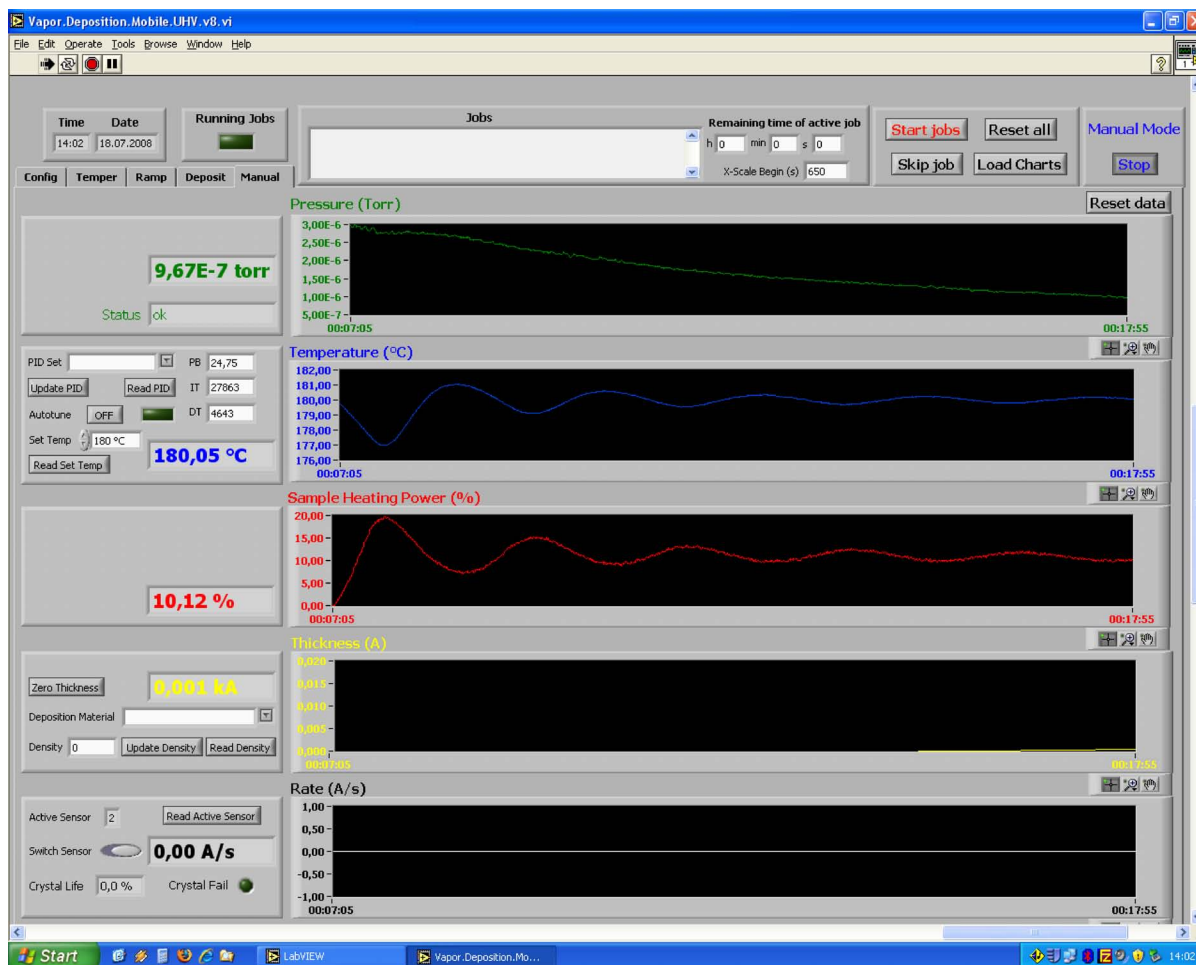


Figure 3.3: Screenshot of the LabVIEW® program used to control the evaporation chamber. A typical sample bakeout situation is displayed, where the samples are heated to 180°C prior to deposition of the organic material.

## 3.2 Pentacene

The small aromatic molecule pentacene ( $C_{22}H_{14}$ , Fig. 3.4,a) is of special interest because of its ability to form layered crystals on smooth inert surfaces [7]. In that structure, the film exhibits semiconducting properties with a high charge carrier mobility [5]. The possibility to grow such thin films in high vacuum using organic molecular beam epitaxy (sec.3.1) allows to coat various surfaces in a very clean and non invasive fashion. Fig. 3.4 (b) shows an atomic force microscopy (AFM) micrograph (amplitude image) of 50nm pentacene film grown on a smooth inert substrate. Furthermore the films can be patterned with the use of shadow masks, which enables the construction of electronic devices such as thin film transistors (TFT). The raw material can meanwhile be purchased in triple sublimed purity from *Sigma Aldrich* ®. It turned out that the purity of the base material plays a crucial role in the performance of the devices.

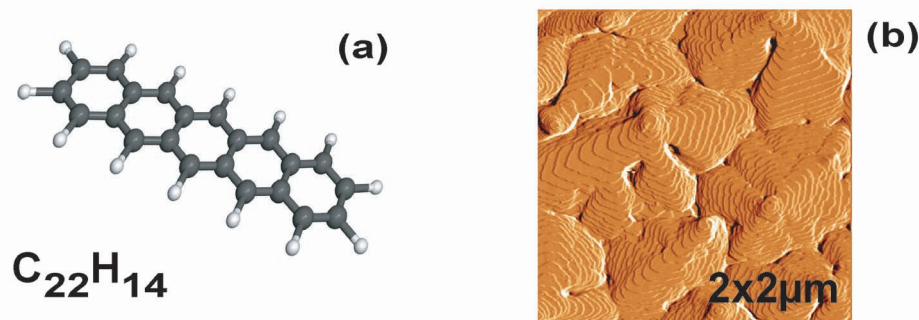


Figure 3.4: (a) The chemical structure of pentacene. (b) micrograph of 50nm pentacene grown on a smooth surface.

Pentacene is sensitive to photo oxidation, thus it should be stored in vacuum and kept dark. The oxidized molecule, pentacene-quinone, severely worsens the transistor characteristics [16] if incorporated in the active layer. Device layouts and performances as well as electronic properties and are specified in [5, 17, 18] and [19]. High-cited contributions in the field are the work of Dimitrakopoulos et.al. [20, 21, 22], Sirringhaus et.al. [23] and Klauk et.al. [24]. A collection of optical experiments can be found in [3, 25, 26].

If grown as a thin film, different polymorphs with slightly modified molecular orientations are found to be stable, depending sensitively on the growth parameters (deposition rate, pressure, etc.) and on the substrate properties (roughness, hydrophobicity, temperature, etc.). A substantial investigation from first principles is presented in [27].

The following sections present an overview of the growth of pentacene on substrates and surfaces relevant for this thesis. At first, a set of possible gate dielectrics for later use in field effect devices is compared in terms of morphology and structure. The second section aims to highlight the strong dependence of the growth on the surface chemistry, illustrated by growing thin films of pentacene on chemically modified diamond surfaces.

### 3.3 Pentacene on Gate Dielectrics

The growth of pentacene thin films is mostly influenced by the electronic properties and the surface roughness of the surface. As gate dielectrics in field effect devices, metal oxides with thicknesses of several hundred nm have proven to be appropriate materials. Qualitatively the growth mode is similar on most insulating surfaces with a roughness in the order of a few Å [7]. Various different surface modification are suggested in the literature to improve device characteristics, ranging from polymers [24,28,29] and sputtered oxides [30] to self assembled monolayers [31].

Here, we modified the bare silicon dioxide surface by spincoating polymers from solution and self assembly of alkane thiols (octadecyltrichlorosilane, OTS). Two different polymers were used, a cyclic olefin copolymer (COC) and polystyrene (PS). These modifications lead to very smooth hydrophobic surfaces. As an example, the specular X-ray pattern of a 6.5nm polystyrene coating on a silicon wafer with 20nm thermally grown oxide is shown in Fig. 3.5. Using X-ray reflectometry the layer thickness and the scattering length density was determined as described in [32].

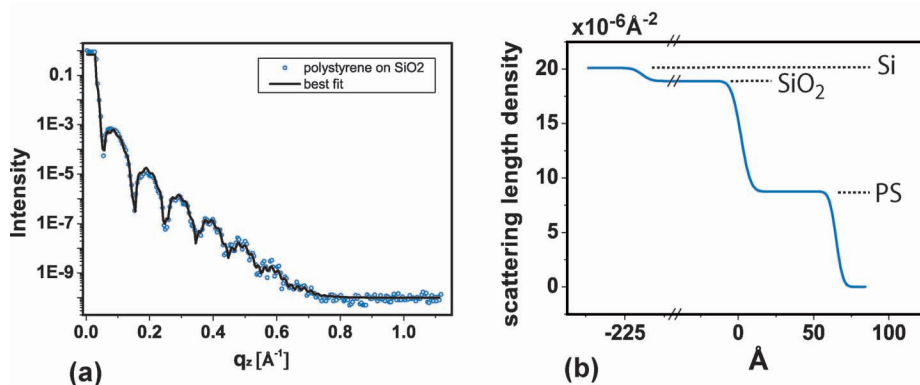


Figure 3.5: (a) Specular X-ray reflectivity of a 6.5nm polystyrene layer on a silicon wafer with 20nm thermally grown oxide (b) Extracted scattering length density profile. Dashed lines indicate the different materials.

A balance of the interaction between the surface and the molecules and the interaction between the molecules themselves will determine the crystal structure (see Ch. 2). Therefore

it is important to study the initial growth by depositing an amount of the material with the mass equal to 1 monomolecular layer, if distributed homogeneously on the surface. An example of 1 monolayer (ML) pentacene on bare silicon dioxide is shown in Fig. 3.6.

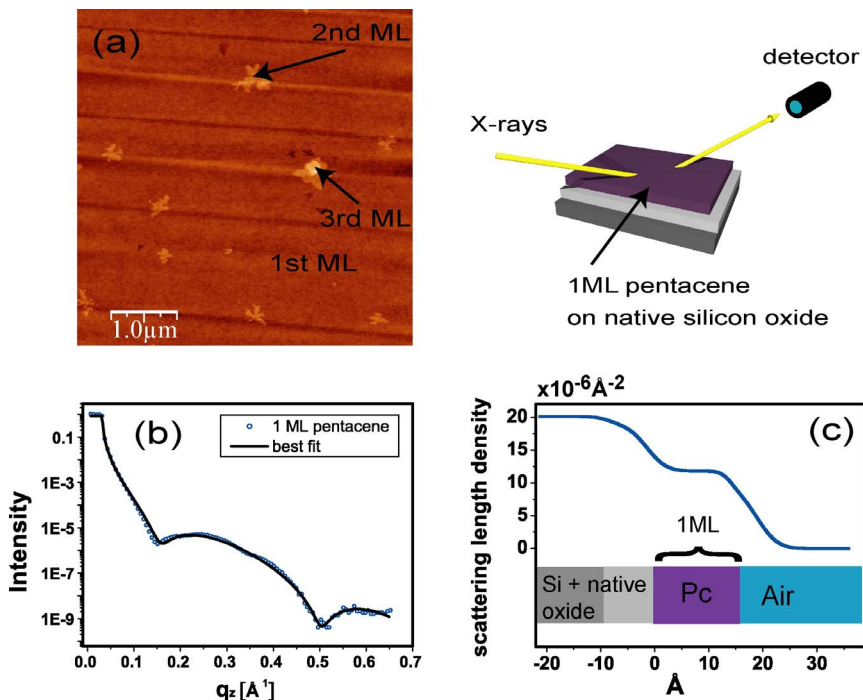


Figure 3.6: (a) AFM micrograph of 1 monolayer pentacene on native  $\text{SiO}_2$ . (b) X-ray reflectometry curve (open symbols) and the best fit (line). (c) extracted scattering length density profile, indicating the presence of a closed first monolayer of pentacene.

The atomic force microscopy (AFM) micrograph in Fig. 3.6a shows that the native  $\text{SiO}_2$  surface is almost completely covered by the first monolayer. Second layer growth already started, which can be seen as small fractal shaped islands on top of the first layer. A very small fraction of third layer growth is also observed. The layer thickness determined to  $1.5 \text{ nm}$  by AFM (Fig. 3.8) and X-ray reflectometry (Fig. 3.6c) indicate that the pentacene molecules arrange in a standing configuration, with its long molecular axis perpendicular to the surface (Fig. 3.7b). This observation is in agreement with the theoretical calculation that a pentacene molecule (geometry  $R/L \approx 0.2$ ) in close contact to other pentacene molecules and a surface feels the strongest forces parallel to the next neighbor and in standing configuration on the surface (Fig. 2.8). Both cases are best matched in the observed film morphology.  $50 \text{ nm}$  thick films of pentacene have been grown as described in 3.1 to further study the internal ordering of the molecules inside the film. AFM analysis showed the formation of layered crystals and the typical pyramid shape of the crystal grains 3.8. Clearly visible are the monomolecular steps of the distinct layers in the form of terraces. The stepheight corresponds to the  $d_{00l}$  spacing of the crystal structure and measures  $1.5 \text{ nm}$

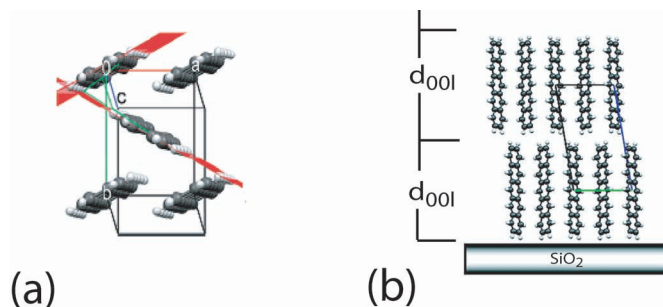


Figure 3.7: Sketch of the orientation of the pentacene molecules inside the thin film. (a) Top view. The herringbone angle (between the red planes) is highlighted. (b) Side view. The  $d_{00l}$  spacing varies in different polymorphs.

(see profile in Fig. 3.8). The high roughness can be explained by the observation that second and third layer growth already started before the first monolayer is completed. This lowers the diffusion on top of the first monolayer and leads to more nucleation sites, where the pentacene molecules may aggregate. With increasing film thickness, an increasing number of nucleation sites is available. Depending on the growth parameters and the surface chemistry, different polymorphs have been found to form stable crystallites [33, 7]. Most commonly found in thin films grown by vacuum deposition are the so-called "thin film" and "bulk" phases, which differ in the angles between the molecules and the surface, leading to a characteristic  $d_{00l}$  spacing (Fig. 3.7b) of 15.4Å (thin film phase) and 14.4Å (bulk phase).

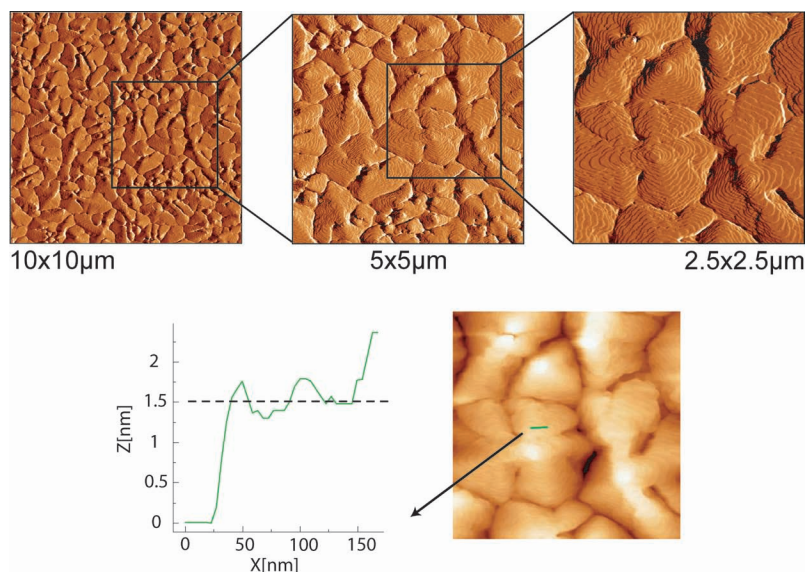


Figure 3.8: Upper row: AFM amplitude images of 50nm pentacene on polystyrene coated SiO<sub>2</sub>. Graphs to the right zoom into the marked region of the respective left graph. Lower row: height image and profile along the green line across a monomolecular step.

As the electronic properties depend on the crystal structure, the main motivation to modify the surface is to improve the device performance. Calculations showed that the "thin film phase" is best suited for the use in field effect devices [34]. The resolution of the atomic force microscope is not sufficient to distinguish between the crystal polymorphs in pentacene thin films. To investigate the molecular orientation inside the thin films, specular and off-specular X-ray diffraction experiments were performed. The molecular orientation of the crystal leads to a characteristic diffraction pattern containing the structural information on a length scale in the order of the wavelength used ( $1.18\text{\AA}$ ). Methods and interpretation are explained in [32]. In the following we compare films with  $\geq 10$  ML of pentacene on different surfaces. X-ray reflectivity curves of 50nm pentacene films on six different surfaces are summarized in Fig. 3.9. All films were grown at ambient temperature in high vacuum (base pressure  $< 10^{-7}\text{mbar}$ ) with a deposition rate of  $0.1\text{\AA}/\text{s}$ . All substrates were cleaned using a standard wafer cleaning procedure before further modifications were applied. The two bare silicon oxide surfaces (commercial and selfmade oxide) were annealed to  $120^\circ\text{C}$  for 10 minutes in vacuum prior to pentacene deposition. Polymers (PS and COC) were dissolved in toluene ( $0.25\text{wt}\%$ ) and spincoated on the surface using a Delta BLE spincoater. The silanization (OTS) is done in dehydrated n-hexan in nitrogen environment. The TTC ( $\text{C}_{44}\text{H}_{90}$ , tetratetracontane) coating was vacuum deposited at ambient temperature with a rate of  $0.1\text{\AA}/\text{s}$ .

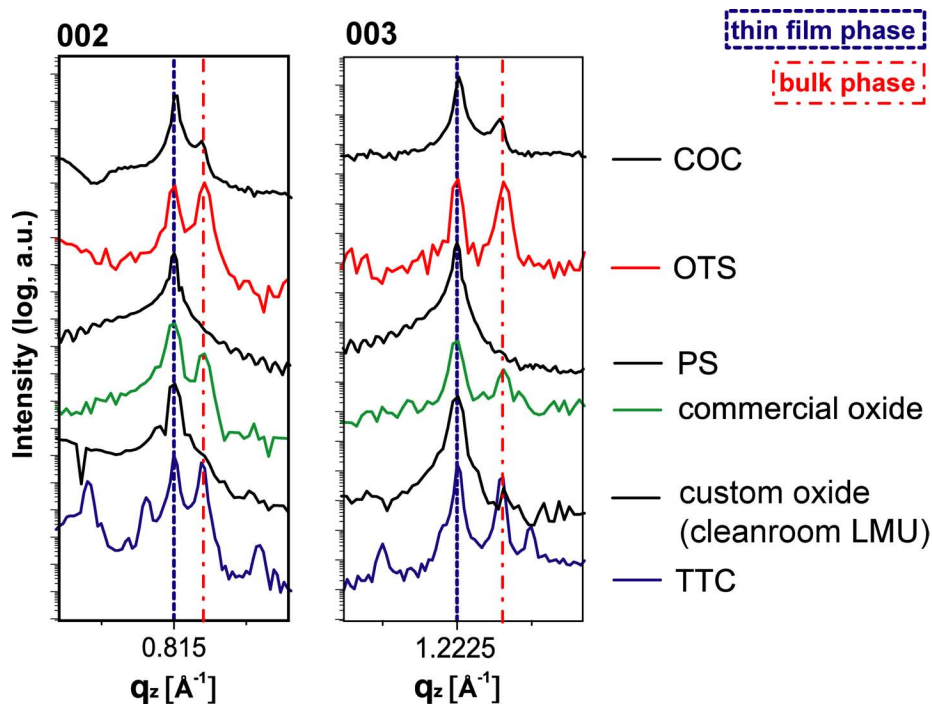


Figure 3.9: Comparison of the measured X-ray reflectivity of 50nm pentacene on different surfaces. Graphs zoom in around the typical 00l reflections of the thin film and the bulk phase of pentacene. Curves are vertically displaced for clarity.

The dashed blue lines in Fig. 3.9 indicate the expected positions of the 00l reflections of the thin film phase ( $q_{00l} = l \cdot 0.4075 \text{ \AA}^{-1}$ ,  $d_{00l} = 15.4 \text{ \AA}$ ) of pentacene. The positions of the 00l reflections of the bulk phase ( $q_{00l} = l \cdot 0.4363 \text{ \AA}^{-1}$ ,  $d_{00l} = 14.4 \text{ \AA}$ ) are depicted with the red dash-dot lines.

We find a mixture of thin film and bulk phase pentacene on the commercial silicon oxide (green curves) and the TTC (blue curves) and OTS (red curves) coated wafers. The COC coated samples (topmost black curve) show a less pronounced bulk phase reflection, whereas the custom made oxide (lowermost black curve) and the PS coated wafer (middle black curve) show exclusively thin film phase reflections.

To solve the orientation of the pentacene molecules inside the thin film, we performed off-specular X-ray diffraction experiments. From a total of 68 Bragg reflections, the molecular orientation was determined by fitting the data to a theoretical model. For details see [7]. It revealed that the molecular arrangement is highly depending on the surface properties, such that calculations of e.g. electronic properties of pentacene films should include these differences. Although the packing is very similar, the slightly tilted orientation of the molecules with respect to each other leads to a different overlap of their pi orbitals, which influences e.g. the intermolecular charge transport.

## 3.4 Pentacene on Modified Diamond Surfaces

Undoped diamond is a good insulator with a large band gap ( $5.5 eV$ ). In 1989 a considerable surface conductivity has been reported on hydrogen terminated single crystal diamond [35] as well as on vapor deposited films [36]. Because of the small temperature dependence and the similar carrier mobilities as in doped diamond, this effect is attributed to holes which accumulate at the surface [37]. In a detailed study, Maier et.al. [38] suggested that electron transfer from diamond to the acidic water redox couple is responsible for the accumulation layer. Underlining the idea of a surface related effect, very high carrier mobility has also been observed using hydrogenated polycrystalline samples [39]. It has also been shown that this surface is sensitive to ions in close vicinity, especially to the adsorption of  $OH^-$  and  $H_3O^+$  ions [40].

Pentacene growth is known to be very sensitive to surface properties. While the structure in thin films grown on smooth insulating surfaces is found to be in a standing configuration (3.7), the molecules form a lying structure on metallic surfaces [41, 42]. This section compares the growth of pentacene thin films on oxygen terminated and hydrogen terminated polycrystalline diamond (PCD:H, PCD:O) and on hydrogen terminated single crystal diamond (SCD:H). In terms of electronic properties, these surfaces are very different. The surface conductivity discussed above is only observed on the hydrogen terminated surface and is absent on the oxygen terminated. In addition, the H-terminated surface is

hydrophobic (contact angle  $\approx 100^\circ$ ) while the O-terminated diamond is hydrophilic (contact angle  $\leq 20^\circ$ ). Pentacene films on the diamond surfaces are grown in high vacuum at ambient temperatures with a deposition rate of  $0.05 \text{ \AA}/s$ , as described in section 3.1. The hydrogen and oxygen terminations were done by the group of Jose Garrido, TUM, Walter Schottky Institute. The oxidation of the surface was achieved by immersing the sample in sulfuric acid (50%) for 30min. The H-termination was done in a hot wire reaction chamber.

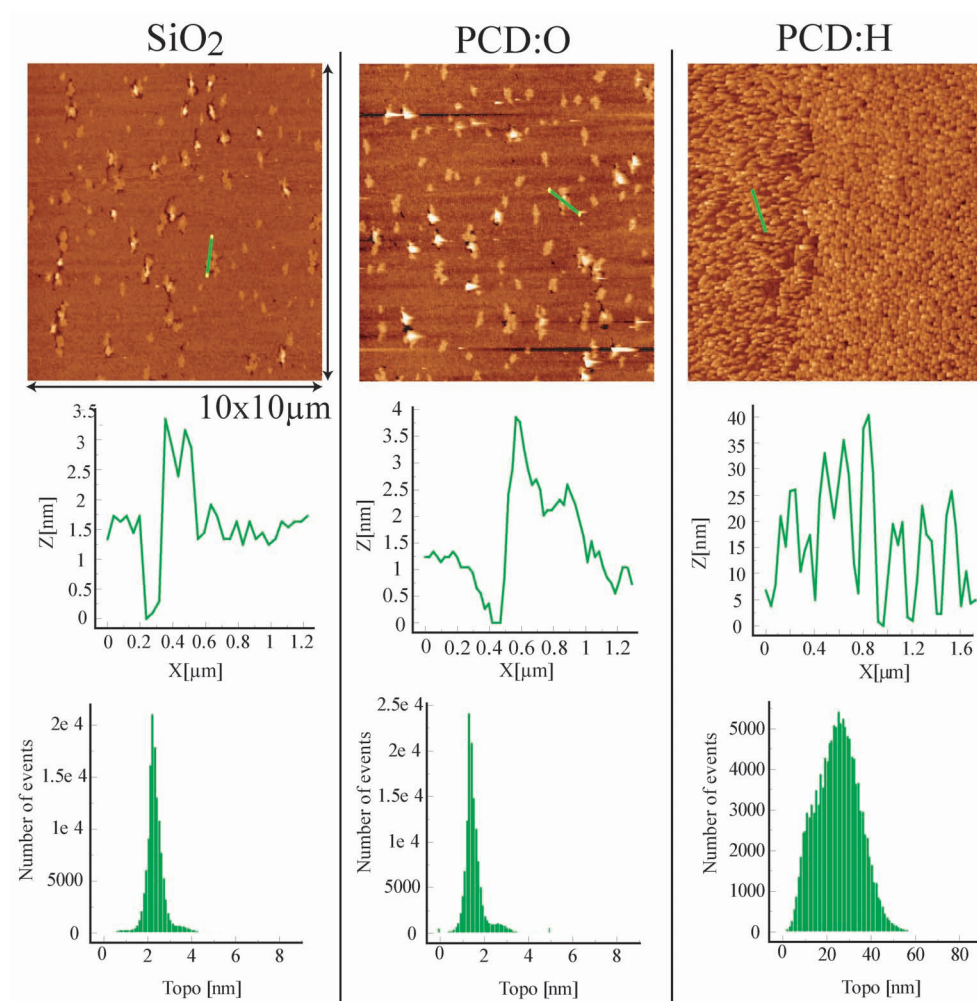


Figure 3.10: Upper row: AFM height images ( $10 \times 10 \mu\text{m}$ ) of 1ML pentacene on SiO<sub>2</sub>, PCD:O and PCD:H. Typical height profiles are shown in the middle. The lowermost row indicate the average height of the film.

The initial growth is observed by depositing nominally<sup>1</sup>  $15 \text{ \AA}$  pentacene (1ML) on the modified diamond surfaces. As a reference, a silicon dioxide surface was co-fabricated in the

<sup>1</sup>”nominally” means that an amount of pentacene has been deposited (measured with a quartz crystal balance) with a mass equivalent to the coverage of 1 complete monolayer

same evaporation process. Fig. 3.10 shows AFM micrographs of the films. We find that the morphology of the film on oxygen terminated diamond is similar to the morphology observed on silicon dioxide. In both cases the first monolayer is almost complete and a small fraction of second layer growth is observed. On the hydrogen terminated diamond surface, rice like grains of considerable size are distributed densely packed on the surface. The height distribution indicates a factor 10 more material adsorbing on that surface. Because of the bulky growth with a peak to valley height of  $\approx 35nm$  a growth mode typically found on metals is expected.

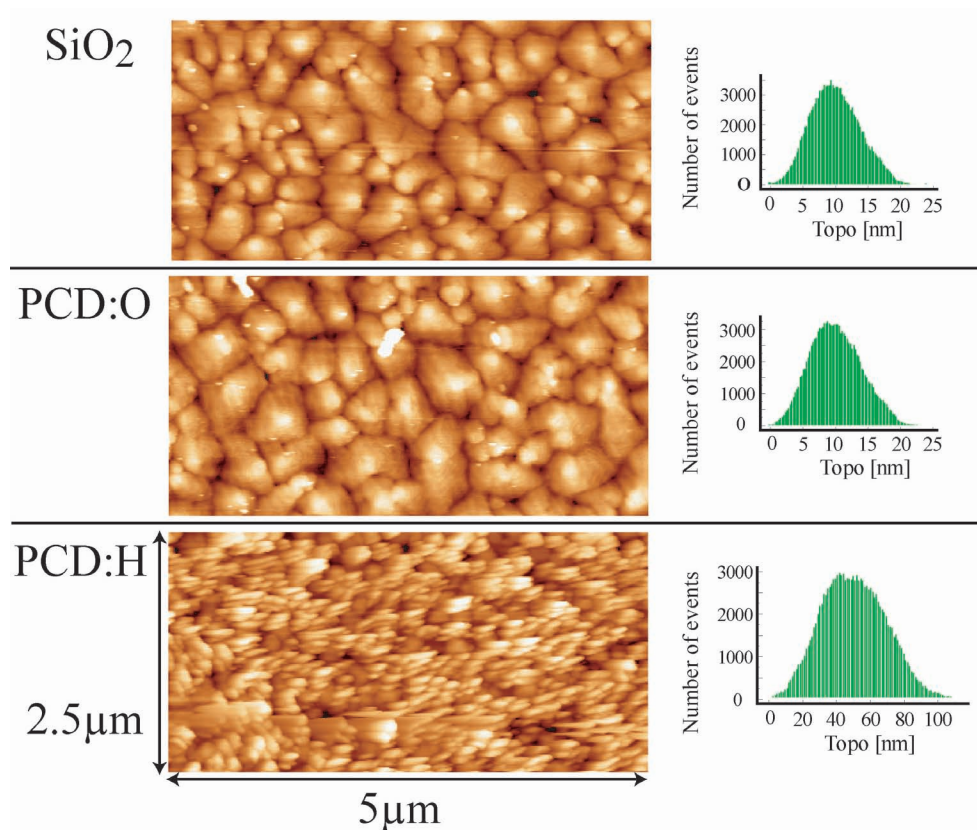


Figure 3.11: AFM height images ( $2.5 \times 5\mu m$ ) of 8ML pentacene on  $SiO_2$ , PCD:O and PCD:H. Results of the roughness analysis are plotted in the graphs to the right respectively.

AFM micrographs and the respective height histograms of 8ML ( $120\text{\AA}$ ) pentacene on  $SiO_2$ , PCD:O and PCD:H are shown in Fig. 3.11. In terms of morphology also the thick pentacene film on PCD:O is similar to the films grown on  $SiO_2$ . The PCD:H coated surface shows rice like bulky grains. The lateral grain size of  $\approx 100 \times 400nm$  on PCD:H is clearly smaller compared to  $\approx 800 \times 800nm$  on PCD:O and  $SiO_2$ , suggesting a lying growth mode.

Further structural investigations using X-ray reflectometry experiments are summarized in Fig. 3.12. In good agreement with the morphological findings, the X-ray diffraction pattern

of pentacene on PCD:O shows Bragg reflections indicating that the "thin film phase" is the dominant structure inside the film. The characteristic  $d_{00l}$  spacing is calculated to 15.4Å which is the same for pentacene on SiO<sub>2</sub>. Hence the molecules are arranged in a standing configuration as depicted in Fig. 3.7. The diffraction pattern of pentacene on PCD:H does not show any Bragg reflections, ruling out a standing conformation of the molecules. The slightly increased signal at the positions of the  $q_z$  positions of the thin film phase ( $l \cdot 0.4075 \text{Å}^{-1}$ ) is attributed to the non perfect hydrogen termination of the surface. Suggesting a small fraction of the surface to be oxidized, pentacene crystals in a standing phase would nucleate there.

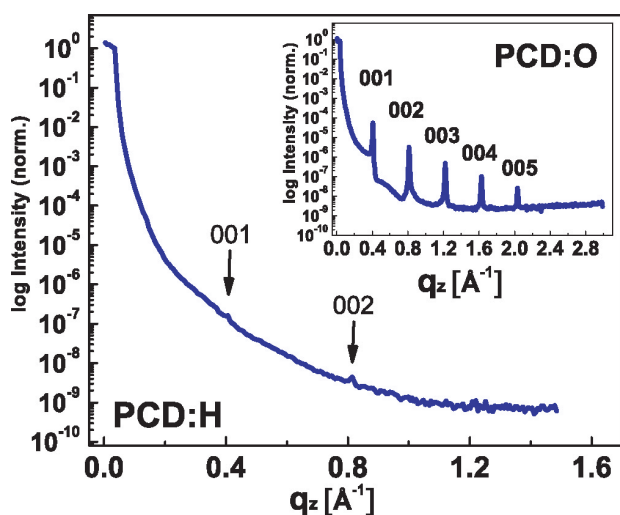


Figure 3.12: X-ray reflectometry curves of 50nm pentacene films on PCD:O and PCD:H. The characteristic Bragg reflections of the thin film phase of pentacene is observed on the O-terminated sample, while the H-terminated samples shows only weak signal at these positions.

To gain further insight, grazing incidence X-ray diffraction patterns were taken. With that technique, ordering phenomena along the surface can be detected by measuring the off-specular diffraction intensities. The measured curve of a pentacene film on PCD:H and the results of the analysis are illustrated in Fig. 3.13. The inset is a Debye-Scherrer image of the bare substrate showing powder rings. In polycrystalline diamond, the first reflection (most inner circle) not extinguished is from the 111 plane. In the off-specular measurement this peaks also shows up, as indicated by the black arrow. The detailed analysis of the 18 Bragg reflections was done with a MatLab simulation, that calculates all Bragg peak positions from a given crystal structure. We find that the reflections around the  $q$ -position at a distance corresponding to the length of the pentacene molecule are split, and that the observed values are in accordance with the  $q_{001}$  values of the well known thin film and bulk phase of pentacene found in vertical direction on other surfaces. Hence both phases coexist on the hydrogenated diamond surface, but in a lying fashion, with the long molecular axis

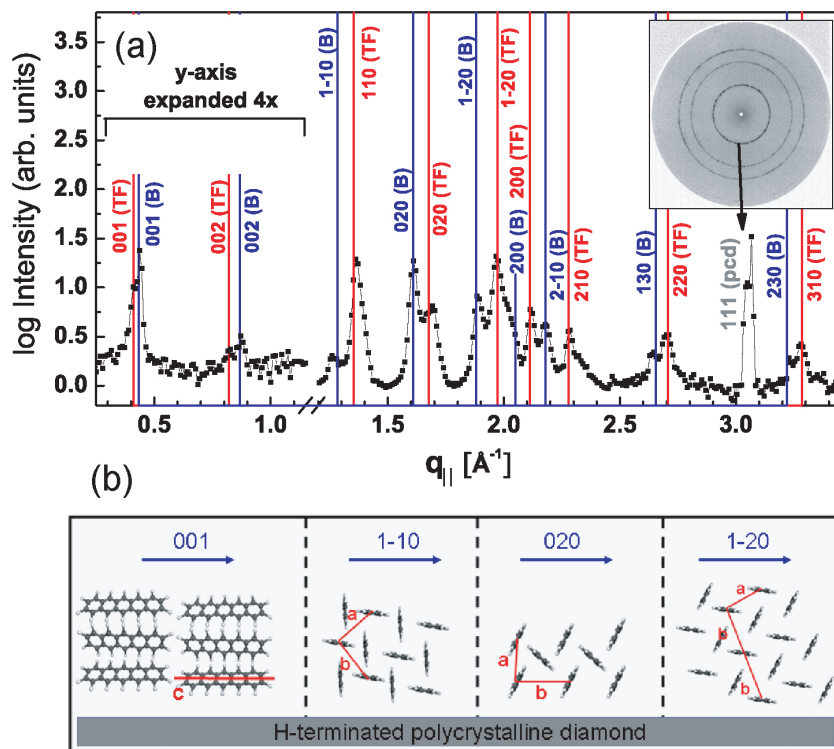


Figure 3.13: (a) off-specular X-ray diffraction pattern of 50nm pentacene films PCD:H. The positions of simulated Bragg reflections of the refined bulk phase (B, blue) and the thin film phase (TF, red) are indicated as lines and indexed. The inset shows a Debye-Scherrer image of the bare substrate, proving the polycrystallinity. The y-axis in the region  $q_{||} \leq 1.2 \text{ \AA}^{-1}$  has been expanded  $4\times$  for clarity. (b) Schematic of the molecular orientation of pentacene on H-terminated diamond.

parallel to the surface. Details of this study can be found in [3]. A schematic of the orientation of the molecules is shown in Fig. 3.13. Four chosen orientations of the pentacene unit cell showing Bragg reflections in the off-specular measurement are illustrated in a side view. Because of the polycrystallinity of the substrate, different planes of the the diamond structure are present at the surface, which leads to different conformations of the adsorbed pentacene molecules who act as a nucleation site for crystal growth. The growth mode determined by X-ray techniques explains well the observed height and shape of the crystal grains found on hydrogen terminated diamond. As also seen in the standing phase, the aggregation of pentacene molecules is faster in the directions vertical to the long molecular axis, which in this case is along the surface normal.

Finding different orientations of the pentacene crystallites on the polycrystalline surface suggests that the crystal plane of the specific adhesion site is of great importance. Further off specular experiments were performed using single crystalline diamond samples (hydro-

generated, SCD:H and oxidized, SCD:O). 2 dimensional grazing incidence maps were taken using a line detector and scanning the area behind the sample while the sample is not moved and illuminated with X-rays under a small angle which is slightly below the angle of total reflection. The maps are shown in Fig. 3.14. While the pentacene film on the oxidized surface (SCD:O) shows the typical pattern of the standing thin film phase [7,43], the pattern on SCD:H suggests a lying structure due to the presence of 00l reflections in the direction along the surface. Similar to pentacene films on polycrystalline diamond samples (Fig. 3.13), these peaks split up demonstrating that the bulk and the thin film phase structure coexist in a lying conformation. Further evidence is given by a ring shaped reflection at the q-position corresponding to the 110 plane of pentacene. The intensity varies along the ring. A region of high intensity is marked with black lines. From the ratio of the q values, an angle of  $\delta = 38.2^\circ$  with respect to the surface normal can be determined (see sketch in Fig. 3.14). Supposing that the  $a$  side of the unit cell is lying on the surface, the calculated angle of the 110 plane and the surface normal is  $\delta = 39.05^\circ$ .

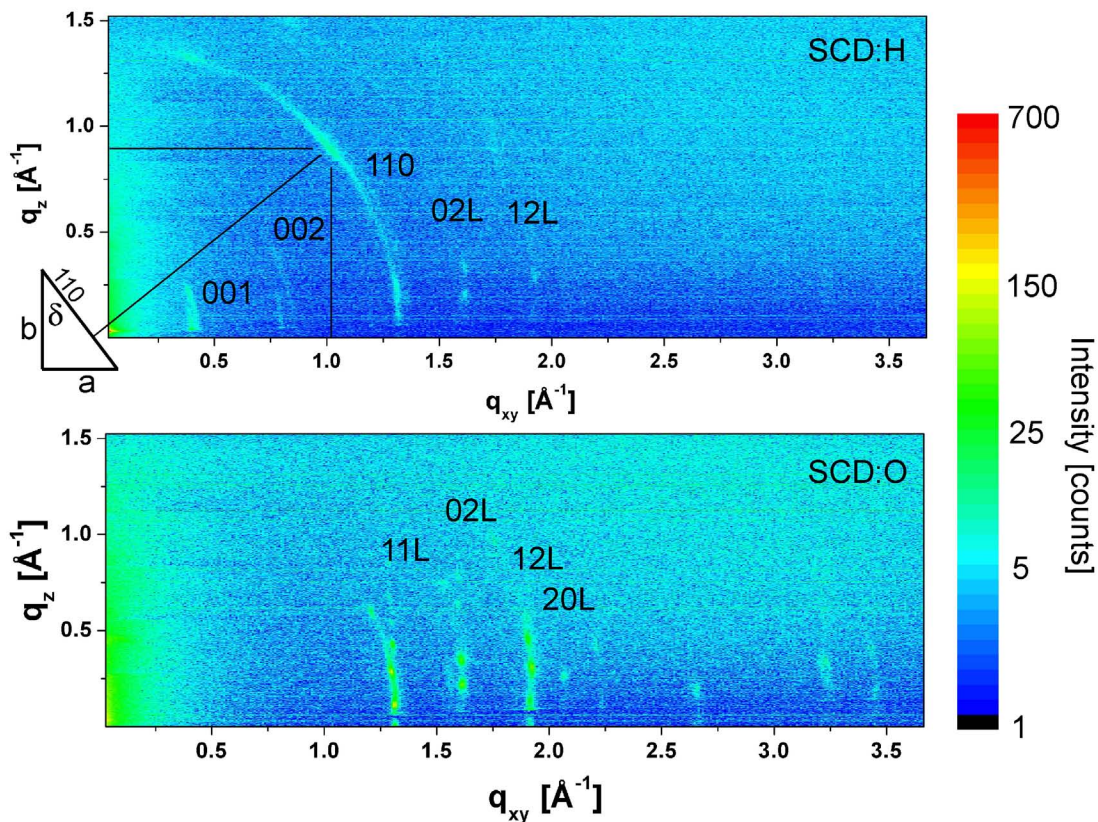


Figure 3.14: 2 dimensional grazing incidence maps of 50nm pentacene films on modified single crystal diamond (hydrogenated, SCD:H and oxidized, SCD:O). While a typical pattern of standing phase pentacene films is found on SCD:O, the pattern of Pc on SCD:H indicates a lying conformation.

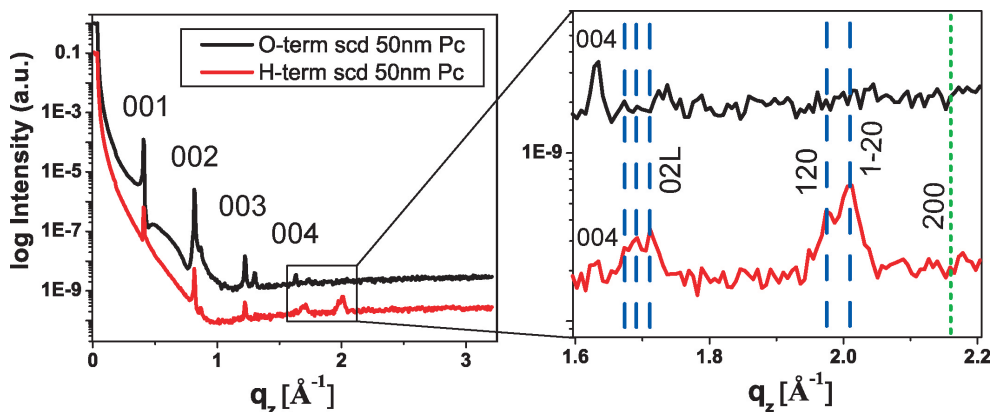


Figure 3.15: Reflectometry measurements of 50nm pentacene films on modified single crystal diamond (hydrogenated, SCD:H and oxidized, SCD:O). The presence of a standing phase (00l peaks visible in vertical direction) also on the SCD:H sample is a sign of an incomplete surface modification. Peaks from the short molecular axis  $b$  appearing in the vertical direction suggest a lying conformation on SCD:H. The missing peak at the 200 position denotes a preferred orientation of the  $a$  axis along the surface.

To further understand the reciprocal space maps shown in Fig. 3.14, the reflectometry curves are shown in Fig. 3.15. The presence of a standing phase (00l peaks visible in vertical direction) on the SCD:H sample is a sign of an incomplete surface modification (oxidized areas on the hydrogenated sample). This also explains the weak appearance of the 02l and 12l reflections in the reciprocal space map of pentacene on SCD:H (Fig. 3.14). In addition the 110 reflection of the lying phase at low  $q_z$  is superimposed with the 110 reflection from the small fraction of standing phase, misguiding the intensity distribution. Looking at the zoom on the middle part of the reflectometry curve (Fig. 3.15), peaks are found that correspond to distances found along the smaller sides of the pentacene unit cell. Calculating the allowed reflections of the pentacene polymorphs allows to index the peaks as the 02l ( $0 < l < 2$ ), 120 and 1-20 reflections as shown in the graph. The missing reflection of the 200 plane in vertical direction suggests the  $a$ -axis being oriented along the surface. Combined with optical measurements [3], the data clearly shows the lying conformation of pentacene on hydrogen terminated diamond in a way that the  $a$ -axis is mainly parallel and the  $b$ -axis mainly perpendicular to the surface. Compared to the theory of molecular aggregation, this is not the expected growth geometry, which is attributed to the electronic properties of the surface. Due to the hydrogenation, a high density of mobile charge carriers is found on the surface, which leads to an almost "metallic" appearance. Pentacene thin films grown on metals also showed a lying conformation [5].

### Conclusion

Organic molecular beam epitaxy is a clean and deterministic method to grow thin films with a controlled thickness and a resolution in the angstrom regime. The thin film growth of vacuum deposited pentacene ( $C_{22}H_{14}$ ) on various surfaces has been studied. Different stable polymorphs have been identified and their structure was determined by diffraction methods. To optimize the electronic performance, a crystalline film in a specific polymorph, the so called "thin film phase", is needed. Structural analysis indicated highly crystalline and a monophasic growth on cyclic olefin copolymer (COC) and polystyrene. Because of the very low roughness, also the selfmade silicon oxide showed the desired "thin film phase" of pentacene. Considering also the chemical stability, COC passivated  $SiO_2$  turned out to be the best suited gate dielectric.

The growth experiments on modified diamond surfaces showed that by changing the surface chemistry one can switch the growth mode of the overlying pentacene film from a standing to a lying phase, which largely influences optical and electronic properties of the film.

In order to operate a transducer device with a thin pentacene film as active layer in physiological environment, it has to be protected against physical and chemical influences. Different approaches to this topic are discussed in the following chapter.

# Chapter 4

## Organic-organic Bilayer for Encapsulation

In ambient environment pentacene thin films degrade due to photo-oxidation as a result of the presence of UV light and oxygen [44]. The electronic performance is weakened by diffusion of molecular oxygen and water through the pentacene film. These elements form surface trap states and possibly disturb the molecular ordering.

In order to operate an organic thin film field effect device in ambient environment the active layer has to be protected. To keep the sensitivity, a capping has to be developed that provides chemical sealing as well as full coverage at a very low thickness. For the use as a biosensor the material has furthermore to be biocompatible (e.g. non toxic). The following sections cover a systematic study of the behavior of pentacene thin films when coated with different materials using three coating techniques, namely spincoating (4.1), sputtering oxides (4.2) and vacuum deposition (4.3).

### 4.1 Spincoating of Thermoplasts

Spincoating is a simple technique that allows to form ultra thin homogeneous layers on a surface. The material of choice (mostly polymers) has to be dissolved in a compatible solvent and is placed in excess on the substrate. By rotating the sample, the solution is spread across the surface. In a second step, the sample is rotated at higher speed to evaporate the solvent. A balance between the viscous forces inside the solution and the centrifugal forces determines the layer thickness and the homogeneity. In a simple approximation, the thickness  $d$  of the film is

$$d \propto \omega^{-a} \cdot t^{-b}$$

where  $\omega$  is the speed of rotation and  $t$  is the time. The values of the exponents  $a$  and  $b$  vary from 1/2 to 1, while  $b$  is only different from zero if the solvent does not evaporate.

Common rotation speeds used are  $500rpm$  in the first spinning step and  $2000 - 6000rpm$  in the second step.

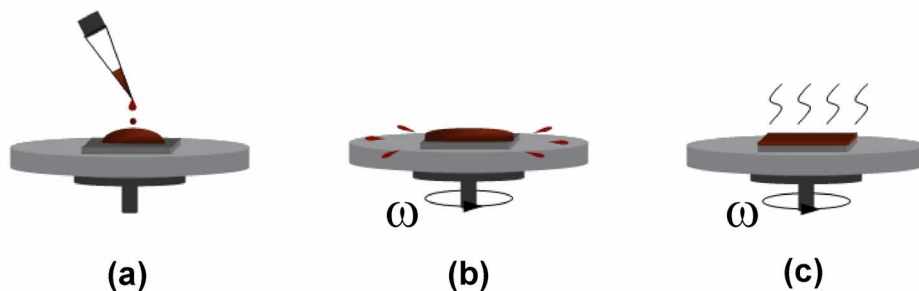


Figure 4.1: Illustration of the spincoating procedure. (a, b, c) illustrate the steps given in the itemization (see text).

A great advantage of this technique is its simplicity which allows for high sample throughput. Therefore spincoating is a technique widely used in the industry. The list below summarizes the steps during a spincoating process, as illustrated in Fig. 4.1:

- dissolving the material of choice in a compatible solvent
- rotating the sample at low speed to spread out the solution (a)
- rotating the sample at high speed to evaporate the (volatile) solvent (b)
- bake out of the layer and/or storage in vacuum (c, optional)

The following section deals with the structural analysis of pentacene thin films before and after spincoating a solvent on the sample. The spincoating was performed with no capping material dissolved in the solvent. A BLE delta spincoater placed in a flow box was used. The aim is to investigate the effect of the solvent on the structure of the film. Samples were 50nm pentacene films grown on native silicon oxide wafer as described in (3.1). X-ray reflectometry measurements were used for structural analysis. The experiments were performed using an inhouse molybdenum X-ray source (Fig. 4.2a) with a wavelength of  $0.722\text{\AA}$  ( $\text{Mo } K_{\alpha}$ ). A typical X-ray diffraction pattern of a 50nm pentacene film on native silicon oxide before the spincoating process is shown in Fig. 4.2b. Only the regions of interest around the 00L Bragg reflections are measured. As indicated by the red grid lines, the q-positions of the Bragg reflections can be attributed to the thinfilm phase of pentacene, showing a  $d_{00l}$  spacing of  $15.4\text{\AA}$  ( $q_{00l,TF} = l \cdot 0.4085\text{\AA}^{-1}$ ,  $d_{00l} = 2\pi/q_{00l}$ ). The measurements

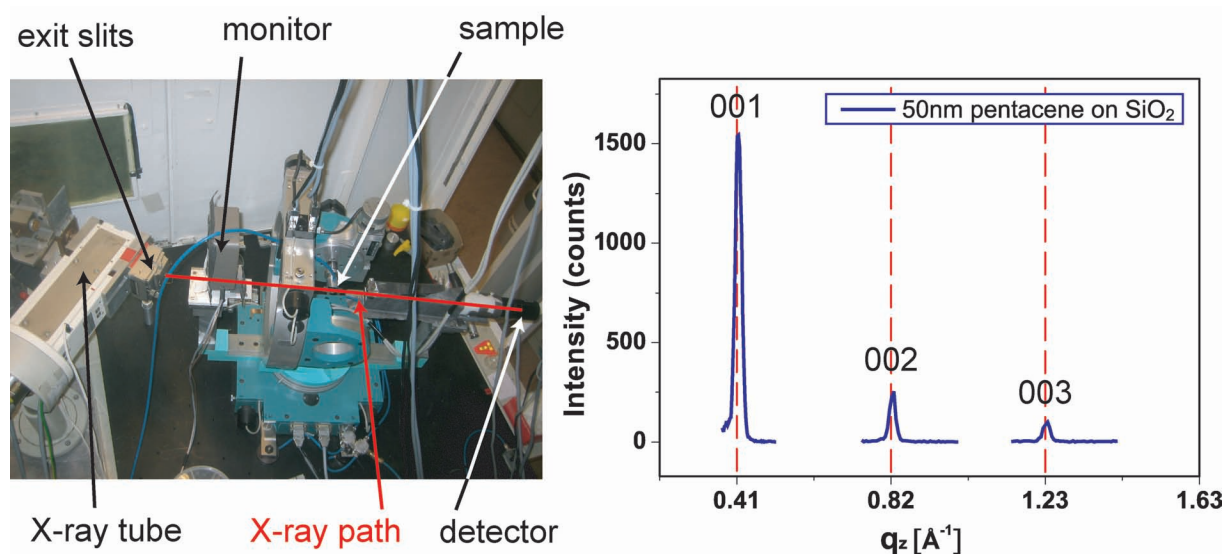


Figure 4.2: (a) Photograph of the inhouse X-ray setup. The red line shows the path of the X-rays from the tube to the detector. The sample is mounted on a 4-circle Huber diffractometer. (b) Reference measurement of a 50nm pentacene film on native silicon oxide. Red dashed grid lines mark the Bragg peak positions of the thinfilm phase.

were done in ambient laboratory environment.

A summary of reflectometry measurements from pentacene films after they were spincoated with different solvents is presented in Fig. 4.3. All the solvents tested here change the crystal phase of the pentacene film from the thin film phase to another polymorph. The different polymorphs are distinguished by determination of their unique  $d_{00l}$  spacing. In addition to the thin film phase the bulk phase ( $d_{00l} = 14.4\text{\AA}$ ,  $q_{00l,B} = l \cdot 0.435\text{\AA}^{-1}$ ), the single crystal phase ( $d_{00l} = 14.0\text{\AA}$ ,  $q_{00l,SC} = l \cdot 0.4488\text{\AA}^{-1}$ ) and a phase with  $d_{00l} = 15.0\text{\AA}$  ( $q_{00l} = l \cdot 0.4189\text{\AA}^{-1}$ ) exist. These positions are marked with dashed (thin film and bulk phase) and dotted lines (single crystal and  $15\text{\AA}$  phase). The graph in (a) shows the 001 reflections while (b) points out the 002 and 003 reflections. The intensity (detector counts) is plotted linearly against the momentum transfer  $q_z = 4\pi/\lambda \cdot \sin(\theta)$ .

The bulk phase is found on the samples after spincoating with toluene (blue curve). If a mixture of 20% toluene and 80% isopropanol is used, most of the pentacene film is converted to the bulk phase while a small fraction remains in thin film phase (cyan curve). The  $15\text{\AA}$  phase is produced by spincoating with hexadecane (magenta curve), which is of interest because silanization chemistry is done in hexadecane environment. Processing the samples with chloroform (trichloromethane, red curve) or dichloromethane (black curve) leads to a conversion to the single crystal phase. Most interesting is the result of the spincoating experiment with chlorobenzene. The 00l peak is split into two components who both can not be identified with a polymorph reported in the literature so far.

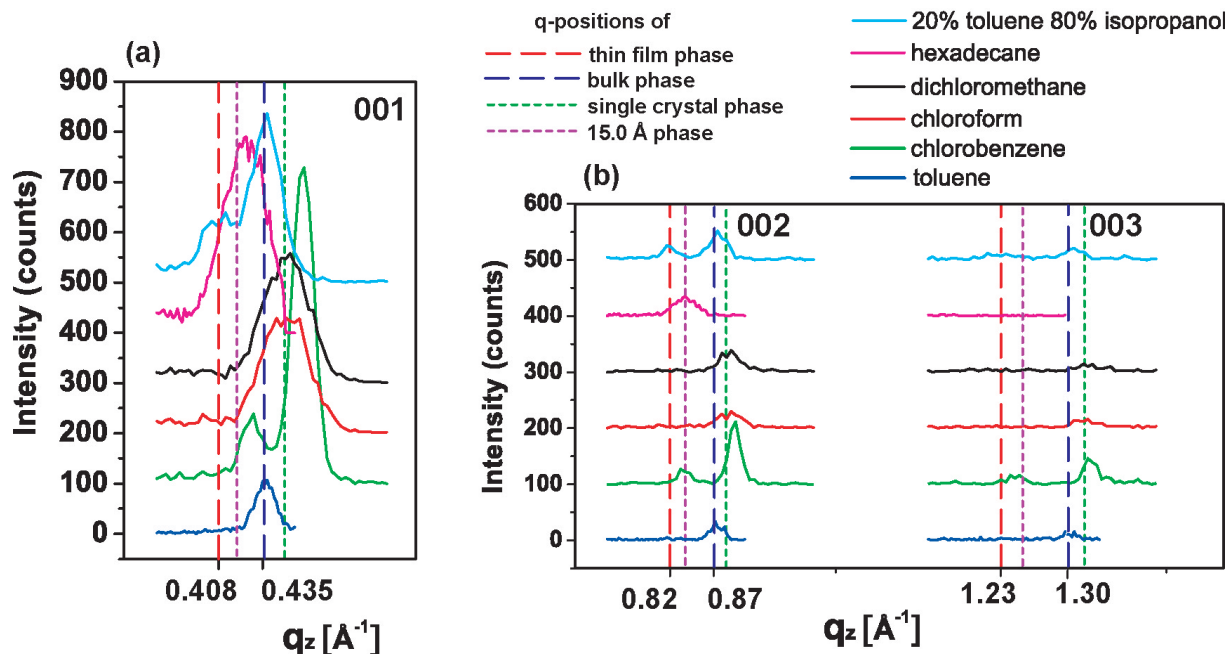


Figure 4.3: Reflectometry curves of 50nm pentacene films after spincoating with various solvents. The dashed lines indicate the positions of the 00l reflections of pentacene in the different polymorphs. (a) Zoom on the region around the 001 reflection. (b) Zoom on the 002 and the 003 reflections. All the solvents tested here change the crystal structure of the pentacene film and are therefore not compatible. The curves have been shifted vertically for clarity.

The interlayer distance corresponding to the stronger peak at  $q_z = 0.46\text{\AA}^{-1}$  converts to  $d_{00l} = 13.6\text{\AA}$ , which is surprisingly small. The weaker peak at  $q_z = 0.428\text{\AA}^{-1}$  converts to  $d_{00l} = 14.7\text{\AA}$ , which is a distance between that shown by the bulk phase and the 15Å phase.

Performing the spincoating process without changing the pentacene crystal structure was only achieved by using water or isopropanol as a solvent. As shown in Fig. 4.4, the Bragg peak positions were not shifted after the coating procedure. The measurement after the isopropanol treatment (green curve) was taken at DESY (Deutsches Elektronen Synchrotron), HASYLAB, Beamline D4, using a wavelength of  $0.623\text{\AA}$  (19.9 keV).

Isopropanol is able to dissolve fat, resin, varnish or ink, but none of the dielectric polymer materials that are used in field effect devices. Apart from the structural change that occurs when using certain solvents, the spincoating process always leads to some loss of material from mechanical issues, therefore that this technique turned out to be not suited to coat a thin pentacene film in a way that it preserves its initial electrical properties plus protecting it from outside influences. Table 4.1 summarizes the spincoating experiments and involved changes.

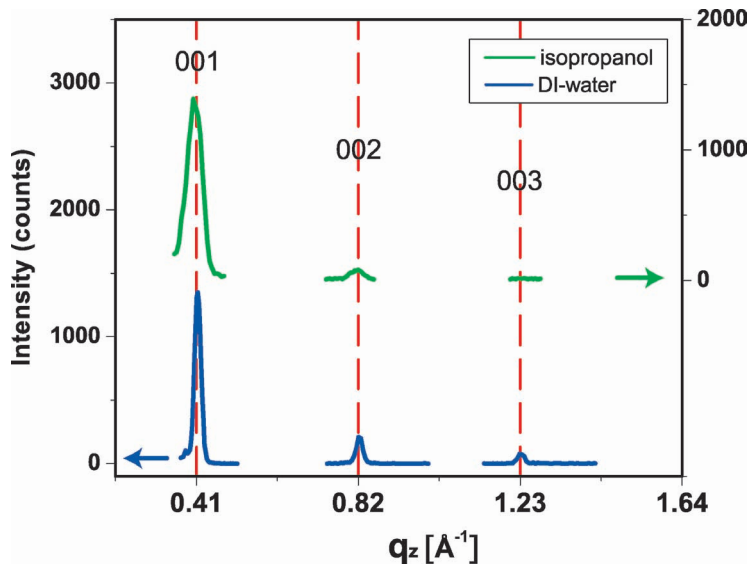


Figure 4.4: Reflectometry curves of 50nm pentacene films after spincoating with isopropanol or deionized water (DI-water). The red dashed lines indicate the positions of the 00l reflections of the pentacene thin film phase. No phase change occurs due to the spincoating process. As indicated by the colored arrows, the respective colored curve corresponds to either the right or left vertical scale.

solvent	crystal structure after coating
DI-water	no change
Isopropanol	no change
Toluene	bulk phase
Hexadecane	15Å phase
Dichloromethane	single crystal phase
Chloroform	single crystal phase
Chlorobenzene	shifts to new phase, see text

Table 4.1: Summary of the results of the spincoating experiments.

## 4.2 Sputter Oxides

Sputtering is a common thin film deposition technique where atoms of a target material are extracted by plasma bombardment. The ejected atoms form a thin layer on the substrate. The theory behind the method can be found in [45]. A great advantage of this technique is that in principle all solid materials can be used as a target material, e.g. metals or metal oxides. A major drawback is the damage of the plasma to the substrate. Fig. 4.5 shows a photograph of the sputter system in the cleanroom, which operates using an argon plasma.



Figure 4.5: Photograph of the sputter machine in the cleanroom.

To investigate the compatibility of this technique with organic substrates, 50nm thick pentacene films were grown on native silicon oxide wafer, as described in (3.1) and coated with different metal oxide layers. X-ray reflectometry experiments were performed at our inhouse X-ray tube (4.2a) before and after the sputter procedure.

According to values found in the lab-book of the sputter system, silicon oxide ( $\text{SiO}_2$ ) and aluminum oxide ( $\text{Al}_2\text{O}_3$ ) have been processed using moderate power (40W and 35W respectively). After sputtering 10-12 minutes, a layer of  $\approx 20\text{nm}$  thickness has been deposited. Subsequent X-ray measurement showed no Bragg reflections thus the pentacene film has been severely damaged. Reducing the power of the AC radio frequency generator to 20W when sputtering aluminum oxide ( $\text{Al}_2\text{O}_3$ ) also reduced the damage to the pentacene film. The respective X-ray reflectometry measurements of the sample before and after the coating are shown in Fig. 4.6.

In conclusion, sputtering is a possible way to coat organic thin films. In order not to

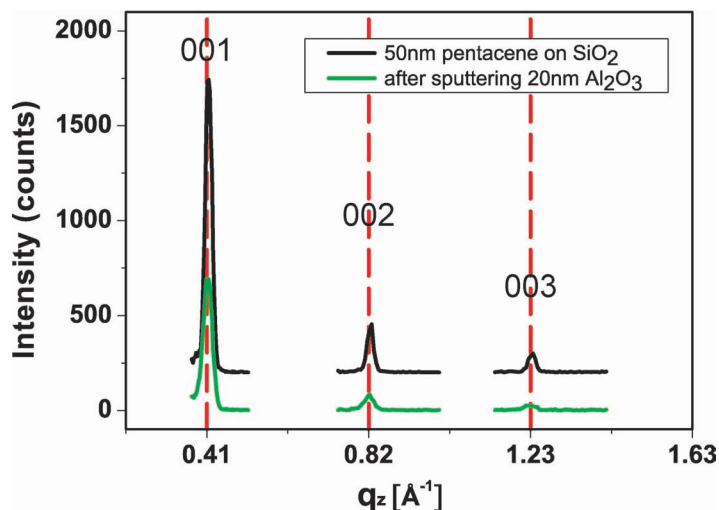


Figure 4.6: Reflectometry curves of 50nm pentacene films before and after sputter depositing 20nm  $\text{Al}_2\text{O}_3$ . The red dashed lines mark the positions of the 00l reflections of the pentacene thin film phase which is conserved during this coating procedure. The black curve has been shifted vertically for clarity.

damage the underlying film, low power has to be applied, which elongates the process. Furthermore the surface that should be coated needs to survive high vacuum. This technique has also been tested to seal pentacene thin film transistors (data not shown) and it turned out that the device still operated in ambient conditions after the coating. An operation under water was not possible.

### 4.3 Vacuum Deposition of Alkanes

The damage to the organic thin film is the major problem of the coating techniques introduced above. Another issue is the diffusion of water into the film [44], thus an appropriate capping should be a hydrophobic material. To guarantee electrical sealing, the material has also to be insulating. A class of material providing these properties are alkanes. These organic compounds consist exclusively of hydrogen and carbon. The carbon atoms are linearly connected via single bonds. Each carbon is saturated by at least two hydrogen atoms. The length of an alkane (also called alkyl chain) is determined by the number of the carbon atoms in the compound. Prominent short alkanes (number of carbons  $\leq 6$ ) are: methane ( $\text{C}_1\text{H}_4$ ), ethane ( $\text{C}_2\text{H}_6$ ), propane ( $\text{C}_3\text{H}_8$ ), butane ( $\text{C}_4\text{H}_{10}$ ), pentane ( $\text{C}_5\text{H}_{12}$ ) and hexane ( $\text{C}_6\text{H}_{14}$ ). A schematic of their structure is shown in Fig. 4.7. The composition follows the simple rule  $\text{C}_n\text{H}_{2n+2}$ ,  $n$  being the number of carbon atoms.

With increasing number of carbon atoms, the stronger intermolecular forces lead to an increase of the melting and boiling temperatures (Fig. 4.8a, values taken from [46]). At

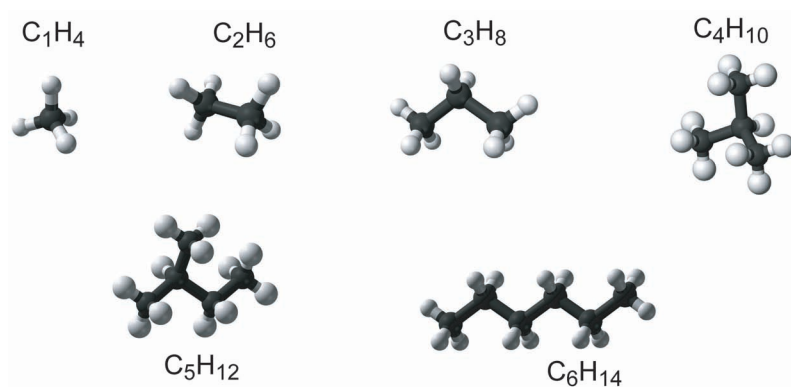


Figure 4.7: Structures of alkanes  $C_1$  to  $C_6$ . Compounds with 4 or more carbon atoms can have different orders (isomers), only one example is shown here.

ambient conditions (blue line)  $C_1$  to  $C_4$  are gases, while  $C_5$  to  $C_{17}$  (heptadecane) are liquids and  $C_{18}$  (octadecane) and higher are solids (phase changes are indicated by dashed lines). One distinguishes between the "normal" form (n-alkanes, Fig. 4.7  $C_1$ - $C_3$ ,  $C_6$ ), for which all carbons are linearly joint, and branched versions (Fig. 4.7  $C_4$ ,  $C_5$ ). Due to their shape, linear molecules are able to form a closer packing thus they show higher van der Waals forces, resulting in a higher melting and boiling point. Furthermore the longer the chains are, the stronger is the interaction between them (compare sec. 2.4).

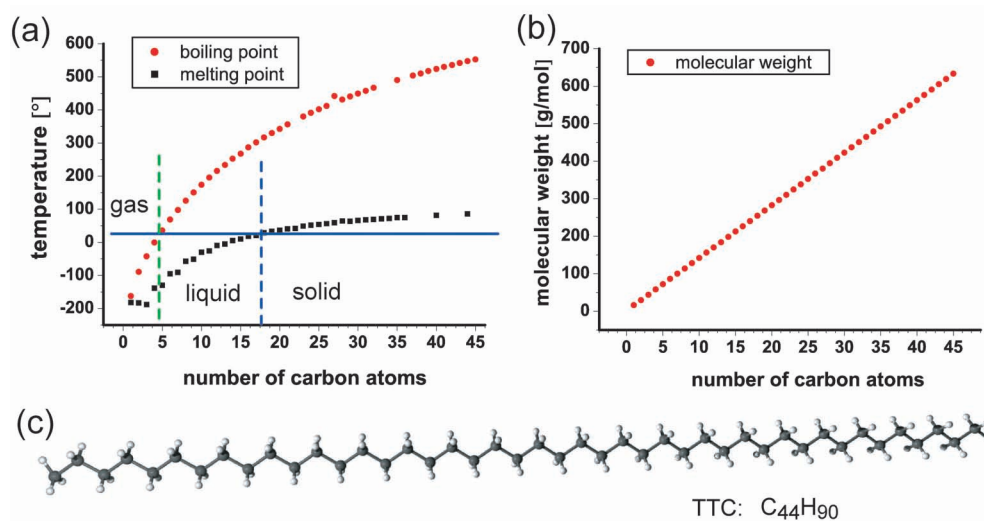


Figure 4.8: (a) Melting and boiling points of n-alkanes. The blue line represents room temperature. (b) Molecular weight as a function of the length of the alkane. (c) Structure of tetratetracontane (TTC,  $CH_3(CH_2)_{42}CH_3$ ).

Here we discuss the possibility to use thermal vacuum deposition (similar to the procedure that is used to grow the pentacene films) to encapsulate the pentacene film. Using this

technique, TTC forms closely packed and crystalline films [47]. Furthermore, the substrate has a high impact on the growth of alkanes, as shown by several studies [48, 49, 50, 51]. In order to seal organic thin films properly, we have chosen  $C_{44}H_{90}$  (tetratetracontane, TTC) as a capping material, which is a solid at ambient conditions. It has a molecular weight of 619.19 g/mol and a melting point of  $86^{\circ}C$ , which allows structural stability in physiological environment. Thin films of TTC are grown by vacuum deposition (sec. 3.1). A 10nm TTC film was grown with a deposition rate of  $0.1\text{\AA}/s$  at room temperature on silicon oxide in vacuum ( $p < 10^{-7}mbar$ ). AFM analysis shows dendritic islands. The first layer almost completely wets the surface (Fig. 4.9, coverage  $97.67\%^1$ ). The black areas in the micrograph show the bare silicon oxide substrate. Second layer growth is observed on top of the first monolayer. A height profile across the terraces shows a step height of  $\approx 5nm$ , suggesting a standing phase with the long molecular axis oriented perpendicular to the surface. The white spots in the micrograph are aggregates with a height which is a multiple of the monomolecular layers below. Hence a configuration of lying molecules inside these aggregates is likely (Fig. 4.9b).

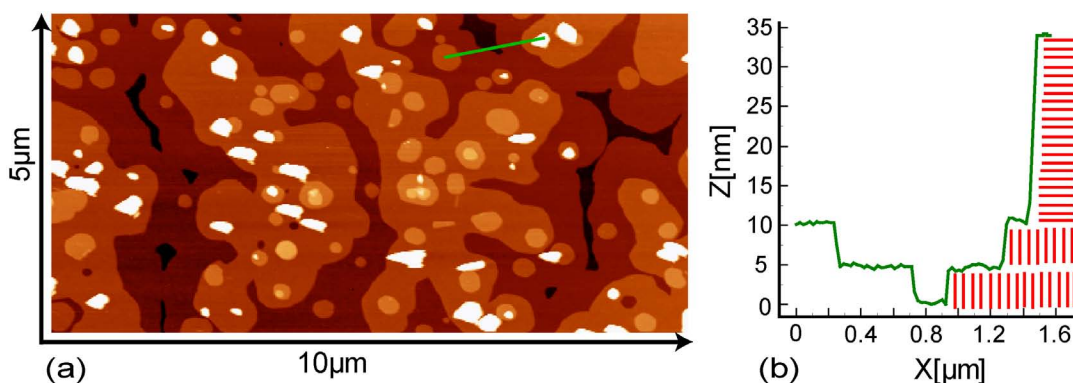


Figure 4.9: (a) AFM height micrograph of 10nm TTC grown on silicon oxide. (b) corresponding height profile. Clearly visible are the monomolecular steps of  $\approx 5nm$  of the first and second layer. The red lines indicate the molecular arrangement in standing or lying conformation.

AFM micrographs of 50nm pentacene (a) and 20nm TTC grown on a 50nm pentacene film (b) are shown in Fig. 4.10. To deposit the TTC layer a high deposition rate ( $\approx 4\text{\AA}/s$ ) was used in order to reduce molecular diffusion on the surface. The sample was kept at ambient conditions during the procedure. Surface analysis showed a slightly decreased roughness after the TTC deposition. The rms (root-mean-squared) value changed from  $\approx 8nm$  (typical 50nm pentacene film) to  $\approx 5nm$ . Hence the TTC molecules partially fill up the valleys between the pentacene pyramids, which is expected to have a positive effect on the sealing properties.

<sup>1</sup>value was determined using the flooding function of the AFM micrograph analysis software WSxM®

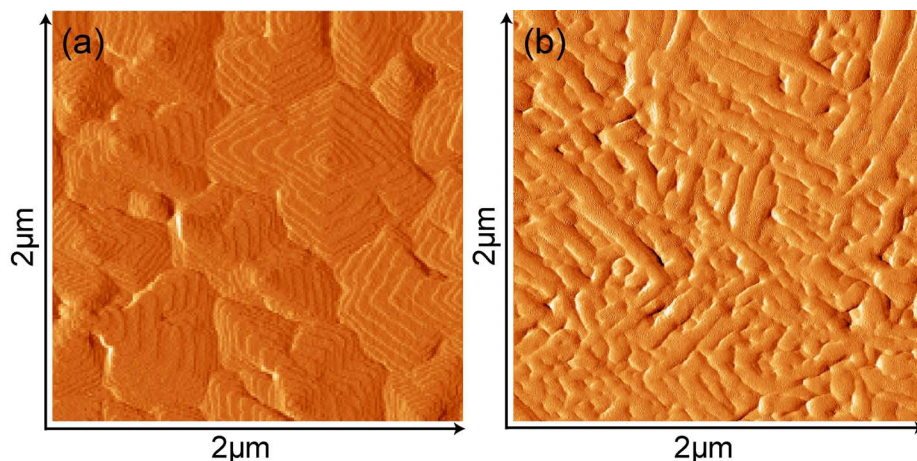


Figure 4.10: AFM amplitude micrographs. (a) 50nm pentacene grown on silicon oxide. (b) 50nm pentacene film capped with 20nm TTC.

In order to reveal the molecular arrangement inside the organic bilayer system, X-ray diffraction experiments were performed at HASYLAB (Hamburger Synchrotronstrahlungs Labor), DESY in Hamburg, beamline W1. The X-ray energy was  $10.5\text{keV}$  ( $\lambda = 1.1808\text{\AA}$ ). A schematic of the sample layout is shown in (Fig. 4.11). Comparison to reference samples containing only one component each is necessary to assign the Bragg reflections in the XRD pattern of the sandwich structure (Fig. 4.11c) to a certain material.

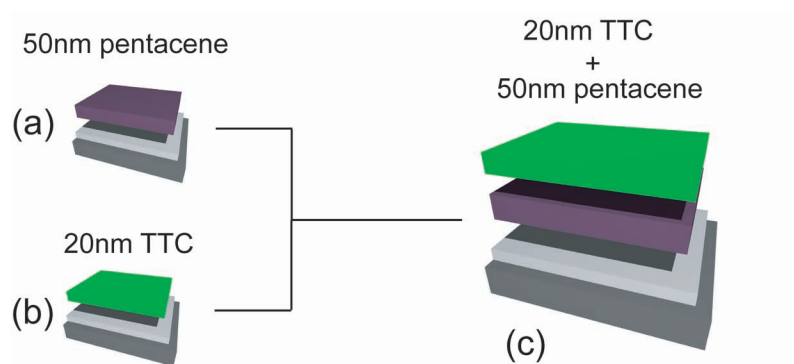


Figure 4.11: Schematic of the sample layout. Two reference samples (a,b) provide the data to evaluate the signal from capped pentacene sample (c).

The reflectometry measurement of the pentacene film (Fig. 4.12, a) shows the expected 00L peak series of the pentacene thinfilm phase ( $q_{00l} = l \cdot 0.4075\text{\AA}^{-1}$  (marked by blue grid lines) as well as a fraction of pentacene bulk phase ( $q_{00l} = l \cdot 0.4363\text{\AA}^{-1}$ ). The layer oscillations at low  $q_z$  originate from the underlying COC layer. Its thickness calculates to  $d = 5.2\text{nm}$  ( $d = 2\pi/\Delta q_z$ ).

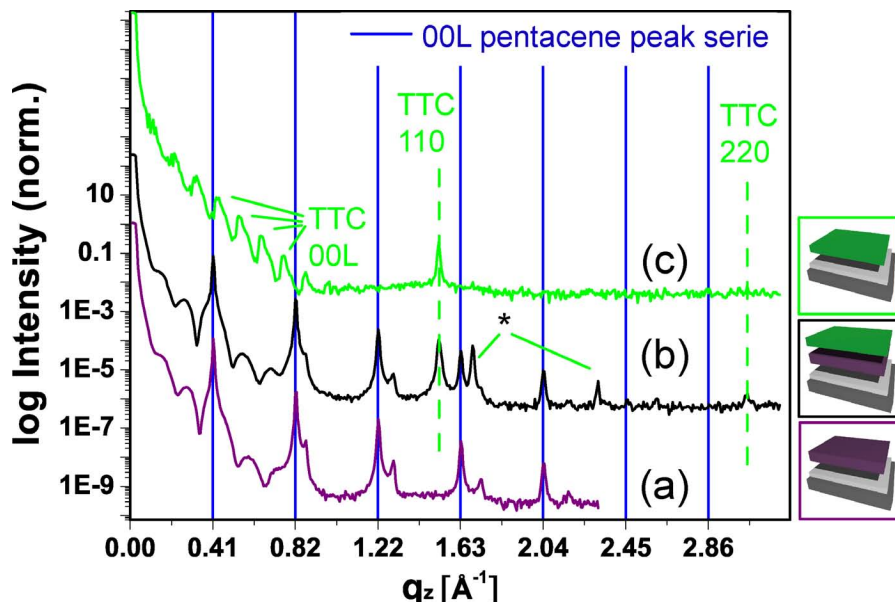


Figure 4.12: Reflectometry curves of (a) pentacene, (b) TTC on pentacene and (c) TTC on modified silicon oxide. Curves are vertically shifted for clarity. Blue grid lines mark the positions of the 00L reflections from the pentacene thin film phase.

The measurement of pure TTC (Fig. 4.12, b) shows a peak series at low  $q_z$  with a period of  $\Delta q_z = 0.1085 \text{ \AA}^{-1}$ . This is attributed to a standing phase where the long molecular axis is oriented perpendicular to the surface, which is in agreement with the AFM measurements (Fig. 4.9) and theoretical calculations discussed in section 2.4. The  $c$ -axis (long molecular axis) of the TTC unit cell is calculated from the standing phase 00L reflections to  $c = 5.791 \text{ nm}$ . The peak found at  $q_z = 1.525 \text{ \AA}^{-1}$  originates from a lying phase. This observation is also in agreement with the AFM studies.

Looking at the XRD pattern of the capped pentacene film (Fig. 4.12, b), we find unchanged signal from the pentacene film, while the standing phase peaks of TTC are absent, most likely due to the high roughness of the underlying pentacene film. The reflection of the TTC lying phase at  $q_z = 1.525 \text{ \AA}^{-1}$  is also observed. Remarkably, we find two additional peaks at  $q_z = 1.69 \text{ \AA}^{-1}$  and  $q_z = 2.31 \text{ \AA}^{-1}$ , which can be assigned to a lying phase of TTC. There are two possible reasons why these peaks are missing in the measurement of the pure TTC sample. Ocko et.al. [52] proposed a hexagonal packing of TTC molecules and calculates the structure factor of other reflections to be zero. Here, it is more likely that an orthorhombic phase [53,47,54,55] is present, but in a higher quantity than on the pure TTC sample. Comparison of the intensity of the 110 peaks in curve (c) and (b) shows a 6 times higher intensity on pentacene. Applying the same factor on the peaks at  $q_z = 1.69 \text{ \AA}^{-1}$  and  $q_z = 2.31 \text{ \AA}^{-1}$  (star labeled peaks in Fig. 4.12, b), we find that these peaks would be hidden in the background signal. Furthermore, the peak at  $q_z = 1.69 \text{ \AA}^{-1}$  is superimposed by the 004 bulk phase pentacene reflection.

To gain further insight into details about the molecular packing off-specular measurements were performed (Fig. 4.13) using a MythenII line detector, scanning the area of interest in 5 intervals, subsequently increasing  $q_z$  (detector angle), while the sample position is kept fix at an incident angle slightly below the angle of total reflection. The data has been merged after being corrected of detector errors (intensity correction of each channel) and subtracting the measurement overlap. A custom MatLab® program was used to process the data files (see C.2).

In the off-specular XRD pattern of the pentacene reference sample (Fig. 4.13a) we can identify the strongest reflections from the thin film phase (11L, 02L, 12L, 02L and 12L, see [7, 43]) as indicated by the purple arrows. At very low  $q_{xy}$  (close to the y-axis) the 00L peaks in vertical direction are weakly visible, having  $q_z$  values of  $L \cdot 0.4075 \text{Å}^{-1}$ . The presence of a fraction of bulk phase pentacene is visible in the reciprocal space map as the powder ring like extensions on the side of the straight crystal truncation rods of the inplane reflections.

The XRD pattern of a 20nm TTC layer (Fig. 4.13, sample c) shows strong reflections at  $q_{xy} = 1.525 \text{Å}^{-1}$  and  $q_{xy} = 1.692 \text{Å}^{-1}$ . Supposing a standing configuration of the molecules on the surface and an orthorhombic crystal structure as previously reported [53, 47, 54, 55], these peaks can be indexed as the 110 and 020 planes. Additional reflections at  $q_{xy} = 1.90 \text{Å}^{-1}$  and  $q_{xy} = 2.51 \text{Å}^{-1}$  can be assigned to the 120 and 200 planes respectively. The peaks labeled with a star occur at the same  $q$  values as the 110 and 020 reflections. In agreement with the AFM analysis (Fig. 4.10b) and the reflectometry measurements, we find a standing phase in the lowermost layers of the TTC film and a lying phase on top of the second or higher layers. In Fig. 4.13c the star labeled peaks are attributed to the reflections of a lying TTC phase.

A combination of the pentacene and the TTC reflections is observed in the XRD pattern of the "sandwich" structured film (Fig. 4.13b, 20nm TTC on 50nm pentacene). Noticeable is the changed intensity of specific reflections. We find a larger intensity of the TTC reflections attributed to the lying phase (star labeled reflections), while the standing phase of TTC shows only weak signal. Furthermore, a dominant fraction of lying phase is supported by the observation of the TTC 00L reflection series at very low  $q_z$  ( $\approx 0$ ) and  $q_{xy} \approx L \cdot 0.11 \text{Å}^{-1}$ , suggesting the TTC long molecular axis orienting parallel to the surface. The peak labeled with two stars is supposed to originate from the 110 plane ( $q_{xy} = 1.525 \text{Å}^{-1}$ ) of a tilted lying phase [54].

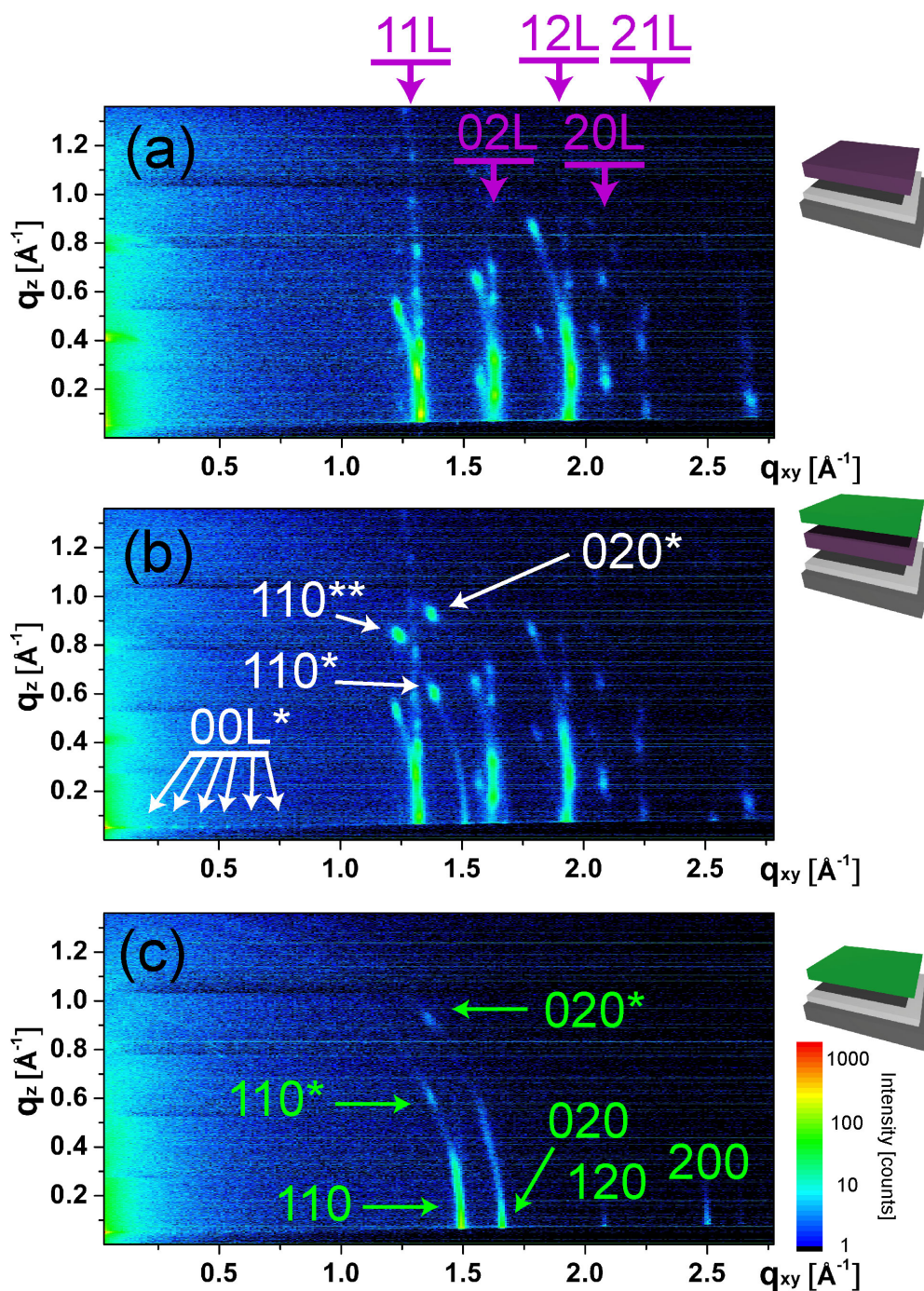


Figure 4.13: Reciprocal space maps of (a) pentacene, (b) TTC on pentacene and (c) TTC on modified silicon oxide. Scale bar is valid for all graphs. (\*) denotes a reflection originating from a lying phase.

### Conclusion

The spincoating experiments showed that a 50nm thin pentacene film is vulnerable to most non or weak polar solvents like toluene, benzene, hexane, hexadecane etc. After direct contact, a change in the crystal structure could be verified by X-ray diffraction experiments. Polar solvents like water or isopropanol do not change the crystal phase of pentacene. However, a drawback of the spincoating techniques is the loss of material due to the sheer forces on the organic film. Transistor devices with a spincoated capping layer showed only weak performance after the treatment.

When coating an organic film with e.g. a metal oxide using the sputter technique, the use of low power enables the conservation of the crystal structure of pentacene films while coating the device. However, even thicker encapsulation films could not protect the film completely from the influence of water. Thus this technique is also not suited for sensor encapsulation.

A major result of the capping experiments using vacuum deposition of alkanes ( $C_{44}$ ) is the unchanged crystal structure of the underlying pentacene film, as verified by the conservation of the out-of-plane peak positions (Fig. 4.12, a and c). Structural investigation showed an ordered lying phase of TTC on top of the pentacene film. The unit cell dimensions and the orientation could be revealed. From the improved (lowered) roughness of the stack, we estimate a good sealing capability.

To add biocompatibility to such a surface, the possibility to coat it with substrate supported lipid bilayers (SLB) is examined in the following chapter.

# Chapter 5

## Lipid Membranes on hydrophobic surfaces

In section 4.3 we identified TTC ( $C_{44}H_{90}$ , tetratetracontane) as a promising capping material to seal the active area in a field effect transistor (FET) device. Here we investigate the wetting behavior of lipid membranes on the TTC capping material in terms of homogeneity and fluidity. The initial setup aimed to seal the active layer (pentacene) exclusively with a lipid bilayer, therefore experiments on the lipid wetting on a pentacene surface are discussed in the first section, followed by membrane coating experiments of TTC surfaces.

### 5.1 Membrane on Pentacene

To form a lipid membrane on a pentacene surface, a 30Å thick pentacene film was vacuum deposited (3.1) on a silicon wafer. The wafer was mounted in a transparent fluidic chamber (modified  $\mu - SlideI$ , purchased from Ibidi GmbH, Germany) which allows to exchange solvents/buffer solutions or lipid solutions without drying out the surface. Fig. 5.1 shows an illustration of the microfluidic setup.

The samples are prepared such that only half of the wafer contains a pentacene coating (Fig. 5.1b) in order to form a membrane simultaneously on pentacene and the bare silicon oxide surface, which serves as a reference. Lipid solutions of 99.5mol% SOPC <sup>1</sup> lipids and 0.5mol% labeled TR-DHPE <sup>2</sup> lipids were mixed in chloroform, dried 4h in a vacuum oven and then dissolved in deionized water (1mg/ml). Lipid vesicles were fabricated using a standard extrusion protocol (100nm pore size). The vesicle solution was diluted 1 : 5

---

<sup>1</sup>1-stearoyl-2-oleoyl-sn-glycero-3-phosphocholine

<sup>2</sup>Spectra can be found in the web under <http://www.invitrogen.com/site/us/en/home/support/Product-Technical-Resources/Product-Spectra.1395lip.html>

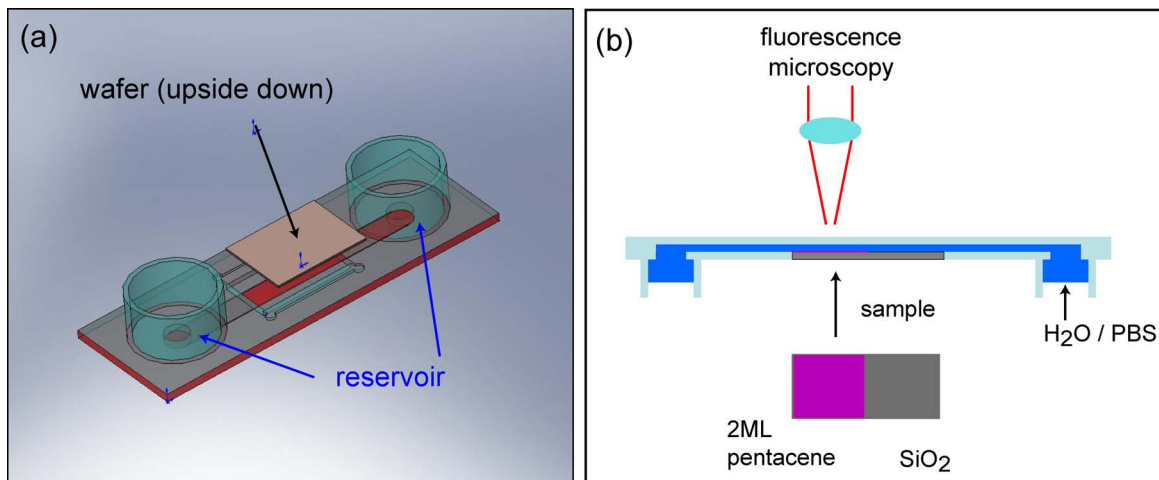


Figure 5.1: Microfluidic setup. (a) shows the backside of the chamber to clarify the position of the silicon wafer. (b) presents a side view of a cut through the fluidic chamber. Only half of the wafer is coated with pentacene to be able to compare membrane formation on both surfaces. The reservoirs are closed while not exchanging solutions and contain the desired environmental medium (DI-water or PBS buffer).

( $200\mu\text{l}$  vesicle solution +  $800\mu\text{l}$  DI water). After flushing the channel of the microfluidic chamber with DI water and ensuring that the surface has been wetted completely (getting rid of all bubbles in the channel can be achieved by filling the reservoirs and leaving the open chamber in an exsiccator while pumping) the reservoirs were emptied without letting the channel dry out. The vesicle solution was introduced into the microfluidic channel and incubated at least 3h.

The fluidic chamber was rinsed multiple times before the membrane formation is investigated with fluorescence microscopy to wash out excess lipids. A homogeneous coverage is confirmed by the absence of black regions and a uniform intensity on the surface. To measure the membrane fluidity, the continuous bleaching technique was used. By constantly illuminating a certain area, the fluorophores bleach after a certain time, which depends on the type of fluorescent dye. Supposing the membrane to be fluid, lipids carrying unbleached fluorophores may diffuse into the area of observation. In case of a fluid membrane, the diffusion leads to an increased intensity in the outer region, while the inner region gets darker. A capture frame of a membrane on pentacene is shown in Fig. 5.2b. (a) compares the intensity profiles of the membrane observed on pentacene (purple dots) and on silicon oxide (blue dots). The increased intensity at the outer region clearly shows a fluid membrane on both surfaces. The images have been taken using a Zeiss optical microscope and recorded with a Hamamatsu C4742-95 digital camera. A HXP-120 VisiTron light source was used for fluorescence illumination.

As already mentioned (compare sec. 6), membranes can exist in different conformations,

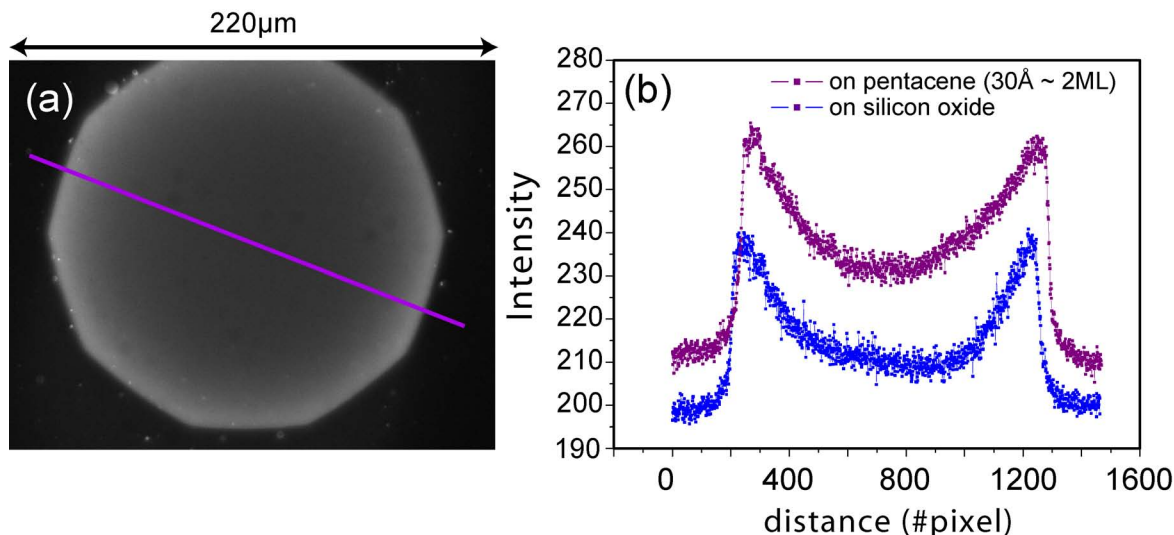


Figure 5.2: Fluorescence microscopy image of a membrane on 2ML pentacene (a). (b) shows the intensity along the respectively colored line in (a). For comparison, a line profile corresponding to an equally long (3min) bleached membrane on silicon oxide is shown in blue. Curves are shifted vertically.

e.g. as a bilayer or monolayer, or form an interdigitated bilayer structure. Often the hydrophobicity is related to the preferred structure a lipid layer will adopt, such that on hydrophobic surfaces predominantly a monolayer conformation is found, while hydrophilic surfaces support bilayer formation. The contact angle of pentacene is  $\approx 90^\circ$  which is neither strong hydrophobic nor hydrophilic.

To investigate the structure of the lipid layer on pentacene, we performed x-ray reflectometry measurements at the European Synchrotron Radiation Facility (ESRF), Beamline ID01, in Grenoble, France. The x-ray energy was 19.8 keV ( $\lambda = 0.626\text{\AA}$ ). The sample environment was similar to the one used for the microscopy experiments. To minimize the roughness, only 1ML ( $\approx 15\text{\AA}$ ) pentacene has been deposited on the substrate. Because of the small lateral beam size, it was possible to measure either the pentacene coated or the bare silicon oxide side of the sample. X-ray reflectometry curves and extracted scattering length density profiles are shown in Fig. 5.3.

In the left graph (a) data points and fitted curves are shown. Data fitting was done with Motofit [32]. While fitting, the sld value and thickness of the pentacene film was fixed to  $15.4\text{\AA}$  [7] and  $11.8 \cdot 10^{-6}\text{\AA}^{-2}$ . The scattering length density (sld) profiles and a schematic of the estimated membrane conformation inferred from the profiles are shown. We find a monolayer conformation on the pentacene surface, while a bilayer configuration is found on silicon oxide. In the case of pentacene as the effective surface, the pentacene layer takes the role of the lower leaflet of the bilayer on silicon oxide. Being more hydrophobic than silicon oxide, the lipid chains orient towards the pentacene surface. The lower sld value

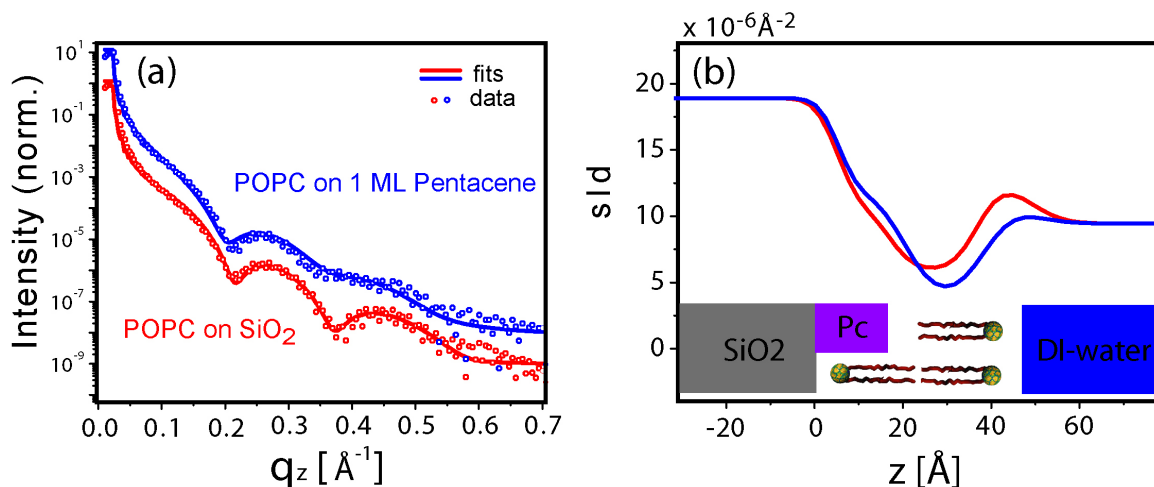


Figure 5.3: X-ray reflectometry measurements (a) and extracted scattering length density profiles (b) of a POPC membrane on 1 ML pentacene (blue curves) and on silicon oxide (red curves). Curves in (a) are shifted vertically for clarity. The schematic in (b) illustrates the different membrane conformations found on the surfaces.

found for the headgroups of the monolayer on pentacene is attributed to a higher roughness of that surface, thus the contrast is smeared out.

In the following it is shown that it is possible to coat the hydrophobic TTC ( $\text{C}_{44}\text{H}_{90}$ , 4.3) surface with a phospholipid membrane. This material has been identified to properly encapsulate pentacene films and protect them against outer influences, without damaging the crystal structure during the fabrication process.

## 5.2 Membrane on an Alkane Layer

The deposition of a lipid layer on top of a TTC encapsulated pentacene thin film is done to improve the electrical sealing of the capping layer, and more importantly to add biospecificity to the surface. In order to profit from the reduced roughness, first experiments were performed with 20nm TTC films grown on silicon oxide. Via vesicle fusion, SOPC lipid membranes (containing 0.5mol% fluorescently labeled lipids) were formed on the surfaces and observed with fluorescence microscopy.

Fig. 5.4 shows microscopy images at the beginning of the continuous bleaching measurement (a) and after 600 seconds of illumination (b). The bright ring forming at the outer region clearly signals a fluid membrane. Evaluation of the diffusion constant with a

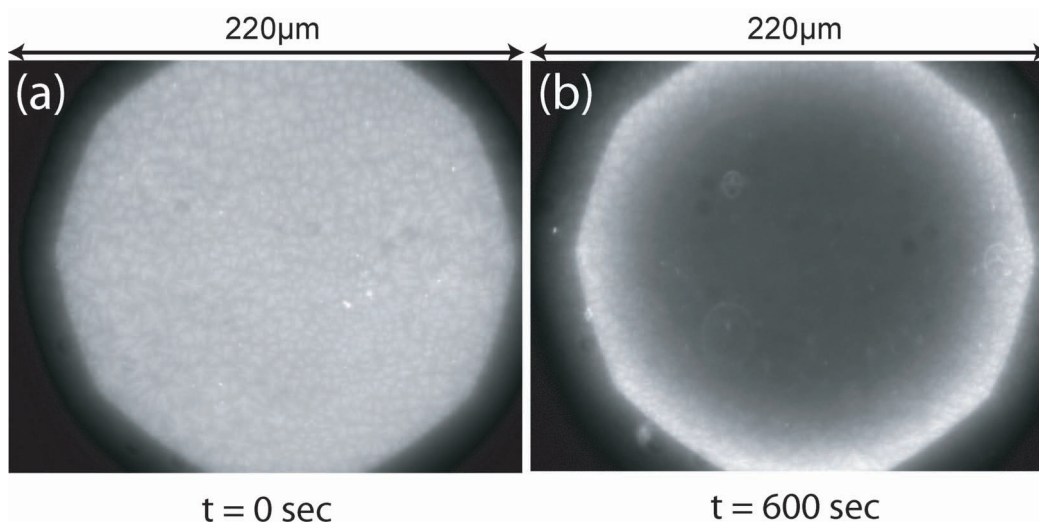


Figure 5.4: Fluorescence microscopy images of a SOPC membrane on 20nm TTC deposited on a silicon wafer right after opening the shutter (a), and after 10min of continuous illumination (b).

MatLab program [56] yielded  $D_{TTC} = 1.9 \pm 0.5 \mu m^2/s$ , which is below the value on silicon oxide ( $\approx 4 \pm 0.5 \mu m^2/s$ ).

The channel region of a thin film transistor (TFT) device is a 50nm pentacene which is encapsulated by 20nm TTC. For details about this surface see section 4.3. Now the surface is coated with a phospholipid layer. Fluorescently labeled lipids were mixed with SOPC lipids in chloroform and dried with nitrogen. After 4h in a vacuum storage the lipids were redissolved in 1mM sodium chloride solution. Lipid vesicles were produced by extrusion (pore size 100nm). Using the same microfluidic setup as described above (section 5.1, Fig. 5.1), the encapsulated pentacene surface was fully hydrated with 1mM NaCl solution before the lipid vesicle solution was introduced. After 3h of incubation, the microfluidic chamber was first rinsed with 1mM NaCl solution to remove excess lipids. In a second step, the fluidic chamber was rinsed with DI-water. The higher salt concentration inside the remaining (surface bound) lipid vesicles leads to a destabilization of the vesicles, which subsequently rupture and form a closed layer on the surface.

Fluorescence microscopy images after membrane formation was completed are shown in Fig. 5.5. (a) shows images after 0, 45, 90 and 135 seconds of continuous illumination. The establishment of a bright ring on the outer region signals a fluid membrane. The intensity profiles along a cross section through the respective image are given in (b). The first 9 frames of the continuous bleaching measurements (snapshots were taken every 5 sec) are used to fit the diffusion constant with a MatLab program [56]. A diffusion constant of  $D_{Pc+TTC} = 2.6 \pm 0.5 \mu m^2/s$  was determined, which is in good agreement with the value found on bare TTC, but still below the expected value on silicon oxide ( $\approx 4 \pm 0.5 \mu m^2/s$ ).

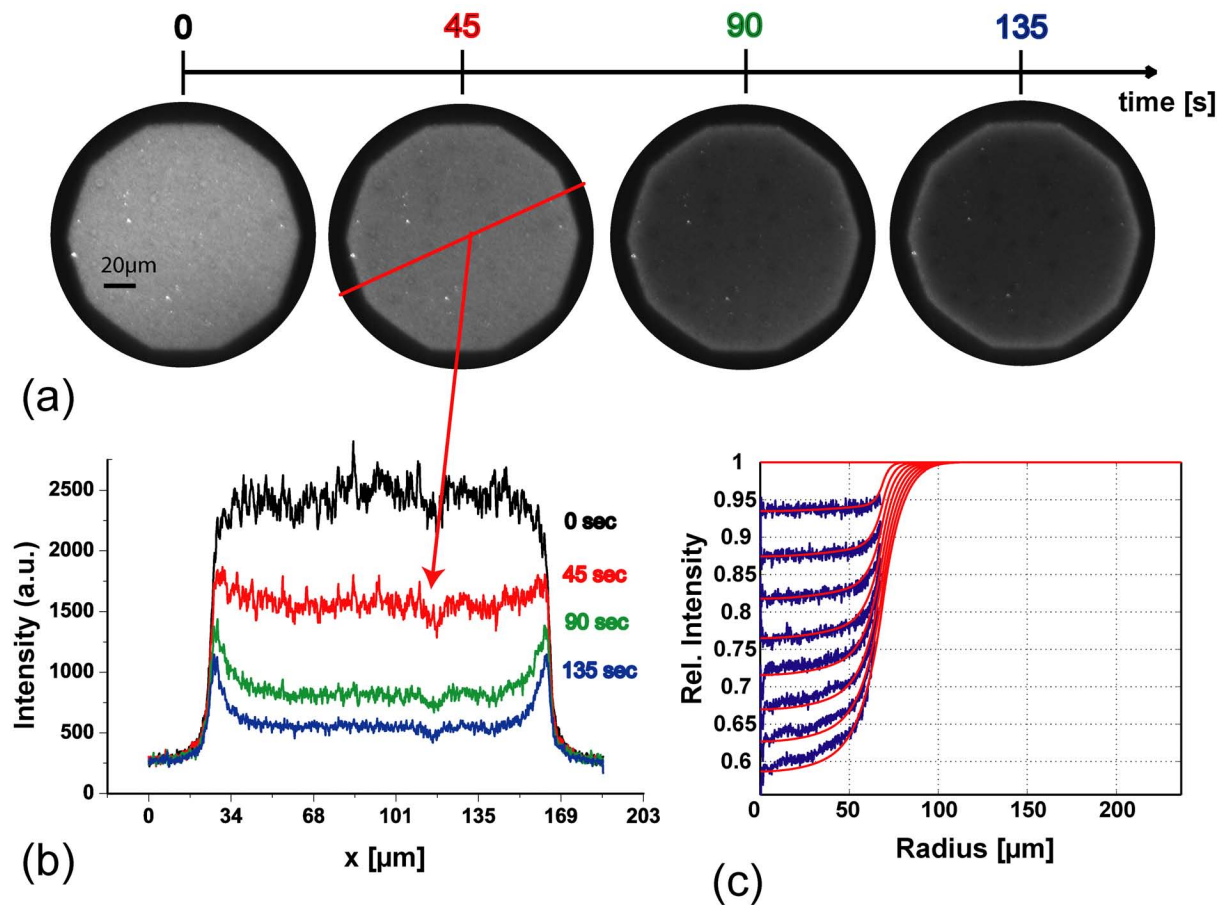


Figure 5.5: (a) Fluorescence microscopy images of a membrane on a 50nm pentacene film which is capped with a 20nm TTC film at different times after start of illumination. (a) shows the intensity profiles of a cross section of the images in (a). (c) plots the output of the Matlab fitting program used to fit the diffusion constant. Measured data is shown in blue (circular averaged intensity of the frames) and the fit is shown as red curves.

In this case, neutron reflectometry measurements have been inconclusive due to the intrinsically high roughness of the Pc/TTC heterolayer. Most likely, the membrane is in monolayer conformation.

### Conclusion

The main result is to confirm fluid membrane formation on a TTC surface, which adds biospecific functionality to the encapsulated sensor device surface. Electrically neutral phospholipids (SOPC<sup>3</sup>) are either dissolved in isopropanol and spincoated or prepared as vesicles (100nm diameter) and brought to the surface in solution. Fluorescence microscopy confirms the homogeneity and fluidity of the self assembled membranes. With the continuous bleaching technique a diffusion constant of  $D_{Pc+TTC} = 2.6 \pm 0.5 \mu m^2/s$  could be determined.

The bare membrane passivation of a surface is expected to improve the sealing properties of the underlying capping layer. In order to create an artificial cell surface, which allows the growth of living cells directly on the coating, the surface has to be functionalized further. A biomimetic approach to build such a coating is presented in the next chapter.

---

<sup>3</sup>1-stearoyl-2-oleoyl-sn-glycero-3-phosphocholine



# Chapter 6

## An Artificial Biomimetic Binding Surface

The sections above cover the issue of creating a transducer capable of measuring subtle changes of electric potentials in aqueous environment. The next challenge is to get an object of interest in close proximity to the active sensor area. Here our major focus lies on the attachment of cells, i.e. neural stem cells. The natural environment of a cell is composed of extracellular matrix (ECM) and the surfaces of other cells, therefore an artificial surface coating has to mimic these conditions. It is also known that cells sustain a special apoptotic fate without proper attachment [57]. In Biology, the cell membrane is a complex composition of lipids and proteins and has different functions, ranging from signal transport to cell motility including cell attachment to various surfaces.

In many ECM proteins (fibronectin, vitronectin, tenascin-C, etc.) the amino acid sequence arginyl-glycyl-aspartic acid (RGD sequence, Fig. 6.1a) is responsible for the binding of the proteins to their receptors on the cell surface. Our approach uses a synthesized peptide-conjugate AK-cyclo[RGDfC] [58] containing multiples of this sequences as an adhesion promoter. It consists of poly-L-lysine backbone decorated with oligo-DL alanine side chains carrying a stretched RGD sequence (arginyl-glycyl-aspartic acid) in a pentapeptide ring (cyclo[RGDfC]). Fig. 6.1 shows a schematic of the synthesis. Details can also be found in [59, 60].

In order to use the binding capabilities of the AK-cyclo[RGDfC], it has to be bound to the surface of interest in a way that its functionality is fully conserved at high and specific coverage. For that purpose we use a combination of supported lipid membrane techniques and biotin linking. These approaches are explained in the following.

Lipid bilayers consist of amphiphilic compartments and belong to the most important self assembling structures in nature. As part of the cell membrane, lipids have different functions, ranging from signal transport to cell motility including cell attachment to various surfaces. Artificially formed on a solid substrate (schematic shown in Fig. 6.2), lipid bilayers

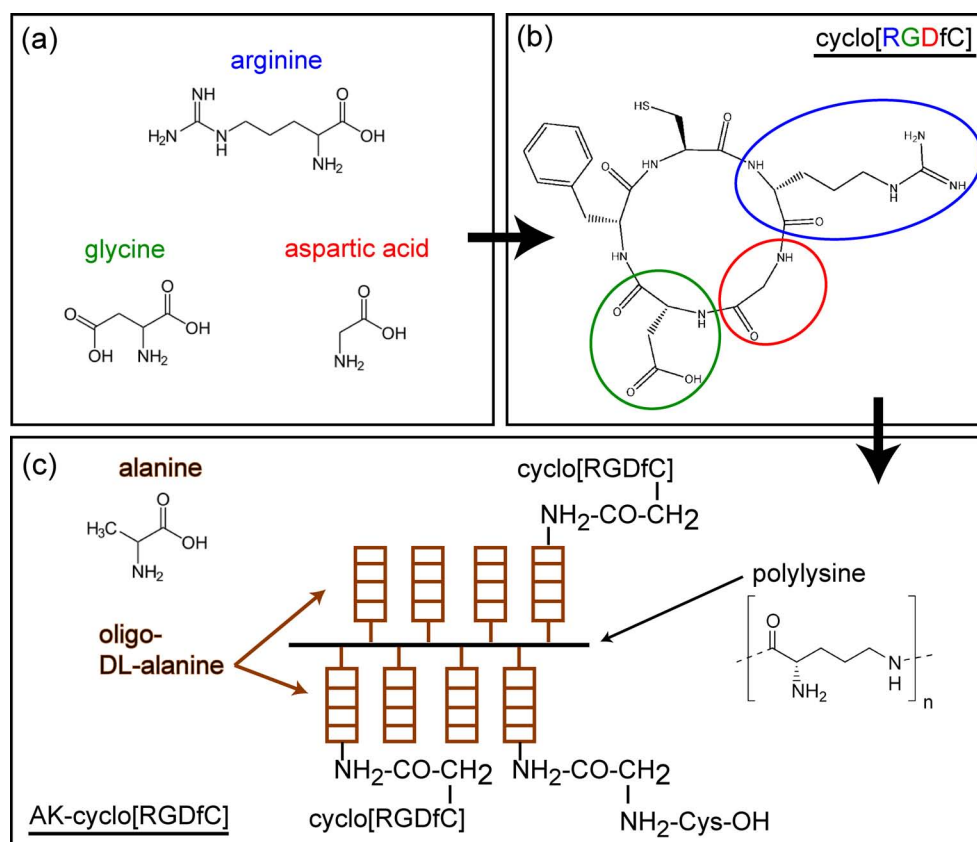


Figure 6.1: Schematic of the polypeptide synthesis. (a) Compartments of the RGD sequence. (b) Chemical structure of the cyclo[RGDfC]. (c) Sketch of the final macromolecule AK-cyclo[RGDfC] where the cyclo[RGDfC] has been bound to oligo-DL-alanine chains carried by a polylysine backbone via thioether linkage.

maintain their fluidity and their biological function, being separated from the substrate by a thin (10–20Å) water layer [61]. Supported lipid bilayers (SLB) have been proven to be an excellent experimental platform [62]. Using microscopy techniques (continuous bleaching, fluorescent recovery after photobleaching (FRAP) or fluorescence correlation spectroscopy (FCS)), biological function and diffusion behavior of membranes and proteins can be studied. Phospholipid membranes exist in different conformations, e.g. as a monolayer or bilayer [63], on some substrates in interdigitated domains [64]. Proteins can be embedded into the membrane or associated externally [65,66]. The possibility to coat various surfaces with SLB [63,64,67,68,69] enables the construction of cellular biosensors based on artificial substrates for cell adhesion. The feasibility to pattern lipid membranes has also been studied intensively. Numerous techniques including surface treatments [70,71,72], stamping [73] and optical post procession [74] have been developed. Dynamic patterning of SLB has been achieved using surface acoustic waves [75].

Biotin linking utilizes the strong affinity between the proteins avidin/streptavidin and bi-

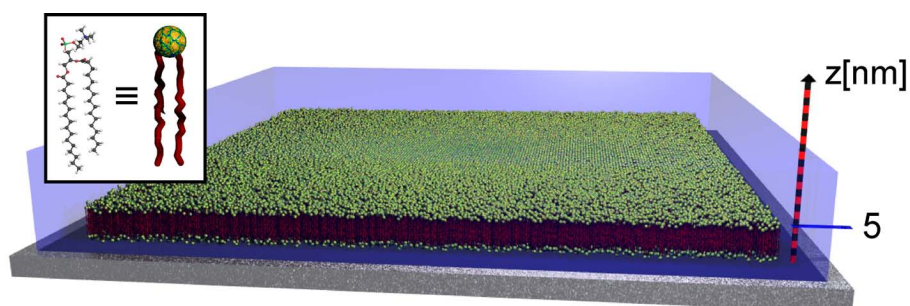


Figure 6.2: Illustration of a supported lipid bilayer (SLB). A vertical axis is given to clarify the dimensions. The inset shows the lipid model and the chemical structure of SOPC.

otin (vitamin B6), which is cofactor of many enzymes. Biotin can be covalently coupled to many proteins, including the AK-cyclo[RGDfC]. By providing an avidin or streptavidin surface, it is possible to specifically bind biotinated complexes. One way to create a stable protein surface is to form a lipid bilayer on a solid substrate, with a fraction of the lipids carrying a biotin anchor which is bound to their headgroup [65].

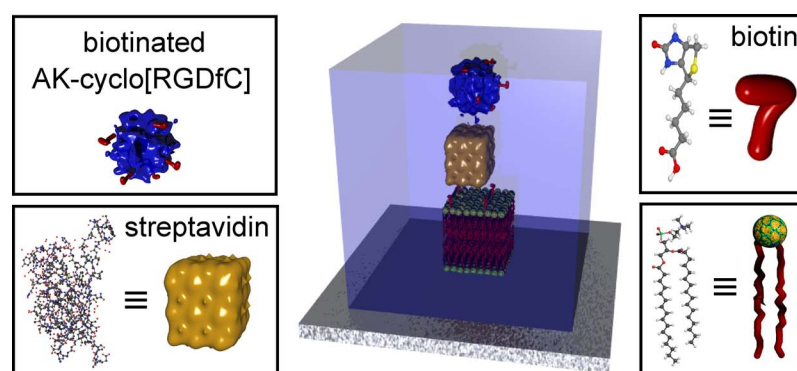


Figure 6.3: Sketch of the architecture of the biomimetic surface. The boxes contain information about the models used to illustrate the system. A lipid bilayer is formed on a silicon wafer. Via a streptavidin interlayer, the synthesized binding macromolecule AK-cyclo[RGDfC] is attached. Please note that different scales apply to the chemical structure models.

A schematic of the stack is shown in Fig. 6.3. Simple models have been used to illustrate the architecture. A preparation protocol is given in the next section (6.3). A detailed structural analysis using x-ray and neutron diffraction is presented in section (6.1). The function has been tested with cell growth experiments. The results are shown in section (6.2).

## 6.1 Trilayer Structure

The structural investigations aim to understand the dimensions and the layered ordering of the coating. Combining x-ray and neutron reflectometry offers unique sensitivity to all important parameters. X-ray experiments were performed at the Hamburger Synchrotronstrahlungslabor (HASYLAB), at the Deutsches Elektronen Synchrotron (DESY) in Hamburg, Germany. The energy was set to 19.75 keV ( $\lambda = 0.628\text{\AA}$ ). Neutron diffraction was measured using the N-REX reflectometer of the Forschung-Neutronenquelle Heinz Maier-Leibniz (FRM II) in Garching, Munich. The wavelength used was  $4.26\text{\AA}$ .

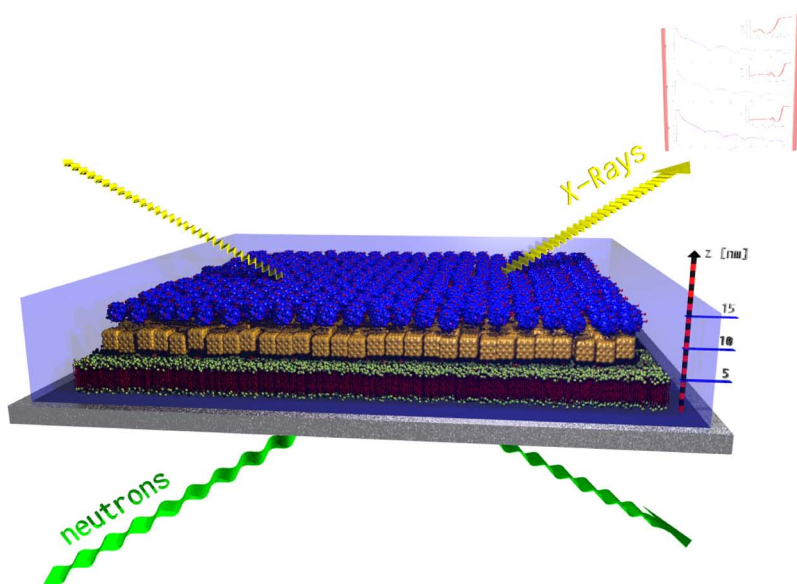


Figure 6.4: Large scale sketch of the architecture of the biomimetic surface. The different methods of characterizing the coating are indicated by the schematic colored waves.

X-ray measurements provide a better resolution which is proportional to  $2\pi/q_{z,max}$  and therefore limited by the maximum momentum transfer  $q_z$  that still yields signal ( $q_z = 4\pi/\lambda \cdot \sin(\theta/2)$ ,  $\theta$  is the diffraction angle). Thus the thickness of the layers could be determined with a resolution of  $9\text{\AA}$  ( $q_{z,max} = 0.7\text{\AA}^{-1}$ , Fig. 6.6). The intrinsic weak contrast of proteins and water for X-rays can be improved using neutrons. By employing a mixture of water and heavy water, the scattering length density (sld) of the solvent can be adjusted from  $-0.5 \cdot 10^{-6}\text{\AA}^{-2}$  (100%  $H_2O$ ) [76] to  $6.4 \cdot 10^{-6}\text{\AA}^{-2}$  (100%  $D_2O$ ) [76], while the values of biomolecules are in between. The total observed sld is a combination of scattering from the

molecule and scattering from the solvent, which allows for determination of the hydration of the layers:

$$sld[layer] = (1 - h) \cdot sld[molecule] + h \cdot [D_2O/H_2O + D_2O] \quad (6.1)$$

Here  $h$  is the hydration of a layer [%]. We performed neutron reflectometry measurements in two different contrasts (100%  $D_2O$ , 57%  $D_2O$  + 43%  $H_2O$ ) to match the  $sld$  of  $SiO_2$  in addition to the X-ray reflectometry.

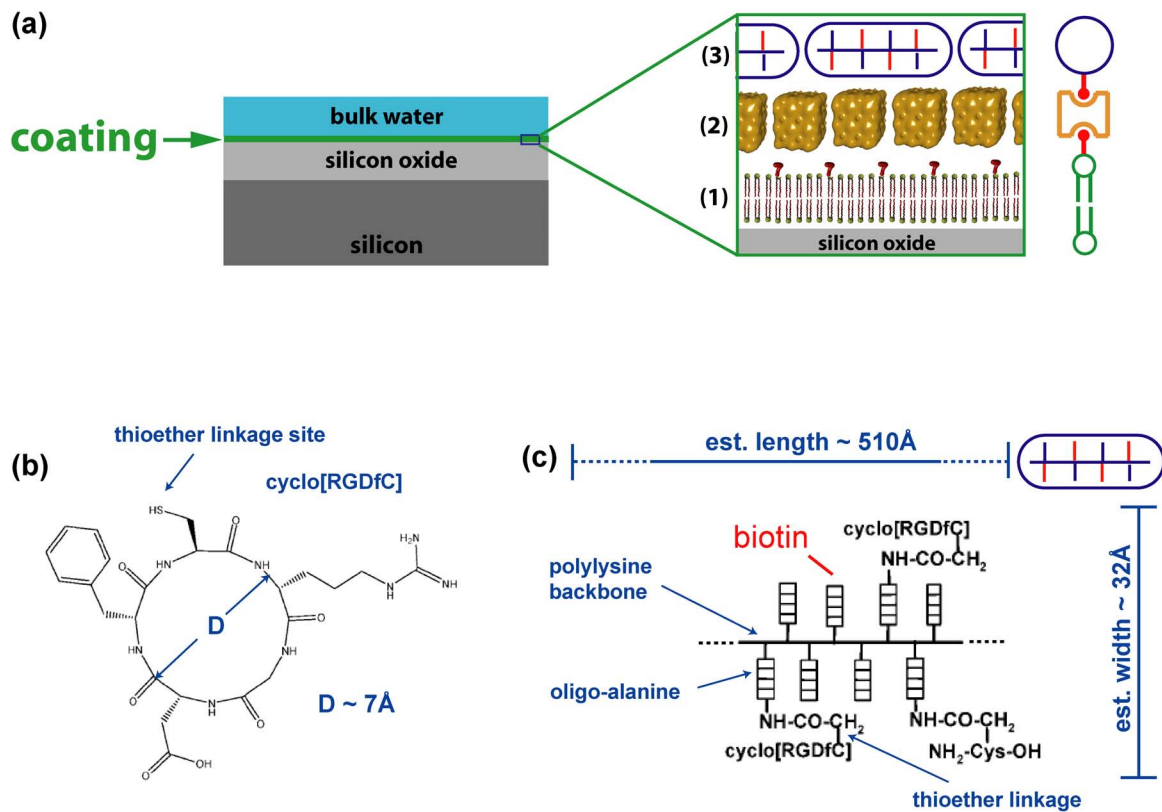


Figure 6.5: Schematics. (a). Sample structure. The lipid bilayer containing 2% of biotinylated lipids (1) is covered by a layer of streptavidin (2) which is bound to the lipid membrane by biotin anchors. A biotinylated adhesion peptide AK-cyclo[RGDfC] is bound on top of the streptavidin layer (3). (b) Chemical structure of the cyclic RGD-containing binding residue. (c) Architecture of the adhesion peptide. (b) and (c) are adapted from [58].

A schematic of the sample layout is shown in Fig. 6.5a. The fluidic chambers are chosen to match the specific requirements of each method, i.e. transparency of the container. The architecture of the binding molecule is illustrated in Fig. 6.5c. Scale bars indicate the

	neutron sld <sup>f</sup> (10 <sup>-6</sup> Å <sup>-2</sup> )	xray sld <sup>f</sup> (10 <sup>-6</sup> Å <sup>-2</sup> )	thickness (Å)	hydration (%)
lipid heads	1.78	13.8	11	54 (lower) 63 (upper)
lipid chains	-0.2	8	18	17
hydrated region	6.36 <sup>D<sub>2</sub>O</sup> /3.9 <sup>a</sup>	9.45	26	100
streptavidin	1.2	10.5	38	0
Ak-cyclo[RGDfC]	1.2	10.2 <sup>b</sup>	30	12

Table 6.1: Parameters obtained from neutron and X-ray reflectometry data. The values describe the slab model of the sld and hydration profiles depicted in Fig. 6.7

calculated dimensions obtained by estimating the size of the constituents. Details of the calculation can be found in A.1. Fig. 6.5b show the details of the part carrying the RGD sequence, which is responsible for the binding to specific receptors (cyclo[RGDfC]).

Solving the structure was achieved by fitting the measured reflectometry curves to a theoretical model. Applying an iterative fitting process, a single set of structural parameters is found to fit the three measurements. Fitting was performed using the Motofit [32] package in Igor®. In detail, the thickness of the layers was determined by fitting the x-ray data. The second step was to evaluate the hydration of the layers by fitting the two neutron measurements simultaneously. More details about the fitting process can be found in A.1, as well as a calculation estimation the molecular weight and the size of the AK-cyclo[RGDfC].

Fig. 6.6 shows the data (open circles) and best fits (lines). The scattering length density profiles are shown in Fig. 6.7b. Fig. 6.7a illustrates the hydration of the layered system and a sketch of the constituents. Tab.6.1 summarizes the parameters of the slab model. The values are given in whole numbers in order to attribute to the quite large errors involved due to fitting three different datasets to one structure, and represent the global best fit found after several iterations.

From the estimation of the dimensions A.1 we derive a configuration where the AK-cyclo[RGDfC] molecule is standing on the side on the streptavidin surface. Because of its length of several times the extension of streptavidin the AK-cyclo[RGDfC] molecule spans over multiple streptavidin neighbors. A simplified 2D sketch of the arrangement is shown in Fig. 6.7c. The estimated width of 32Å fits very well to the observed layer thickness of 30Å. Hence it has been shown that biomimetic coatings can be realized on the basis of a phospholipid bilayer. The structure was determined by finding one set of

parameters capable of fitting three different reflectometry curves. The combination of x-ray and neutron diffraction experiments clearly showed the layer by layer structure of the system and the respective thicknesses and hydration levels. The following part presents cell growth experiments on artificial coatings to test the specific cell adhesivity.

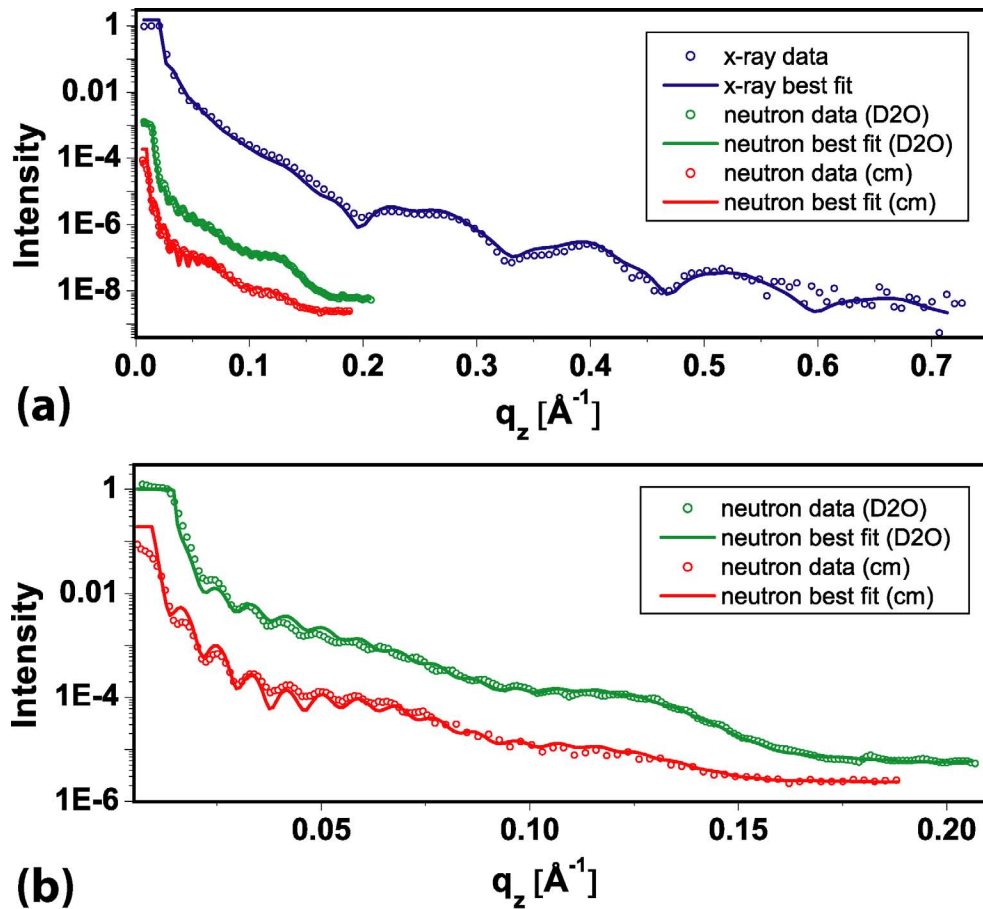


Figure 6.6: Reflectometry data and best fits. (a) The reflected intensity is plotted against the momentum transfer  $q_z$ . Intensity scale is logarithmic and normalized to a total reflection signal of 1. The reflectometry data are represented by open symbols, curves represent best fits. The neutron measurements are shown in green [ $D_2O$ ] and red [cm], the X-ray measurement is shown in blue. (b) Detailed view of the neutron data and best fits. Color and symbols as in (a).

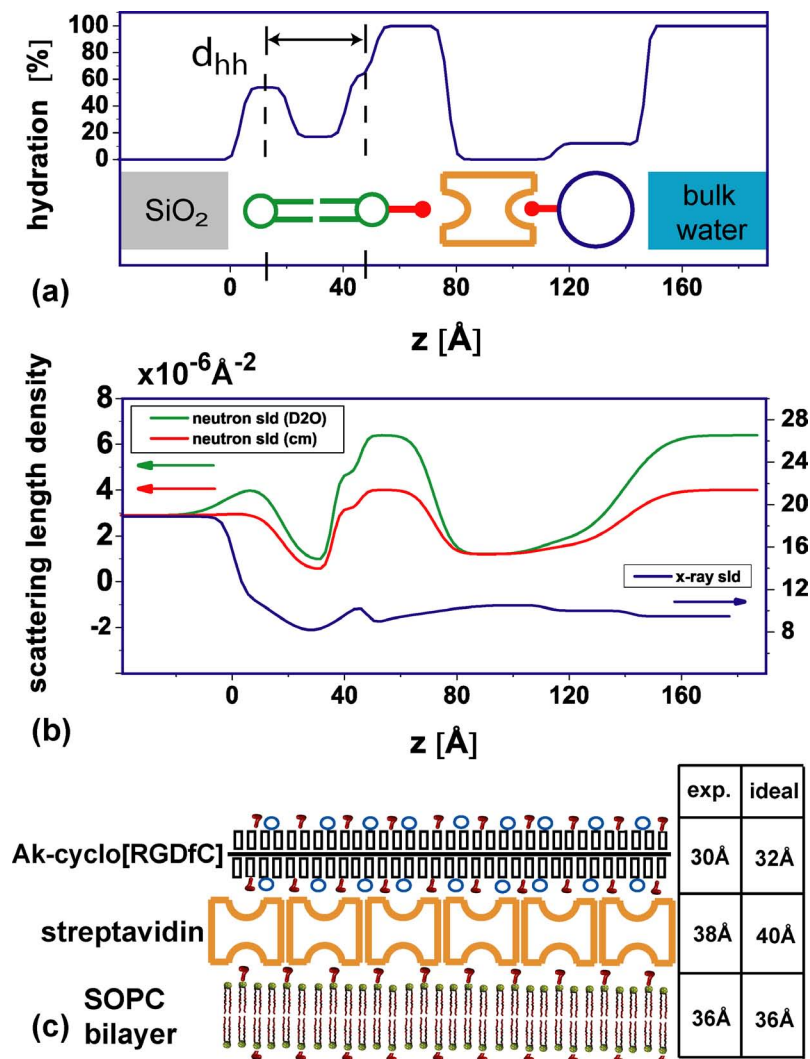


Figure 6.7: Scattering length density and hydration profile. (a) Hydration profile of the layers including a schematic of the layer components.  $d_{hh}$  indicates the head to head distance of the lipid bilayer. (b) Sld profiles of layers. Colored arrows indicate the respective y-axis. (c) Schematic of the synthetic peptide on top of the streptavidin interlayer. Red hooks depict the biotin residues, blue circles indicate the positions of a cyclo(RGDfC) residue. The bilayer- streptavidin interlayer is omitted. The table compares experimental findings and literature values.

## 6.2 Cell Adhesion

The cell adhesive features of biotinated and lipid-anchored AK-cyclo[RGDfC] molecules were checked by evaluating binding to cell surface receptors and anchoring cells to SLBs, respectively. Neural stem cells known to carry cyclo[RGDfC] binding integrins at high density on cell surfaces were suspended in artificial liquor solution (ACSF) and were incubated with biotinated or not-biotinated AK-cyclo[RGDfC] for 30 min at 37°C, in suspension. After removing the excess peptides by three-times washing with ACSF, avidin-coupled fluorochrome (Alexa488-Avidin; Molecular Probes) was added to both preparations for 20 min. After rinsing, the binding of the biotinated peptide was clearly demonstrated by fluorescence microscopic observations (Fig. 6.8). The adhesion of neural stem cells to AK-cyclo[RGDfC] - functionalized SLBs was investigated by introducing the cells to microfluidic chambers carrying different surface-coatings (Fig. 6.9).

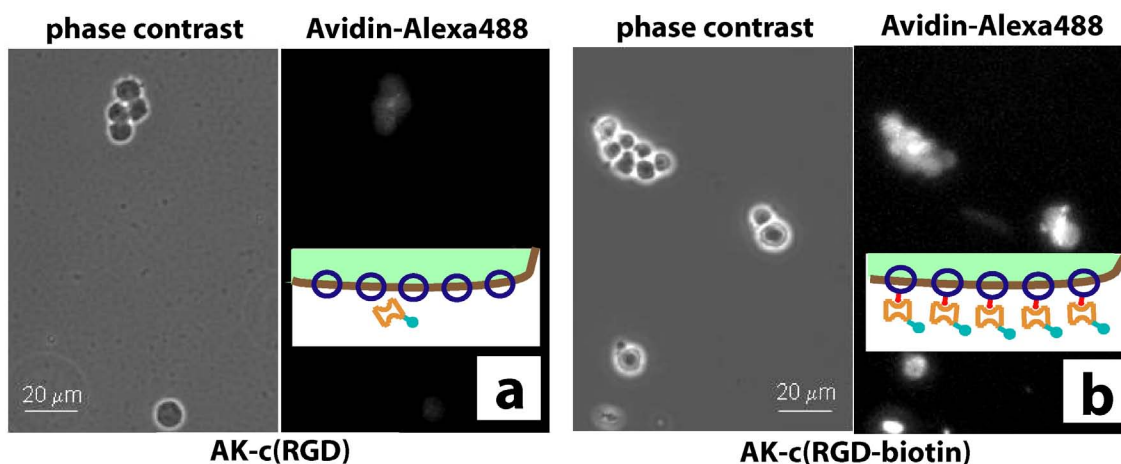


Figure 6.8: Phase-contrast and fluorescence microscopy (FM). (a) Neural stem cells are imaged by phase-contrast microscopy. Cells are first exposed to non-biotinated AK-cyclo[RGDfC] peptides, and secondly to fluorescently labeled avidin, and finally imaged by FM. (b) Cell exposure to biotinated AK-cyclo[RGDfC] enhances avidin absorption to cells. The insets illustrate the surface of a cell decorated with AK-cyclo[RGDfC] (shown in blue) or the biotinated AK-cyclo[RGDfC] (shown in blue with red bars) and the binding to fluorescently labeled avidin (shown in orange, label shown in turquoise).

The plain or biotin-avidin functionalized lipid layers did not support the attachment of neural stem cells as it was seen by the non-spreading (spheroid) cell morphology and enhanced aggregate formation. The presence of both AK-cyclo[RGDfC] and biotinated AK-cyclo[RGDfC] improved the attachment in each case indicating that the peptide was stuck on the surface, either at discontinuities of the lipid layer, or to the lipid layer itself, even in the absence of biotin-avidin binding. The most rapid and complete attachment, however, was observed if the adhesive peptide was firmly bound to the lipid membrane by

biotin-avidin coupling.

The results showed that AK-c(RGDfC) can be bound to lipid layers without corrupting its adhesive features, and after functionalization with adhesive substances, supported lipid layers can anchor cells.

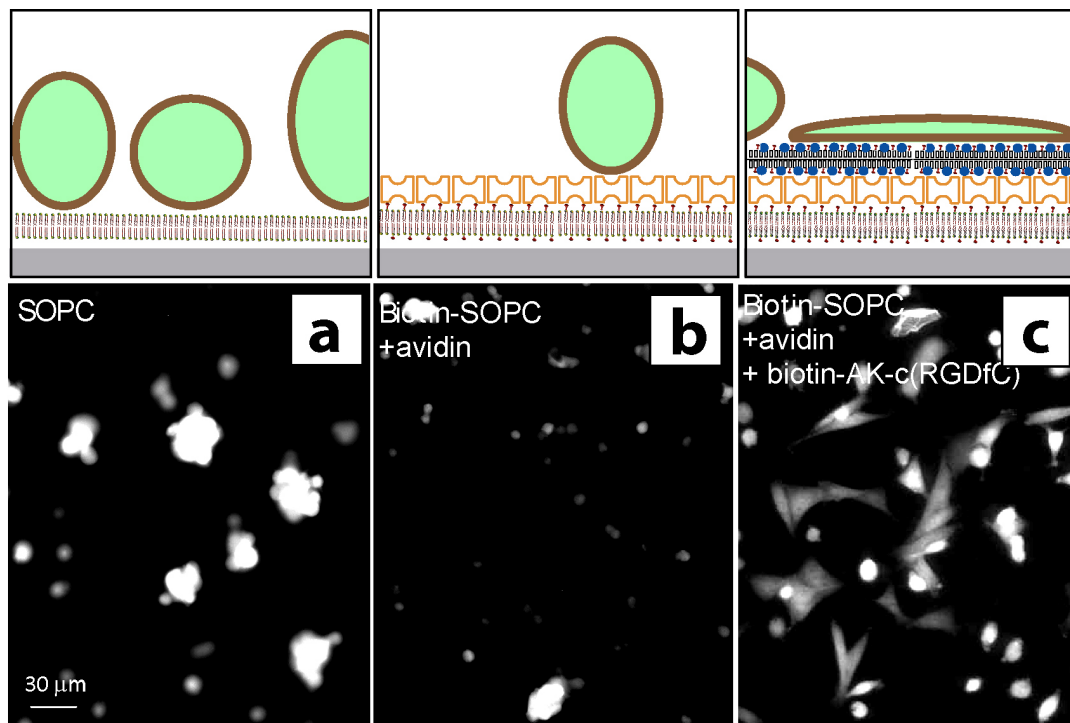


Figure 6.9: Fluorescence microscopy (FM) images of GFP expressing (fluorescent) radial glial cells. The FM images were recorded 4 hours after cell seeding. (a) Radial glial cells attached to SOPS coated surfaces show a spheroid shape. (b) Cell attachment to an avidin functionalized biotinated membrane is largely suppressed. (c). Rapid spreading of glial cells is observed for the biotin-AK-c[RGDfC] functionalized membrane. Schematics illustrate the conformation of the cells on the surface.

### 6.3 Preparation Details

In the following, the protocol to fabricate the biomimetic coating is presented. Commercially available silicon wafers with a thermally grown oxide layer of 100 nm thickness, purchased from SiMat, Germany, were used as substrates for the x-ray and cell experiments. The neutron reflectometry measurement was done using a polished silicon block (10x10x1cm) with a 60nm thermally grown oxide layer. Substrates were cleaned by standard solvents and wet chemistry steps. In detail, wafer pieces were immersed in Acetone

and Isopropanol, followed by sonication in deionized water (DI), followed by a alkaline step (NH<sub>4</sub>OH:H<sub>2</sub>O<sub>2</sub>:DI mixed 1:1:5 at 80°C, 20 min), an acidic step (HCl:H<sub>2</sub>O<sub>2</sub>:DI mixed 1:1:5 at 80°C, 15 min) and again the alkaline step.

Lipid solutions were produced by mixing SOPC <sup>1</sup> lipids with 0.5mol% of DHPE <sup>2</sup> lipids labeled with a fluorescent dye (Oregon Green) and alternatively adding 2mol% biotin-X-DHPE <sup>3</sup>. The lipids were mixed in Chloroform and dried with nitrogen. The supported lipid bilayers (SLB) were produced by spincoating. Therefore the appropriate lipid solution was dissolved in Isopropanol (1.5mg/ml) and spincoated on the bare substrate with a BLE delta spincoater, using maximum acceleration and a ramp with 3 sec 2000 rpm followed by 60 sec 3000 rpm. To minimize solvent residues, the samples were kept in vacuum at room temperature for at least 4h. Sterile tissue culture plates were used for transport and storage of the samples to prevent bacterial contamination. Mounting of the samples in the microfluidic chamber [77], as well as the change of buffer-solutions or DI water was done in sterile environment.

To form the supported lipid bilayer, the fluidic chamber was filled with deionized water and kept in the dark over night at ambient temperature. After extensive rinsing, excess lipids in solution and multilayers forming on the surface were removed, under fluorescence microscopic control.

The DI water was replaced by PBS buffer ( $pH = 7.4$ ) and 200 $\mu$ l of streptavidin (Sigma-Aldrich) dissolved in PBS buffer (40 $\mu$ g/ml) was introduced in the fluidic chamber and again stored in the dark over night at ambient temperature. Finally, the Streptavidin solution was replaced by DI water and extensively rinsed. The AK-cyclo[RGDfC] peptide-conjugate [58] was synthesized and kindly provided by G. Mezo (Peptidechemistry Research Unit of Hung. Acad. Sci., Budapest). The peptides (1 $\mu$ g/ $\mu$ l) were biotinated by overnight incubation with SNHS-biotin (2 $\mu$ g/ $\mu$ l, Sigma) in 1 M phosphate buffer ( $pH = 7.6$ ). The excess biotin and salts were removed by 24-hour dialization (3500 kDa dialyzing membrane; Serva) against distilled water with three fluid changes. After dialization, the protein content was determined and the preparation was occasionally concentrated by vacuum dialization.

Biotinated Ak-cyclo[RGDfC] molecules (10 $\mu$ g/ml in DI water) were injected into the microfluidic chamber and were let to bind overnight, in dark. After incubation, the chamber was rinsed with DI water to remove excess AK-cyclo[RGDfC] molecules, those not bound the streptavidin layer. Samples were freshly prepared for each experiment.

---

<sup>1</sup>1-stearoyl-2-oleoyl-sn-glycero-3-phosphocholine

<sup>2</sup>1,2-dihexadecanoyl-sn-glycero-3-phosphoethanolamine

<sup>3</sup>N-((6-(biotinoyl)amino)hexanoyl)-DHPE, triethylammonium salt

### Conclusion

With these experiments we have shown that a variety of different surfaces can be coated in a way that neuronal stem cells attach, grow and spread on the surface. Supported lipid bilayers provide a substantial toolbox for coating several types of surfaces. With the biotin linking technique, adhesion peptide conjugates can be bound to the supported bilayer via a streptavidin interlayer. Scattering techniques using synchrotron and reactor sources enable the structural analysis of such a multilayer system and help to understand the function.

Together with the encapsulated organic thin film transistor, which can operate in physiological environment, the basis for a neuronal sensor device has been developed. The next step is to measure changes of the electrical potential in the electrolyte by detecting reference signals induced with a platinum and a Ag/AgCl counter electrode.

# Chapter 7

## Conclusions and Outlook

### Conclusions

Organic molecular beam epitaxy is a clean and reproducible method to grow organic thin films with a controlled thickness in the Angstrom regime. The strong anisotropy of the organic molecules leads to complex molecular arrangements, which are highly sensitive to the fabrication parameters, like the deposition rate and the substrate temperature used during film deposition. The morphology and the electrical properties of the film are strongly influenced by the growth conditions. To access the structural details on the molecular level, investigations of organic thin films and organic-organic heterolayers could be performed at synchrotron and neutron reactor sources with almost atomic resolution.

First, the deposition of pentacene ( $C_{22}H_{14}$ ) on smooth inert surfaces, which are used as gate dielectrics in a field effect transistor later on, was examined. Silicon dioxide, coated with a 20nm thin layer of a cyclic olefin copolymer (COC), could be identified as a substrate allowing for a large yield of the required "thin film phase" of pentacene. The thin film phase is a polymorph showing the highest charge carrier mobility and thus is highly recommended for the use in organic electronics.

The comparison of experimental results to theoretical calculations of van der Waals interactions of anisotropic molecules and a smooth surface led to a deeper understanding of the involved aggregation mechanism. Single rod like model molecules with a geometry corresponding to a pentacene molecule can not adhere to a smooth inert surface due to the thermal energy. While attaching and detaching, they are able to diffuse long distances (up to several  $\mu m$ ) along the surface. When molecules meet, they form clusters which are stable if three or more molecules aggregate, because of the high intermolecular interaction energy. While growing, those clusters change their geometry towards a configuration which has the highest interaction energy when attaching to the surface in standing phase, which is exactly what we have experimentally observed, if pentacene or alkanes are vacuum deposited on smooth inert surfaces. Charged surfaces lead to a different situation. Pentacene thin films

deposited on chemically modified diamond surfaces showed that the growth mode can be switched from a lying phase on the almost metallic hydrogenated surface to a standing phase on the oxidized diamond. This underlines the dominant effect of the surface charges on the adhesion mechanism.

The next challenge was the operation of an organic transducer under physiological conditions, which can be seen as the essential step towards sensor technology. The uncoated pentacene film was found to be structurally stable in water, but an electronic operation was not possible. A solution to this drawback was developed by vapor depositing an insulating encapsulation layer on top of the pentacene film. The material of the capping layer is tetratetracontane (TTC,  $C_{44}H_{90}$ ), an alkane which forms a smooth and hydrophobic layer on top of the pentacene film. Most importantly, the electronically favorable "thin film phase" of pentacene is conserved during the encapsulation process, which was confirmed by diffraction experiments. Structural investigation of the pentacene - TTC heterolayer showed a horizontal conformation of TTC molecules on the rough pentacene surface.

In order to add biocompatibility, the possibility of coating the TTC surface with a substrate supported lipid membrane was investigated. Fluid membrane formation could be achieved by using the vesicle fusion technique and choosing electrically neutral phospholipids (SOPC<sup>1</sup>) as the main component. A homogeneous membrane passivation of the surface, as verified by fluorescence microscopy techniques, is expected to improve the sealing properties of the underlying encapsulation layer. Furthermore, supported lipid membranes provide a substantial toolbox for coating several types of surfaces and add further functionalizations.

The last step was the development of a biomimetic interface, that allows for a proper attachment of neural stem cells to a variety of different surfaces. We utilized an amino acid sequence (RGD<sup>2</sup>), which is responsible for the binding of extracellular matrix proteins to their receptors on the cell surface. This adhesion motif found in nature has been synthetically conjugated to an adhesion peptide, which can be bound to a SLB via a streptavidin interlayer using the biotin linking technique. Combined X-ray and neutron scattering structural investigation showed a dense packing of the synthetic adhesion motif in the uppermost layer of the SLB / streptavidin / adhesion peptide trilayer stacking, and revealed a stretched out on-edge conformation of the synthetic peptide on the streptavidin surface. The combination of using SLB and the biomimetic adhesion functionalization provides a method allowing for the proper attachment of neural stem cells to different technically relevant surfaces.

---

<sup>1</sup> 1-stearoyl-2-oleoyl-sn-glycero-3-phosphocholine

<sup>2</sup> arginyl-glycyl- aspartic acid

## Outlook

The major topics covered in this thesis were the structure - function interdependence of pentacene thin films, their encapsulation with an alkane layer and the subsequent coating with a lipid membrane. Furthermore, a bioadhesive coating based on lipid bilayers has been developed. Combining this coating with the functional layers of a field effect transistor, the basis for a biocompatible sensor device has been developed which can operate under physiological conditions and envisions the electronic characterization of the nanoenvironment of the a cell.

The complex topic of utilizing functional organic thin films in sensor devices remains a challenge in terms of parameter optimizing and relating their structure and function. Besides a high charge carrier mobility in the semiconducting layer, a good electrical and chemical sealing is expected from the encapsulation layer, while remaining as thin and smooth as possible. The possibility to operate a field effect transistor in liquid environment poses a new question of how the electrochemical potential close to the transistor channel can be understood and controlled. In this versatile environment, new phenomena occur in comparison with TFT operation in vacuum or at ambient conditions. At the interface between the encapsulated semiconductor and the buffer solution (e.g. cell medium, serum), different electrochemical effects could occur like charge transfer, redox reactions or leakage currents from the contacts. These effects have to be avoided, as e.g. the electrolysis of water would lead to a degradation of the heterolayer. Additionally, a microfluidic system has to be developed that allows for a consistent electronic characterization and provides a controlled way of exchanging solutions.

While the physisorption of charged molecules could directly be measured with the encapsulated TFT, a specific adhesion coating is necessary in order to bring living cells close enough to the transistor channel and to ensure their viability. On the way to sense cell signaling of e.g. neurons on the surface, at first the lipid membrane based coating has to be created on the sensor surface, and its influence on the transistor characteristics has to be studied. In a second step, the electrochemical potential can be set by an electrode or by manipulating the pH value. After understanding the sensors response, living cells can be attached to the coated sensor surface and characterized. If the device is sensitive enough to detect e.g. action potentials of a neuronal network of some cells, this would provide an excellent toolkit for medical research. Using very low concentrations, various substances and their influence on the cell signaling could be studied.



# Bibliography

- [1] M. Huth, S. Hertrich, G. Mezo, E. Madarasz, and B. Nickel. Neural stem cell spreading on lipid based artificial cell surfaces, characterized by x-ray and neutron reflectometry. *submitted to Materials*, 2010.
- [2] M. Göllner, M. Huth, and B. Nickel. Pentacene thin film transistors encapsulated by a thin alkane layer operated in an aqueous ionic environment. *Advanced Materials*, 2010.
- [3] W. Gajewski, M. Huth, F. Buth, B. Nickel, M. Stutzmann, and J. A. Garrido. Photoresponse and morphology of pentacene thin films modified by oxidized and reduced diamond surfaces. *Physical Review B*, 80, 2009.
- [4] E. Bystrenova, M. Jelitai, I. Tonazzini, A. N. Lazar, M. Huth, P. Stoliar, C. Dionigi, M. G. Cacace, B. Nickel, E. Madarasz, and F. Biscarini. Neural networks grown on organic semiconductors. *Advanced Functional Materials*, 18:1751–1756, 2008.
- [5] B. Nickel, M. Fiebig, S. Schiefer, M. Goellner, M. Huth, C. Erlen, and P. Lugli. Pentacene devices: Molecular structure, charge transport and photo response. *Physica Status Solidi A-Applications And Materials Science*, 205:526–533, 2008.
- [6] H. Marciniak, M. Fiebig, M. Huth, S. Schiefer, B. Nickel, F. Selmaier, and S. Lochbrunner. Ultrafast exciton relaxation in microcrystalline pentacene films. *Physical Review Letters*, 99, 2007.
- [7] S. Schiefer, M. Huth, A. Dobrinevski, and B. Nickel. Determination of the crystal structure of substrate-induced pentacene polymorphs in fiber structured thin films. *Journal Of The American Chemical Society*, 129:10316–+, 2007.
- [8] W. E. Klunk, H. Engler, A. Nordberg, Y. M. Wang, G. Blomqvist, D. P. Holt, M. Bergstrom, I. Savitcheva, G. F. Huang, S. Estrada, B. Aussen, M. L. Debnath, J. Barletta, J. C. Price, J. Sandell, B. J. Lopresti, A. Wall, P. Koivisto, G. Antoni, C. A. Mathis, and B. Langstrom. Imaging brain amyloid in alzheimer’s disease with pittsburgh compound-b. *Annals Of Neurology*, 55:306–319, 2004.
- [9] I. T. Lott and E. Head. Alzheimer disease and down syndrome: factors in pathogenesis. *Neurobiology Of Aging*, 26:383–389, 2005.

- [10] A. Nistor, A. Don, M. Parekh, F. Sarsoza, A. Goodus, G. E. Lopez, C. Kawas, J. Levenenz, E. Doran, I. T. Lott, A. Hill, and E. Head. Alpha- and beta-secretase activity as a function of age and beta-amyloid in down syndrome and normal brain. *Neurobiology Of Aging*, 28:1493–1506, 2007.
- [11] H. C. Hamaker. The london - van der waals attraction between spherical particles. *Physica*, 4:1058–1072, 1937.
- [12] R. Eisenschitz and F. London. Ober das verhältnis der van der waalsschen kräfte zu den homöopolaren bindungskräften. *Z. Physik*, 60:491, 1930.
- [13] Israelachvili. Intermolecular & surface forces. 1991.
- [14] M. Gsanger, J. H. Oh, M. Konemann, H. W. Hoffken, A. M. Krause, Z. N. Bao, and F. Wurthner. A crystal-engineered hydrogen-bonded octachloroperylene diimide with a twisted core: An n-channel organic semiconductor. *Angewandte Chemie-International Edition*, 49:740–743, 2010.
- [15] W. Kern and D. Puotinen. Cleaning solutions based on hydrogen peroxide for use in silicon semiconductor technology. *Rca Review*, 31:187, 1970.
- [16] E. Gomar-Nadal, B. R. Conrad, W. G. Cullen, and E. A. Williams. Effect of impurities on pentacene thin film growth for field-effect transistors. *Journal Of Physical Chemistry C*, 112:5646–5650, 2008.
- [17] D. Knipp, R. A. Street, A. Volkel, and J. Ho. Pentacene thin film transistors on inorganic dielectrics: Morphology, structural properties, and electronic transport. *Journal Of Applied Physics*, 93:347–355, 2003.
- [18] R. Pekoz and S. Erkoç. Density functional theory calculations on polyacene molecules. *Advanced Science Letters*, 3:43–48, 2010.
- [19] Y. Natsume, T. Minakata, and T. Aoyagi. Structures and electronic properties of thin-films of polycyclic aromatic hydrocarbons. *Thin Solid Films*, 517:3005–3010, 2009.
- [20] C. D. Dimitrakopoulos and P. R. L. Malenfant. Organic thin film transistors for large area electronics. *Advanced Materials*, 14:99–+, 2002.
- [21] C. D. Dimitrakopoulos and D. J. Masearo. Organic thin-film transistors: A review of recent advances. *Ibm Journal Of Research And Development*, 45:11–27, 2001.
- [22] C. D. Dimitrakopoulos, S. Purushothaman, J. Kymissis, A. Callegari, and J. M. Shaw. Low-voltage organic transistors on plastic comprising high-dielectric constant gate insulators. *Science*, 283:822–824, 1999.

- [23] H. Sirringhaus. Device physics of solution-processed organic field-effect transistors. *Advanced Materials*, 17:2411–2425, 2005.
- [24] H. Klauk, M. Halik, U. Zschieschang, G. Schmid, W. Radlik, and W. Weber. High-mobility polymer gate dielectric pentacene thin film transistors. *Journal Of Applied Physics*, 92:5259–5263, 2002.
- [25] D. Faltermeier, B. Gompf, M. Dressel, A. K. Tripathi, and J. Pflaum. Optical properties of pentacene thin films and single crystals. *Physical Review B*, 74, 2006.
- [26] A. Hinderhofer, U. Heinemeyer, A. Gerlach, S. Kowarik, R. M. J. Jacobs, Y. Sakamoto, T. Suzuki, and F. Schreiber. Optical properties of pentacene and perfluoropentacene thin films. *Journal Of Chemical Physics*, 127, 2007.
- [27] C. Ambrosch-Draxl, D. Nabok, P. Puschnig, and C. Meisenbichler. The role of polymorphism in organic thin films: oligoacenes investigated from first principles. *New Journal Of Physics*, 11, 2009.
- [28] T. H. Huang, H. C. Huang, and Z. W. Pei. Temperature-dependent ultra-thin polymer layer for low voltage organic thin-film transistors. *Organic Electronics*, 11:618–625, 2010.
- [29] C. Kim, J. R. Quinn, A. Facchetti, and T. J. Marks. Pentacene transistors fabricated on photocurable polymer gate dielectrics: Tuning surface viscoelasticity and device response. *Advanced Materials*, 22:342–+, 2010.
- [30] H. Yang, C. Yang, S. H. Kim, M. Jang, and C. E. Park. Dependence of pentacene crystal growth on dielectric roughness for fabrication of flexible field-effect transistors. *Acs Applied Materials & Interfaces*, 2:391–396, 2010.
- [31] M. Shtein, J. Mapel, J. B. Benziger, and S. R. Forrest. Effects of film morphology and gate dielectric surface preparation on the electrical characteristics of organic-vapor-phase-deposited pentacene thin-film transistors. *Applied Physics Letters*, 81:268–270, 2002.
- [32] A. Nelson. Co-refinement of multiple-contrast neutron/x-ray reflectivity data using motofit. *Journal Of Applied Crystallography*, 39:273–276, 2006.
- [33] C. C. Mattheus, A. B. Dros, J. Baas, G. T. Oostergetel, A. Meetsma, J. L. de Boer, and T. T. M. Palstra. Identification of polymorphs of pentacene. *Synthetic Metals*, 138:475–481, 2003.
- [34] A. Troisi and G. Orlandi. Band structure of the four pentacene polymorphs and effect on the hole mobility at low temperature. *Journal Of Physical Chemistry B*, 109:1849–1856, 2005.

- [35] M. I. Landstrass and K. V. Ravi. Hydrogen passivation of electrically active defects in diamond. *Applied Physics Letters*, 55:1391–1393, 1989.
- [36] M. I. Landstrass and K. V. Ravi. Resistivity of chemical vapor-deposited diamond films. *Applied Physics Letters*, 55:975–977, 1989.
- [37] K. Tsugawa, K. Kitatani, H. Noda, A. Hokazono, K. Hirose, M. Tajima, and H. Kawarada. High-performance diamond surface-channel field-effect transistors and their operation mechanism. *Diamond And Related Materials*, 8:927–933, 1999.
- [38] F. Maier, M. Riedel, B. Mantel, J. Ristein, and L. Ley. Origin of surface conductivity in diamond. *Physical Review Letters*, 85:3472–3475, 2000.
- [39] H. J. Looi, R. B. Jackman, and J. S. Foord. High carrier mobility in polycrystalline thin film diamond. *Applied Physics Letters*, 72:353–355, 1998.
- [40] A. Hartl, J. A. Garrido, S. Nowy, R. Zimmermann, C. Werner, D. Horinek, R. Netz, and M. Stutzmann. The ion sensitivity of surface conductive single crystalline diamond. *Journal Of The American Chemical Society*, 129:1287–1292, 2007.
- [41] D. Kafer, L. Ruppel, and G. Witte. Growth of pentacene on clean and modified gold surfaces. *Physical Review B*, 75, 2007.
- [42] L. Casalis, M. F. Danisman, B. Nickel, G. Bracco, T. Toccoli, S. Iannotta, and G. Scoles. Hyperthermal molecular beam deposition of highly ordered organic thin films. *Physical Review Letters*, 90, 2003.
- [43] H. Yoshida, K. Inaba, and N. Sato. X-ray diffraction reciprocal space mapping study of the thin film phase of pentacene. *Applied Physics Letters*, 90, 2007.
- [44] A. Vollmer, O. D. Jurchescu, I. Arfaoui, I. Salzmann, T. T. M. Palstra, P. Rudolf, J. Niemax, J. Pflaum, J. P. Rabe, and N. Koch. The effect of oxygen exposure on pentacene electronic structure. *European Physical Journal E*, 17:339–343, 2005.
- [45] P. Sigmund. Theory of sputtering.i. sputtering yield of amorphous and polycrystalline targets. *Physical Review*, 184:383, 1969.
- [46] <http://www.chemspider.com>. Database of chemical structures and property predictions. *Journal*.
- [47] J. Fenrych, E. C. Reynhardt, and I. Basson. Temperature dependence of the structures of solution-grown and melt-grown samples of n-hexatetracontane. *Powder Diffraction*, 12:49–52, 1997.
- [48] S. Basu and S. K. Satija. In-situ x-ray reflectivity study of alkane films grown from the vapor phase. *Langmuir*, 23:8331–8335, 2007.

- [49] H. Mo, H. Taub, U. G. Volkmann, M. Pino, S. N. Ehrlich, F. Y. Hansen, E. Lu, and P. Miceli. A novel growth mode of alkane films on a sio2 surface. *Chemical Physics Letters*, 377:99–105, 2003.
- [50] S. Trogisch, M. J. Simpson, H. Taub, U. G. Volkmann, M. Pino, and F. Y. Hansen. Atomic force microscopy measurements of topography and friction on dotriacontane films adsorbed on a sio2 surface. *Journal Of Chemical Physics*, 123, 2005.
- [51] C. Merkl, T. Pfohl, and H. Riegler. Influence of the molecular ordering on the wetting of sio2/air interfaces by alkanes. *Physical Review Letters*, 79:4625–4628, 1997.
- [52] B. M. Ocko, X. Z. Wu, E. B. Sirota, S. K. Sinha, O. Gang, and M. Deutsch. Surface freezing in chain molecules: Normal alkanes. *Physical Review E*, 55:3164–3182, 1997.
- [53] S. C. Nyburg and Potworow.Ja. Prediction of units cells and atomic coordinates for normal alkanes. *Acta Crystallographica Section B-Structural Science*, B 29:347–352, 1973.
- [54] E. B. Sirota. Remarks concerning the relation between rotator phases of bulk n-alkanes and those of langmuir monolayers of alkyl-chain surfactants on water. *Langmuir*, 13:3849–3859, 1997.
- [55] S. R. Craig, G. P. Hastie, K. J. Roberts, and J. N. Sherwood. Investigation into the structures of some normal-alkanes within the homologous series c13h28 to c60h122 using high-resolution synchrotron x-ray-powder diffraction. *Journal Of Materials Chemistry*, 4:977–981, 1994.
- [56] Kirstin Fritz geb. Seidel. Dissertation. 2010.
- [57] A. K. Howe, A. E. Aplin, and R. L. Juliano. Anchorage-dependent erk signaling - mechanisms and consequences. *Current Opinion In Genetics & Development*, 12:30–35, 2002.
- [58] K. Marko, M. Ligeti, G. Mezo, N. Mihala, E. Kutnyanszky, E. Kiss, F. Hudecz, and E. Madarasz. A novel synthetic peptide polymer with cyclic rgd motifs supports serum-free attachment of anchorage-dependent cells. *Bioconjugate Chemistry*, 19:1757–1766, 2008.
- [59] G. Mezo, E. de Oliveira, D. Krikorian, M. Feijlbrieff, A. Jakab, V. Tsikaris, C. Sakarellos, S. Welling-Wester, D. Andreu, and F. Hudecz. Synthesis and comparison of antibody recognition of conjugates containing herpes simplex virus type 1 glycoprotein d epitope vii. *Bioconjugate Chemistry*, 14:1260–1269, 2003.
- [60] M. Manea, G. Mezo, F. Hudecz, and M. Przybylski. Polypeptide conjugates comprising a beta-amyloid plaque-specific epitope as new vaccine structures against alzheimer’s disease. *Biopolymers*, 76:503–511, 2004.

- [61] S. J. Johnson, T. M. Bayerl, D. C. McDermott, G. W. Adam, A. R. Rennie, R. K. Thomas, and E. Sackmann. Structure of an adsorbed dimyristoylphosphatidylcholine bilayer measured with specular reflection of neutrons. *Biophysical Journal*, 59:289–294, 1991.
- [62] E. T. Castellana and P. S. Cremer. Solid supported lipid bilayers: From biophysical studies to sensor design. *Surface Science Reports*, 61:429–444, 2006.
- [63] S. T. Wang, M. Fukuto, and L. Yang. In situ x-ray reflectivity studies on the formation of substrate-supported phospholipid bilayers and monolayers. *Physical Review E*, 77, 2008.
- [64] M. B. Hochrein, C. Reich, B. Krause, J. O. Radler, and B. Nickel. Structure and mobility of lipid membranes on a thermoplastic substrate. *Langmuir*, 22:538–545, 2006.
- [65] M. R. Horton, C. Reich, A. P. Gast, J. O. Radler, and B. Nickel. Structure and dynamics of crystalline protein layers bound to supported lipid bilayers. *Langmuir*, 23:6263–6269, 2007.
- [66] V. Yamazaki, O. Sirenko, R. J. Schafer, and J. T. Groves. Lipid mobility and molecular binding in fluid lipid membranes. *Journal Of The American Chemical Society*, 127:2826–2827, 2005.
- [67] E. Sackmann. Supported membranes: Scientific and practical applications. *Science*, 271:43–48, 1996.
- [68] I. Burgess, M. Li, S. L. Horswell, G. Szymanski, J. Lipkowski, J. Majewski, and S. Satija. Electric field-driven transformations of a supported model biological membrane - an electrochemical and neutron reflectivity study. *Biophysical Journal*, 86:1763–1776, 2004.
- [69] P. K. Ang, K. P. Loh, T. Wohland, M. Nesladek, and E. Van Hove. Supported lipid bilayer on nanocrystalline diamond: Dual optical and field-effect sensor for membrane disruption. *Advanced Functional Materials*, 19:109–116, 2009.
- [70] A. N. Parikh. Membrane-substrate interface: Phospholipid bilayers at chemically and topographically structured surfaces. *Biointerphases*, 3:FA22–FA32, 2008.
- [71] P. Kim, S. E. Lee, H. S. Jung, H. Y. Lee, T. Kawai, and K. Y. Suh. Soft lithographic patterning of supported lipid bilayers onto a surface and inside microfluidic channels. *Lab On A Chip*, 6:54–59, 2006.
- [72] J. T. Groves, N. Ulman, and S. G. Boxer. Micropatterning fluid lipid bilayers on solid supports. *Science*, 275:651–653, 1997.

- 
- [73] J. S. Hovis and S. G. Boxer. Patterning barriers to lateral diffusion in supported lipid bilayer membranes by blotting and stamping. *Langmuir*, 16:894–897, 2000.
- [74] C. H. Yu, A. N. Parikh, and J. T. Groves. Direct patterning of membrane-derivatized colloids using in-situ uv-ozone photolithography. *Advanced Materials*, 17:1477–1480, 2005.
- [75] M. Hennig, J. Neumann, A. Wixforth, J. O. Radler, and M. F. Schneider. Dynamic patterns in a supported lipid bilayer driven by standing surface acoustic waves. *Lab On A Chip*, 9:3050–3053, 2009.
- [76] J. Pencer, T. Mills, V. Anghel, S. Krueger, R. M. Epanand, and J. Katsaras. Detection of submicron-sized raft-like domains in membranes by small-angle neutron scattering. *European Physical Journal E*, 18:447–458, 2005.
- [77] C. Reich, M. B. Hochrein, B. Krause, and B. Nickel. A microfluidic setup for studies of solid-liquid interfaces using x-ray reflectivity and fluorescence microscopy. *Review Of Scientific Instruments*, 76, 2005.



# Appendix



# Appendix A

## Publications

All publications to which MH contributed are listed in the following.

In a header page, all important information, including a list of authors, permanent web link and the abstract is given separately. Additionally the type of contribution is mentioned. The publications are sorted in inverse chronological order.



## A.1 Full text of Ref. [1]

Martin Huth, Samira Hertrich, Gabor Mezo, Emilia Madarasz and Bert Nickel

*Neural stem cell spreading on lipid based artificial cell surfaces, characterized by X-ray and neutron reflectometry*

Materials 2010, **3**, 4994

### **Abstract:**

We develop a bioadhesive coating based on a synthetic peptide-conjugate (AK-cyclo[RGDfC]) which contains multiples of the arginyl-glycyl-aspartic acid (RGD) amino acid sequence. Biotinated AK-cyclo[RGDfC] is bound to a supported lipid bilayer via a streptavidin interlayer. Layering, hydration and packing of the coating is quantified by x-ray and neutron reflectometry experiments. AK-cyclo[RGDfC] binds to the streptavidin interlayer in a stretched-out on edge configuration. The highly packed configuration with only 12% water content maximizes the number of accessible adhesion sites. Enhanced cell spreading of neural stem cells was observed for AK-cyclo[RGDfC] functionalized bilayers. Due to the large variety of surfaces which can be coated by physisorption of lipid bilayers, this approach is of general interest for the fabrication of biocompatible surfaces.

MH contribution:

- sample design and fabrication.
- performing the x-ray experiments and analysis.
- writing the paper.
- participation in discussions.

Article

## Neural stem cell spreading on lipid based artificial cell surfaces, characterized by combined X-ray and neutron reflectometry

Martin Huth <sup>1</sup>, Samira Hertrich <sup>1</sup>, Gabor Mezo <sup>2</sup>, Emilia Madarasz <sup>3</sup> and Bert Nickel <sup>1,\*</sup>

1 Ludwig-Maximilians-Universität, Department für Physik and CeNS, Geschwister-Scholl-Platz 1, 80539 Munich, (Germany)

2 Peptide Chemistry Research Group of Hungarian Academy of Science, Szigony u. 43, Budapest, H-1083 (Hungary)

3 Laboratory of Cellular and Developmental Neurobiology, Institute of Experimental Medicine of Hungarian Academy of Science, Szigony u. 43, Budapest, H-1083 (Hungary)

E-Mails: [m.huth@lmu.de](mailto:m.huth@lmu.de) (M.H.); [Samira.Hertrich@physik.lmu.de](mailto:Samira.Hertrich@physik.lmu.de) (S.H.); [gmezo@elte.hu](mailto:gmezo@elte.hu) (G.M.); [madarasz.emilia@koki.hu](mailto:madarasz.emilia@koki.hu) (E.M.); [nickel@lmu.de](mailto:nickel@lmu.de) (B. N.);

\* Author to whom correspondence should be addressed; Tel.: +49-89-2180-1460; Fax: +49-89-2180-3281

Received: / Accepted: / Published:

---

**Abstract:** We develop a bioadhesive coating based on a synthetic peptide-conjugate (AK-cyclo[RGDfC]) which contains multiples of the arginyl-glycyl-aspartic acid (RGD) amino acid sequence. Biotinylated AK-cyclo[RGDfC] is bound to a supported lipid bilayer via a streptavidin interlayer. Layering, hydration and packing of the coating is quantified by x-ray and neutron reflectometry experiments. AK-cyclo[RGDfC] binds to the streptavidin interlayer in a stretched-out on edge configuration. The highly packed configuration with only 12% water content maximizes the number of accessible adhesion sites. Enhanced cell spreading of neural stem cells was observed for AK-cyclo[RGDfC] functionalized bilayers. Due to the large variety of surfaces which can be coated by physisorption of lipid bilayers, this approach is of general interest for the fabrication of biocompatible surfaces.

**Keywords:** Supported lipid bilayers, Biomimetics, Bionanotechnology, Functional Coatings, Self-Assembly.

---

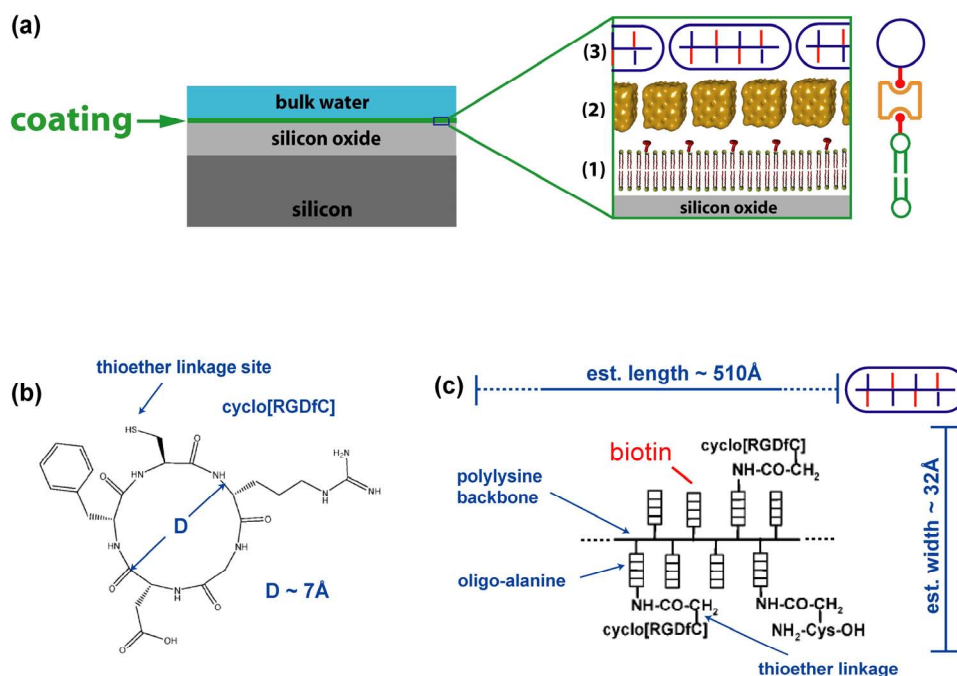
## 1. Introduction

Control of cell attachment on surfaces is a fundamental requirement in biophysical situations where close contact between cells and a technical surface is required, such as in sensing applications or tissue engineering. The natural environment of a cell is composed of extracellular matrix (ECM) and the surfaces of other cells, therefore an artificial surface coating has to mimic these conditions. Without proper attachment, cells sustain a special apoptotic fate called anoikis [1].

Here, cell attachment is promoted by a synthetic peptide-conjugate AK-cyclo[RGDfC]. AK-cyclo[RGDfC] is a novel, synthetic cell-adhesive peptide [2] comprising a poly-L-lysine backbone with oligo-D/L alanine side chains (AK, see Fig. 1c) composed of both D- and L-enantiomers of alanine and carrying the adhesive end-motif cyclo[RGDfC] at the N-termini. As it was shown previously by CD analyses [3, 4], the spacer built from raceme alanine residues results in non-structured peptide side-chains with increased sterical flexibility for the adhesive end-motif and improves the solubility of the carrier [5]. As a biologically active, cell adhesive moiety, the cyclo[RGDfC] cyclic pentapeptide (see Fig. 1b) was chosen due to the strong affinity of cyclic RGD pentapeptides to selected types of cell surface integrins [6]. The Cys residue provided sites for conjugation and the introduction of a D-enantiomer phenylalanine into the peptide ring was thought to result in a rigid RGD motif [7] easily recognized by  $\alpha_v\beta_3/\alpha_5\beta_5/\beta_1$  integrins known to be present on the surface of a number of neural [8, 9] and non-neural stem-like cells [2]. The resulted adhesive peptide conjugate was shown to support adhesion-based selection and serum-free propagation of neural stem cells [10]. This selectivity for adhering neural stem-like cells prompted us to functionalize lipid bilayers with AK-c(RGDfC) rather than peptides carrying linear RGD sequences [11] or laminin-motifs [12]. The cyclic RGD peptide was conjugated to a branched chain polypeptide AK through thioether linkage, which is an efficient tool for the preparation of polypeptide conjugates [13, 14]. The RGD sequence is present in many extracellular matrix proteins (fibronectin, vitronectin, tenascin-C, etc.). It is responsible for the binding of ECM proteins to their receptors on the cell surfaces. Previous studies of cells grown on AK-cyclo[RGDfC] adsorbed on SiO<sub>2</sub> in We use biotinylated AK-cyclo[RGDfC] (cf. Fig. 1c and Experimental) which is bound to streptavidin template on a biotinylated lipid bilayer (Fig. 1a) [15]. Supported lipid bilayers (SLB) have been proven to be an excellent experimental platform [16] to mimic functions of cell membranes. Using microscopy techniques, diffusion and protein binding can be studied [17]. For the characterization of the composition and layering of native or artificial membranes, a variety of surface techniques are available [18]. Structural properties can be accessed using diffraction techniques [19-21]. Recently, X-ray experiments have revealed the structure of biotinylated phospholipid bilayers [15] decorated with streptavidin. This two-dimensional lipid-protein template is of special interest because of its biotin-binding properties, since biotin (vitamin B6, a cofactor of many enzymes) can be covalently bound to many proteins. The possibility to coat various surfaces with SLB [15, 22-26] by physisorption, i.e. without need for surface chemistry is a strong point of this concept. Phospholipid membranes exist in different conformations, i.e. as monolayer, bilayer [22], and on some substrates as interdigitated bilayers [23]. Proteins can be embedded into the membrane or associated externally [15, 27]. Note that SLBs can also be patterned by surface treatments [28-30], stamping [31] and optical post procession [32]. Dynamic patterning of SLB has been achieved using surface acoustic waves [33]. A sensor array coated with lipid bilayers was recently envisioned by Kumar et al. [34] and patterned

attachment of human epithelial cells to SLB as a function of lipid composition was recently reported by Oliver et.al.[35]. Here we study neural stem cell attaching to a synthetic cell surface based on a trilayer structure of adhesion protein, streptavidin interlayer and lipid bilayer. The nanostructure of this bioselective surface was investigated with X-ray and neutron diffraction experiments.

**Figure 1.** Schematics. (a). Sample structure. The lipid bilayer containing 2% of biotinylated lipids (1) is covered by a layer of streptavidin (2) which is bound to the lipid membrane by biotin anchors. A biotinylated adhesion peptide (AK-cyclo[RGDfC]) is bound on top of the streptavidin layer (3). (b) Chemical structure of the cyclic RGD-containing binding residue. (c) Architecture of the adhesion peptide. (b) and (c) are adapted from ref. [2].



## 2. Results and Discussion

### 2.1. Coating structure and arrangement

The structural analysis combines X-ray and neutron reflectometry. The resolution  $\sigma[\text{\AA}]$  in a reflectometry experiment can be estimated by  $2\pi/q_z$  and is therefore limited by the maximum momentum transfer  $q_z$  that still yields a reflectometry signal. The momentum transfer  $q_z$  is given by  $q_z = 4\pi/\lambda \cdot \sin(2\theta/2)$ . Here,  $2\theta$  is the diffraction angle and  $\lambda$  is the wavelength. For X-ray, we achieve a  $q_z = 0.7 \text{ \AA}^{-1}$  (Fig. 2a), thus the internal structure of the layers can be determined with a resolution of  $\sigma = 9 \text{ \AA}$ . The intrinsic weak scattering contrast of proteins and water for X-rays can be improved using neutron beams [36]. For neutrons, the scattering length density (sld) of the solvent can be adjusted

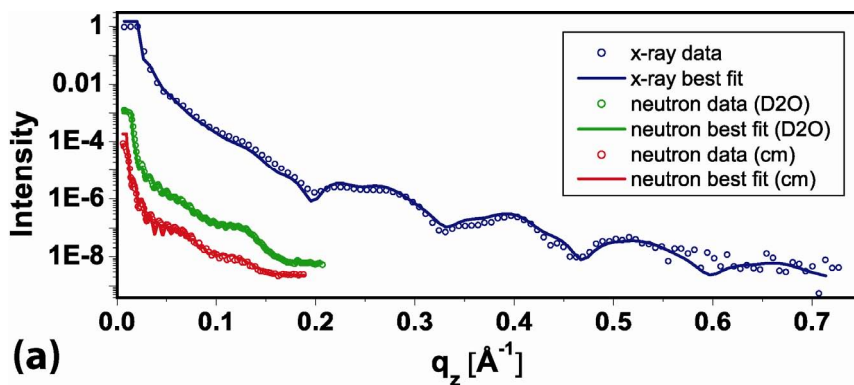
from  $-0.5 \cdot 10^{-6} \text{Å}^{-2}$  [100% H<sub>2</sub>O] [37] to  $6.36 \cdot 10^{-6} \text{Å}^{-2}$  [100% D<sub>2</sub>O] [37] by using a mixture of water and heavy water. The sld of biomolecules are typically in between. The total sld of a layer is a combination of the sld of the molecules in the layer and the sld from hydration water. Thus, measuring in two different water mixtures allows separating the molecular density and layer hydration:.

$$sld[layer] = (1 - h) \cdot sld[molecule] + h \cdot sld[D_2O / (H_2O + D_2O)] \quad (1)$$

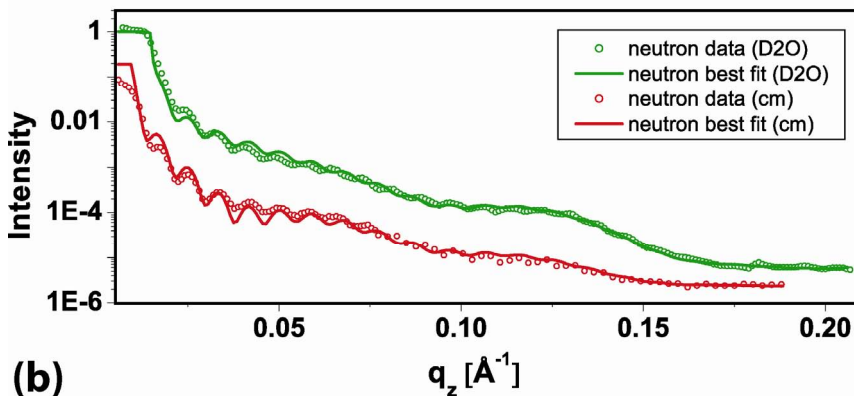
Here  $h$  is the hydration of a layer in [%]. Therefore, in addition to the X-ray reflectometry experiment, we performed neutron reflectometry measurements in two different contrasts. One measurement was performed in 100 % D<sub>2</sub>O [D<sub>2</sub>O], and one using a mixture which was contrast matched to the sld of SiO<sub>2</sub> [57% D<sub>2</sub>O + 43% H<sub>2</sub>O, *cm*] (Fig. 2). The value for the sld of the contrast matched medium was allowed to change between  $3.3 \cdot 10^{-6} \text{Å}^{-2}$  and  $4 \cdot 10^{-6} \text{Å}^{-2}$  to allow for small deviations in the mixing ratio in case that the previous medium might not have been exchanged completely. The fit yielded for the mixture a sld value of  $3.9 \cdot 10^{-6} \text{Å}^{-2}$ , indicating a 7.5% higher D<sub>2</sub>O fraction in the mixture. Combined fitting was performed using the Motofit [38] package in Igor®. A single set of structural parameters reproduces the neutron and X-ray reflectometry data.

**Figure 2.** Reflectometry data and best fits of the coating in liquid environment (Fig.1a). **(a)** The reflected intensity is plotted against the momentum transfer  $q_z$ . Intensity scale is logarithmic

and normalized to a total reflection signal of 1. The reflectometry data are represented by open symbols, curves represent best fits. The neutron measurements are shown in green [D<sub>2</sub>O] and red [*cm*], the X-ray measurement is shown in blue. **(b)** Expanded view of the neutron data and best fits. Colors and symbols as in (a).



(a)



(b)

In detail, first the thickness of the layers was determined from the X-ray data. The second step was to evaluate the hydration of the layers from the two neutron measurements. To estimate the hydration level, the molecular slds of lipids and streptavidin have been fixed according to the literature values [37, 39] (Tab. 1). The neutron scattering length density of the AK-cyclo[RGDfC] was also fixed to the value of streptavidin. In an iterative process, the hydration values from the neutron measurements were used to refine the X-ray measurement. The X-ray sld of the AK-cyclo[RGDfC] was allowed to vary by 5% around the sld of streptavidin. The data (open circles) and final best fits (lines) are shown in (Fig. 2). The scattering length density profiles are summarized in (Fig. 3b). The hydration (Eq. 1) of the layered system and a sketch of the constituents are illustrated in (Fig. 3a). The parameters of the slab model are summarized in (Tab.1).

**Table 1.** Parameters obtained from neutron and X-ray reflectometry data. The values describe the slab model of the sld and hydration profiles depicted in Fig. 3.

	Neutron sld [ $10^{-6}\text{\AA}^{-2}$ ] [f]	X-ray sld [ $10^{-6}\text{\AA}^{-2}$ ] [f]	Thickness [ $\text{\AA}$ ]	hydration [%]
lipid heads	1.78	13.8	11	54 (lower) / 63 (upper)
lipid chains	-0.2	8	18	17
hydrated region	6.36 [a] / 3.9 [b]	9.45	26	100
streptavidin	1.2	10.5	38	0
AK-cyclo[RGDfC]	1.2	10.2 [b]	30	12

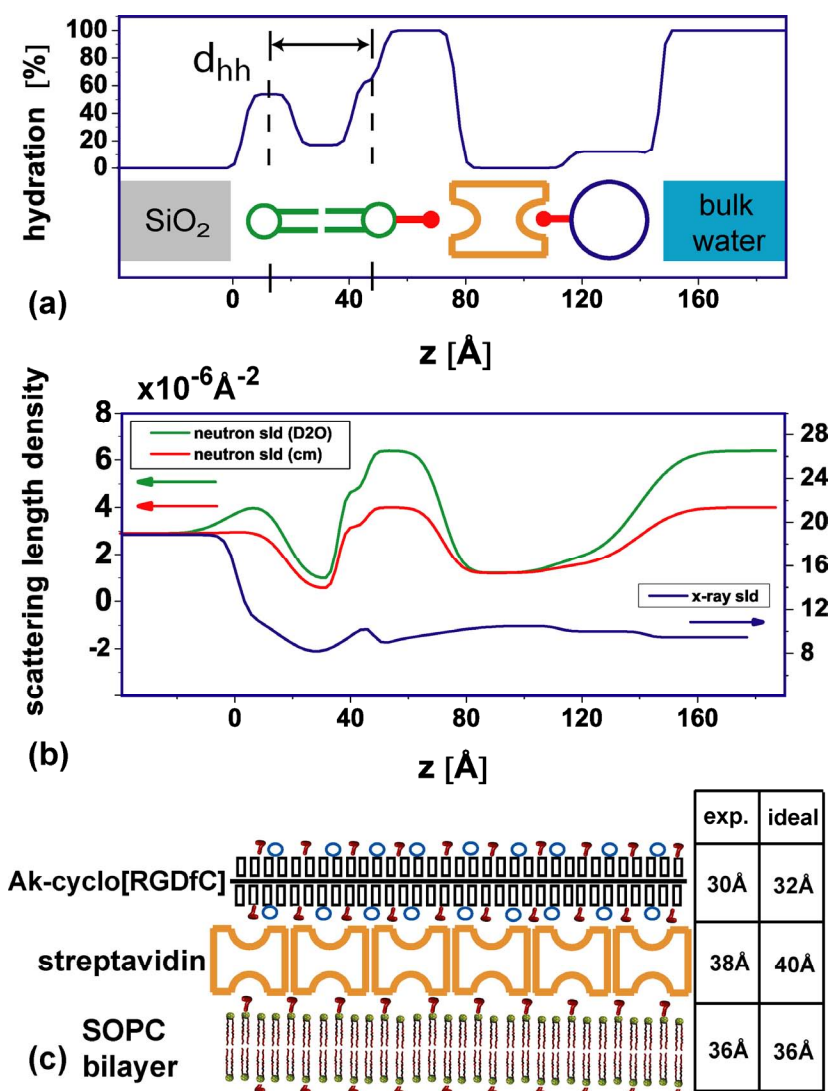
[a] D<sub>2</sub>O [b] fitted value, see text [f] fixed values

The head to head distance  $d_{hh}$  of the membrane of 36 $\text{\AA}$  (Fig. 3a) is in agreement with values previously published[23]. A highly hydrated interlayer of 26 $\text{\AA}$  between the membrane and the streptavidin layer is observed. It contains the biotin anchor of the lipids (2% are biotinylated). Orthorhombic crystals of biotin yielded a unit cell with a long axis of 21 $\text{\AA}$ [40]. Structure determination of crystallized streptavidin-biotin complexes indicates that biotin can extend the dimension of streptavidin by 20%[41] which is in the order of 10 $\text{\AA}$ . The thickness of the close packed streptavidin layer (38 $\text{\AA}$ , no hydration) is in good agreement with the thickness of 40 $\text{\AA}$  found by Horton et.al.[15]

For the AK-cyclo[RGDfC] layer, we obtain a thickness of 30 $\text{\AA}$  and a water content of 12%. In order to address the packing and configuration of the AK-cyclo[RGDfC] peptide on the streptavidin interlayer, we first estimate the length of the molecule in stretched conformation to 510 $\text{\AA}$  (Fig. 1c) by multiplying the length of a lysine compartment (8.5 $\text{\AA}$ ) [42] with the degree of polymerization DP<sub>n</sub> (=60) [2]. The width of the molecule is estimated to 32 $\text{\AA}$  by adding the length of two side chains, i.e. twice the sum of oligo-alanine (7 $\text{\AA}$ ), the thioether linkage (2 $\text{\AA}$ ) and the diameter of the cyclo[RGDfC] compound (7 $\text{\AA}$ ). A schematic of the dimensions is given in (Fig. 1c). From the comparison of the

observed thickness of 30Å with the estimated width of 32Å, and the observation that the hydration of the layer is only 12%, we infer a configuration where the AK-cyclo[RGDfC] molecule is bound in an on edge configuration to the streptavidin surface. This implies an AK-cyclo[RGDfC] packing efficiency of 88%. Because of its length of 510Å, the AK-cyclo[RGDfC] molecule in on edge configuration binds to several streptavidin molecules. A simplified 2D sketch of the arrangement is shown in (Fig.3c).

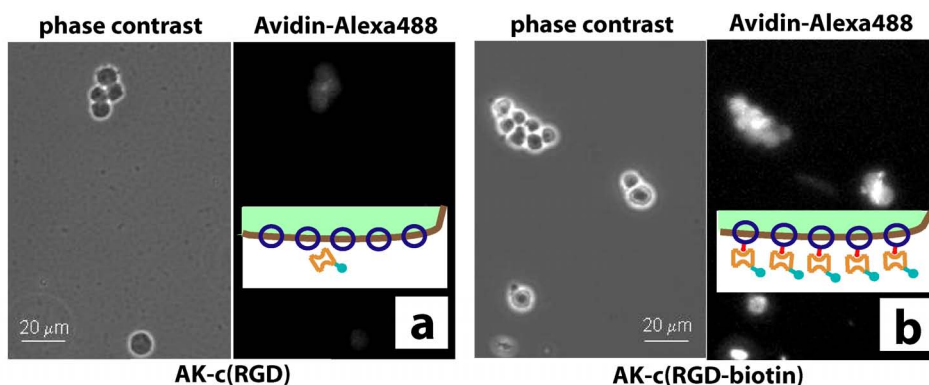
**Figure 3.** Scattering length density and hydration profile. (a) Hydration profile of the layers including a schematic of the layer components.  $d_{hh}$  indicates the head to head distance of the lipid bilayer. (b) Sld profiles of layers. Colored arrows indicate the respective y-axis. (c) Schematic of the synthetic peptide on top of the streptavidin interlayer. Red hooks depict the biotin residues, blue circles indicate the positions of a cyclo(RGDfC) residue. The bilayer- streptavidin interlayer is omitted. The table compares experimental findings and literature values.



## 2.2. Stem cell growth experiments

Neural stem cells carry a high density of integrins able to bind to the cyclo[RGDfC] domain of the synthetic adhesion molecule. In turn, the binding properties of the AK-cyclo[RGDfC] were evaluated by the binding of avidin to biotinylated and not-biotinylated AK-cyclo[RGDfC] (offered as cell surface receptors), (Fig. 4). Decoration of the stem cells with biotinylated or not-biotinylated AK-cyclo[RGDfC] was verified by subsequent binding of fluorescently labeled avidin to the cells after exposure to AK-cyclo[RGDfC]. In detail, the cells were suspended in artificial liquor solution (ACSF) and were incubated with AK-cyclo[RGDfC] (biotinylated or not-biotinylated) for 30 min at 37°C, in suspension. After removing the excess peptides by three-times washing with ACSF, avidin-coupled fluorochrome (Alexa488-Avidin; Molecular Probes) was added to both preparations for 20 min. After rinsing, the binding of avidin to the biotinylated peptide was verified by fluorescence microscopic observations (Fig. 4).

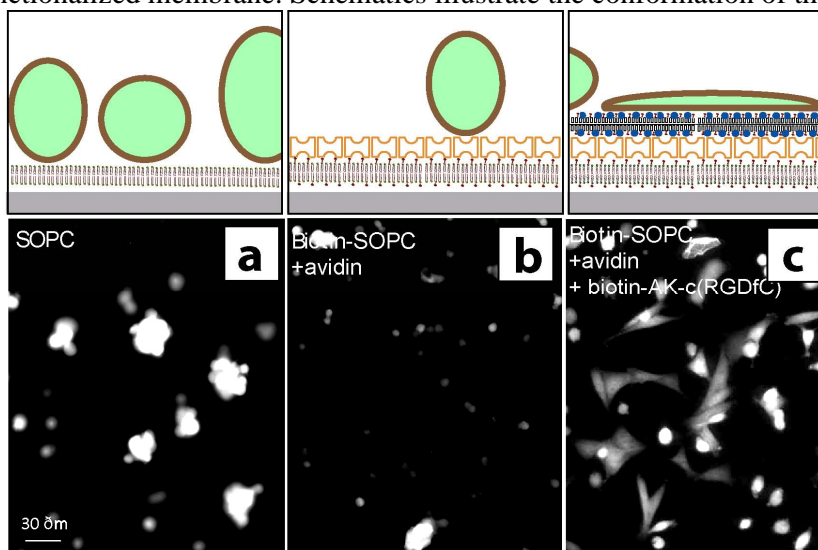
**Figure 4.** Phase-contrast and fluorescence microscopy (FM). **(a)** Neural stem cells are imaged by phase-contrast microscopy. Cells are first exposed to non-biotinylated AK-cyclo[RGDfC] peptides, and secondly to fluorescently labeled avidin, and finally imaged by FM. **(b)** Cell exposure to biotinylated AK-cyclo[RGDfC] enhances avidin absorption to cells. The insets illustrate the surface of a cell decorated with AK-cyclo[RGDfC] (shown in blue) or the biotinylated AK-cyclo[RGDfC] (shown in blue with red bars) and the binding to fluorescent labeled avidin (shown in orange, label shown in turquoise).



The spreading of green fluorescent protein (GFP) expressing neural stem cells upon exposure to different surface-coatings was investigated by fluorescence microscopy (**Fig. 5**). For the plain SOPC membrane, a non-spreading, spheroid cell morphology and enhanced formation of cell aggregates indicated poor attachment of the cells to the surface (Fig. 5a). Also the lipid layers functionalized with avidin only did not support the attachment of neural stem cells (Fig. 5b). Control experiments using non-biotinylated AK-cyclo[RGDfC], or biotinylated AK-cyclo[RGDfC] without avidin interlayer, indicated some enhancement of cell attachment. Previous studies showed that AK-cyclo[RGDfC] adsorbs on SiO<sub>2</sub> in loose packed films [2], therefore we refer this enhancement to unspecific adsorption of AK-cyclo[RGDfC] to membrane defects or bare surface parts. For the biotinylated AK-

cyclo[RGDfC], templated by an avidin-SLB support, improved and rapid spreading of the cells was observed (Fig. 5c). The cell morphology indicates cell attachment to the RGD motives.

**Figure 5.** Fluorescence microscopy (FM) images of GFP expressing (fluorescent) radial glial cells. The FM images were recorded 4 hours after cell seeding. **(a)** Radial glial cells attached to SOPC coated surfaces show a spheroid shape. **(b)** Cell attachment to an avidin functionalized biotinylated membrane is largely suppressed. **(c)** Rapid spreading of glial cells is observed for the biotin-AK-c[RGDfC] functionalized membrane. Schematics illustrate the conformation of the cells on the surface.



### 3. Experimental Section

Commercially available silicon wafers with a thermally grown oxide layer of 100nm thickness, purchased from SiMat, Germany, were used as substrates for the X-ray reflectometry and the cell adhesion experiments. The neutron reflectometry measurement was performed using a polished silicon block (10x5x1cm) with a 60nm thermally grown oxide layer. Substrates were cleaned by standard solvents and wet chemistry steps. In detail, wafer pieces were immersed in acetone and isopropanol, followed by sonication in deionized water (DI), followed by an alkaline step ( $\text{NH}_4\text{OH}:\text{H}_2\text{O}_2:\text{DI}$  mixed 1:1:5 at  $80^\circ\text{C}$ , 20min), an acidic step ( $\text{HCl}:\text{H}_2\text{O}_2:\text{DI}$  mixed 1:1:5 at  $80^\circ\text{C}$ , 15min), and again the alkaline step. Lipid solutions were produced by mixing SOPC (1-stearoyl-2-oleoyl-sn-glycero-3-phosphocholine) lipids with 0.5mol% of DHPE (1,2-dihexadecanoyl-sn-glycero-3-phosphoethanolamine) lipids labeled with a fluorescent dye (Oregon Green) and alternatively adding 2mol% biotin-X-DHPE (N-((6-(biotinoyl)amino)hexanoyl)-DHPE, triethylammonium salt). The lipids were mixed in chloroform and dried with nitrogen. The supported lipid bilayers were produced by spincoating. The appropriate lipid solution was dissolved in isopropanol (1.5mg/ml) and spincoated on the bare substrate with a BLE delta spincoater, using maximum acceleration and a ramp with 3 sec 2000 rpm followed by 60 sec 3000 rpm. To minimize solvent residues, the samples were kept in

vacuum at room temperature for at least 4h. Sterile tissue culture plates were used for transport and storage of the samples to prevent bacterial contamination. Mounting of the samples in the microfluidic chamber [43], as well as the change of buffer-solutions or DI water was done in sterile environment. To form the supported lipid bilayer, the fluidic chamber embedding the lipid coated wafer was filled with deionized water and kept in the dark over night at ambient temperature. After extensive rinsing, excess lipids in solution and multilayers forming on the surface were removed, using fluorescence microscopy as control. The DI water was first replaced by PBS buffer (pH= 7.4). Then 200 $\mu$ l of streptavidin (Sigma-Aldrich) dissolved in PBS buffer (40 $\mu$ g/ml) was injected into the fluidic chamber, which was stored in the dark over night at ambient temperature. Finally, the Streptavidin solution was replaced by DI water and extensively rinsed. The AK-cyclo[RGDfC] peptide-conjugate was synthesized according to ref.[2] (Peptidechemistry Research Unit of Hung. Acad. Sci., Budapest) using the following protocol (see [2, 13, 14] for details). The peptides (1  $\mu$ g/ $\mu$ l) were biotinylated by overnight incubation with SNHS-biotin (2  $\mu$ g/ $\mu$ l; Sigma) in 1 M phosphate buffer (pH= 7.6). The excess biotin and salts were removed by 24-hour dialization (3500 kDa dializing membrane; Serva) against distilled water with three fluid changes. After dialization, the protein content was determined and the preparation was occasionally concentrated by vacuum dialization. Biotinylated AK-cyclo[RGDfC] molecules (10 $\mu$ g/ml in DI water) were injected into the microfluidic chamber and were let to bind overnight, in dark. After incubation, the chamber was rinsed with DI water to remove excess AK-cyclo[RGDfC] molecules, which were not bound to the streptavidin layer. Samples were freshly prepared for each experiment.

The X-ray scattering experiments have been carried out at the Hamburger Synchrotronstrahlungslabor (HASYLAB) in Hamburg, Germany (beamline D4). The wavelength was  $\lambda=0.62\text{\AA}$  and measurements on samples representing subsequent steps of the sample preparation series were carried out at different positions of the sample surface to avoid beam damage effects. Neutron experiments were performed at the NREX experiment at the FRM II in Garching, Munich, Germany. The neutron wavelength used was  $\lambda=4.26\text{\AA}$ .

GFP-expressing sub-clone of NE-4C embryonic neuroectodermal stem cells [44] (GFP-4C; ATCC CRL-2926) were propagated on poly-L-lysine coated culture dishes in Minimum Essential Medium (MEM, Sigma, Hungary) supplemented with 5% fetal calf serum, while radial glia-like (RG-1) cells cloned from GFP-expressing fetal mouse forebrain [10] were cultivated on AK-c(RGDfC)-coated dishes in DMEM / F12 (1:1; Sigma Hungary) supplemented with B-27 (Invitrogen, Hungary) and 10 ng/ml EGF. After harvesting by trypsinization the cells were suspended in artificial cerebrospinal fluid (ACSF). After 20 min recovery at 37°C in a gas atmosphere containing 5% CO<sub>2</sub>, the cells (at density of 10<sup>5</sup> cells/ml) were introduced into lipid-coated chambers or were treated with plain or biotinylated AK-cyclo[RGDfC] (0.25 microgr/ml) for 30 min, in suspension at mild agitation in CO<sub>2</sub>-incubator.

#### 4. Conclusions

The combination of x-ray and neutron reflectometry experiments allows quantifying the layered structure of the AK-cyclo[RGDfC]/streptavidin/SLB system in terms of layer thickness, hydration, and packing. AK-cyclo[RGDfC] binds to the streptavidin template in a stretched on edge orientation. The high molecular packing efficiency of 88% provides a dense layer containing the RGD adhesion motive.

Neural stem cells readily spread on such surfaces, while the bare SLB does not support the attachment of neural stem-like cells. A large variety of surfaces can be coated by lipid bilayers using physisorption and various techniques for bilayer patterning are available. Using this approach, the preparation of highly effective coatings for stem cells growth on technical surfaces is possible.

### Acknowledgements

This work was supported by the EU-STREP 0032352 BIODOT, BMBF 05KN7WMA and by the National Development Program, Hungary Bio\_Surf. The “Nanosystems Initiative Munich (NIM) is gratefully acknowledged.

### References and Notes

1. Howe, A. K.; Aplin, A. E.; Juliano, R. L., Anchorage-dependent ERK signaling - mechanisms and consequences. *Current Opinion In Genetics & Development* **2002**, *12*, 30-35.
2. Marko, K.; Ligeti, M.; Mezo, G.; Mihala, N.; Kutnyanszky, E.; Kiss, E.; Hudecz, F.; Madarasz, E., A novel synthetic peptide polymer with cyclic RGD motifs supports serum-free attachment of anchorage-dependent cells. *Bioconjugate Chemistry* **2008**, *19*, 1757-1766.
3. Votavova, H.; Hudecz, F.; Kajtar, J.; Szekerke, M.; Sponar, J.; Blaha, K., Conformation Of Branched Polypeptides Based On Poly(L-Lysine) - Circular-Dichroism Study. *Collection Of Czechoslovak Chemical Communications* **1980**, *45*, 941-949.
4. Mezo, G.; Hudecz, F.; Kajtar, J.; Szekerke, M., Synthesis And Chiroptical Properties Of Model Peptides Suitable For The Immunological Characterization Of Branched Polypeptides With The General Formula Poly[Lys (Xi-Dl-Alam)]. *Acta Chimica Hungarica-Models In Chemistry* **1990**, *127*, 803-812.
5. Szokan, G.; Mezo, G.; Hudecz, F.; Majer, Z.; Schon, I.; Nyeki, O.; Szirtes, T.; Dolling, R., Racemization Analyses Of Peptides And Amino-Acid Derivatives By Chromatography With Pre-Column Derivatization. *Journal Of Liquid Chromatography* **1989**, *12*, 2855-2875.
6. Aumailley, M.; Gurrath, M.; Muller, G.; Calvete, J.; Timpl, R.; Kessler, H., Arg-Gly-Asp Constrained Within Cyclic Pentapeptides - Strong And Selective Inhibitors Of Cell-Adhesion To Vitronectin And Laminin Fragment-P1. *Febs Letters* **1991**, *291*, 50-54.
7. Pfaff, M.; Tangemann, K.; Muller, B.; Gurrath, M.; Muller, G.; Kessler, H.; Timpl, R.; Engel, J., Selective Recognition Of Cyclic Rgd Peptides Of Nmr Defined Conformation By Alpha-Ii-Beta-3, Alpha-V-Beta-3, And Alpha-5-Beta-1 Integrins. *Journal Of Biological Chemistry* **1994**, *269*, 20233-20238.
8. Anton, E. S.; Kreidberg, J. A.; Rakic, P., Distinct functions of alpha(3) and alpha(v) integrin receptors in neuronal migration and laminar organization of the cerebral cortex. *Neuron* **1999**, *22*, 277-289.
9. Hirsch, E.; Gullberg, D.; Balzac, F.; Altruda, F.; Silengo, L.; Tarone, G., Alpha(V) Integrin Subunit Is Predominantly Located In Nervous-Tissue And Skeletal-Muscle During Mouse Development. *Developmental Dynamics* **1994**, *201*, 108-120.

10. Marko, K.; Kohidi, T.; Mezo, G.; Jelitai, M.; Hadinger, N.; Madarasz, E., Neural stem cells can be isolated, cultured and grown as patterned monolayers using a novel synthetic adhesive peptide. *submitted* **2010**.
11. Ananthanarayanan, B.; Little, L.; Schaffer, D. V.; Healy, K. E.; Tirrell, M., Neural stem cell adhesion and proliferation on phospholipid bilayers functionalized with RGD peptides. *Biomaterials* **31**, 8706-8715.
12. Thid, D.; Holm, K.; Eriksson, P. S.; Ekeröth, J.; Kasemo, B.; Gold, J., Supported phospholipid bilayers as a platform for neural progenitor cell culture. *Journal Of Biomedical Materials Research Part A* **2008**, *84A*, 940-953.
13. Mezo, G.; de Oliveira, E.; Krikorian, D.; Fejlbrieff, M.; Jakab, A.; Tsikaris, V.; Sakarellos, C.; Welling-Wester, S.; Andreu, D.; Hudecz, F., Synthesis and comparison of antibody recognition of conjugates containing herpes simplex virus type 1 glycoprotein D epitope VII. *Bioconjugate Chemistry* **2003**, *14*, 1260-1269.
14. Manea, M.; Mezo, G.; Hudecz, F.; Przybylski, M., Polypeptide conjugates comprising a beta-amyloid plaque-specific epitope as new vaccine structures against Alzheimer's disease. *Biopolymers* **2004**, *76*, 503-511.
15. Horton, M. R.; Reich, C.; Gast, A. P.; Radler, J. O.; Nickel, B., Structure and dynamics of crystalline protein layers bound to supported lipid bilayers. *Langmuir* **2007**, *23*, 6263-6269.
16. Castellana, E. T.; Cremer, P. S., Solid supported lipid bilayers: From biophysical studies to sensor design. *Surface Science Reports* **2006**, *61*, 429-444.
17. Faiss, S.; Kastl, K.; Janshoff, A.; Steinem, C., Formation of irreversibly bound annexin A1 protein domains on POPC/POPS solid supported membranes. *Biochimica Et Biophysica Acta-Biomembranes* **2008**, *1778*, 1601-1610.
18. Lee, C.; Wacklin, H.; Bain, C. D., Changes in molecular composition and packing during lipid membrane reconstitution from phospholipid-surfactant micelles. *Soft Matter* **2009**, *5*, 568-575.
19. Miller, C. E.; Majewski, J.; Watkins, E. B.; Mulder, D. J.; Gog, T.; Kuhl, T. L., Probing the local order of single phospholipid membranes using grazing incidence x-ray diffraction. *Physical Review Letters* **2008**, *100*.
20. Watkins, E. B.; Miller, C. E.; Mulder, D. J.; Kuhl, T. L.; Majewski, J., Structure and Orientational Texture of Self-Organizing Lipid Bilayers. *Physical Review Letters* **2009**, *102*.
21. Smith, H. L.; Howland, M. C.; Szmodis, A. W.; Li, Q. J.; Daemen, L. L.; Parikh, A. N.; Majewski, J., Early Stages of Oxidative Stress-Induced Membrane Permeabilization: A Neutron Reflectometry Study. *Journal Of The American Chemical Society* **2009**, *131*, 3631-3638.
22. Wang, S. T.; Fukuto, M.; Yang, L., In situ x-ray reflectivity studies on the formation of substrate-supported phospholipid bilayers and monolayers. *Physical Review E* **2008**, *77*.
23. Hochrein, M. B.; Reich, C.; Krause, B.; Radler, J. O.; Nickel, B., Structure and mobility of lipid membranes on a thermoplastic substrate. *Langmuir* **2006**, *22*, 538-545.

24. Sackmann, E., Supported membranes: Scientific and practical applications. *Science* **1996**, *271*, 43-48.
25. Burgess, I.; Li, M.; Horswell, S. L.; Szymanski, G.; Lipkowski, J.; Majewski, J.; Satija, S., Electric field-driven transformations of a supported model biological membrane - An electrochemical and neutron reflectivity study. *Biophysical Journal* **2004**, *86*, 1763-1776.
26. Ang, P. K.; Loh, K. P.; Wohland, T.; Nesladek, M.; Van Hove, E., Supported Lipid Bilayer on Nanocrystalline Diamond: Dual Optical and Field-Effect Sensor for Membrane Disruption. *Advanced Functional Materials* **2009**, *19*, 109-116.
27. Yamazaki, V.; Sirenko, O.; Schafer, R. J.; Groves, J. T., Lipid mobility and molecular binding in fluid lipid membranes. *Journal Of The American Chemical Society* **2005**, *127*, 2826-2827.
28. Parikh, A. N., Membrane-substrate interface: Phospholipid bilayers at chemically and topographically structured surfaces. *Biointerphases* **2008**, *3*, FA22-FA32.
29. Kim, P.; Lee, S. E.; Jung, H. S.; Lee, H. Y.; Kawai, T.; Suh, K. Y., Soft lithographic patterning of supported lipid bilayers onto a surface and inside microfluidic channels. *Lab On A Chip* **2006**, *6*, 54-59.
30. Groves, J. T.; Ulman, N.; Boxer, S. G., Micropatterning fluid lipid bilayers on solid supports. *Science* **1997**, *275*, 651-653.
31. Hovis, J. S.; Boxer, S. G., Patterning barriers to lateral diffusion in supported lipid bilayer membranes by blotting and stamping. *Langmuir* **2000**, *16*, 894-897.
32. Yu, C. H.; Parikh, A. N.; Groves, J. T., Direct patterning of membrane-derivatized colloids using in-situ UV-ozone photolithography. *Advanced Materials* **2005**, *17*, 1477-1480.
33. Hennig, M.; Neumann, J.; Wixforth, A.; Radler, J. O.; Schneider, M. F., Dynamic patterns in a supported lipid bilayer driven by standing surface acoustic waves. *Lab On A Chip* **2009**, *9*, 3050-3053.
34. Kumar, K.; Tang, C. S.; Rossetti, F. F.; Textor, M.; Keller, B.; Voros, J.; Reimhult, E., Formation of supported lipid bilayers on indium tin oxide for dynamically- patterned membrane-functionalized microelectrode arrays. *Lab On A Chip* **2009**, *9*, 718-725.
35. Oliver, A. E.; Ngassam, V.; Dang, P.; Sani, B.; Wu, H. W.; Yee, C. K.; Yeh, Y.; Parikh, A. N., Cell Attachment Behavior on Solid and Fluid Substrates Exhibiting Spatial Patterns of Physical Properties. *Langmuir* **2009**, *25*, 6992-6996.
36. Smith, H. L.; Hickey, J.; Jablin, M. S.; Trujillo, A.; Freyer, J. P.; Majewski, J., Mouse Fibroblast Cell Adhesion Studied by Neutron Reflectometry. *Biophysical Journal* *98*, 793-799.
37. Pencer, J.; Mills, T.; Anghel, V.; Krueger, S.; Epanand, R. M.; Katsaras, J., Detection of submicron-sized raft-like domains in membranes by small-angle neutron scattering. *European Physical Journal E* **2005**, *18*, 447-458.
38. Nelson, A., Co-refinement of multiple-contrast neutron/X-ray reflectivity data using MOTOFIT. *Journal Of Applied Crystallography* **2006**, *39*, 273-276.

39. Schmidt, A.; Spinke, J.; Bayerl, T.; Sackmann, E.; Knoll, W., Streptavidin binding to biotinylated lipid layers on solid supports: A neutron reflection and surface plasmon optical study. *Biophysical Journal* **1992**, *63*, 1185-1192.
40. Traub, W., Crystal Structure Of Biotin. *Nature* **1956**, *178*, 649-650.
41. Weber, P. C.; Ohlendorf, D. H.; Wendoloski, J. J.; Salemme, F. R., Structural Origins Of High-Affinity Biotin Binding To Streptavidin. *Science* **1989**, *243*, 85-88.
42. Salunke, D. M.; Vijayan, M., X-Ray Studies On Crystalline Complexes Involving Amino-Acids And Peptides.11. Crystal-Structure Of The Amino-Acid Vitamin Complex Lysine Pantothenate. *Biochimica Et Biophysica Acta* **1984**, *798*, 175-179.
43. Reich, C.; Hochrein, M. B.; Krause, B.; Nickel, B., A microfluidic setup for studies of solid-liquid interfaces using x-ray reflectivity and fluorescence microscopy. *Review Of Scientific Instruments* **2005**, *76*.
44. Schlett, K.; Madarasz, E., Retinoic acid induced neural differentiation in a neuroectodermal cell line immortalized by p53 deficiency. *Journal Of Neuroscience Research* **1997**, *47*, 405-415.

© 2010 by the authors; licensee MDPI, Basel, Switzerland. This article is an open-access article distributed under the terms and conditions of the Creative Commons Attribution license (<http://creativecommons.org/licenses/by/3.0/>).

## A.2 Full text of Ref. [2]

Martin Göllner, Martin Huth, and Bert Nickel

*Pentacene thin film transistors encapsulated by a thin alkane layer operated in an aqueous ionic environment.*

Advanced Materials 2010, **XX**, 1-5

### **Abstract:**

The encapsulation of pentacene thin film transistors (TFTs) by a  $50\text{nm}$  thick layer of a long chain alkane ( $C_{44}H_{90}$ ) enables the operation in an aqueous solution of  $1\text{mM}$  NaCl. It is the first time that pentacene TFTs operate successfully in a liquid environment. This opens new perspectives for biocompatible sensor devices based on pentacene TFTs.

permanent weblink:

<http://onlinelibrary.wiley.com/doi/10.1002/adma.201001345/pdf>

MH contribution:

- performing the x-ray experiments (at DESY) and structural analysis.
- writing the structure related part of the paper.
- participation in discussions.

# Pentacene Thin-Film Transistors Encapsulated by a Thin Alkane Layer Operated in an Aqueous Ionic Environment

By Martin Göllner, Martin Huth, and Bert Nickel\*

Thin-film transistors (TFTs), used as small-area, highly sensitive transducer devices for chemical and biological purposes,<sup>[1–3]</sup> have attracted a lot of attention in the recent years. The integration of a TFT in a liquid environment poses two major challenges. On the one hand side, device stability in liquid has to be ensured by appropriate passivation or capping schemes. On the other hand, biocompatibility is mandatory for applications aiming on monitoring of e.g., molecule concentrations in blood or tissue.<sup>[4,5]</sup> Organic semiconductors exhibit a non-toxic and most notably soft ambience to neuronal networks<sup>[6]</sup> and can be processed on flexible plastic substrates and organic dielectric layers.<sup>[7]</sup> Therefore, organic thin-film transistors (OTFTs) are considered as promising candidates for biosensing.

Bernards et al.<sup>[8]</sup> demonstrated enzymatic sensing of an organic electrochemical transistor based on the p-type semiconductor PEDOT:PSS. This device operates in depletion mode, i.e. it is in the on-state when no gate-voltage is applied. However, when a positive voltage is applied via an electrolyte, positive ions enter the semiconductor, de-dope it, and decrease the source-drain current. This mechanism can be used to detect glucose levels in phosphate buffered saline. A concept based on OTFTs in accumulation mode was recently presented by Roberts et al., showing that several organic semiconductor materials like linear sexithiophene (6T) and thiophene-fluorene oligomer (FTTF) derivatives are suited for TFT operation in water.<sup>[9,10]</sup> The sensor properties are probably based on the diffusion of analyte molecules into the semiconductor, resulting in trapping or doping effects.<sup>[9,10]</sup>

Hence, OTFTs are applicable for biosensing devices. For low-voltage operation and a high signal-to-noise ratio, the use of high-mobility organic semiconductors such as pentacene is highly desirable.<sup>[11]</sup> There are three problems that have to be addressed for a stable device operation. Firstly, so-called leakage currents may originate from the metal contacts of the device if the contact is not efficiently isolated from the solvent. Secondly, hole injection from the electrolyte into the pentacene film, as it has been observed for anthracene in an iodine solution<sup>[12]</sup> may result in additional leakage currents. Finally, redox reactions at the organic semiconductor-electrolyte interface which degrade the organic semiconductor should be suppressed. For pentacene, the formation of hydrogen- and hydroxyl related defects,<sup>[13]</sup>

resulting in a degradation of the transistor channel,<sup>[14]</sup> and notable hysteresis<sup>[15]</sup> have been observed. In turn, bare pentacene devices degrade within seconds in aqueous environment, which makes them unsuited for sensor applications.<sup>[9]</sup> Capping of the TFT by a thin passivation layer is a possible solution. A suited capping material should be insulating and hydrophobic, in order to prevent water from leaking to the pentacene layer, and it should be biocompatible.

Alkanes are good insulators with a resistivity greater than  $10^{15} \Omega \cdot \text{cm}$ , and they typically show a breakdown voltage of about 20 MV/m.<sup>[16]</sup> Alkanes are highly hydrophobic, i.e. insoluble in polar solvents such as water. Therefore, they are promising candidates for the passivation of TFTs in aqueous environment. Moreover, the lack of  $\pi$ -electrons results in a chemical inert nature and good biocompatibility. As the melting point of alkanes increases with the molecular weight, it is preferable to choose a long chain alkane like tetratetracontane ( $\text{CH}_3(\text{CH}_2)_{42}\text{CH}_3$ ) with a melting point of 358–360 K, i.e., above physiological conditions. A further advantage is that tetratetracontane (TTC) forms closely packed and highly crystalline films by thermal vacuum deposition.<sup>[17]</sup>

In this paper we show that a 50 nm alkane layer of TTC (see inset **Figure 1**) evaporated on top of pentacene (Pc) prevents degradation and ionic currents of pentacene TFTs in aqueous solutions, allowing for stable TFT operation.

In order to optimize the evaporation of well defined TTC layers on Pc, we perform atomic force microscopy (AFM) and X-ray diffraction reflectometry measurements. For this purpose we use silicon substrates covered by a 500 nm thick thermally grown  $\text{SiO}_2$  layer (purchased from Si-Mat). Triple-sublimed pentacene (purchased from Sigma-Aldrich) is deposited at a pressure of about  $10^{-8}$  mbar, room temperature, and a rate of about 0.1 Å/s. The TTC layer is added via subsequent vacuum deposition at room temperature, at a pressure of about  $10^{-7}$  mbar, and a rate of about 4.0 Å/s. The thickness of the Pc film and the TTC layer is 50 nm each.

At these conditions, TTC forms rod-shaped grains with a size of some 100 nm. The TTC surface has a RMS roughness of 5.6 nm and shows a rather perfect coverage as shown in the AFM amplitude image (**Figure 1**). Contact angle measurements yield a contact angle of  $115^\circ$  indicating a hydrophobic surface. Thus, the TTC layer should provide a good protection of pentacene against water molecules. See supporting information for the influence of temperature and rate on the structure of the TTC layer.

The structure of the TTC passivation layer on top of the organic semiconductor is determined by X-ray diffraction in reflection geometry. Experiments have been carried out at the Hamburger Synchrotronstrahlungslabor (HASYLAB, beamline W1) in Hamburg, Germany. The X-ray energy was 10.5 keV.

[\*] M. Göllner, M. Huth, Dr. B. Nickel  
Fakultät für Physik & CeNS  
Ludwig-Maximilians-Universität  
Geschwister-Scholl-Platz 1, 80539 München (Germany)  
E-mail: nickel@lmu.de

DOI: 10.1002/adma.201001345

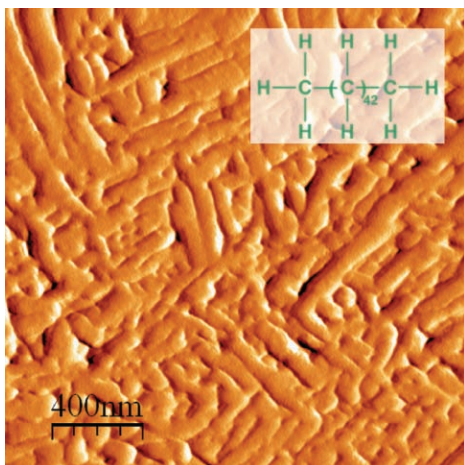


**Figure 1.** AFM amplitude image of a 50 nm thick TTC layer on a 50 nm pentacene thin film.

Reflectometry curves of thin films of 50 nm pentacene and 50 nm TTC on a cyclic olefin copolymer (COC) layer on SiO<sub>2</sub> are shown in **Figure 2**. The normalized reflected intensity is plotted against the momentum transfer  $q_z = 4\pi/\lambda \cdot \sin\theta$ . Here,  $\lambda$  is the wavelength and  $\theta$  is the incident angle. The observation of an (00L) series allows us to calculate the  $d_{001}$ -spacing of the TTC film grown on COC/SiO<sub>2</sub> (Figure 2a) to  $c = 57.91 \text{ \AA}$  ( $d_{001} = 2\pi/\Delta q_z$ ), which is in good agreement with the orthorhombic structure predicted by Nyburg et al.<sup>[18]</sup> and an orientation of the  $c$ -axis along the surface normal. The additional peak at  $q_z = 1.525 \text{ \AA}^{-1}$  can be indexed as TTC (110), which implies that some fraction of the TTC has the  $c$ -axis along the surface. The reflected intensity of a 50 nm pentacene film covered with a 50 nm TTC film on COC/SiO<sub>2</sub> is shown in Figure 2b. This film stacking

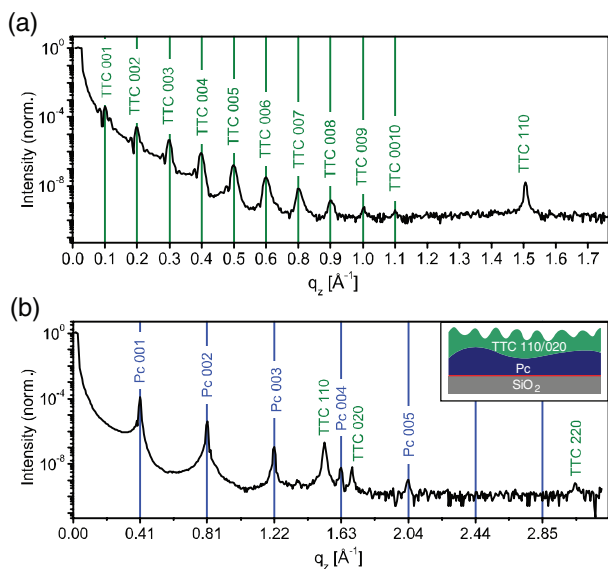


**Figure 2.** X-ray reflectivity curves of (a) a 50 nm TTC film on COC/SiO<sub>2</sub> and (b) a 50 nm TTC film on top of a 50 nm pentacene film on COC/SiO<sub>2</sub>. The  $x$ -axis increments are chosen to match the 00L peak series of TTC (a) and pentacene (b).

corresponds to the channel region in a TFT device. The 00L peak series of the pentacene thin film phase<sup>[19]</sup> is observed while the 00L series of TTC is absent. Using orthorhombic structures proposed by Craig et al.,<sup>[20]</sup> Fenrych et al.<sup>[17]</sup> and Nyburg,<sup>[18]</sup> the peaks at  $q_z = 1.525 \text{ \AA}^{-1}$  and  $q_z = 3.05 \text{ \AA}^{-1}$  can be indexed as the (110) and (220) planes of TTC. Combined with the (020) peak at  $q_z = 1.692 \text{ \AA}^{-1}$  we calculate the unit cell dimensions to  $a = 4.957 \pm 0.02 \text{ \AA}$  and  $b = 7.426 \pm 0.02 \text{ \AA}$ . This is in very good agreement with the values of Craig and coworkers.<sup>[20]</sup> This measurement also shows that the evaporation of a TTC layer does not change the Pc thin film structure.<sup>[19]</sup> As shown in several other studies, the growth of alkanes is strongly influenced by the properties of the substrate.<sup>[21–24]</sup> In the case of pentacene acting as substrate, we find the  $c$ -axis oriented along the surface, i.e., the alkane chains are oriented along the surface.

To verify the electronic sealing properties of TTC, we compare four types of sandwich structures: bare gold (Au), 50 nm Pc/Au, 50 nm TTC/Au and 50 nm TTC/50 nm Pc/Au (see insets **Figure 3**). The 50 nm thick Au-structures (4 mm × 4 mm) are deposited via shadow masks. Pc and TTC are evaporated at the deposition parameters described above. A polydimethylsiloxane (PDMS) microfluidic chamber filled with a 1 mM NaCl solution in deionized and degassed water is used to perform water-stability measurements.

We take cyclic voltammetry measurements of the sandwich structures in a solution of sodium chloride, i.e. we measure the current  $I_{Pt}$  between a gold structure capped with organic materials and a platinum electrode (see insets **Figure 3**). All electrical measurements are performed using a Keithley 2612 Sourceter. The voltage at the Pt-electrode  $V_{Pt}$  is swept from +0.6 V to –0.6 V and back, thus avoiding electrolysis of water, which sets in for voltages larger than 1 V. The contact area of the Au pad with the electrolyte is 2 mm × 4 mm. The current for a blank gold structure reaches maximum values of about 30 nA, i.e.  $0.4 \mu\text{A}/\text{cm}^2$ . It shows the characteristic features of a reversible redox reaction, i.e. a pronounced current peak for each scan direction and the build-up of an electrical double layer (Figure 3a, black and red filled symbols).<sup>[25]</sup> From the two current peak positions, a half-wave potential  $E_{1/2}$  close to zero is estimated.<sup>[26]</sup> However, the rather large current peak position difference indicates that the redox reaction involved is slow<sup>[26]</sup> and, strictly speaking, this analysis assumes that the Pt-electrode here can be idealized as a standard hydrogen electrode which might not be the case. In any case, these electrochemical effects at the gold contacts are significantly reduced for a gold structure capped by a 50 nm thick pentacene layer (Figure 3a, green and blue open symbols). For positive voltages at the Pt-electrode (0 V up to +0.5 V) we observe a linear increase of the current. Here, we suspect that injection of holes into pentacene occurs.<sup>[12]</sup> For voltages higher than  $\pm 0.5$  V, leakage currents to the Au film set in, presumably in particular at the boundaries of the pentacene grains. For small negative voltages (0 V up to –0.5 V) the current is nearly zero. This is not surprising, since it is not clear if efficient electron injection into pentacene from solution is possible. Secondly, electron mobility in pentacene is expected to be low. Capping of gold by a 50 nm TTC layer further reduces the currents by a factor of about 10 (Figure 3b, black and red filled symbols) compared to the presence of the pentacene film. Here, no asymmetry is observed in the voltage sweep.

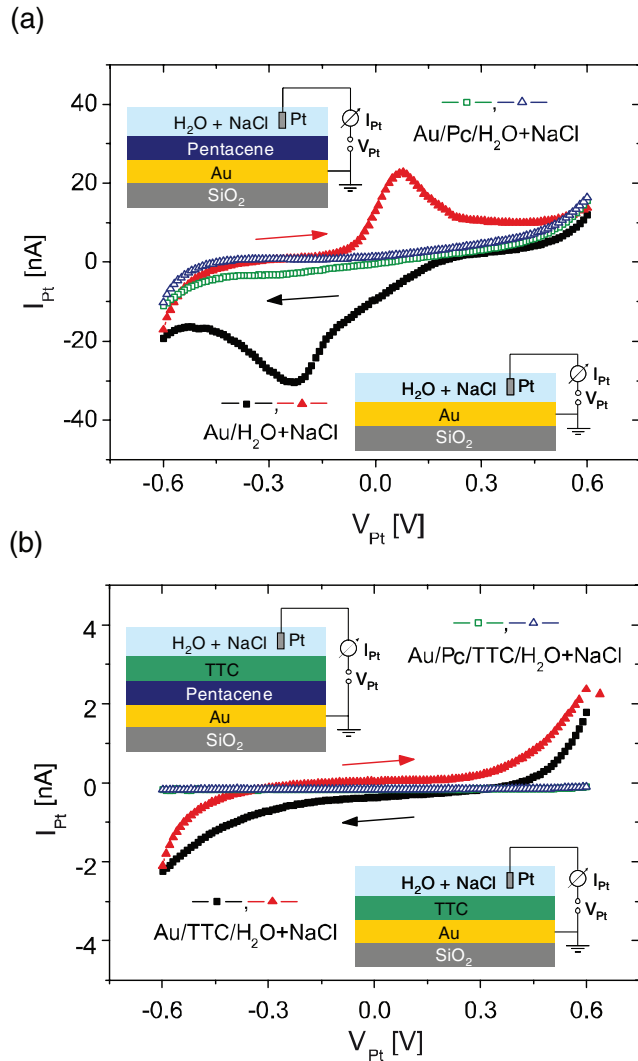


**Figure 3.** Cyclic voltammetry measurements. (a) A bare Au pad in an aqueous solution of 1 mM NaCl (black and red filled symbols), and a Au pad capped with 50 nm Pc (green and blue open symbols). (b) Au capped with 50 nm TTC in an aqueous solution of 1 mM NaCl (black and red filled symbols) and Au capped with 50 nm Pc and 50 nm TTC (green and blue open symbols).

For the voltammetry measurements of an Au-structure capped with both a 50 nm Pc and a 50 nm TTC passivation layer the currents are reduced to values smaller than 60 pA, i.e.,  $0.8 \text{ nA/cm}^2$  (Figure 3b, green and blue open symbols). Assuming a resistivity of  $10^{15} \Omega \cdot \text{cm}$ ,<sup>[16]</sup> the current through an ideal TTC layer of 50 nm would be about 10 pA. The measured current  $I_{Pt}$  (<60 pA) differs from the ideal value by a factor of 6, presumably due to pinholes or incomplete coverage, but is in the same range than the off-current of pentacene TFTs and therefore acceptable. These results show that hole injection and redox reactions can be sufficiently suppressed by a TTC capping layer.

Now we verify whether a TTC/Pc bilayer allows stable operation of a TFT in aqueous solution. To test this, top-contact pentacene TFTs (inset Figure 4b) are fabricated on a highly p-doped

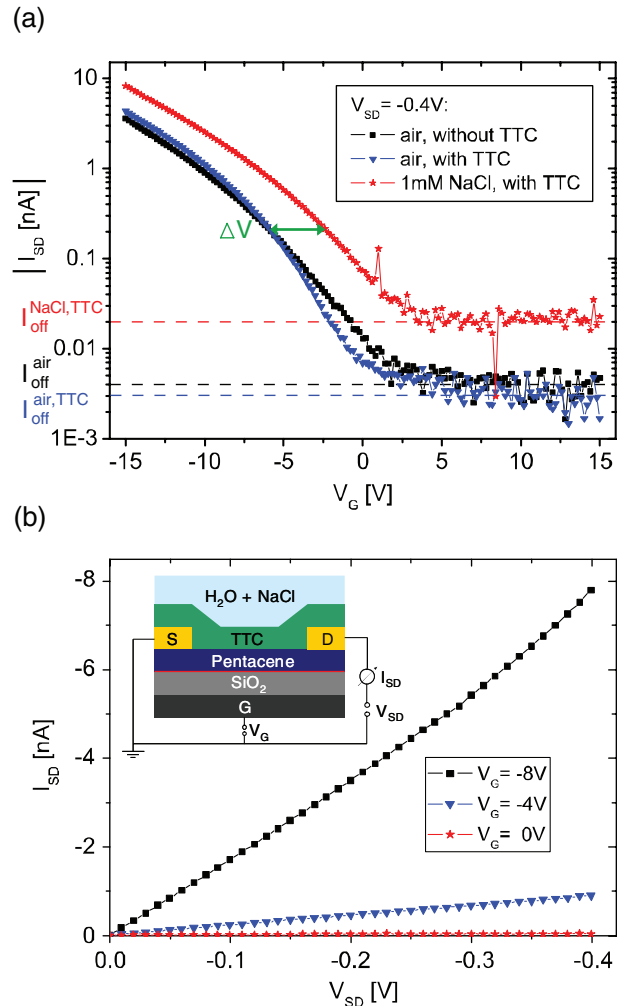


**Figure 4.** (a) Transfer curves of a pentacene TFT in air (black rectangles), a TTC passivated pentacene transistor in air (blue triangles), and a TTC passivated pentacene TFT in a 1 mM NaCl solution (red stars). (b) Respective output curves of the devices in an aqueous solution of 1 mM NaCl.

silicon substrate acting as a back gate and a 500 nm thick thermally grown  $\text{SiO}_2$  layer serving as a gate dielectric (as purchased from Si-Mat). To enhance the performance of the TFT, a 2 nm thick buffer layer of COC is spin coated on top of the silicon oxide. A 50 nm thick layer of pentacene is subsequently deposited. The source and drain top-contacts, which consist of a 50 nm thick Au-layer, are deposited via shadow masks. The resulting channel length and width of our samples are  $L = 50 \mu\text{m}$  and  $W = 2000 \mu\text{m}$ , respectively. After characterization of the transistor performance in air, a 50 nm layer of TTC is added via vacuum deposition at room temperature.

Capped and uncapped pentacene TFTs in ambient air conditions are compared in Figure 4a (blue and black curves). The TTC layer causes small changes in the TFT characteristics. This result is consistent with the work of Jung et al., who demonstrated that TTC on Pc has little effect on the transport properties, but enhances lifetime of OTFTs in humid atmosphere.<sup>[27]</sup> In detail, the transfer characteristic showed that the onset

voltage upon TTC capping shifts in air from  $V_{\text{on}}^{\text{air}} = 2.5$  V to  $V_{\text{on}}^{\text{air,TTC}} = 0.2$  V and the subthreshold slope changes from  $S^{\text{air}} = 4.8$  V/decade to  $S^{\text{air,TTC}} = 4.6$  V/decade. The mobility slightly decreases from  $\mu^{\text{air}} = 2.2 \cdot 10^{-2}$  cm<sup>2</sup>/V s to  $\mu^{\text{air,TTC}} = 1.9 \cdot 10^{-2}$  cm<sup>2</sup>/V s (extracted from transfer curves in the linear regime at a source-drain voltage of  $V_{\text{SD}} = -20$  V).<sup>[28]</sup> The off-current decreases from  $I_{\text{off}}^{\text{air}} = 4$  pA to  $I_{\text{off}}^{\text{air,TTC}} = 3$  pA.

In a second step, we fully immerse our transistors into an aqueous solution of 1 mM NaCl. In this configuration, the device corresponds to a double gate transistor with a highly doped silicon substrate acting as bottom gate, SiO<sub>2</sub> acting as bottom gate dielectric, the electrolyte acting as floating top gate, and the TTC layer acting as the top gate dielectric. Under these conditions, the pentacene TFT passivated with TTC shows a stable performance over many hours (red curve, Figure 4a), while an uncapped pentacene transistor in water has a lifetime of only few seconds. Overall, the transistor characteristics are nearly unchanged, except for an increased off-current and a shift of the transfer curve. The on-set voltage  $V_{\text{on}}^{\text{NaCl,TTC}} = 2.3$  V and the subthreshold slope of  $S^{\text{NaCl,TTC}} = 5.4$  V/decade in water are in the same range as for the uncapped OTFT in air. The off-current is about  $I_{\text{off}}^{\text{NaCl,TTC}} = 20$  pA and, hence, one order of magnitude higher than in ambient conditions. Due to the small source-drain voltage of  $V_{\text{SD}}$  of  $-0.4$  V, it is difficult to quantify the threshold voltage. Overall, the transfer curves in water shifts by  $\Delta V = 3.6$  V towards positive voltages, i.e. the device opens more early and the device shut down is incomplete. As the source-drain voltage  $V_{\text{SD}}$  is small, contact effects should strongly influence the source-drain current  $I_{\text{SD}}$ ,<sup>[29]</sup> making an accurate calculation of the channel mobility difficult in this regime. The curves suggest that the channel mobility of the capped transistor in aqueous solution  $\mu^{\text{NaCl,TTC}}$  is comparable to the mobility in ambient air.

Li et al. showed that the off-currents of pentacene TFTs increase with increasing relative humidity while the threshold voltage shifts toward positive values.<sup>[14]</sup> In agreement to this results, the off-current of the TTC capped TFT in air decreases, and the threshold voltage shifts toward negative values compared to the uncapped transistor. Thus, the main effect of TTC capping is to reduce the humidity effects on the device.

Once the TFT is immersed into an aqueous solution of 1 mM NaCl the off-current increases by one order of magnitude, and the threshold voltage shifts toward positive values. Since the intrinsic Fermi level of pentacene is about  $-4.0$  eV,<sup>[30]</sup> i.e. above the electrochemical potential of water (about  $-4.5$  eV at standard conditions), hole injection<sup>[12]</sup> into the pentacene film due to charge transfer from pentacene to the electrolyte seems quite likely. In turn, these extra holes in the film need to be compensated by a more positive gate voltage to shut down the device, as observed. Incomplete sealing drastically increases these effects (cf. supporting information). The transistor output curves (Figure 4b) show a linear behavior and the measurement for  $V_{\text{G}} = 0$  V particularly demonstrates that currents to the electrolyte are negligible. These measurements confirm that pentacene TFT operation in aqueous solution is possible due to TTC capping.

A transducer based on the device discussed above could work on the principle of a double-gate transistor. Here, the ratio of the thickness of the bottom-gate dielectric and of the capping layer should determine its sensitivity.<sup>[31]</sup> Consequently, the

small thickness of the TTC layer should allow for highly sensitive devices based on pentacene TFTs. As the device operates at very low source-drain voltages  $V_{\text{SD}}$ , the reduction of hole-injection barriers at the source and drain contacts should be part of the optimization strategy. Measurements on how the electrochemical potential of the electrolyte influences the TFT characteristics are currently being made. First test measurements indicate that a sensitivity of 20 mV or better can be achieved with the present design allowing for applications such as enzymatic sensing.<sup>[8]</sup> Fine tuning of the deposition parameters like substrate temperature, deposition rate, and TTC thickness may further improve the sensitivity towards readout of action potentials.<sup>[1]</sup>

In conclusion, we demonstrate that the passivation by a 50 nm thick TTC layer enables the operation of pentacene TFTs in aqueous environment. X-ray measurements and AFM images show that TTC covers a pentacene thin film densely and in a structure with the alkane chains along the surface. Voltammetry measurements of sandwich structures reveal that TTC is a suitable material for protecting pentacene in an aqueous solution. Finally, we show that the onset voltage  $V_{\text{on}}^{\text{NaCl,TTC}}$ , the subthreshold slope  $S^{\text{NaCl,TTC}}$  and the mobility  $\mu^{\text{NaCl,TTC}}$  of a TTC-capped pentacene TFT in 1 mM NaCl aqueous solution remain nearly unchanged, while the whole transfer curve is shifted by  $\Delta V = 3.6$  V.

## Supporting Information

Supporting Information is available from Wiley Online Library or from the author.

## Acknowledgements

This work was supported by the EU-NMP-STRP 032652 BIODOT project and the Nanosystems Initiative Munich (NIM).

Received: January 14, 2010

Revised: May 12, 2010

Published online:

- [1] P. Fromherz, A. Offenhäusser, T. Vetter, J. Weis, *Science* **1991**, 252, 1290.
- [2] M. Dankerl, S. Eick, B. Hofmann, M. Hauf, S. Ingebrandt, A. Offenhäusser, M. Stutzmann, J. A. Garrido, *Adv. Func. Mater.* **2009**, 19, 2915.
- [3] G. Steinhoff, B. Baur, G. Wrobel, S. Ingebrandt, A. Offenhäusser, A. Dadgar, A. Krost, M. Stutzmann, M. Eickhoff, *Appl. Phys. Lett.* **2005**, 86, 033901.
- [4] P. Bergveld, *Sens. Actuators, B* **2003**, 88, 1.
- [5] S. Meyburg, M. Goryll, J. Moers, S. Ingebrandt, S. Böcker-Meffert, H. Lüth, A. Offenhäusser, *Biosens. Bioelectron.* **2006**, 21, 1037.
- [6] E. Bystrenova, M. Jelitai, I. Tonazzini, A. N. Lazar, M. Huth, P. Stoliar, C. Dionigi, M. G. Cacace, B. Nickel, E. Madarasz, F. Biscarini, *Adv. Funct. Mater.* **2008**, 18, 1751.
- [7] D. Feili, M. Schuettler, T. Doerge, S. Kammer, K. P. Hoffmann, T. Stieglitz, *J. Micromech. Microeng.* **2006**, 16, 1555.
- [8] G. A. Bernards, D. J. Macaya, M. Nikolou, J. A. De Franco, S. Takamatsu, G. G. Malliaras, *J. Mater. Chem.* **2008**, 18, 116.
- [9] M. E. Roberts, A. N. Sokolov, Z. Bao, *J. Mater. Chem.* **2009**, 19, 3351.

- [10] M. E. Roberts, S. C. B. Mannsfeld, N. Queraltó, C. Reese, J. Locklin, W. Knoll, Z. Bao, *Proc. Natl. Acad. Sci. USA* **2008**, *105*, 12134.
- [11] P. Stoliar, E. Bystrenova, S. D. Quiroga, P. Annibale, M. Facchini, M. Spijkman, S. Setayesh, D. de Leeuw, F. Biscarini, *Biosens. Bioelectron.* **2009**, *24*, 2935.
- [12] H. Kallmann, M. Pope, *Nature* **1960**, *185*, 753.
- [13] K. Gmucová, M. Weis, M. Della Pirriera, J. Puigdollers, *Phys. Status Solidi A* **2009**, *206*, 1404.
- [14] D. Li, E. Borkent, R. Nortrup, H. Moon, H. Katz, Z. Bao, *Appl. Phys. Lett.* **2005**, *86*, 042105.
- [15] Z. Zhu, J. T. Mason, R. Dieckmann, G. G. Malliaras, *Appl. Phys. Lett.* **2002**, *81*, 4643.
- [16] *Handbook of Chemistry and Physics*, 55<sup>th</sup> ed. (Ed: R. C. Weast), CRC Press, Cleveland, Ohio, **1974**.
- [17] J. Fenrych, E. C. Peynhardt, I. Basson, *Powder Diffr.* **1997**, *12*, 49.
- [18] S. C. Nyburg, J. A. Potworowski, *Acta Crystallogr., Sect. B: Struct. Sci.* **1973**, *29*, 347.
- [19] S. Schiefer, M. Huth, A. Dobrinevski, B. Nickel, *J. Am. Chem. Soc.* **2007**, *129*, 10316.
- [20] S. R. Craig, G. P. Hastie, K. J. Roberts, J. N. Sherwood, *J. Mater. Chem.* **1994**, *4*, 977.
- [21] S. Basu, S. K. Satija, *Langmuir* **2007**, *23*, 8331.
- [22] H. Mo, H. Taub, U. G. Volkmann, M. Pino, S. N. Ehrlich, F. Y. Hansen, E. Lu, P. Miceli, *Chem. Phys. Lett.* **2003**, *377*, 99.
- [23] S. Trogisch, M. J. Simpson, H. Taub, *J. Chem. Phys.* **2005**, *123*, 154703.
- [24] C. Merkl, T. Pfohl, H. Riegler, *Phys. Rev. Lett.* **1997**, *79*, 23.
- [25] A. J. Bard, L. R. Faulkner, in *Electrochemical Methods*, 2nd ed. (Eds: D. Harris, E. Swain, C. Robey, E. Aiello), Wiley, New York **2001**.
- [26] J. Heinze, *Angew. Chem. Int. Ed.* **1984**, *23*, 831.
- [27] H. Jung, T. Lim, Y. Choi, M. Yi, J. Won S. Pyo, *Appl. Phys. Lett.* **2003**, *92*, 163504.
- [28] S. M. Sze, in *Physics of Semiconductor Devices*, 2nd ed., Wiley, New York, **1981**.
- [29] D. J. Gundlach, L. Zhou, J. A. Nichols, T. N. Jackson, P. V. Necliudov, M. S. Shur, *J. Appl. Phys.* **2006**, *100*, 024509.
- [30] E. A. Silinsh, A. I. Belkind, D. R. Balode, A. J. Biseniece, V. V. Grechov, L. F. Taure, M. V. Kurik, J. I. Vertzymacha, I. Box, *Phys. Status Solidi A* **1974**, *25*, 339.
- [31] M. Spijkman, E. C. P. Smits, P. W. M. Blom, D. M. de Leeuw, Y. Bon Saint Côme, S. Setayesh, E. Cantatore, *Appl. Phys. Lett.* **2008**, *92*, 143304.

## A.3 Full text of Ref. [3]

Wojciech Gajewski, Martin Huth, Felix Buth, Bert Nickel, Martin Stutzmann, and Jose A. Garrido

*Photoresponse and morphology of pentacene thin films modified by oxidized and reduced diamond surfaces.*

PHYSICAL REVIEW B **80**, 235311 (2009).

### **Abstract:**

Because of its large band gap and variety of stable surface terminations, diamond is a suitable material to study the optical and electronic properties of organic films. Optical absorption and photocurrent experiments with pentacene on hydrogen- and oxygen-terminated diamond surfaces reveal a strong, polarization-dependent photoresponse of pentacene films. The diamond surface reconstruction as well as the molecule-surface interactions influence the morphology and the molecular structure of the films, causing the associated polarization dependence. On oxygen-terminated diamond, the pentacene thin-film phase typical for electronically inert substrates such as SiO<sub>2</sub> is formed. On hydrogen-terminated diamond, on the other hand, a three-dimensional growth mode of a filamentlike pentacene morphology is observed by atomic force microscopy, with pentacene molecules arranged with their long molecular axis oriented along the hydrogen-terminated diamond surface, as confirmed by x-ray diffraction. Furthermore, on hydrogen-terminated single crystalline diamond, the b axis of the pentacene unit cell is found to orient preferentially perpendicular to the surface, in agreement with photocurrent and optical-absorption experiments.

Permanent weblink:

<http://prb.aps.org/pdf/PRB/v80/i23/e235311>

MH contribution:

- sample design and fabrication.
- performing the x-ray experiments (at DESY) and analysis (includes programming a simulation).
- writing the structure related part of the paper.
- participation in discussions.

# Photoresponse and morphology of pentacene thin films modified by oxidized and reduced diamond surfaces

W. Gajewski,<sup>1</sup> M. Huth,<sup>2</sup> F. Buth,<sup>1</sup> B. Nickel,<sup>2</sup> M. Stutzmann,<sup>1</sup> and J. A. Garrido<sup>1</sup>

<sup>1</sup>*Walter Schottky Institut, Technische Universität München, Garching, Germany*

<sup>2</sup>*Physics Department and CeNS, Ludwig-Maximilians-Universität, Munich, Germany*

(Received 17 September 2009; published 9 December 2009)

Because of its large band gap and variety of stable surface terminations, diamond is a suitable material to study the optical and electronic properties of organic films. Optical absorption and photocurrent experiments with pentacene on hydrogen- and oxygen-terminated diamond surfaces reveal a strong, polarization-dependent photoresponse of pentacene films. The diamond surface reconstruction as well as the molecule-surface interactions influence the morphology and the molecular structure of the films, causing the associated polarization dependence. On oxygen-terminated diamond, the pentacene thin-film phase typical for electronically inert substrates such as SiO<sub>2</sub> is formed. On hydrogen-terminated diamond, on the other hand, a three-dimensional growth mode of a filamentlike pentacene morphology is observed by atomic force microscopy, with pentacene molecules arranged with their long molecular axis oriented along the hydrogen-terminated diamond surface, as confirmed by x-ray diffraction. Furthermore, on hydrogen-terminated single crystalline diamond, the *b* axis of the pentacene unit cell is found to orient preferentially perpendicular to the surface, in agreement with photocurrent and optical-absorption experiments.

DOI: [10.1103/PhysRevB.80.235311](https://doi.org/10.1103/PhysRevB.80.235311)

PACS number(s): 68.55.am, 73.50.Pz, 78.66.Qn

## I. INTRODUCTION

Pentacene (Pc) has attracted much attention as the prototypical conjugated organic molecule for organic thin-film transistors (OTFTs). Using single crystalline as well as polycrystalline Pc films, carrier mobilities in OTFTs as high as those in amorphous silicon TFTs have been reported.<sup>1</sup> In order to optimize the transistor characteristics, the structural properties of the polycrystalline Pc films grown by thermal evaporation in ultrahigh vacuum were investigated in detail.<sup>1,2</sup> In general, two different types of substrates were used: (i) electronically inert substrates such as SiO<sub>2</sub> or Al<sub>2</sub>O<sub>3</sub> and (ii) metals, such as Au or Ag, and highly oriented pyrolytic graphite (HOPG). The initial growth of pentacene on electronically inert substrates is governed by a two-dimensional (2D) (layer-by-layer) growth mode.<sup>1</sup> In the resulting thin-film phase, the Pc molecules are arranged in an upright orientation, i.e., the long molecular axis points along the surface normal within 7°. On the other hand, three-dimensional (3D) growth is observed for Pc on metals.<sup>4</sup> Additionally, several groups have reported a flat-lying first monolayer of Pc on metal surfaces, attributed to the enhanced interaction between the Pc  $\pi$  orbitals and the metal surface.<sup>1,5,6</sup> Furthermore, by coating the metal surfaces with self-assembled monolayers (SAMs), several groups were able to modify the growth of Pc from 3D to 2D.<sup>2</sup> It has also been confirmed that the observed change from 2D to 3D growth induces a change of the pentacene film morphology.<sup>2,5,6</sup> The understanding of the influence of the growth mode on the optoelectronic properties of Pc thin films is, however, still poor, mostly due to the variety of different substrates used in previous studies.

In this work, we show that the optoelectronic properties of pentacene thin films can be modulated by controlled modification of diamond surfaces, though the variation of the growth mode of pentacene. In contrast to other semiconduc-

tors and metals, both oxygen-terminated and hydrogen-terminated diamond surfaces are stable in vacuum and under ambient conditions. While O-terminated diamond surfaces are hydrophilic, H-terminated surfaces are hydrophobic, which allows the preparation of substrates with different surface energies but the same morphology. The surface termination in diamond has a remarkable influence on the surface's electronic properties: while O-terminated surfaces show a positive electron affinity, H-terminated surfaces exhibit a negative electron affinity.<sup>7</sup> Thus, the surface termination can also be used to tune the position of the diamond conduction and valence bands at the surface. This has been applied to induce charge transfer between the diamond surface and the highest occupied molecular orbital (HOMO) or lowest unoccupied molecular orbital (LUMO) levels of organic molecules such as fullerenes.<sup>8</sup> Additionally, due to the large band gap of diamond (5.45 eV at room temperature), the optical and optoelectronic characterization of the deposited organic films is not limited by the substrate. Therefore, diamond surfaces are ideal substrates to investigate optoelectronic properties of organic thin films, since they combine the properties of standard electronically inert surfaces such as SiO<sub>2</sub> for oxidized diamond surfaces and, on the other hand, electronically active surfaces, such as graphite or metals, when the surface is hydrogenated.

## II. EXPERIMENTAL

Commercially available intrinsic (100)- and (111)-oriented single-crystal diamond (SCD) and polycrystalline diamond (PCD) films were chemically oxidized in a boiling H<sub>2</sub>SO<sub>4</sub>+KNO<sub>3</sub> solution for 1 h or hydrogenated by exposure to atomic hydrogen generated by a hot wire in a high-vacuum chamber at a substrate temperature of about 550 °C. The diamond films have a very smooth surface, with a typical roughness (rms) of 0.3 and 0.6 nm for SCD and PCD,

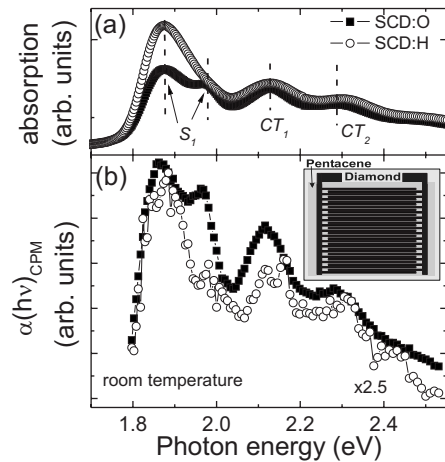


FIG. 1. (a) Room temperature optical absorption and (b) CPM spectra of Pc films on SCD:O and SCD:H. For better comparison, the CPM spectrum of Pc on SCD:H is multiplied by a factor of 2.5. Inset of (b) shows a top view on the diamond-pentacene sample. The absorption maxima are attributed to singlet exciton ( $S_1$ ) Davydov doublet (1.84 and 1.96 eV) and CT excitons (2.11 and 2.27 eV).

respectively. For optoelectronic characterization, Ti/Au (20/200 nm) interdigitated metal contacts (spacing of 45  $\mu\text{m}$ ) were evaporated on the substrates. Prior to pentacene deposition (rate 0.05–0.1  $\text{\AA}/\text{s}$ ), the diamond films were annealed *in situ* at 480 K (base pressure of  $10^{-7}$  mbar). Pentacene films with a nominal thickness of 50 nm (measured using a quartz microbalance) were deposited simultaneously on H- and O-terminated diamond substrates.  $\text{SiO}_2$  substrates were used for calibration and reference. The optical-absorption measurements between 2000 and 200 nm were done under ambient conditions using a Perkin Elmer  $\lambda$ -900 spectrometer. Constant photocurrent spectroscopy (CPM) (Ref. 9) was used to investigate the optoelectronic properties of the pentacene films. The CPM measurements were performed in vacuum ( $10^{-6}$  mbar) using chopped (4 Hz) monochromatic light from a xenon arc lamp for optical excitation in the energy range 1.8–2.8 eV. In contrast to conventional photocurrent spectroscopy, CPM probes the spectral variation of the absorption coefficient; this is done by adjusting the light intensity so that the photocurrent is kept constant at different wavelengths. The prepared diamond/pentacene samples were illuminated over the whole device structure (about  $2.3 \times 2.3 \text{ mm}^2$ ) from the pentacene layer side. The morphology of the Pc films was investigated with AFM in tapping mode under ambient conditions and by x-ray diffraction experiments, which were performed at the synchrotron x-ray facility HASYLAB (Hamburg, Germany).

### III. RESULTS AND DISCUSSION

Typical absorption spectra of 50-nm-thick Pc films deposited on oxygen- (SCD:O) and hydrogen-terminated (SCD:H) surfaces of single crystalline diamond are depicted in Fig. 1(a). In the case of the Pc films on SCD:O substrates, the absorption spectra is similar to those reported previously for single crystalline pentacene<sup>10</sup> or polycrystalline thin films

prepared on inert surfaces,<sup>11–13</sup> revealing the Davydov doublet due to Pc singlet exciton absorption ( $S_1$ ) at 1.84 and 1.96 eV as well as the charge-transfer (CT) excitons<sup>14</sup> at 2.11 and 2.27 eV. In the case of Pc films on SCD:H, however, the  $S_1$  absorption peak with its maximum at 1.85 eV is broader and the peak at 1.96 eV has almost vanished. Also, the peak assigned to charge-transfer exciton is broader and is slightly shifted to 2.12 eV, as compared to Pc films on SCD:O. The constant photocurrent method (CPM) was applied to investigate whether the observed differences in the absorption spectra of the pentacene films on O- and H-terminated diamond surfaces are also reflected in the optoelectronic properties of the investigated diamond/pentacene heterostructures.<sup>9</sup> The photoresponse of the films can be directly related to the absorption features observed in Fig. 1(a) for both diamond surface terminations, indicating that all excitations, including the excitonic peaks, are electronically active. The CPM spectra of pentacene films on SCD:O and SCD:H [Fig. 1(b)] closely follow the corresponding absorption spectra [Fig. 1(a)]. Note, however, that the CPM signal for the pentacene films on SCD:H surfaces is lower by a factor of 2.5. This can be attributed to the higher dark current of the H-terminated diamond substrate due to the surface conductivity of hydrogenated diamond.<sup>7</sup> The higher background current results in a decrease of the photocurrent sensitivity, which may partly contribute to the lowering of the CPM signal. For Pc films on SCD:O, the CPM signal maxima at 1.87 and 1.98 eV correspond to the Davydov doublet of the  $S_1$  exciton observed in the absorption spectra. In addition, the positions of the charge-transfer excitons are in good agreement with those estimated from the absorption spectra. For Pc films on SCD:H, a broad absorption peak is observed in the CPM spectrum [Fig. 1(b)] at about 1.86 eV and, as in the case of the absorption spectra [Fig. 1(a)], the presence of the second peak of the Davydov doublet at about 1.96 eV is either weak, absent, or in the shoulder of the peak at lower energy. The polarization dependence of the light absorption observed in other aromatic molecules such as anthracene shows the highest absorption when the electric field of the incoming light is parallel to one of the short crystal axes  $a$  and  $b$ .<sup>10</sup> The polarization-dependent absorption of pentacene films has recently been observed by ellipsometry experiments using single crystalline pentacene crystals.<sup>15</sup> Accordingly, the presence of the Davydov  $S_1$  doublet as observed here for Pc on oxidized diamond suggests that the  $a$ - $b$  plane is parallel to the polarization plane of the incident light and thereby parallel to the diamond surface. This result is in agreement with the broadly accepted model of the pentacene thin-film growth on electronically inert surfaces such as  $\text{SiO}_2$ , where typically an upright standing pentacene phase has been observed.<sup>2</sup> The decrease of the Davydov doublet intensity for pentacene films on the H-terminated diamond films reported here suggests a different molecular arrangement, i.e., no upright orientation of the long molecular axis and in particular, the  $b$ -axis oriented perpendicular to the surface.

In order to verify the conclusions made above and to correlate the observed optical-absorption and photocurrent data with the Pc films structure, we have performed a detailed study of the pentacene film morphology. Typical AFM micrographs of Pc film morphology on oxidized and hydrogen-

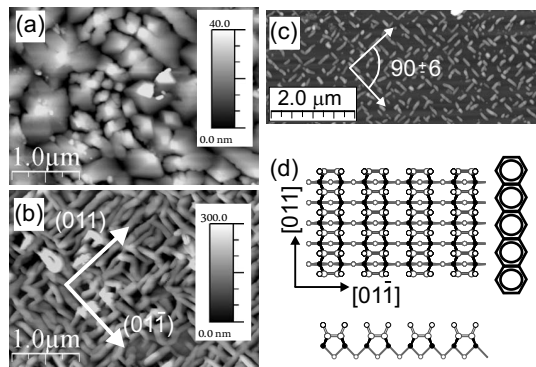


FIG. 2. AFM micrographs of pentacene films on the (a) oxidized and [(b) and (c)] hydrogenated surfaces of SCD. Nominal film thicknesses are [(a) and (b)] 50 nm and (c) 0.8 nm. On the oxidized surface, pentacene grains with sizes up to  $1 \mu\text{m}$  are observed, exhibiting a terraced structure with a step spacing of about 1.5 nm. A filamentlike structure (average height: 150 nm) is observed for the H-terminated diamond. The main crystallographic directions parallel to the SCD:H surface are indicated by arrows. (d) shows a schematic top and side view of the  $(2 \times 1)$  reconstruction of the (100) diamond surface. A pentacene molecule is shown for comparison.

ated surfaces of single crystalline diamond films are presented in Fig. 2. The Pc texture observed on oxidized diamond [Fig. 2(a)] is very similar to the one on inert substrates such as  $\text{SiO}_2$ .<sup>1-3,16</sup> For films with a nominal thickness of 50 nm, the formation of terraced pyramidal structures (grain size  $\sim 0.5\text{--}1 \mu\text{m}$ ) is seen. The step heights observed by AFM are in good agreement with the  $d_{(001)}$  distance of the thin-film phase of pentacene.<sup>2</sup> The morphology of the pentacene film on the hydrogen-terminated diamond surface [Fig. 2(b)] is entirely different. Filamentlike islands typical for a 3D growth mode are observed. The average height of the Pc structures is about 150 nm, with a length of  $0.4\text{--}0.5 \mu\text{m}$ . Furthermore, two preferential orientations are observed on the SCD:H surface with an angle of  $90^\circ$  relative to each other. For the (100)-oriented SCD [SCD(100)] used for this study, the main crystallographic directions parallel to the surface are the (011) and  $(01\bar{1})$ , marked with arrows in Fig. 2(b). For the H-terminated diamond surface SCD(100)- $(2 \times 1)$ :H, these directions correspond to the directions of the dimer rows of the  $(2 \times 1)$  reconstructed surface [Fig. 2(d)].<sup>17</sup> In addition, they are in good agreement with the preferential direction of the filamentlike texture of the pentacene islands observed in the atomic force microscopy (AFM) micrographs. A similar filamentlike morphology has been observed for Pc films on single crystalline and polycrystalline Au(111).<sup>4,5</sup> Recently, Koini *et al.* reported an influence of the surface corrugation of weakly interacting oxygen-passivated Cu(100) single crystals on the morphology pattern of pentacene films.<sup>18</sup> These authors observed preferential alignment of the pentacene molecules with the long crystal axis,  $c$ , along the surface corrugation due to the presence of the oxygen atoms. In analogy, the filamentlike island morphology of the Pc films on SCD(100)- $(2 \times 1)$ :H surface can be assigned to the influence of surface corrugation of the H-terminated diamond due to the presence of the dimer rows. In order to verify this hypothesis, additional growth experiments have

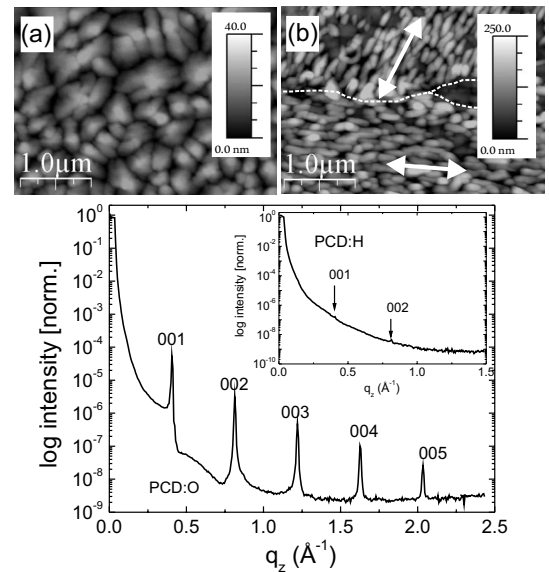


FIG. 3. AFM micrographs of pentacene films grown on the (a) oxidized and (b) hydrogenated surfaces of PCD used for the x-ray experiments. (c) Out-of-plane x-ray reflectivity pattern of pentacene on PCD:O. Inset shows the out-of-plane x-ray reflectivity pattern of pentacene on PCD:H.

been performed on the H-terminated (100)- and (111)-oriented surfaces of SCD films, SCD(100)- $(2 \times 1)$ :H and SCD(111)- $(1 \times 1)$ :H, respectively. Deposition of a 0.8 nm thin pentacene film allowed us a detailed investigation of the orientation and shape of the pentacene structures. For the SCD(100)- $(2 \times 1)$ :H substrate [Fig. 2(c)], the filamentlike structures are again perpendicular to each other, in agreement with the thicker films [Fig. 2(b)]. The main symmetry directions of the SCD(100)- $(2 \times 1)$ :H surface have been marked with arrows in the schematic model representing the top and side views of the diamond surface in Fig. 2(d). In the case of the (111) diamond surface, with a typical  $(1 \times 1)$  reconstruction,<sup>7</sup> filamentlike growth of the pentacene layer in three rotational domains with a rotation angle close to  $60^\circ$  is observed (data not shown), as expected from the symmetry of this surface reconstruction. Thus, our data confirm a strong influence of the diamond surface symmetry on the directional growth of the pentacene thin film on H-terminated diamond.

For a verification of the pentacene molecular arrangement induced by the different diamond surface terminations, observed by the AFM experiments, x-ray diffraction experiments have been conducted. The initial experiments were performed on 50-nm-thick pentacene films deposited on polycrystalline diamond substrates (PCD, O- and H-terminated). As depicted in Figs. 3(a) and 3(b), the morphology of pentacene films on oxygen- and hydrogen-terminated PCDs is similar to Pc on SCD surfaces [Fig. 2]. A filamentlike structure and preferential orientation of the pentacene filaments is observed for PCD:H substrates, where the presence of the grain boundaries [marked in dashed line in Fig. 3(b)] appears as an orientation-domain boundary. A Debye-Scherrer image of a PCD:H substrate depicted as the inset of [Fig. 4(a)] shows powderlike rings, as expected for a

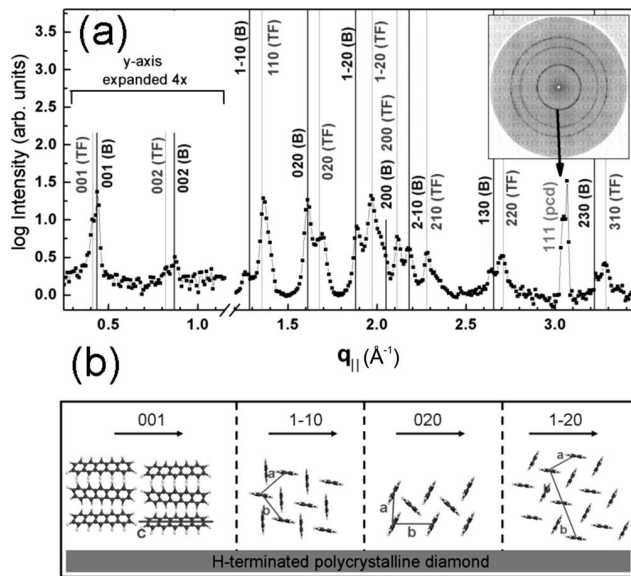


FIG. 4. (a) In-plane XRD data for Pc film on PCD:H. Vertical lines mark the calculated positions of the main diffraction peaks of the bulk phase (b) and the TF phase. In the low  $q_{||}$  range, the vertical scale has been expanded 4 times for clarity. A Debye-Scherrer image of a PCD:H substrate (inset) shows powder rings. (b) shows schematic side views of selected orientations of pentacene on hydrogenated diamond. Cross sections along 001, 1–10, 020, and 1–20 directions are depicted. For all schematics, the orientations of the  $a$ ,  $b$ , and/or  $c$  axes have been shown for clarity.

polycrystalline material without any preferential orientation. The results of the x-ray reflectometry experiments for both PCD surface terminations are shown in Fig. 3(c). For the oxidized diamond surfaces [inset in Fig. 3(c)], the graph reveals a clear Bragg pattern with peak separations corresponding to a layer spacing of  $d_{(00l)} = 1.54 \pm 0.01$  nm. From the evaluation of the full width at half maximum ( $0.019 \pm 0.002$  Å<sup>-1</sup>) of the XRD spectra, a crystalline grain size along the surface normal of about 33 nm is deduced for Pc on PCD:O. Thus, the presence of the upright standing pentacene phase typical for electronically inert surfaces<sup>3,16</sup> is confirmed for the O-terminated diamond substrates. This is consistent with the data obtained from the optoelectronic characterization, supporting a parallel orientation of the crystal  $a$ - $b$  plane with respect to the diamond surface. The x-ray out-of-plane reflectivity spectrum of Pc on PCD:H reveals only very weak ( $00l$ ) Bragg peaks at the position for the upright standing Pc molecules. The presence of a very small fraction of the standing phase on SCD:H and PCD:H surfaces is assigned to a nonperfect hydrogenation process, which can result in the presence of a few oxygen-terminated sectors in nominally hydrogenated surfaces. Complementary in-plane XRD diffraction, depicted in Fig. 4(a), has been used to further characterize the Pc ordering for the hydrogenated diamond surface. (001) reflections occur in the in-plane XRD pattern, which indicates that the long molecular axis ( $c$  axis) is parallel to the sample surface. This also has been observed for Pc on HOPG,<sup>20</sup> gold,<sup>5</sup> and oxygen-passivated copper surfaces.<sup>18</sup> Furthermore, the (001) reflex is split, which suggests the presence of different pentacene poly-

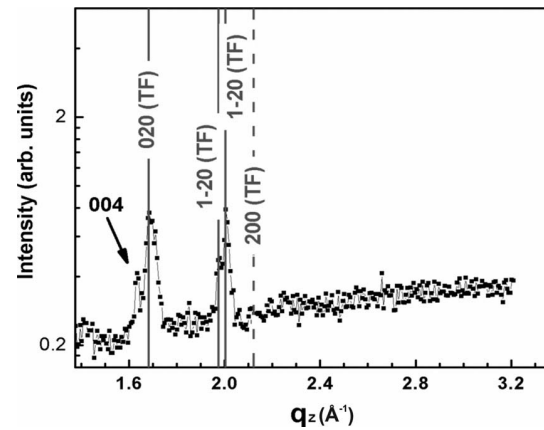


FIG. 5. Zoom into the out-of-plane x-ray reflectivity pattern of pentacene on SCD:H. Note that the (020) and the (120), (1–20) planes show Bragg reflections, whereas the (200) peak is not observed, indicating the  $a$  axis being mainly parallel and the  $b$  axis being mainly perpendicular to the surface.

morphs. The  $d_{00l}$  spacing ( $d = 2\pi/q$ ;  $d_{00l} = 15.4$  and  $14.5$  Å, respectively) indicates the presence of a bulk phase and a thin-film phase polymorph. Using the structure of these polymorphs reported in the literature,<sup>3,19</sup> all Bragg peaks can be attributed to a specific polymorph, either thin-film phase (TF) or bulk phase (B), and indexed. In order to refine the structural information, the measured peak positions were fitted to simulated peak values using a combination of a Monte Carlo method and a Levenberg-Marquardt nonlinear least-squares fit routine.<sup>21</sup> The best fits obtained for the unit-cell parameters of the thin-film structure are  $a = 5.96$  Å,  $b = 7.60$  Å,  $c = 15.33$  Å,  $\alpha = 80.88^\circ$ ,  $\beta = 87.18^\circ$ , and  $\gamma = 90.1^\circ$ , whereas the bulk phase structure parameters are  $a = 6.29$  Å,  $b = 7.82$  Å,  $c = 14.50$  Å,  $\alpha = 86.94^\circ$ ,  $\beta = 76.93^\circ$ , and  $\gamma = 91.15^\circ$ . These values are in good agreement with the values for the bulk pentacene polymorph, reported by Campbell *et al.*,<sup>19</sup> and the values for the thin-film pentacene polymorph, reported by Schiefer *et al.*,<sup>3</sup> respectively. A sketch of selected orientations of Pc molecules based on the observed peaks is depicted in Fig. 4(b). The arrangement of the pentacene molecules partly explains the differences observed in the optical-absorption and photocurrent spectra of Pc films deposited on O- and H-terminated diamond surfaces. The absorption and photocurrent spectra of the pentacene film on SCD:H surfaces show a strong intensity decrease of the higher-energy peak of  $S_1$  at 1.96 eV. An almost perpendicular arrangement of the  $b$  axis would explain the absence of the 1.96 eV peak in the absorption spectra.<sup>10,15</sup> The in-plane x-ray data on PCD:H in the available  $q_z$  range do not reveal a clear preference for an orientation of the  $a$  or  $b$  axis. However, the observed lack of the Bragg series characteristic for an upright standing pentacene film does not unequivocally rule out an arrangement with the  $c$  axis of the Pc crystal aligned parallel to the H-terminated diamond surface.

To confirm this experimentally, out-of-plane x-ray reflectivity measurements have been performed on a 50-nm-thick pentacene film grown on (100) SCD:H (Fig. 5) in the extended  $q_z$  range. The indexed peaks correspond to the (020), the (120), and the (1–20) crystal planes of pentacene. At the

$q$  position of the (200) plane, no peak is observed, which suggests that the  $a$  axis is mainly parallel to the surface, while the  $b$  axis is mainly perpendicular to the surface. This is in good agreement with the optical measurements performed on Pc films on SCD:H substrates and also confirms our growth model depicted schematically in Fig. 4(b).

The nature of the molecule-surface interactions governing the different molecular structure of the Pc films is discussed in the following. First of all, the different values of the surface free energy of pentacene and diamond surfaces with different termination should be considered as a possible explanation of the observed differences in the pentacene film morphology. The growth orientation of pentacene thin films results from the competition between Pc crystal planes with different surface energies. As suggested by Northrup *et al.*,<sup>16</sup> the lowest surface energy corresponds to the (001) plane of a pentacene crystal and is 1.5 times lower than that of (100) or (110) planes. Therefore, on electronically inert surfaces such as O-terminated diamond, pentacene growth shows a (001) layer-by-layer structure. Yoshikawa *et al.*<sup>22</sup> modified the surface energy by using self-assembled monolayers on SiO<sub>2</sub> surfaces. In the case of low surface energies, the authors observed a spontaneous aggregation of pentacene films which led to the formation of long filamentlike structures next to bare SiO<sub>2</sub> substrate regions. In the case of hydrogenated diamond, the surface free energy is relatively low compared to oxidized diamond surfaces<sup>23</sup> or the SiO<sub>2</sub> surface. This difference in the surface energy could explain the observed filamentlike structures on H-terminated diamond surfaces.<sup>22</sup> Second, the formation of a chemical bond between the pentacene  $\pi$  orbitals and a surface dangling bond could be considered as the origin of the preferential nucleation, similar to the (2 $\times$ 1) reconstructed Si surface.<sup>24</sup> The low density of dangling bonds on the H-terminated diamond surface, though, makes chemisorption induced by dangling bonds not very probable. However, a strong electronic interaction between the Pc molecules and the substrate surface could also explain the preferential orientation observed for H-terminated diamond surfaces. Such strong electronic interactions have been reported between metallic surfaces and various molecular  $\pi$  systems, including pentacene.<sup>4</sup> Thus, we tentatively assign the corrugation of the electronic structure of the hydrogenated (100) diamond surface, which results from the dimer reconstruction, to be responsible for the preferential orientation of the filamentlike structures. The alignment of the long molecular axis of pentacene on the diamond surface along the dimer rows was confirmed in Fig. 2, where

the angle measured for the pentacene filaments directions is in close agreement with the directions of the dimer rows of the SCD(100)-(2 $\times$ 1):H surface. Such a specific alignment of pentacene molecules seems to be consistent with the accepted model of the formation of molecular crystals,<sup>10</sup> where dispersive forces, dipole-dipole interaction, and hydrogen bonds formation govern the crystal growth.

#### IV. SUMMARY

In summary, we have shown that diamond surfaces are excellent platforms to manipulate the morphology and the optoelectronic properties of pentacene thin films. Our experiments demonstrate that the surface termination of diamond determines the growth mode of pentacene: quasi-2D growth on O-terminated surfaces and 3D growth on H-terminated surfaces. The observed change of the Pc film morphology is considered to be responsible for the differences in the optoelectronic properties of the pentacene films and manifested in a polarization-dependent optical absorption of the pentacene films. For O-terminated diamond, the presence of an upright standing thin-film phase has been observed, with a characteristic interlayer spacing,  $d_{(001)}$ , of  $1.54 \pm 0.01$  nm and a strong Davydov doublet of the singlet exciton absorption. Both diamond surface terminations result in different surface energies, but also different electronic properties due to the influence of C-H and C-O interfacial dipoles. By changing the surface termination to hydrogen, the growth of filamentlike structures of pentacene in a bulklike crystal phase has been induced, characterized by a suppressed Davydov doublet component. Complementary x-ray experiments have confirmed the presence of the dominant lying-down phase on the hydrogen-terminated diamond films with the  $c$  axis oriented parallel to the diamond surface. Furthermore, for SCD(100)-(2 $\times$ 1):H substrates, a preferential orientation of the pentacene  $a$  axis parallel and  $b$  axis perpendicular to the diamond surface has been found, explaining the differences of the optical properties of pentacene on both surface terminations.

#### ACKNOWLEDGMENTS

This work was supported by the EC Research Training Network "DRIVE" under Contract No. RTN-CT-2004-512224 and by the EU-STREP Contract No. 032652 BIODOT. The "Nanosystems Initiative Munich" (NIM) is gratefully acknowledged.

<sup>1</sup>R. Ruiz, B. Nickel, N. Koch, L. C. Feldman, R. F. Haglund, A. Kahn, and G. Scoles, Phys. Rev. B **67**, 125406 (2003).

<sup>2</sup>R. Ruiz, D. Choudhary, B. Nickel, T. Toccoli, K.-C. Chang, A. C. Mayer, P. Clancy, J. M. Blakely, R. L. Headrick, S. Iannotta, and G. G. Malliaras, Chem. Mater. **16**, 4497 (2004).

<sup>3</sup>S. Schiefer, M. Huth, A. Dobrinevski, and B. Nickel, J. Am. Chem. Soc. **129**, 10316 (2007).

<sup>4</sup>D. Käfer, L. Ruppel, and G. Witte, Phys. Rev. B **75**, 085309 (2007).

<sup>5</sup>D. Käfer and G. Witte, Chem. Phys. Lett. **442**, 376 (2007).

<sup>6</sup>L. Casalis, M. F. Danisman, B. Nickel, G. Bracco, T. Toccoli, S. Iannotta, and G. Scoles, Phys. Rev. Lett. **90**, 206101 (2003).

<sup>7</sup>J. Ristein, Appl. Phys. A: Mater. Sci. Process. **82**, 377 (2006).

<sup>8</sup>P. Strobel, M. Riedel, J. Ristein, and L. Ley, Nature (London)

- 430**, 439 (2004).
- <sup>9</sup>M. Vanecek, J. Kocka, J. Stuchlik, and A. Triska, *Solid State Commun.* **39**, 1199 (1981).
- <sup>10</sup>M. Pope and C. E. Swenberg, *Electronic Processes in Organic Crystals and Polymers*, 2nd ed. (Oxford University Press, New York, 1999), p. 1328, ISBN 0195129636.
- <sup>11</sup>D. Knipp, D. K. Murti, B. Krusor, R. Apte, L. Jiang, J. P. Lu, B. S. Ong, and R. A. Street, *Mater. Res. Soc. Symp. Proc.* **665**, C5.44.1 (2001).
- <sup>12</sup>M. Breban, D. B. Romero, S. Mezhenny, V. W. Ballarotto, and E. D. Williams, *Appl. Phys. Lett.* **87**, 203503 (2005).
- <sup>13</sup>J. Gao and F. A. Hegmann, *Appl. Phys. Lett.* **93**, 223306 (2008).
- <sup>14</sup>L. Sebastian and G. Weiser, *Chem. Phys.* **61**, 125 (1981).
- <sup>15</sup>M. Dressel, B. Gompf, D. Faltermeier, A. K. Tripathi, J. Pflaum, and M. Schubert, *Opt. Express* **16**, 19770 (2008).
- <sup>16</sup>J. E. Northrup, M. L. Tiago, and S. G. Louie, *Phys. Rev. B* **66**, 121404(R) (2002).
- <sup>17</sup>J. Ristein, *Surf. Sci.* **600**, 3677 (2006).
- <sup>18</sup>M. Koini, T. Haber, O. Werzer, S. Berkebile, G. Koller, M. Oehzelt, M. G. Ramsey, and R. Resel, *Thin Solid Films* **517**, 483 (2008).
- <sup>19</sup>R. B. Campbell, J. M. Robertson, and J. Trotter, *Acta Crystallogr.* **14**, 705 (1961).
- <sup>20</sup>N. Koch, A. Vollmer, I. Salzmann, B. Nickel, H. Weiss, and J. P. Rabe, *Phys. Rev. Lett.* **96**, 156803 (2006).
- <sup>21</sup>D. W. Marquardt, *J. Soc. Ind. Appl. Math.* **11**, 431 (1963).
- <sup>22</sup>G. Yoshikawa, J. T. Sadowski, A. Al-Mahboob, Y. Tsuruma, S. Ikeda, and K. Saiki, *Appl. Phys. Lett.* **90**, 251906 (2007).
- <sup>23</sup>L. Ostrovskaya, V. Perevertailo, V. Ralchenko, A. Dementjev, and O. Loginova, *Diamond Relat. Mater.* **11**, 845 (2002).
- <sup>24</sup>D. Choudhary, P. Clancy, and D. R. Bowler, *Surf. Sci.* **578**, 20 (2005).



## A.4 Full text of Ref. [4]

Eva Bystrenova, Marta Jelitai, Ilaria Tonazzini, Adina N. Lazar, Martin Huth, Pablo Stoliar, Chiara Dionigi, Marcello G. Cacace, Bert Nickel, Emilia Madarasz, and Fabio Biscarini

*Neural Networks Grown on Organic Semiconductors.*

Adv. Funct. Mater. 2008, **18**, 1751 – 1756

### **Abstract:**

We report adhesion, growth, and differentiation of mouse neural cells on ultra-thin films of an organic semiconductor, pentacene. We demonstrate that i) pentacene is structurally and morphologically stable upon prolonged contact with water, physiological buffer, and cell culture medium; ii) neural stem cells adhere to pentacene and remain viable on it for at least 15 days; iii) densely interconnected neural networks and glial cells develop on the pentacene surface after several days. This implies that adhesion proteins secreted by the cells find suitable adsorption loci to anchor the cells. Pentacene is also a suitable substrate for casting thin layers of cell adhesion molecules, such as laminin and poly-L-lysine. Our results show that pentacene, albeit being an aromatic molecule, allows neurons to adhere to and grow on it, which is possibly due to its tightly packed solid state structure. This structure remains unaltered upon exposure to water and interfacial force exerted by the cells. The integration of living cells into organic semiconductors is an important step towards the development of bio-organic electronic transducers of cellular signals from neural networks.

Permanent weblink:

<http://www3.interscience.wiley.com/cgi-bin/fulltext/119876445/PDFSTART>

MH contribution:

- x-ray sample fabrication.
- synchrotron x-ray experiments and analysis.
- writing the x-ray related part of the paper.

DOI: 10.1002/adfm.200701350

# Neural Networks Grown on Organic Semiconductors\*\*

By Eva Bystrenova, Marta Jelitai, Ilaria Tonazzini, Adina N. Lazar, Martin Huth, Pablo Stoliar, Chiara Dionigi, Marcello G. Cacace, Bert Nickel, Emilia Madarasz, and Fabio Biscarini\*

We report adhesion, growth, and differentiation of mouse neural cells on ultra-thin films of an organic semiconductor, pentacene. We demonstrate that i) pentacene is structurally and morphologically stable upon prolonged contact with water, physiological buffer, and cell culture medium; ii) neural stem cells adhere to pentacene and remain viable on it for at least 15 days; iii) densely interconnected neural networks and glial cells develop on the pentacene surface after several days. This implies that adhesion proteins secreted by the cells find suitable adsorption loci to anchor the cells. Pentacene is also a suitable substrate for casting thin layers of cell adhesion molecules, such as laminin and poly-L-lysine. Our results show that pentacene, albeit being an aromatic molecule, allows neurons to adhere to and grow on it, which is possibly due to its tightly packed solid state structure. This structure remains unaltered upon exposure to water and interfacial force exerted by the cells. The integration of living cells into organic semiconductors is an important step towards the development of bio-organic electronic transducers of cellular signals from neural networks.

## 1. Introduction

There is a need for devices and functional systems that transduce cell responses to quantitative signals while avoiding invasive monitoring or loading with molecular probes. Such devices are not only sought after for the real-time monitoring of *in vitro* systems, but also for developing loco-regional therapies, where a signal from a transducer triggers a device that dispenses drugs locally and in real-time. In order to preserve cellular metabolism and function, the interface between the device and the cell must mimic the natural chemical environment of the cell; while at the same time offering the possibility to control the interactions with the cell.

Monitoring electrical and chemical signalling within neural networks is a fundamental issue in neuroscience. Extracellular

metal electrodes can record network activity, but the resolution is too poor to record individual cell responses or single chemical events.<sup>[1]</sup> The widely used patch clamp approach provides a highly sensitive method for the detection of single cell responses or channel reactions both *in vivo* and *in vitro*, but it only allows real-time monitoring for one or very few cells and it is difficult to upscale in number as well as downscale in size.<sup>[2]</sup> Moreover, the direct effect on the cells is to limit the time of the assay and prevent long-term monitoring. A less invasive approach consists of coupling neurons to inorganic semiconductor devices, such as field effect transistors.<sup>[3]</sup> Although important observations, e.g., the “firing” in small neural networks, were accomplished using this approach, it struggles with sensitivity due to low capacitive coupling and faces difficulties in chemically tailoring the surface for the attachment of neurons. More recently, it was proposed that silicon nanowires may be used to monitor the action potential on axon membranes.<sup>[4]</sup> Thus, low dimensional charge transport devices seem to be a promising route for overcoming limitations due to low sensitivity. Attempts to adhere and grow neurons on functionalized carbon nanotubes,<sup>[5]</sup> are headed in the same direction and have already been successful.

In organic electronic devices the semiconducting layer is made of either a molecular or a polymeric conjugated material, which offers several potential advantages: i) the materials are intrinsically inert and mostly hydrophobic, thus molecular layers of cell adhesion proteins exhibiting hydrophobic domains can be adsorbed; ii) the roughness of the organic interface can be controlled through the deposition process;<sup>[6]</sup> and iii) the charge carriers move within the region of the organic semiconductor thin film, close to the gate dielectric interface, thereby presenting the organic field-effect transistor as a low-dimensional device.<sup>[7]</sup> Latter feature is important because

[\*] Dr. F. Biscarini, Dr. E. Bystrenova, Dr. I. Tonazzini, Dr. A. N. Lazar, Dr. P. Stoliar, Dr. C. Dionigi, Dr. M. G. Cacace  
CNR-Institute for the Study of Nanostructured Materials  
Via Gobetti 101, Bologna, I-40129 (Italy)  
E-mail: fabio.biscarini@bo.ismn.cnr.it

Dr. M. Jelitai, Prof. E. Madarasz  
Laboratory of Cellular and Developmental Neurobiology  
Institute of Experimental Medicine of the Hungarian Academy of Sciences  
Szigony u. 43, Budapest, H-1083 (Hungary)

Dr. M. Huth, Dr. B. Nickel  
Department für Physik, CeNS, and NIM, Ludwig-Maximilians-Universität München Geschwister-Scholl-Platz 1, Munich, D-80539 (Germany)

[\*\*] We thank Dr. Antonietta Rizzo for help. This work was carried out with support from the EU-STRP 0032352 BIODOT project. Partial support by the DFG Nanosystems Initiative Munich (NIM) is also acknowledged. Supporting Information is available online from Wiley InterScience or from the author.

the response of ultra-thin-film transistors can be enhanced through the close proximity of cell membrane and charge transport region. The distance between the cell membrane and the surface of a silicon dioxide substrate is in the order of tens of nanometers.<sup>[8,9]</sup> Moreover, when the organic material is coated with a lipid membrane, this membrane acts as bi-functional,<sup>[10]</sup> ultra-thin dielectric layer (floating top gate) separating the biological system from the charge transport layer.<sup>[11]</sup>

On this rationale, we investigated the possibility to seed, adhere, and grow both primary neurons and one-cell derived neural stem cells on the most widely investigated organic semiconductor pentacene.<sup>[12]</sup> We grew ultra-thin-films of pentacene (nominal thickness: 5–6 monolayers (ML) = 10 nm) using high vacuum sublimation. The conditions applied allowed us to control layer morphology, molecular orientation, and packing. The choice of pentacene was motivated by the fact that pentacene transistors are amongst the most stable and best performing organic devices as well as pentacene's insolubility in any type of solvent. The processing of pentacene by high-vacuum sublimation is clean and potentially compatible with sterility standards, whereas organic solvents, which may denature proteins and membranes thereby causing cell death, are completely absent.

Our results clearly indicate that the morphology of pentacene thin-films does not change significantly upon exposure to water or physiological solutions. More importantly, we show that both primary neurons obtained from embryonic mouse forebrain and one-cell derived embryonic mouse neural stem cells remain viable for many days on pentacene surfaces. Furthermore, the stem cells can be differentiated into neurons, giving rise to densely interconnected networks. Another interesting option is the casting of ultra-thin-films of classical adhesion proteins, i.e., laminin and poly-L-lysine, on pentacene layers. These proteins support the formation of neural networks, while leaving the morphology of the underlying pentacene film unchanged.

The paper is organized as follows: the section “Results” describes results obtained by atomic force microscopy (AFM) and X-ray reflectivity on pentacene films, and displays images of cells grown on pentacene, which were obtained by bright field microscopy, fluorescence microscopy, and AFM; the section “Discussion” presents reasons why pentacene works effectively as a cell culture substrate; and finally we draw the “Conclusions”. The Experimental part details the conditions for sample preparation and the characterization techniques used.

## 2. Results

The morphology of ultra-thin pentacene films on silicon wafers is shown in Figure 1. The peak-to-valley variation

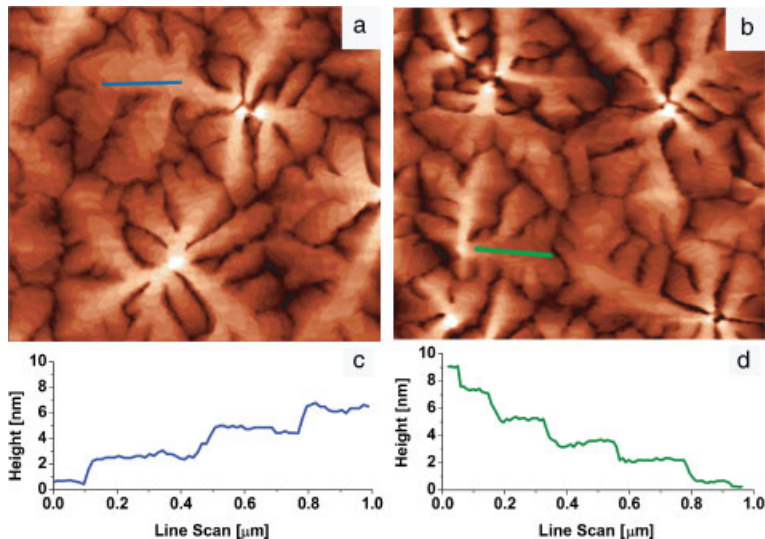


**Figure 1.** a,b) Typical atomic force microscopy (AFM) images of pentacene thin-films grown on SiO<sub>2</sub>/Si wafers, acquired in contact mode in air and water, respectively. c, d) The height profiles corresponding to the blue and green lines in the topographical images, respectively, clearly show the monolayer stacking.

measured across different profiles is up to 10 nm. The stacked monolayers are clearly visible both in the image acquired in air (Fig. 1a) and in ultra-high quality (UHQ) water (Fig. 1b); whereby each image reveals a step height of  $\sim 1.5$  nm, which corresponds to the projected height of a standing pentacene molecule in a thin-film phase,<sup>[18]</sup> confirming that the pentacene molecules form a rather compact *ab* plane (i.e., the one with the highest density of molecules per unit area). This morphology is retained in water on the mesoscopic length scale, and there is no evidence for extensive molecular dissolution, which would result in meandering of the terraces or widespread nucleation of vacancies. Threshold voltage and mobility, measured after a pentacene organic field-effect transistor (OFET) was immersed in water for many days, are shown in Figure 2. The mobility decreased by about one order of magnitude, while the threshold voltage approached a asymptotically a steady state value of 35 V with a characteristic time of two days. As it turns out, a pentacene OFET immersed in water for a long time still operates. However, in some instances and after many days of immersion of pentacene films in medium, we observed the appearance of randomly positioned and sharp-edged voids (average size: tens of nanometers in width). This suggests that some domains of the pentacene films may detach from the film upon prolonged immersion (several weeks) in liquid (see Fig. SI-1a in Supplementary Information). It is important to remark that the continuity of the pentacene film in close proximity with the substrate (the region where charge carriers are accumulated and transported to the organic field effect transistor) is retained.

The structural stability of the pentacene films in water was studied by X-Ray reflectivity. The reflected intensities of a 12 nm thick pentacene film, measured at ambient conditions

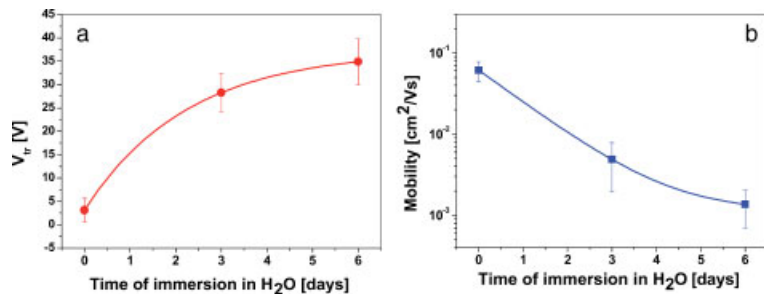


**Figure 2.** Device response of a pentacene organic field-effect transistor (OFET) in air, and after immersion in water for three and six days. a) Threshold voltage. b) Charge mobility.

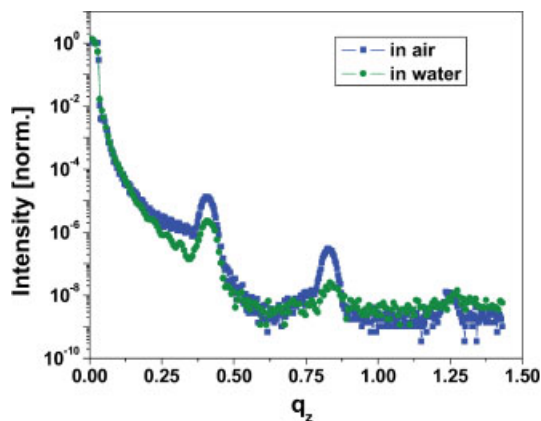


**Figure 3.** X-ray reflectivity of a 12 nm thick pentacene film at ambient conditions (blue) and after backfilling of the sample chamber with de-ionized water (green). Lines were drawn between data points to guide the eye.

and after backfilling of the sample chamber with de-ionized (DI) water are shown in Figure 3. While backfilling, a shear tension of  $\sim 10^{-5} \text{ N} \cdot \text{cm}^{-2}$  is present. The (00 $l$ ) Bragg peaks series is described by a vertical momentum transfer of  $q_z$  (00 $l$ ) =  $0.408 \cdot l \text{ \AA}^{-1}$ . This corresponds to an interlayer  $d$ -spacing of  $d_{001} = 2\pi/q_z = 15.4 \text{ \AA}$ , which equals the spacing in a pentacene thin-film phase,<sup>[18]</sup> and is in agreement with data obtained from AFM measurements. The Bragg peak positions do not shift after hydration, which indicates that the crystal structure of pentacene thin-films does not swell or undergo a phase transition in water, contrary to what is observed in some organic solvents, e.g., toluene.<sup>[19]</sup>

Also, the peak full width at half maximum (FWHM) of the 00 $l$  reflection before and after backfilling is nearly unchanged, which indicates that the crystal thickness  $D$  is not affected by hydration. The observed peak width,  $\delta q$ , is equivalent to a  $D$  value of 18 nm and 17 nm before and after filling, respectively. This allows us to conclude that there is not re-crystallization or water-induced annealing of the crystalline domains in the thin film. However,

the Bragg peak intensity is reduced after backfilling, which is indicative of some film material being detached by the shear force. This is again consistent with our AFM observation of non-conserved mass of films that are exposed to water. The complementary information from AFM and X-ray reflectivity measurements in water leads to the conclusion that pentacene is structurally and morphologically suitable to sustain the prolonged exposure to water that is required for experiments with living cells.

Primary neural cells, isolated from the forebrains of 15-day old mouse embryos, did not attach to bare pentacene as individual cells but rapidly aggregated into larger assemblies (Fig. 4a). This indicates that cell surfaces provide more favorable adhesion sites than the pentacene surface. The bare pentacene, even without providing an optimum surface for rapid attachment of primary neural cells, still allowed them to survive for several days and develop a substrate-attached layer of glial cells (Fig. 4b). Therefore, we infer that pentacene thin-films are non-toxic for neural cells within a time period of several days.

Adhesion of individual neurons and rapid (24 h) outgrowth of processes were achieved when the pentacene surface was covered with well-known adhesive molecules such as laminin and poly-L-lysine (Figs. 4c, d). The behavior of neurons on adhesion-protein-coated pentacene was comparable to that observed on glass surfaces coated with the same adhesion molecules. This indicates that there is a favorable interaction between adhesion molecules (either cast in a thin-film or secreted by the cell) and the pentacene substrate. The movie enclosed in the supporting information shows the neuronal

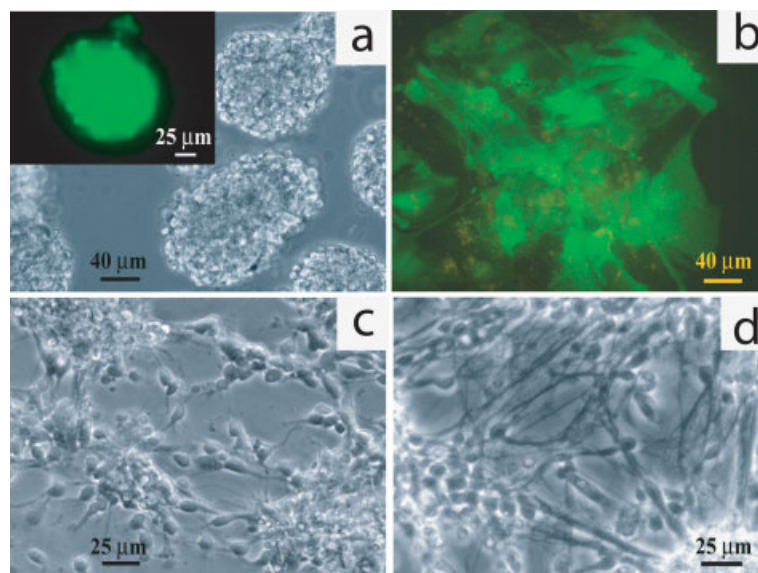


**Figure 4.** Phase-contrast images of primary neural cells 24 h post-attachment (left column) and after eight days of cultivation (right column) on: a, b) bare pentacene and c, d) poly-L-lysine coated pentacene. Insert top-left and b) show fluorescence images of primary neurons prepared from the forebrains of 15-day old CAMIIKinase-GFP transgenic mouse embryos. Pentacene was grown on glass except for the upper insert and b), where the substrate was a  $\text{SiO}_2/\text{Si}$  wafer. Note the dense network of neuronal processes in d).

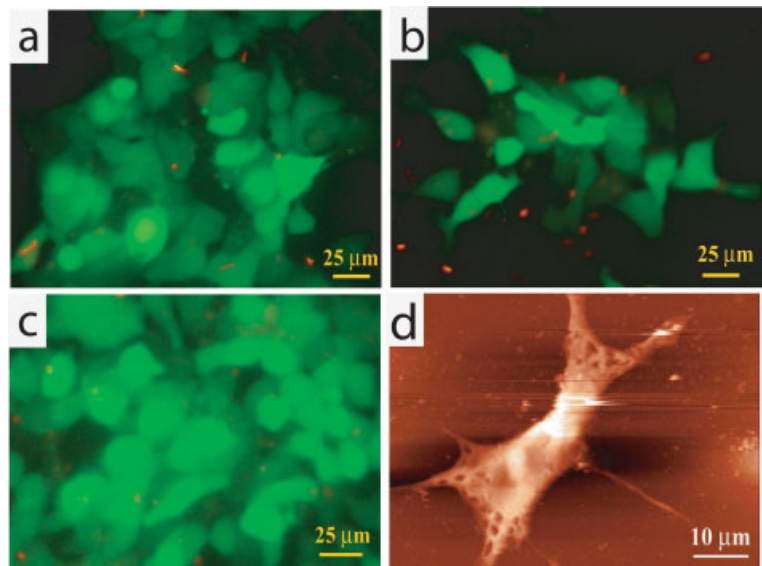


**Figure 5.** Fluorescent micrographs of GFP-4C neural stem cells after 24 h cultivation on: a) bare pentacene, b) poly-L-lysine coated pentacene, and c) laminin coated pentacene. d) Typical AFM image of a NE-4C cell on a poly-L-lysine coated pentacene surface. Cells were fixed with 4% paraformaldehyde and scanned in semi-contact mode in air. Holes visible on the cell periphery indicate delayed motility of the cell membrane. Pentacene films were evaporated on SiO<sub>2</sub>/Si wafers.

process elongation on poly-L-lysine coated pentacene. After one week in culture, primary neurons formed dense networks on pentacene surfaces coated with adhesion molecules (Fig. 4d).

Another set of experiments concerned one-cell derived neural stem cells (NE-4C or GFP-4C). These cells readily attached to all surfaces within 24 h, including bare pentacene (Fig. 5a) and poly-L-lysine or laminin coated pentacene (Figs. 5b, c). In the fluorescence microscopy images shown in Figure 5a–c the typical morphology of viable stem cells can be recognized. The AFM image displayed in Figure 5d shows the morphology of a fixed stem cell after five days of culture. The morphology of the cell is well retained. AFM imaging was performed in air after fixation of the cells with 4% paraformaldehyde (PFA) solution.

While growing on pentacene thin-films neural stem cells maintained their potential to differentiate into neurons,<sup>[12]</sup> in response to treatment with retinoic acid (RA). At the beginning of the second week post-induction, morphologically mature neurons were formed (Figs. 6b, 6d, 6f), which developed a dense network of neuronal processes (Fig. 6f) on bare (Figs. 6a, 6b) or laminin coated pentacene (Figs. 6c–f). Beneath the neurons some flat, substrate-attached, non-neuronal cells were observed (Figs. 6a, 6c, 6e), many of them displaying glial fibrillary acidic protein (GFAP) immunoreactivity (data not reported).

However, this non-neuronal, substrate-covering cell layer did not accompany all neuronal processes (Fig. 7) which indicates that after one week in culture neuronal processes can attach to the pentacene surface without the support of

non-neuronal cells. AFM images (Fig. 7) clearly resolve a number of individual processes that are not surrounded by additional cellular or molecular adhesion layers; instead they grew on the bare pentacene surface. Such evidence shows the possibility to realize an intimate contact between the membranes of axons and dendrites and the charge transport layer of the organic semiconductor. This is an important requirement for achieving the transduction of the action potential.

### 3. Discussion

Our data shows unambiguously that stem cells can be grown and differentiated on pentacene thin-films without causing any apparent damage to the structure and morphology of the organic semiconductor layer. We did not observe substantial difference in the growth and differentiation of primary neurons or embryonic neuronal stem cells. Pentacene surfaces coated with an additional layer of adhesive macromolecules (i.e., laminin or poly-L-lysine) provided good adhesive support for freshly isolated brain cells. Moreover, pentacene did not

prevent the cells from supplying their own environment. After one week in culture the bare pentacene surface had been converted into a good adhesive surface and was able to provide support for the migration of neural cells and the outgrowth of neuronal processes. This implies that adhesion molecules secreted by the cells themselves were adsorbed onto the pentacene layer surface in functional conformations.

Non-differentiated embryonic neural NE-4C stem cells adhere to bare pentacene as well as to surfaces coated with adhesion proteins. With the advancement of RA induced neuron formation, the cell-deposited material generated a suitable substrate for the migration of neuronal precursors and the elongation of neuronal processes.

There may be two reasons why pentacene films appear to be suitable substrates for cell growth: Firstly, the pentacene surface is anisotropic with the terrace edges exposing the  $\pi$ -systems of the pentacene molecules hence being less hydrophobic than the basal *ab* plane of pentacene (the water contact angle in our pentacene films is 88–89°). And while the *ab* plane exhibits competing interactions with either hydrophilic or amphiphilic species, the terrace edges provide convenient loci for adsorption, nucleation, and pinning of hydrophilic groups. The second important feature of pentacene is its compact molecular assembly, which is accompanied by a large packing energy (about 1–1.6 eV per pentacene molecule),<sup>[20,21]</sup> within the ordered molecular layers. This renders a potentially cytotoxic, conjugated molecule such as pentacene practically insoluble in both water and medium as well as in the cell membrane since the extraction of pentacene molecules from the film would require an excessive amount of energy.

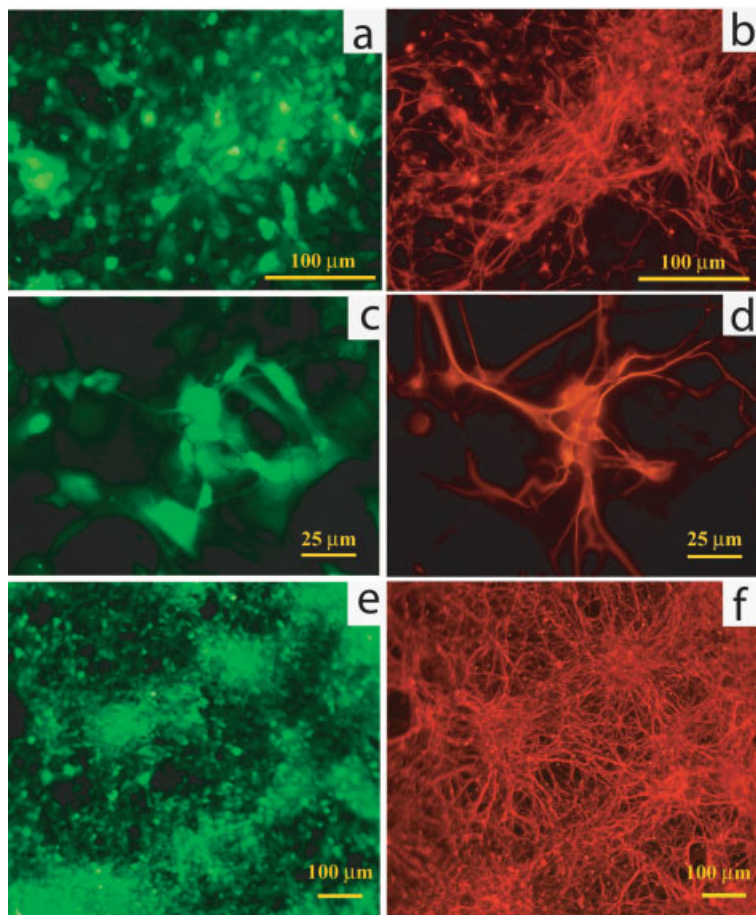


**Figure 6.** GFP-4C neural stem cells differentiated into neurons and formed dense neuronal networks on pentacene surfaces 8 days post-induction with all-trans retinoic acid. a, c, e) The visualization of GFP-4C cells by GFP fluorescence reveals a number of surface-attached, non-neuronal cells as well. b, d, f) Neurons were identified by neuron-specific III $\beta$ -tubulin. Pictures in the same row were taken from the same microscopic field. Bare pentacene surfaces were used for a) and b) and laminin-coated pentacene surfaces for c-e). Pentacene films were grown on SiO<sub>2</sub>/Si wafers.

This suggests that other conjugated semiconductors – be they either molecular (e.g. sexithiophene, results not shown) or polymeric – may be also be suitable functional substrates for cell growth.

We estimated that with regard to the pentacene packing energy and the adsorption energy on silicon oxide the energy required to displace a single pentacene molecule or pentacene aggregate out of plane has to exceed 0.5 GPa or 0.3 MPa, respectively. This is about three orders of magnitude larger than the force per unit area exerted by neurons according to Discher et al.<sup>[22]</sup> We are therefore confident of the fact that neurons will not disrupt the pentacene layer under normal culture conditions. In order to study the substrate beneath cultured cells we imaged different areas of a pentacene film by AFM after the detachment of viable, 80–90% confluent neuroblastoma cells (from a cloned line; see Fig. SI-1b in Supplementary Information). The morphology of the pentacene film was unaltered and the film retained its continuity, although, compared to Figure 1, some additional deposited material was left behind on the pentacene surface after the removal of the cells.

One important point to be carefully analyzed in future experiments though, is whether the neuron-pentacene hybrid system still survives upon device operation. Our data on the sensitivity of pentacene to water either in a controlled relative humidity (RH) atmosphere or under water, shows that the pentacene transistors survive the exposure to water, although their characteristics degrade substantially. The deposition of an ultra-thin capping layer (e.g., Megaohm seal) separating pentacene from the aqueous environment or the control of the morphology of the upper pentacene layers, or the use of a microfluidics system that confines the solution into the FET channel may effectively avoid the fast degradation of the FET characteristics in the presence of water. This concept is currently under investigation.

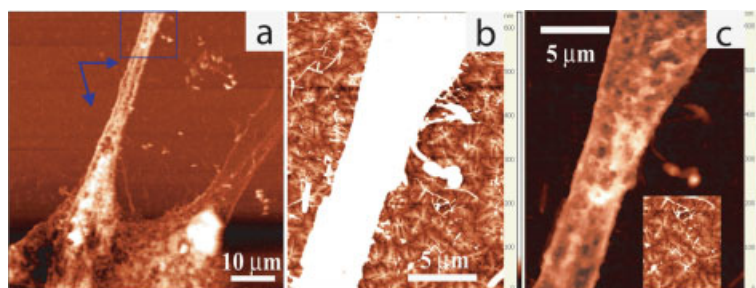


**Figure 7.** a) AFM image of a differentiated NE-4C-derived neuron (arrows). b) The magnified image shows that the morphology of the pentacene thin-film is neither damaged nor modified by the interactions with the cell. c) Same image as (b), with a different height scale to highlight the axon morphology. Inset shows the unaltered pentacene film from (b). The change in height scale highlights the axons.

#### 4. Conclusions

We showed the possibility to integrate living neural cells and organic semiconductor thin-films made of a few monolayers of pentacene. Stem cells remain viable, differentiate, and form dense neuronal networks. These results are promising for the development of electronic transducers based on organic field-effect transistors with ultra-thin-films, which may be used for real-time monitoring of biological activities at the level of interconnected living cells. This would have an enormous potential in replacing highly invasive interventions or probes.

It also provides a prospect for further developments in the monitoring and sensing of biological reactions as well as controlled drug delivery through digital logic feedback which is consistent with the quest for new tools for loco-regional therapies.

## 5. Experimental

Pentacene thin films were grown in two different high vacuum chambers (Bologna and Munich) via sublimation from a Knudsen cell. One batch of thin-films was grown on silicon oxide substrates as it is typically the case for field-effect transistors. The nominal thickness of these films according to the microbalance (Inficon XTC/2) was 10–12 nm, the deposition temperature 25 °C and the deposition rate 0.2–3 Å · s<sup>-1</sup>, while the baseline vacuum was 10<sup>-7</sup>–10<sup>-8</sup> mbar. Field-effect transistors made with these films typically exhibited a charge mobility equal to 10<sup>-1</sup>–10<sup>-2</sup> cm<sup>2</sup> · V<sup>-1</sup> · s<sup>-1</sup> in vacuum and air, respectively. A second batch of pentacene thin-films was grown directly onto glass coverslips for daily control of cell growth. These films had the same specifications as mentioned above and exhibited a very similar morphology.

Pentacene films on silicon were imaged by atomic force microscopy (AFM) in contact mode in air and in water. Silicon NT-MDT cantilevers of the NSG10 and CSG10 series were used throughout the experiments. The set point force in contact mode was a few nN. Diffraction experiments were carried out on films deposited onto glass with a microfluidics device placed on top of the pentacene film to create a stable water/pentacene interface. This assembly was placed on the diffractometer stage of beamline D4 at HASYLAB (DESY, Hamburg, Germany). Parameters, geometry, measurement setup, and slit settings are described elsewhere [13].

Freshly isolated (primary) embryonic forebrain neurons or NE-4C immortalized neural stem cells [14], were seeded onto pentacene-coated silicon wafers or pentacene-coated coverslips in 24-well tissue culture plates (Greiner Bio-One GmbH) at a density of 1–5 × 10<sup>5</sup> cells · cm<sup>-2</sup>. Primary brain cells, which were isolated from wild-type mice, and non-labelled NE-4C cells were cultivated on transparent coverslips, while cells expressing green fluorescent protein (GFP) were cultured on non-transparent silicon wafers. GFP-expressing primary cells were obtained from transgenic mouse embryos carrying a CAMII kinase promoter-driven GFP construct (kindly donated by G. Szabo, IEM-HAS, Budapest). The GFP-expressing NE-4C sub-clone (GFP-4C) was established by transfecting NE-4C clones with a CMV promoter driven GFP construct.<sup>[15]</sup> Pentacene samples were either used as obtained or coated with additional monolayers of laminin (Sigma L2020) or poly-L-lysine (Sigma P1591). Cells were seeded in Minimum Essential Medium Eagle (MEM, Sigma M2279) supplemented with 4 mM L-glutamine and 5% fetal calf serum (FCS, Bovimex). After 24 hours, the serum-containing medium was changed to serum-free Neurobasal<sup>TM</sup> medium (Invitrogen) supplemented with B-27 and N-2. After this initial medium change, half of the medium was replaced with fresh medium twice a week.

NE-4C and GFP-4C cells were induced to differentiate by treatment with 10<sup>-6</sup> M all-trans retinoic acid for 48 h and were maintained in defined medium for 7–12 days. The schedule for neuron formation [16,17], was observed by phase-contrast or fluorescence microscopy of living cultures using a Nikon Eclipse 200 microscope.

Neurons were identified by immuno-cytochemical staining of fixed and permeabilized (0.05% Triton X-100, 5 min) cultures with anti-IIIβ-tubulin primary and Alexa Fluor 594-conjugated anti-mouse secondary antibodies. Immunofluorescence was evaluated using a Zeiss Axiovert 200M microscope equipped with an ApoTome system and AxioVision 4 program.

An inverted epifluorescence microscope attached to an optical stereomicroscope Olympus IX71 with SPM Biosolver (NTM-DT) was used to image all cells (blue filter U-MNB2, excitation at 470–490 nm) and neurons (green filter U-MWG2, excitation at 510–550 nm) simultaneously.

Received: November 11, 2007

Revised: March 13, 2008

Published online: June 12, 2008

- [1] W. G. Gross, B. K. Rhoades, H. M. E. Azzazy, M. Wu, *Biosens. Bioelectron.* **1995**, *10*, 553.
- [2] M. C. Kiernan, M. D. Baker, H. Bostock, *Neuroscience* **2003**, *119*, 653.
- [3] A. Offenhausser, W. Knoll, *Trends Biotechnol.* **2001**, *19*, 62.
- [4] F. Patolsky, B. P. Timko, G. Yu, Y. Fang, A. B. Greytak, G. Zheng, C. M. Lieber, *Science* **2006**, *313*, 1100.
- [5] a) V. Lovat, D. Panzarotto, L. Lagostena, B. Cacciari, M. Grandolfo, M. Righi, G. Spalluto, M. Prato, L. Ballerini, *Nano Lett.* **2005**, *5*, 1107; b) A. Mazzatenta, M. Giugliano, S. Campidelli, L. Gambazzi, L. Businaro, H. Markram, M. Prato, L. Ballerini, *J. Neurosci.* **2007**, *27*, 6931.
- [6] F. Biscarini, P. Samori, O. Greco, R. Zamboni, *Phys. Rev. Lett.* **1997**, *78*, 2389.
- [7] F. Dinelli, M. Murgia, J. F. Moulin, M. Cavallini, P. Levy, F. Biscarini, D. M. de Leeuw, *Phys. Rev. Lett.* **2004**, *92*, 116802.
- [8] D. Braun, P. Fromherz, *Appl. Phys. A* **1997**, *65*, 341.
- [9] D. Braun, P. Fromherz, *Phys. Rev. Lett.* **1998**, *81*, 5241.
- [10] M. R. Horton, C. Reich, A. P. Gast, J. O. Rädler, B. Nickel, *Langmuir* **2007**, *23*, 6263.
- [11] P. L. H. M. Cobben, R. J. M. Egberink, J. G. Bomer, P. Bergveld, W. Verboom, D. N. Reinhoudt, *J. Am. Chem. Soc.* **1992**, *114*, 10573.
- [12] D. Knipp, R. A. Street, A. Volkel, J. Ho, *J. Appl. Phys.* **2003**, *93*, 347.
- [13] C. Reich, M. Hochrein, B. Krause, B. Nickel, *Rev. Sci. Instrum.* **2005**, *76*, 095103.
- [14] K. Schlett, E. Madarász, *J. Neurosci. Res.* **1997**, *47*, 405.
- [15] K. Demeter, B. Herberth, E. Duda, E. Kúsz, T. Jaffredo, J. P. Herman, E. Madarász, *Exp. Neurol.* **2004**, *188*, 254.
- [16] a) M. Jelitai, K. Schlett, P. Varju, U. Eisel, E. Madarász, *J. Neurobiol.* **2002**, *51*, 54. b) K. Tárnok, Á. Pataki, J. Kovács, K. Schlett, E. Madarász, *Eur. J. Cell. Biol.* **2002**, *81*, 403.
- [17] M. Jelitai, M. Anderova, A. Chvatal, E. Madarász, *J. Neurosci. Res.* **2007**, *85*, 1606.
- [18] S. Schiefer, M. Huth, A. Dobrinevski, B. Nickel, *J. Am. Chem. Soc.* **2007**, *129*, 10316.
- [19] D. J. Gundlach, T. N. Jackson, D. G. Schlom, S. F. Nelson, *Appl. Phys. Lett.* **1999**, *74*, 3302.
- [20] N. Wakayama, H. Inokuchi, *Bull. Chem. Soc. Jap.* **1967**, *40*, 2267.
- [21] E. Northrup, M. L. Tiago, S. G. Louie, *Phys. Rev. B.* **2002**, *66*, 121.
- [22] D. E. Discher, P. A. Janmey, Y.-L. Wang, *Science* **2005**, *310*, 1139.



## A.5 Full text of Ref. [5]

Bert Nickel, Matthias Fiebig, Stefan Schiefer, Martin Göllner, Martin Huth, Christoph Erlen, and Paolo Lugli

*Pentacene devices: Molecular structure, charge transport and photo response*

phys. stat. sol. (a) **205**, No. 3, 526-533 (2008) / DOI 10.1002 / pssa.200723372

### **Abstract:**

In this feature article, we will discuss to which extent the peculiar growth properties of pentacene on metallic contacts and on gate dielectrics contribute to the device performance of organic thin film transistors. The early growth state of pentacene monolayers is reviewed, as well as the molecular structure of the so called thin film phase. Then, the relation of structural defect densities to trap densities is discussed. The spatially resolved photo response of a pentacene transistor will be presented in the context of injection barriers and contact homogeneity.

Permanent weblink:

<http://www3.interscience.wiley.com/cgi-bin/fulltext/117916611/PDFSTART>

MH contribution:

- involved in electronic and structural experiments.
- participation in discussions.

# Pentacene devices: Molecular structure, charge transport and photo response

## Feature Article

Bert Nickel<sup>1</sup>, Matthias Fiebig<sup>1</sup>, Stefan Schiefer<sup>1</sup>, Martin Göllner<sup>1</sup>, Martin Huth<sup>1</sup>, Christoph Erlen<sup>2</sup>, and Paolo Lugli<sup>2</sup>

<sup>1</sup> Ludwig-Maximilians-Universität, Department für Physik and CeNS, Geschwister-Scholl-Platz 1, 80539 München, Germany

<sup>2</sup> Technische Universität München, Institut für Nanoelectronics, Arcisstraße 21, 80333 München, Germany

Received 14 August 2007, revised 15 November 2007, accepted 23 November 2007

Published online 25 February 2008

PACS 68.35.-p, 68.55.-a, 73.40.Cg, 73.50.Gr, 81.05.Lg, 85.30.Tv

\* Corresponding author: e-mail nickel@lmu.de, Phone: +49(0)8921801460, Fax: +49(0)8921803182

In this feature article, we will discuss to which extend the peculiar growth properties of pentacene on metallic contacts and on gate dielectrics contribute to the device performance of organic thin film transistors. The early growth state of pentacene monolayers is reviewed, as well as the molecular struc-

ture of the so called thin film phase. Then, the relation of structural defect densities to trap densities is discussed. The spatially resolved photo response of a pentacene transistor will be presented in the context of injection barriers and contact homogeneity.

© 2008 WILEY-VCH Verlag GmbH & Co. KGaA, Weinheim

**1 Introduction** Today, the field of organic electronics is wide open [1, 2]. While organic light emitting diodes (OLEDs) have already successfully entered the market, the roadmap for integrated circuits is still not settled. Mobilities  $\mu$  for pentacene organic thin film transistors (OTFTs) commonly ranging between 0.1 cm/V s and 1 cm/V s have been reproduced by many groups world wide [3–6]. In spite of the enormous activities in synthesizing and screening for new materials for transistor applications, pentacene has successfully defended its leading position for the production of OTFTs.

The reason for pentacene being superior for the production of TFT devices [7, 8] when compared to other molecules [9] is still not obvious. In this feature article, we will discuss to which extend the peculiar growth properties [10] of pentacene on metallic contacts and gate dielectrics contribute to the device performance. For this purpose, first the early growth state of pentacene films and the molecular structure of the so called thin film phase is reviewed. Then, major sources of crystal defects in thin films as determined by advanced synchrotron diffraction techniques are discussed. The relation of these defects to the frequently discussed electronic traps that strongly influence transport properties of TFTs [6, 11, 12] is indicated.

Finally, the spatially resolved photo response of pentacene OTFTs will be discussed in the context of injection barriers and contact homogeneity.

## 2 Pentacene thin films

**2.1 Film formation on inert surfaces** Pentacene can be evaporated quite conveniently by resistive heating of a tantalum crucible filled with purified pentacene powder. This procedure is ultra high vacuum compatible and a molecular beam with typical deposition rates ranging from below 0.01 nm/s up to 1 nm/s can be easily achieved [13], as verified by a quartz micro balance at the sample position. Also alternative methods such as laser evaporation have been reported [14]. Growth temperatures typically range from room temperature up to 50 °C. At higher temperatures, a much higher deposition rate is needed to compensate for desorption. Thus, with MBE techniques, the maximum growth temperature is limited to about 75 °C. A typical example for a pentacene film grown on a thermal oxide with Au bottom contacts is shown in Fig. 1a. If substrate and growth conditions are properly chosen, a continuous film forms on SiO<sub>2</sub> (Fig. 1a) with grains of the order of several microns which exhibit step heights comparable to the length of the pentacene molecule (Fig. 1b). On

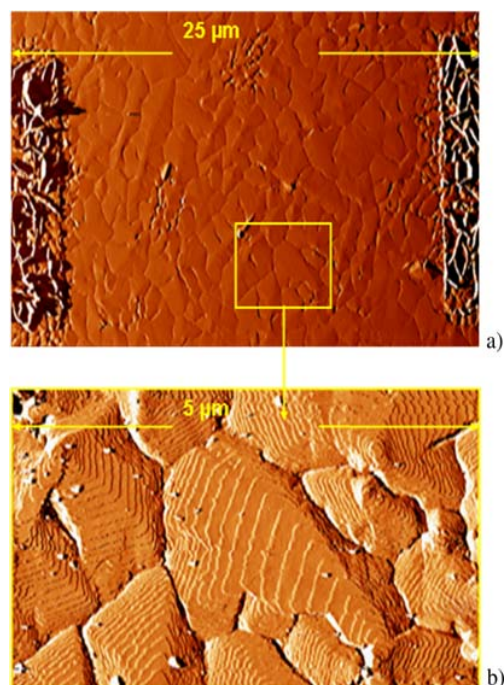


**Figure 1** (online colour at: [www.pss-a.com](http://www.pss-a.com)) AFM amplitude micrograph of a pentacene OTFT structure. (a) Gold contacts on  $\text{SiO}_2$  have been covered by a 50 nm pentacene film. (b) A zoom reveals a grainy structure and terraces with step heights of ca. 15.4 Å.

the gold contacts, the film morphology is much more rugged (Fig. 1a). The reason for the profound difference in growth behavior on  $\text{SiO}_2$  and Au is discussed below.

The initial stage of pentacene thin film growth on  $\text{SiO}_2$  can be described by diffusion limited aggregation (DLA) [15]. In this growth mode, incoming molecules initially diffuse across the surface. Once they meet a critical number of molecules, they form a stable nuclei, which subsequently grows in area during deposition. The submonolayer islands stemming from the growth of such nuclei exhibit a fractal shape, which is the fingerprint of this growth mode. Pentacene submonolayers grown on bare Si surfaces show such fractal shapes, as revealed first by in-situ photo electron emission microscopy experiments [16]. Subsequent AFM studies have shown that the diffusion length on silicon oxide is significantly reduced [17] compared to e.g. H-terminated Si. A detailed analysis of the island size and island density as a function of coverage by AFM and synchrotron experiments fully confirmed scaling predictions of the DLA theory [18, 19] and allowed to determine the stable nuclei size to four pentacene molecules [20]. If the growth temperature is lowered to 0 °C, the diffusion length is reduced by a factor  $\sim 4$  [20].

Pentacene submonolayer islands exhibit a layer thickness of 15.4 Å which has been measured by AFM and by X-ray reflectometry [17]. This layer thickness implies that the molecules are oriented in an upright configuration, i.e.

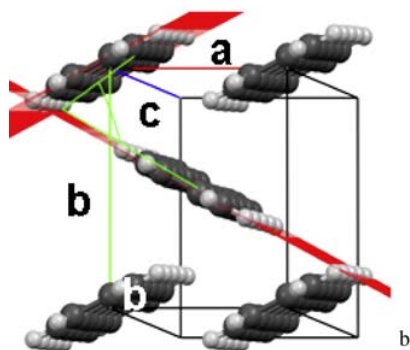
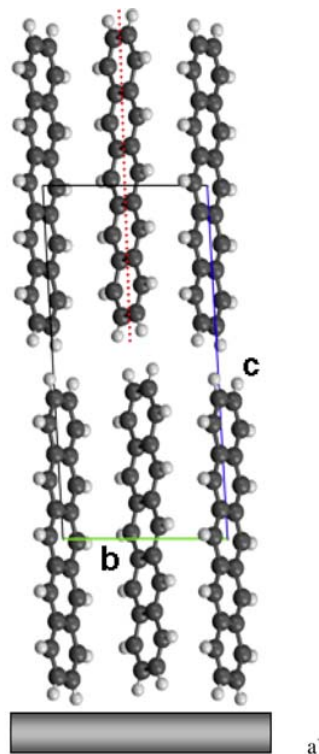


**Figure 2** (online colour at: [www.pss-a.com](http://www.pss-a.com)) Thin film phase unit cell. (a) The side view illustrates the layered structure of the thin film phase. (b) The top view emphasizes the herringbone ordering motive, which is a common feature of all pentacene polymorphs.

the long molecular axis is oriented predominantly along the surface normal, see Fig. 2a. Multilayer films exhibit different crystalline phases, which are usually identified by their  $d_{001}$  spacing along the surface normal. The substrate-induced  $d_{001} = 15.4$  Å polymorph, which is commonly termed *thin film phase*, is the most relevant for OTFT applications. Grazing incidence in plane diffraction experiments [21, 22] confirmed that the grains of the thin film phase are (001) oriented. The lateral dimension of the two dimensional unit cell inferred from these experiments, as well as the observed selection rules, suggest a unit cell

with two non-equivalent molecules in a Herringbone arrangement, similar to the bulk pentacene ordering motive [23, 24].

In a recent study, the detailed molecular arrangement of the *thin film phase* was resolved by a grazing incidence truncation rod scattering study [25]. The crystal structure was found to be triclinic [26] with the following unit cell parameters:  $a = 5.958 \pm 0.005 \text{ \AA}$ ,  $b = 7.596 \pm 0.008 \text{ \AA}$ ,  $c = 15.61 \pm 0.01 \text{ \AA}$ ,  $\alpha = 81.25 \pm 0.04^\circ$ ,  $\beta = 86.56 \pm 0.04^\circ$  and  $\gamma = 89.80 \pm 0.10^\circ$  [27]. A detailed analysis of the Bragg peak intensities for pentacene on  $\text{SiO}_2$  allowed to determine the tilt between the long molecular axis of the two unit cell molecules and the surface normal to  $5.6 \pm 0.05^\circ$  and  $6.0 \pm 0.4^\circ$  and the Herringbone angle to  $54.3 \pm 1.3^\circ$  [27]. The unit cell is shown in Fig. 2b). Here, the unit cell vectors  $\mathbf{a}$  (red),  $\mathbf{b}$  (green) and  $\mathbf{c}$  (blue) are color coded. The Herringbone angle (green arc) is defined as the intersection angle between molecular planes (red planes). In one case, also a molecular axis (red dotted line) is indicated.

Surface energy calculations [28] reveal that the (001) cleaving plane is the surface with the lowest surface energy. In turn, the formation of (001) oriented films can be expected, if the interaction of the pentacene molecules with the surface is negligible to the pentacene–pentacene interaction. Experiments show that this condition apparently fulfilled for various inert substrates such as reduced and oxidized Si, as well as many polymeric films used as gate dielectric. Note that the surface energy of the *thin film phase* is rather isotropic within the pentacene film plane [28], probably a direct result of the large herringbone angle. In turn, pentacene islands show on  $\text{SiO}_2$  a rather isotropic shape, thus favoring the formation of closed films up to several monolayers [16, 29]. Beyond this thickness, strong roughening occurs [30] and competing phases start nucleating [31].

**2.2 Film formation on metallic and conductive surfaces** Bottom contact TFTs involve either metallic or conducting polymer contacts. Therefore, the growth of pentacene on metallic surfaces has also been studied in detail [32–35]. The most commonly used contact material for pentacene TFTs is Au, whose work function value  $\phi = 5.1 \text{ eV}$  [36] matches quite well with the ionization energy of pentacene  $\chi = 4.9 \text{ eV}$  [37]. Also, being a noble metal, Au contacts are sometimes considered insensitive to air exposure even if it has been observed that the Au work function is quite sensitive to ambient conditions. The observed growth behavior for pentacene on Au depends strongly on the substrate, i.e. different growth is observed for single Au crystal surfaces [32] and for thin Au film composed out of polycrystalline grains [33]. Also the roughness and cleaning procedure influence the growth. For the technically most relevant polycrystalline Au film surfaces, pentacene shows a complex growth behavior. If a Au(111) texture is present, a flat lying monolayer forms, which can be interpreted as a wetting layer. This layer then

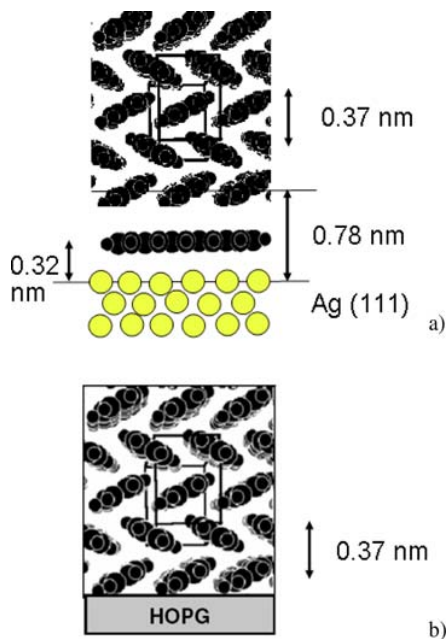


**Figure 3** (online colour at: [www.pss-a.com](http://www.pss-a.com)) Pentacene growth on Ag and graphite. (a) Side view of the film structure of pentacene on Ag(111). A flat lying pentacene monolayer acts as a growth template. (b) Side view of the growth of pentacene on graphite. The structure resembles the growth on Ag, but it is not clear whether a pentacene wetting layer is present.

acts as a growth template for subsequently deposited pentacene forming microscopic grains. For these grains, the long molecular axis is oriented along the surface (*lying down phase*). Elevated temperatures promote a pronounced dewetting [34]. This behavior is not unexpected, since the surface energy of a *lying down phase* is higher than the surface energy of the *thin film phase* [28] and thus dewetting is a direct result of the minimization of the film surface area. Thus, surface diffusion is counter-productive for the formation of closed films and the formation of well ordered closed films seems quite impossible. To resolve this problem, two strategies have been pursued. One approach, which has been demonstrated for single crystal Ag(111) surfaces makes use of cryogenic substrate temperatures to suppress dewetting. In this case, the pentacene molecules are deposited making use of a hyperthermal He-beam [38] which provides the impinging pentacene molecules with energies up to 5 eV, well above thermal energies. Thus, a well ordered film can form at 200 K [35] (see Fig. 3a).

Another way to avoid dewetting is to passivate the metallic surface by a self assembled monolayer (SAM), e.g. an alkane thiol monolayer (C-18). After passivation, the growth structure resembles the growth mode on inert surfaces [33], the same holds for growth of pentacene on conducting polymers such as PEDOT: PSS [poly(3,4-ethylenedioxythiophene)/poly(styrenesulfonate)] [39]. It is interesting to note that on bare Si, pentacene initially forms a flat lying monolayer, but on-top of this monolayer, the

thin film phase readily forms [16] without need for passivation.

Other more exotic materials which have been studied include graphite and Bi. Graphite is an interesting substrate since it also promotes the formation of a *lying down phase* with Herringbone order textured in the (200) orientation [40] (see Fig. 3b). This enabled an angular resolved photoelectron emission study (APES) for this pentacene polymorph along the (200) direction of the Brillouin zone. The experiments reveal indications of strong band dispersion [40]. Recently, a well defined epitaxial relationship between a pentacene film and the Bi substrate has been realized. This well defined epitaxial relationship allowed to explore the band dispersion of different crystallographic directions of the Brillouin zone of pentacene by APES, also revealing a pronounced band dispersion [41].

**2.3 Mixed films** For some applications such as organic photovoltaic devices or ambipolar transistors, a co-deposition of hole and electron conducting materials is needed, e.g. pentacene and C60. This gives rise to a whole zoo of possible growth scenarios, depending on how the different materials mix. For the co-deposition of pentacene and 6,13-pentacenequinone (an oxidized state of pentacene) a pronounced phase separation is observed, depending on deposition rates [42]. At the same time, the formation of the pentacene bulk phase is suppressed in mixed film.

### 3 Pentacene OTFT properties

**3.1 Mobility and charge carrier density** The most simple pentacene OTFT test structure used in many labs is based on a Si wafer piece covered with a thermal oxide. Here, the heavily doped Si wafer takes the role of the back gate electrode, and the SiO<sub>2</sub> takes the role of the gate dielectric. A pentacene thin film is deposited as the semiconducting layer. Source and drain electrodes are deposited either on the silicon oxide (bottom contact) or on top of the pentacene film (top contact).

A pentacene TFT works in hole accumulation, i.e. a sufficiently negative voltage ( $V_G$ ) is applied to the gate, accumulating holes at the pentacene/SiO<sub>2</sub> interface. If now a moderate voltage is applied between the source and drain electrode, a hole current flows. A characteristic output curve for a typical pentacene TFT from our lab is shown in Fig. 4a. Here, as a substrate, heavily n-doped Si-wafers with a 150 nm thick thermal SiO<sub>2</sub> layer on top of it were used. Additionally, a very thin layer of polyesterene (ca. 2–3 nm) was spin cast on top of the silicon oxide layer. A shadow mask was used to define 50 nm thick source and drain Au contacts that were evaporated in vacuum. Finally a 50 nm pentacene layer was evaporated at room temperature at a deposition rate of about 1 nm/min in a separate evaporation chamber, also using a shadow mask. This way, transistor channels with a length of  $L = 25 \mu\text{m}$  and a width of  $W = 1000 \mu\text{m}$  were obtained, cf. schematic in Fig. 4. The output curve of this device shows a linear increase of the

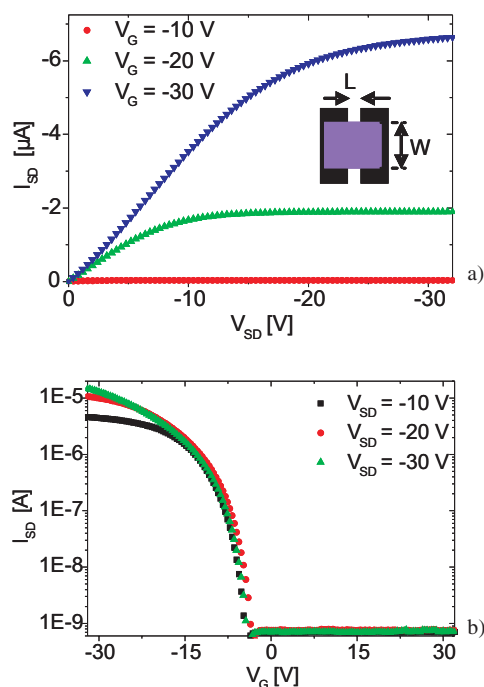


**Figure 4** (online colour at: www.pss-a.com) Characteristics of a bottom contact pentacene OTFT. Channel geometry:  $L = 25 \mu\text{m}$ ,  $W = 1000 \mu\text{m}$  (see text and inset). Sweep rate: 0.4 V/s, the measurement was performed in vacuum. (a) Output characteristics ( $I_{SD}$  vs.  $V_{SD}$ ,  $V_G$  as indicated in the inset) and (b) transfer characteristics ( $I_{SD}$  vs.  $V_G$  in log. scale,  $V_{SD}$  as indicated in the inset).

drain current for small drain voltages, and subsequently saturation occurs. The transfer characteristics of this device are shown in Fig. 4b. The logarithmic scale reveals a sharp onset of the transistor activity and a subthreshold swing  $S = V_G / \log(I_{SD}) = 1.1 \text{ V per decade}$ .

Pentacene OTFT curves are usually analyzed within MOSFET theory [43]. For the geometry of the device used in Fig. 4, which has a channel width  $W = 1000 \mu\text{m}$  and a channel length  $L = 25 \mu\text{m}$ , the source-drain current ( $I_{SD}$ ) in the linear regime ( $V_{SD} \ll V_G - V_T$ ) can be written as:

$$I_{SD}^{\text{lin}} = W/L \cdot \mu^{\text{lin}} \cdot C_i \cdot (V_G - V_T) \cdot V_{SD} \quad (1)$$

Here, the graded channel approximation has been used.  $C_i$  is the capacitance per unit area of the dielectric and  $V_T$  is the threshold voltage.  $\mu^{\text{lin}}$  is the mobility in the linear regime. The respective measurements are shown in Fig. 5a.

For the saturation regime ( $V_{SD} \gg V_G - V_T$ ) the accumulation within the channel is incomplete. This so called *pinch off* arises due to the superposition of the gate and drain potential. The source–drain current ( $I_{SD}$ ) in the saturation regime reads:

$$I_{SD}^{\text{sat}} = W/(2L) \cdot \mu^{\text{sat}} \cdot C_i \cdot (V_G - V_T)^2 \quad (2)$$

The respective measurements are shown in Fig. 5b. The mobility in the saturated regime ( $\mu^{\text{sat}}$ ) can be read off from the slope of the output curve (straight lines in Fig. 5b,

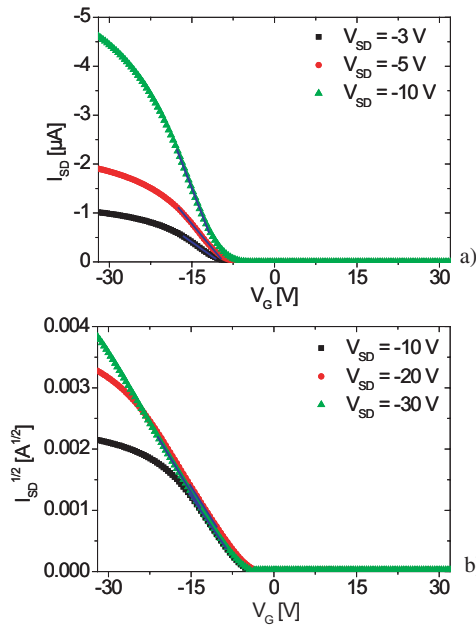


**Figure 5** (online colour at: www.pss-a.com) Transfer characteristics. (a) Linear regime ( $I_{SD}$  vs.  $V_G$ ), the straight lines indicate the slope determining  $\mu^{lin}$  according to Eq. (1). (b) Saturated regime ( $\sqrt{I_{SD}}$  vs.  $V_G$ ), the straight lines indicate the slope determining  $\mu^{sat}$  according to Eq. (2). Same device as in Fig. 4.

square root scale at  $y$ -axis) using Eq. (2). We obtain  $\mu^{sat} = 0.06 \text{ cm}^2/(\text{V s})$ , which compares reasonably well to typical values for the bottom contact geometry ( $\mu \approx 0.1 - 0.3 \text{ cm}^2/(\text{V s})$ ). The mobility in the linear regime ( $\mu^{lin}$ ) can be read off from the slope of the output curve (Fig. 5a, linear scale at  $y$ -axis) using Eq. (1). We obtain  $\mu^{lin} = 0.04 \text{ cm}^2/(\text{V s})$ , which is slightly reduced compared to  $\mu^{sat} = 0.06 \text{ cm}^2/(\text{V s})$ , indicating some non-ideal behavior.

The most important physical parameter of an OTFT beyond the mobility  $\mu$  is the number of charge carriers ( $n_h$ ) induced by a given gate voltage ( $V_G$ ).  $n_h$  can be estimated from the measured channel conductivity  $\sigma$  by

$$n_h \cdot q \cdot \mu = \sigma/d = L/(W \cdot R). \quad (3)$$

Here,  $d$  is the active channel thickness (1–2 molecular layers) and  $q$  is the elementary charge of a hole. For the transistor used in Fig. 4, we measure  $R = 2.8 \times 10^6 \Omega$  at  $V_G = -30 \text{ V}$  and  $V_{SD} = -10 \text{ V}$ . In turn, according to Eq. (3), the hole carrier density at this set point is  $n_h = 0.9 \times 10^{12} \text{ cm}^{-2}$ .

**3.2 Influence of trap states and fixed interface charges** An example for the dynamic behavior of a pentacene OTFT is shown in Fig. 6a. Here, the gate voltage ( $V_G$ ) is first swept from positive to negative voltages (sweep rate

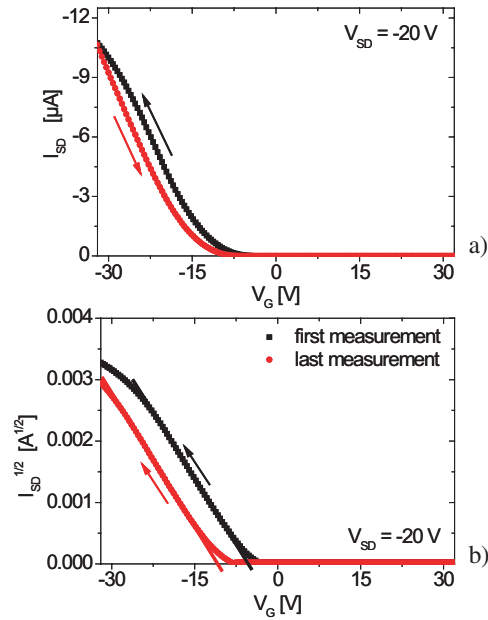


**Figure 6** (online colour at: www.pss-a.com) Hysteresis effects and voltage drifts in the transfer characteristics. Sweep rate is  $0.4 \text{ V/s}$ , same device as in Fig. 4. (a) A gate sweep from positive to negative voltages (black data points), and back (red data points) for the same fixed value of the drain voltage ( $V_{SD} = -20 \text{ V}$ ) reveals a hysteresis effect. (b) After a couple of measurements (one hour later), a rather stable shift of the transfer curve due to fixed charges is established for the same device.

$= 0.4 \text{ V/s}$ , black data points in Fig. 6a), and then immediately from negative to positive voltages (red data points in Fig. 6a) for the same fixed value of the drain voltage ( $V_{SD} = -20 \text{ V}$ ). A pronounced hysteresis is observed. This hysteresis can be interpreted as an apparent shift of the threshold voltage ( $\Delta V_T$ ) induced by a charging  $Q_t$  of the pentacene/SiO<sub>2</sub> interface due to filling and emptying of trap states. The number of trap states can be estimated by

$$n_t = Q_t/q = \Delta V \cdot C_i/q. \quad (4)$$

The observed threshold shift of  $\Delta V_T = 2.0 \text{ V}$  results in a trap density  $n_t = 2.4 \times 10^{11} \text{ traps/cm}^2$ . This number is not so small compared to the number of charge carriers  $n_h$ , indicating that traps largely influence the device performance. One may speculate whether structural defects within the pentacene film contribute to trap states. An X-ray analysis of the defect densities in pentacene films revealed defect densities in the order of  $n_t = 2 \times 10^{11} \text{ defects/cm}^2$  [44], in good agreement with the trap density  $n_t$  inferred from the electronic characterization. Thus, the observed structural defects apparently contribute to trap states. It is well known, that the hysteresis and thus the trap density depends on the nature of the gate dielectric surface. Especially hydroxyl groups are considered as potential trap

states, therefore a passivation of the gate oxide by either silylation [45] or polymer capping (here: polystyrene film) is needed to minimize trap densities.

A subsequent study of the pentacene TFT reveals also an irreversible drift of the transfer curve with operating time, cf. Fig. 6b. This drift can be interpreted as an interface charging due to deep trap levels, also termed fixed charges. The observed voltage shift of  $\Delta V = 6.5$  V implies a fixed charge density  $n_{\text{dt}} = 7.7 \times 10^{11} \text{ cm}^{-2}$ . Note that this density is already of the order of the charge carrier density  $n_{\text{h}}$ . In turn, voltage shifts in pentacene TFTs can completely redefine the working point of a transistor. For the application of such TFT devices in e.g. ring oscillators [46], one should find a way to control these drifts. Recent work suggests that controlled generation of fixed charges at the gate dielectric by UH-light exposure might be used to store electronically readable information in a pentacene TFT (one bit per transistor).

**3.3 Injection** The whole TFT performance is largely influenced by injection efficiencies. In particular surface contaminations such as remanent photo resist or organic adsorbates due to air or solvent exposure can modify the work function of the Au electrode up to a point, that charge injection is locally suppressed. The injection properties of two selected TFT devices from our lab are compared in Fig. 7. Both devices are operated at  $V_{\text{G}} = -30$  V. The output characteristics of the two devices show a pronounced difference for small drain voltage  $V_{\text{SD}}$ . While one device (so called *good device*, black data points in Fig. 7) shows an ohmic increase of  $I_{\text{SD}}$  as a function of  $V_{\text{SD}}$ , the other device shows a damped response (so called *bad device*, red data points in Fig. 7). Note that the amplitude of  $I_{\text{SD}}$  of the bad device has been rescaled for better comparison. Both devices are bottom contact TFTs of similar geometry, however, the preparation of the contacts was different. The contacts of the good device were fabricated using a shadow mask, while the contacts of the bad device were produced using optical lithography. Optical lithography involves

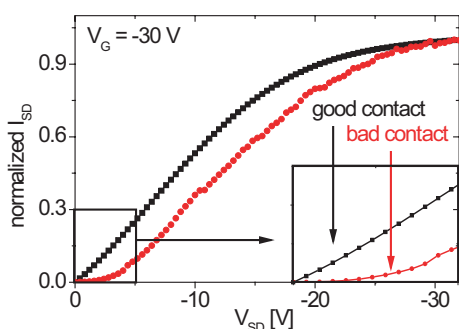


**Figure 7** (online colour at: [www.pss-a.com](http://www.pss-a.com)) Injection efficiencies of pentacene TFTs. Comparison of ohmic and non-ohmic behavior. The contacts of the so called *good device* were fabricated using shadow masks, and the contacts of the so called *bad device* were fabricated using optical lithography.

resist and use of solvents such as acetone, which apparently can lead to less efficient contact properties. The physical mechanism which gives rise to the non-ohmic behavior remains unclear at this level of analysis and thus using equivalent circuits [47] which take account of the observed deviations from ideal MOSFET behavior seem to be the most practical way to deal with these effects.

**4 Photoresponse** Pentacene shows a strong absorption in the visible (see Fig. 8), more optical properties of pentacene films can be found in [48]. If pentacene is combined with a proper n-conductor such as C60, it can be used as active region in a solar cell [49]. Transient photoconductivity experiments using optical pump terahertz probe techniques suggest that charge photo generation occurs in pentacene on a subpicosecond timescale [50].

Here, we employ photo generated electron–hole pairs to analyze local properties of a TFT device. For this purpose, we have adapted a laser scanning confocal microscope experiment to spatially resolve the photo response of a TFT. The experimental setup is shown schematically in Fig. 9a. The laser spot size on the TFT is less than  $1 \mu\text{m}$ . A  $x$ – $y$ – $z$  piezo-positioner stage [51] which is mounted on top of a  $x$ – $y$  translation stage is used to translate the sample with respect to the laser. The reflected beam allows to identify the contact and the channel region. The laser beam is modulated by a chopper, and the difference signal is extracted using a lock-in amplifier.

We observe a strong photo response localized at the anode [52]. The response is inhomogeneous along the contact indicating variations in the transport or injection properties of the device. These variations may be due to local variations of the contact work function, or due to bad physical contact of the pentacene grains adjacent to the electrode, or due to a local enhancement of defect densities in the pentacene film. Thus, a systematic study of the photo response in combination with the respective characteristic transistor curves allows visualizing problematic regions of an OTFT, which is a key prerequisite for device optimization.

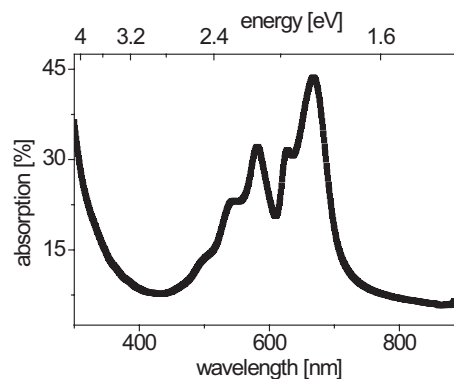


**Figure 8** Absorption spectra. Wavelength dependency of the absorption of a 50 nm pentacene thin film on glass.

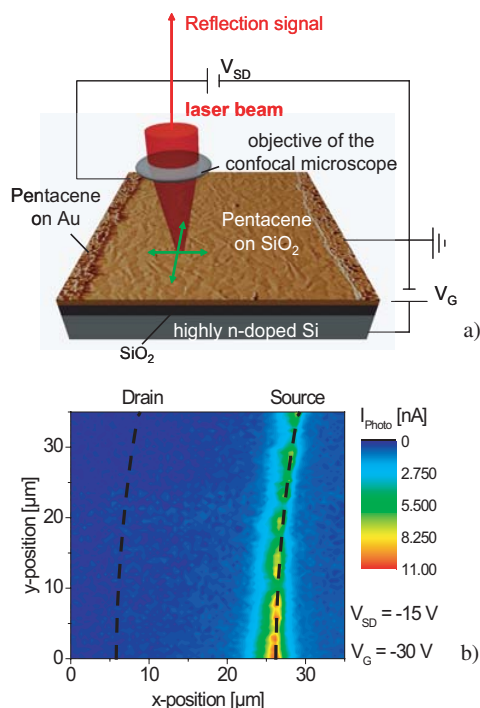


**Figure 9** (online colour at: [www.pss-a.com](http://www.pss-a.com)) Spatially resolved photo response experiment. (a) Schematic of the experimental setup for spatially resolved photo response measurements. (b) Spatially resolved photo response data in the linear regime ( $V_G = -30$  V and  $V_{SD} = -15$  V). A Corbino device structure has been used (disk and ring geometry,  $L = 20$   $\mu\text{m}$  [channel length],  $W = 1005$   $\mu\text{m}$  [channel width, i.e. circumference]). The photo response measurement covers a small fraction of the whole device.

**5 Outlook** Pentacene has all the qualities needed for an OTFT. The main challenge is the control of the contact and dielectric interfaces to suppress the voltage drifts and hysteresis effects associated with trap states. Also the dependency of the injection efficiencies on contact preparation suggest that even if pentacene deposition technology can be applied under rather rough conditions, ultra high vacuum and clean environments may still be useful on the way of learning how to produce reliable devices.

**Acknowledgements** BN acknowledges financial support by Deutsche Forschungsgemeinschaft under contract no. Ni-632/1-1 (research fellowship at Princeton U.) and Ni-632/2-1 (research proposal within SPP1121) and hospitality from G. Scoles and J. Rädler. We also acknowledge financial support by Elite Netzwerk Bayern, CeNS and NIM. Purified pentacene was received from J. Pflaum, Universität Stuttgart. The X-ray experiments were performed at NSLS in Brookhaven and at HASYLAB in Hamburg. We are grateful to J. Kotthaus for providing access to clean room facilities at LMU. Finally, it is a pleasure to acknowledge fruitful discussions with the participants of SPP1112, and with N. Koch and U. Beierlein.

## References

- [1] G. G. Malliaras and R. Friend, *Phys. Today* **58**, 53 (2005).
- [2] S. R. Forrest, *Nature* **428**(6986), 911–918 (2004).
- [3] C. D. Dimitrakopoulos, A. R. Brown, and A. Pomp, *J. Appl. Phys.* **80**(4), 2501–2508 (1996).
- [4] D. J. Gundlach, Y. Y. Lin, T. N. Jackson, S. F. Nelson, and D. G. Schlom, *IEEE Electron Device Lett.* **18**(3), 87–89 (1997).
- [5] Y. Y. Lin, D. J. Gundlach, S. F. Nelson, and T. N. Jackson, *IEEE Electron Device Lett.* **18**(12), 606–608 (1997).
- [6] D. Knipp, R. A. Street, A. Volkel, and J. Ho, *J. Appl. Phys.* **93**(1), 347–355 (2003).
- [7] C. D. Dimitrakopoulos and D. J. Mascaro, *IBM J. Res. Dev.* **45**(1), 11–27 (2001).
- [8] C. D. Dimitrakopoulos and P. R. L. Malenfant, *Adv. Mater.* **14**(2), 99–117 (2002).
- [9] G. R. Desiraju and A. Gavezzotti, *Acta Crystallogr. B, Struct. Sci.* **45**, 473–482 (1989).
- [10] R. Ruiz, D. Choudhary, B. Nickel, T. Toccoli, K.-C. Chang, A. C. Mayer, P. Clancy, J. M. Blakely, R. L. Headrick, S. Iannotta, G. G. Malliaras, B. Nickel, T. Toccoli, K.-C. Chang, A. C. Mayer, P. Clancy, J. M. Blakely, R. L. Headrick, S. Iannotta, and G. G. Malliaras, *Chem. Mater.* **16**(23), 4497 (2004).
- [11] G. Horowitz and P. Delannoy, *J. Appl. Phys.* **70**(1), 469 (1991).
- [12] G. Gu, M. G. Kane, J. E. Doty, and A. H. Firester, *Appl. Phys. Lett.* **87**(24), 243512 (2005).
- [13] S. R. Forrest, *Chem. Rev.* **97**(6), 1793–1896 (1997).
- [14] G. B. Blanchet, C. R. Fincher, and I. Malajovich, *J. Appl. Phys.* **94**(9), 6181–6184 (2003).
- [15] J. A. Venables, G. D. T. Spiller, and M. Hanbrücken, *Rep. Prog. Phys.* **47**, 339–459 (1984).
- [16] F.-J. Meyer zu Heringdorf, M. C. Reuter, and R. M. Tromp, *Nature* **412**, 517–520 (2001).
- [17] R. Ruiz, B. Nickel, N. Koch, L. C. Feldman, R. F. Haglund, A. Kahn, and G. Scoles, *Phys. Rev. B* **67**(12), 125406 (2003).
- [18] J. G. Amar, F. Family, and Pui-Man Lam, *Phys. Rev. B* **50**(12), 8781–8797 (1994).
- [19] J. G. Amar and F. Family, *Phys. Rev. Lett.* **74**(11), 2066–2069 (1995).
- [20] R. Ruiz, B. Nickel, N. Koch, L. C. Feldman, R. F. Haglund, A. Kahn, and G. Scoles, *Phys. Rev. Lett.* **91**, 136102 (2003).
- [21] S. E. Fritz, S. M. Martin, C. D. Frisbie, M. D. Ward, and M. F. Toney, *J. Chem. Soc.* **126**(13), 4084 (2004).
- [22] A. C. Malliaras, G. G. Nickel, B. Scoles, G. Kazimirov, A. Kim, H. Headrick, R. L. Islam, Z. Ruiz, and R. Mayer, *Appl. Phys. Lett.* **85**(21), 4926 (2004).
- [23] R. B. Campbell, J. Trotter, and J. M. Robertson, *Acta Crystallogr.* **14**(7), 705 (1961).
- [24] R. B. Campbell, J. Trotter, and J. Moneath, *Acta Crystallogr.* **15**(3), 289 (1962).
- [25] R. Feidenhansl, *Surf. Sci. Rep.* **10**(3), 105–188 (1989).
- [26] H. Yoshida, N. Inaba, and K. Sato, *Appl. Phys. Lett.* **90**(189), 181930 (2007).
- [27] S. Schiefer, M. Huth, A. Dobrinevski, and B. Nickel, *J. Chem. Soc.*, in press (2007).
- [28] J. E. Northrup, M. L. Tiago, and S. G. Louie, *Phys. Rev. B* **66**(12), 121404 (2002).

- [29] R. Ruiz, B. Nickel, N. Koch, L. C. Feldman, R. F. Haglund, A. Kahn, and G. Scoles, *Phys. Rev. B* **67**(12), 125406 (2003).
- [30] S. Kowarik, A. Gerlach, W. Leitenberger, W. Hu, G. Witte, C. Wöll, U. Pietsch, and F. Schreiber, *Thin Solid Films* **515**(14), 5606 (2007).
- [31] A. C. Mayer, A. Kazimirov, and G. G. Malliaras, *Phys. Rev. Lett.* **97**, 105503 (2006).
- [32] D. Käfer and G. Witte, *Chem. Phys. Lett.* **442**, 376 (2007).
- [33] D. Käfer, L. Ruppel, and G. Witte, *Phys. Rev. B* **75**, 085309 (2007).
- [34] G. Beernink, T. Strunskus, G. Witte, and Ch. Wöll, *Appl. Phys. Lett.* **85**, 398 (2004).
- [35] L. Casalis, M. F. Danisman, B. Nickel, G. Bracco, T. Toccoli, S. Iannotta, and G. Scoles, *Phys. Rev. Lett.* **90**(20), 206101 (2003).
- [36] D. R. Lide (ed.), *Handbook of chemistry and physics* (CRC Press, Cleveland, Ohio, 1981).
- [37] E. A. Silinsh and V. Čápek, *Organic molecular crystals: Interaction, localization and transport phenomena* (AIP, New York, 1994).
- [38] F. De Angelis, T. Toccoli, A. Pallaoro, N. Coppede, L. Mariucci, G. Fortunato, and S. Iannotta, *Synth. Met.* **146**(3), 291–295 (2004).
- [39] N. Koch, B. Nickel, J. Ghijsen, A. Elschner, J. Schwartz, J.-J. Pireaux, and A. Kahn, *Mater. Res. Soc. Symp. Proc.* **771**(20), L3.6.1 (2003).
- [40] N. Koch, A. Vollmer, I. Salzmann, B. Nickel, H. Weiss, and J. P. Rabe, *Phys. Rev. Lett.* **95**(15), 156803 (2006).
- [41] H. Kakuta, T. Hirahara, I. Matsuda, T. Nagao, S. Hasegawa, N. Ueno, and K. Sakamoto, *Phys. Rev. Lett.* **98**, 247601 (2007).
- [42] I. Salzmann, S. Opitz, R. Rogaschewski, J. P. Rabe, B. Nickel, and N. Koch, *Phys. Rev. B* **75**, 174108 (2007).
- [43] S. M. Sze, *Physics of semiconductor devices* (Wiley, Singapore, 1981).
- [44] B. Nickel, R. Barabash, R. Ruiz, N. Koch, A. Kahn, L. C. Feldman, R. F. Haglund, and G. Scoles, *Phys. Rev. B* **70**(12), 125401 (2004).
- [45] M. Shtein, J. Mapel, J. B. Benziger, and S. R. Forrest, *Appl. Phys. Lett.* **81**(2), 268 (2002).
- [46] C. Erlen, P. Lugli, M. Fiebig, and B. Nickel, *J. Comput. Electron.* **5**(4), 345 (2006).
- [47] P. V. Necliudov, M. S. Shur, D. J. Gundlach, and T. N. Jackson, *J. Appl. Phys.* **88**(11), 6594–6597 (2000).
- [48] D. Faltermeier, B. Gompf, M. Dressel, A. K. Tripathi, and J. Pflaum, *Phys. Rev. B* **74**(12), 125416 (2006).
- [49] S. Yoo, B. Domercq, and B. Kippelen, *Appl. Phys. Lett.* **85**(22), 5427 (2004).
- [50] O. Ostroverkhova, D. G. Cooke, F. A. Hegmann, J. E. Anthony, V. Podzorov, M. E. Gershenson, O. D. Jurchescu, and T. T. M. Palstra, *Appl. Phys. Lett.* **88**(12), 162101 (2006).
- [51] Atto Cube Systems AG in München.
- [52] M. Fiebig et al., submitted (2007).



## A.6 Full text of Ref. [6]

Henning Marciniak, Matthias Fiebig, Martin Huth, Stefan Schiefer, Bert Nickel, Florian Selmaier, and Stefan Lochbrunner

*Ultrafast Exciton Relaxation in Microcrystalline Pentacene Films*

PRL **99**, 176402 (2007)

### **Abstract:**

The exciton dynamics in microcrystalline pentacene films is investigated by transient absorption measurements with 30 fs time resolution. It is found that the emission from photoexcited Frenkel excitons decays within 70 fs due to the ultrafast formation of an excitonic species with a strongly reduced transition dipole to the ground state and an absorption dipole in the plane of the film. We propose that an excimer exciton is formed and stabilized by changes of the local crystal structure. The subsequent dynamics is dominated by diffusion controlled annihilation and trapping.

Permanent weblink:

<http://prl.aps.org/pdf/PRL/v99/i17/e176402>

MH contribution:

- sample fabrication.
- participation in discussions.

## Ultrafast Exciton Relaxation in Microcrystalline Pentacene Films

H. Marciniak,<sup>1</sup> M. Fiebig,<sup>2</sup> M. Huth,<sup>2</sup> S. Schiefer,<sup>2</sup> B. Nickel,<sup>2</sup> F. Selmaier,<sup>1</sup> and S. Lochbrunner<sup>3</sup>

<sup>1</sup>*Lehrstuhl für BioMolekulare Optik, Physics Department, Ludwig-Maximilians-Universität, Oettingenstr. 67, 80538 München, Germany*

<sup>2</sup>*Physics Department and CeNS, Ludwig-Maximilians-Universität, Geschwister-Scholl-Platz 1, 80539 München, Germany*

<sup>3</sup>*Institut für Physik, Universität Rostock, Universitätsplatz 3, 18051 Rostock, Germany*

(Received 4 May 2007; published 26 October 2007)

The exciton dynamics in microcrystalline pentacene films is investigated by transient absorption measurements with 30 fs time resolution. It is found that the emission from photoexcited Frenkel excitons decays within 70 fs due to the ultrafast formation of an excitonic species with a strongly reduced transition dipole to the ground state and an absorption dipole in the plane of the film. We propose that an excimer exciton is formed and stabilized by changes of the local crystal structure. The subsequent dynamics is dominated by diffusion controlled annihilation and trapping.

DOI: [10.1103/PhysRevLett.99.176402](https://doi.org/10.1103/PhysRevLett.99.176402)

PACS numbers: 71.35.Aa, 72.80.Le, 73.61.Ph, 78.66.Qn

The electronic properties of organic materials have been studied intensively to promote their application in electronic devices [1–3]. The research is driven by the expectation of cheap and flexible devices as well as new application areas, particularly in optoelectronics. Microcrystalline pentacene films with a thickness of a few monolayers are used as active layers in many prototype applications, such as organic field effect transistors, because their hole mobility is extraordinarily high for organic materials and can adopt values of more than  $1 \text{ cm}^2/(\text{V s})$  [4,5]. Crystalline pentacene is also intensively studied to investigate basic physical properties of organic crystals [6–8]. The performance of organic devices depends on the internal electronic structure and dynamics of the organic material as well as on its interaction with other device components such as contacts [3]. Femtosecond pump probe experiments allow us to study the internal properties with an unprecedented selectivity because they probe local processes and provide the time resolution necessary to observe the originally generated species, as well as their relaxation and trapping pathways [9,10].

The nature and evolution of the primarily generated excitons in pentacene are not clear at all. The low photoluminescence yield indicates that the photoexcited excitons relax quickly to a nonfluorescing state. It was argued that an ultrafast fission into two triplet excitons can occur in less than 100 fs since the energy of the triplet state is somewhat less than half of the monomeric  $S_1$  energy [7]. On the other hand, terahertz experiments indicate that within their time resolution of 400 fs free charge carriers appear [8]. In this Letter we approach the problem with transient absorption spectroscopy with 30 fs time resolution and provide evidence that within the first 70 fs the photoexcited Frenkel excitons transform to excimer excitons.

Microcrystalline thin film samples are prepared by vacuum deposition of pentacene on a transparent polymer substrate (TOPAS; thermoplastic olefin polymer of amor-

phous structure). The film consists of closely packed crystalline grains with a diameter of about  $1 \mu\text{m}$  and a height of roughly 30 monolayers [11]. The samples are kept under nitrogen for storage and during the optical experiments. In the pump probe measurements the samples are excited by 30 fs long pulses which are generated with a noncollinearly phase matched optical parametric amplifier (NOPA) [12] pumped by a 1 kHz regenerative Ti:sapphire amplifier system (CPA 2001; Clark MXR). The absorption changes are probed over the whole visible spectral range with a white light continuum generated in a 3 mm thick sapphire substrate. For measurements with a higher time resolution but restricted spectral coverage 25 fs long probe pulses from a second NOPA are used. Pump and probe beam are overlapped and focused to a spot of  $260 \mu\text{m}$  in diameter at the sample, which is oriented normal to the beams or with an angle of incidence of  $65^\circ$ . The recollimated probe beam is dispersed with a SF10 prism after the sample [10] and the transmitted energy is spectrally resolved, measured with a photodiode behind a slit. The cross correlation is measured by sum frequency mixing in a  $100 \mu\text{m}$  thick BBO crystal at the sample position. The pump polarization is adjusted parallel to the probe beam with an achromatic  $\lambda/2$ -wave plate.

The steady state absorption spectrum of the pentacene films is identical to earlier published ones [see Fig. 1(a)] [8,13]. The center wavelength 670 nm of the pump pulse is at the maximum of the lowest and strongest absorption band. Transient spectra are measured at various time delays after photoexcitation of the films with an angle of incidence of  $0^\circ$  and  $65^\circ$  [see Figs. 1(b) and 1(c)]. They show a strong bleach due to the reduction of the ground state population and excited state absorption (ESA), which is most evident from the positive absorption between 610 and 650 nm and which is attributed to the photogenerated species. The absorption changes show a continuous decay indicating that the excited species returns to the electronic ground state within several hundred picoseconds. To obtain

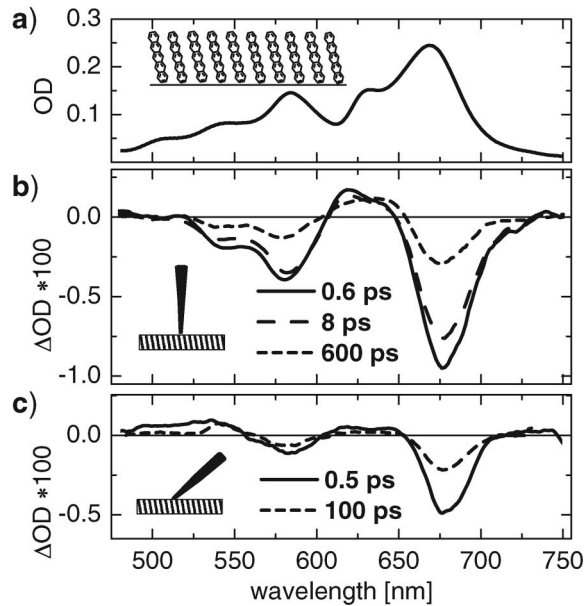


FIG. 1. (a) Steady state absorption spectrum of the microcrystalline pentacene films, (b) transient absorption spectra 0.6, 8, and 600 ps after photoexcitation at 670 nm measured with laser beams vertical to the substrate and (c) transient spectra at 0.5 and 100 ps with an angle of incidence of 65°.  $\Delta OD = -\log(T/T_0)$  is the optical density change,  $T$  the sample transmission with photoexcitation, and  $T_0$  without photoexcitation.

the spectrum of the excited species the bleach was subtracted from the transient spectrum measured at a delay of 8 ps and normal incidence (see Fig. 2). The pump pulse excites preferentially grains with transition dipoles enclosing a small angle with the pump polarization, resulting in an anisotropic excitation. The anisotropy of the transient absorption does hardly change with time [14]. Since the steady state spectrum is an average over all polarizations, transient spectra measured with parallel and perpendicular

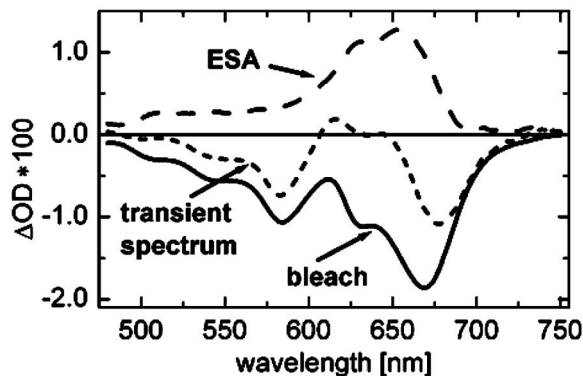


FIG. 2. Decomposition of the polarization averaged transient spectrum (short dashed line) at a delay of 8 ps into ground state bleach (solid line) and the absorption of the excitons (ESA, broken line).

polarizations were averaged prior to subtraction of the bleach.

The resulting ESA is of similar strength as the bleach. There are no indications for stimulated emission which would show up as a negative contribution and which is expected from the optically excited excitons in the red wing of the ground state absorption. Its lack indicates that the primarily excited Frenkel excitons have already transformed into a non fluorescing species. To observe this transformation, spectra with a resolution of 30 fs were measured in the spectral region of the lowest absorption band (see Fig. 3).

They show a strong negative signal between 670 and 710 nm where stimulated emission from Frenkel excitons is expected. This signal decays extremely fast to the transient spectrum measured 600 fs after excitation. To determine the decay time kinetic traces were recorded with 25 fs long probe pulses with pulse spectra centered at 635 and 676 nm [see Fig. 3(b)]. For this purpose the dispersion prism was removed because a spectrally integrating detection avoids artifacts at time zero. The data can be perfectly modeled by a convolution [solid lines in Fig. 3(b)] of an exponential decay with the cross correlation (broken lines). The obtained time constants of 65 and 79 fs are equal within the experimental error. The results show that the emission of the optically excited excitons decays with a time constant of  $70 \pm 10$  fs, reflecting the transformation of the Frenkel excitons into a nonfluorescing species.

This species can neither be attributed to triplet excitons nor to free charge carriers. The lowest absorption band of monomeric pentacene in the triplet state has its origin at 505 nm [15]. It is about 10 times stronger than the  $S_0 \rightarrow S_1$  absorption and its transition dipole is oriented along the long molecular axis. Since the pentacene molecules are tilted from a perpendicular orientation with respect to the substrate by only 6° [16] such a transition dipole can hardly interact with laser light polarized parallel to the substrate. To strengthen signatures from potential triplet excitons we tilted the sample to an angle of incidence of 65° and obtained the spectra shown in Fig. 1(c). Taking refraction into account, the laser polarization is now oriented with an angle of about 55° to the long molecular axis. Accordingly, the bleach signal is reduced since it results from transitions polarized along the short molecular axis. The same is obviously true for the ESA. However, a weak additional absorption band is now observed around 525 nm. We assign this band to a small triplet population because its spectral position is as expected moderately redshifted with respect to the triplet absorption of the monomer in solution [15] and its dependence on the angle of incidence shows that it is associated with a transition dipole along the long molecular axis. However, if all excitons would experience fission into triplets this band would be several times stronger than the bleach. We conclude that only a fraction of less than 10% transforms into

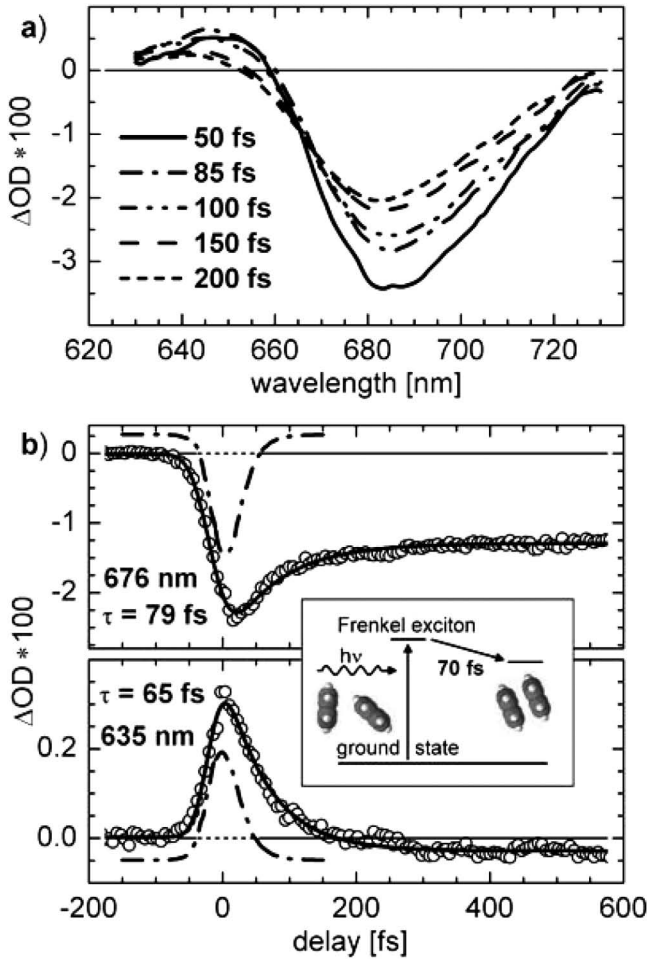


FIG. 3. (a) Transient spectra under normal incidence during the first 200 fs in the region of the first absorption band. (b) Time traces (circles) measured with 25 fs probe pulses centered at 635 and 676 nm. Monoexponential decays (solid lines) are convoluted with the cross correlation (dash-dotted lines, vertically shifted for better visibility) and fitted to the data. The inset shows the corresponding energy diagram.

triplets. The majority adapts a state with an absorption dipole in the plane of the film. Monomeric pentacene cations and anions exhibit no absorption band in the visible spectrum [17] and ionic transitions cannot explain the ESA band even if a strong spectral shift due to the crystalline structure is assumed. This excludes the idea that free charges contribute dominantly to the observed signatures.

We propose that a species very similar to excimers is generated. Two neighboring pentacene molecules form a bound dimer in the electronically excited state [6]. Most probably the two molecules rotate around the long molecular axis to change from the tilted geometry of the original herringbone structure to a parallel geometry and reduce their intermolecular distance to minimize the energy [see inset of Fig. 3(b)]. This electronic configuration corresponds to a symmetric combination of the first excited singlet states of the two molecules but can contain a

significant charge transfer contribution. The transition to this state is electric dipole forbidden as soon as the molecules have adapted a parallel geometry [6]. We think this effect is responsible for the ultrafast decay of the exciton emission. The observed time constant corresponds to the rotation of the molecules. The ESA results from a transition to a doubly excited dimer state.

A detailed analysis of the subsequent picosecond dynamics at several probe wavelengths and excitation intensities will be given in a forthcoming publication [14]. Here we focus on the most important findings and discuss them on the basis of the recovery of the ground state bleach measured at 685 nm and shown in Fig. 4 on a logarithmic time scale. It reflects diffusion controlled annihilation [9] as well as trapping of the excitons. We modeled the exciton decay and the bleach recovery by numerical integration of the rate Eqs. (1) and (2).

$$\frac{dn}{dt} = -\frac{1}{2}8\pi D\bar{a}\left(1 + \frac{\bar{a}}{\sqrt{2\pi Dt}}\right)n^2 - 4\pi D\bar{a}\left(1 + \frac{\bar{a}}{\sqrt{\pi Dt}}\right)n(n_{T0} - n_T); \quad (1)$$

$$\frac{dn_T}{dt} = 4\pi D\bar{a}\left(1 + \frac{\bar{a}}{\sqrt{\pi Dt}}\right)n(n_{T0} - n_T) - \frac{1}{\tau}n_T. \quad (2)$$

$n$  is the time dependent exciton concentration,  $D$  the diffusion constant,  $n_{T0}$  the concentration of traps, and  $n_T$  the concentration of traps that are already occupied. They have a finite lifetime  $\tau$  till they return to the ground state.  $\bar{a}$  describes the distance to which an exciton must approach another exciton or a trap for efficient interaction. It is set to 1 nm, which is in the order of the geometrical average of

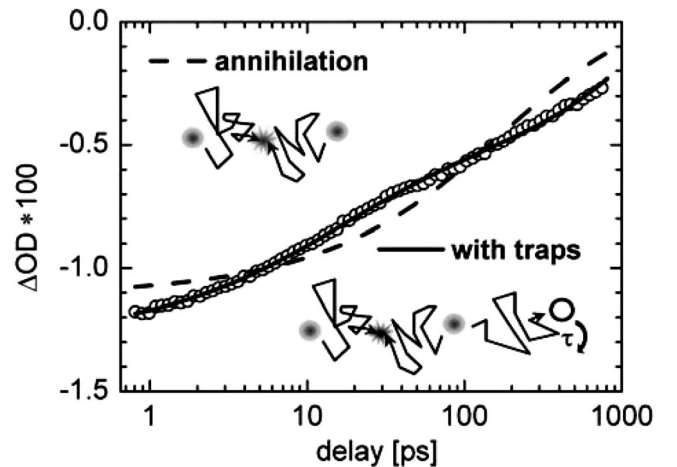


FIG. 4. Bleach recovery probed at 685 nm (circles). Modeling by exciton-exciton-annihilation only (broken line and left sketch) gives poor results, while good agreement is achieved if immobilization of excitons by traps is included (solid line and right sketch).

the lattice constants [9,16]. The exciton concentration  $n_0 = 4.8 \times 10^{19} \text{ cm}^{-3}$  at  $t = 0$  is calculated from the excitation energy of 85 nJ. The time dependent bleach can be very well reproduced with  $D = 5 \times 10^4 \text{ cm}^2/\text{s}$ ,  $n_{T0} = 2 \times 10^{19} \text{ cm}^{-3}$ , and  $\tau = 850 \text{ ps}$  (solid line in Fig. 4). These parameters also correctly describe the dependence of the dynamics on the excitation energy (not shown here) [14]. In contrast, neglecting the traps and assigning an intrinsic lifetime to the excitons gives very dissatisfactory results (broken line in Fig. 4).

The observed bleach recovery also provides some evidence against triplet fission as a major relaxation channel. The lifetime  $\tau$  describing the repopulation of the electronic ground state in the low excitation limit is too short for a triplet state [6,15]. The observed dependence on the excitation intensity is poorly reproduced if it is assumed that each absorbed photon results in two triplet excitons (not shown). Furthermore, triplet excitons in anthracene exhibit two dimensional diffusion [6]. Assuming two dimensional diffusion fails in reproducing the observed kinetics.

If the photoexcited Frenkel excitons would predominantly dissociate into free charge carriers, annihilation would correspond to the recombination of opposite charges. In pentacene highly mobile holes usually determine the mobility. The mobility of a single charged species can be calculated with the Einstein relation  $\mu = De_0/(k_B T)$  [18]. From the found diffusion constant a mobility of  $0.02 \text{ cm}^2/(\text{V s})$  would result. However, the mobility of holes should be higher than  $1 \text{ cm}^2/(\text{V s})$  [5], indicating that the diffusion of a neutral species instead of holes is observed. Time resolved terahertz [8] and photoconductivity experiments [19] find a significant population of free charge carriers. The observed signals are sensitive to the products' photogeneration yield times mobility or times lifetime [8,19]. With a mobility of  $1 \text{ cm}^2/(\text{V s})$  and a lifetime of a few hundred ps for the trapped electrons an efficiency of a few percent for the photogeneration of free charges results from these experiments. This is fully compatible with our findings.

In conclusion, transient absorption measurements with 30 fs time resolution show that in microcrystalline pentacene films the stimulated emission of photoexcited Frenkel excitons decays within 70 fs. The decay is attributed to the ultrafast formation of excitons with excimer character. The assignment is supported by the polarization dependence and the diffusion properties as well as the lifetime of the excitons. The time needed for the stabilization of the excimer state reflects changes in the local crystal structure. These deformations should lead to a large effective mass [18] and to small band widths that are comparable to thermal fluctuations [20]. At room temperature a high degree of localization is therefore expected and the propagation of the excitons is better described as a hopping process than as a band-like transport. This conclusion is

supported by the small diffusion constant observed in our experiments.

Purified Pentacene was provided by J. Pflaum, Universität Stuttgart. We thank Eberhard Riedle for continuous support and acknowledge financial support from No. DFG-SPP1121-Ni632/2-1, CeNS, and individual support from the Elitenetwork Bavaria.

- 
- [1] S. R. Forrest, *Nature (London)* **428**, 911 (2004).
  - [2] G. Malliaras and R. Friend, *Phys. Today*, **58**, No. 5, 53 (2005).
  - [3] M. E. Gershenson, V. Podzorov, and A. F. Morpurgo, *Rev. Mod. Phys.* **78**, 973 (2006).
  - [4] C. D. Dimitrakopoulos, S. Purushothaman, J. Kymissis, A. Callegari, and J. M. Shaw, *Science* **283**, 822 (1999).
  - [5] O. D. Jurchescu, J. Baas, and T. T. M. Palstra, *Appl. Phys. Lett.* **84**, 3061 (2004).
  - [6] M. Pope and C. E. Swenberg, *Electronic Processes in Organic Crystals and Polymers* (Oxford University Press, New York, 1999), 2nd ed..
  - [7] C. Jundt, G. Klein, B. Sipp, J. Le Moigne, M. Joucla, and A. A. Villaeys, *Chem. Phys. Lett.* **241**, 84 (1995).
  - [8] O. Ostroverkhova, D. G. Cooke, S. Shcherbyna, R. F. Egerton, F. A. Hegmann, R. R. Tykwinski, and J. E. Anthony, *Phys. Rev. B* **71**, 035204 (2005).
  - [9] E. Engel, K. Leo, and M. Hoffmann, *Chem. Phys.* **325**, 170 (2006).
  - [10] M. Schlosser and S. Lochbrunner, *J. Phys. Chem. B* **110**, 6001 (2006).
  - [11] B. Nickel, R. Barabash, R. Ruiz, N. Koch, A. Kahn, L. C. Feldman, R. F. Haglund, and G. Scoles, *Phys. Rev. B* **70**, 125401 (2004).
  - [12] T. Wilhelm, J. Piel, and E. Riedle, *Opt. Lett.* **22**, 1494 (1997).
  - [13] D. Faltermeier, B. Gompf, M. Dressel, A. K. Tripathi, and J. Pflaum, *Phys. Rev. B* **74**, 125416 (2006).
  - [14] H. Marciniak, F. Selmaier, M. Huth, S. Schiefer, M. Fiebig, B. Nickel, and S. Lochbrunner (to be published).
  - [15] C. Hellner, L. Lindqvist, and P. C. Rodberge, *J. Chem. Soc., Faraday Trans. 1* **68**, 1928 (1972).
  - [16] S. Schiefer, M. Huth, A. Dobrinevski, and B. Nickel, *J. Am. Chem. Soc.* **129**, 10316 (2007).
  - [17] D. Distler and G. Hohlneicher, *Ber. Bunsen-Ges. Phys. Chem.* **74**, 960 (1970); V. Coropceanu, M. Malagoli, D. A. da Silva Filho, N. E. Gruhn, T. G. Bill, and J. L. Brédas, *Phys. Rev. Lett.* **89**, 275503 (2002); R. Ruiz, A. C. Mayer, G. G. Malliaras, B. Nickel, G. Scoles, A. Kazimirov, H. Kim, R. L. Headrick, and Z. Islam, *Appl. Phys. Lett.* **85**, 4926 (2004).
  - [18] S. M. Sze, *Physics of Semiconductor Devices* (John Wiley & Sons, New York, 1981), p. 28.
  - [19] M. Fiebig *et al.*, (to be published).
  - [20] A. Troisi and G. Orlandi, *Phys. Rev. Lett.* **96**, 086601 (2006).



## A.7 Full text of Ref. [7]

Stefan Schiefer, Martin Huth, Alexander Dobrinevski, and Bert Nickel

*Determination of the Crystal Structure of Substrate-Induced Pentacene Polymorphs in Fiber Structured Thin Films.*

J. AM. CHEM. SOC. 2007, **129**, 10316-10317

### **Abstract:**

It is widely recognized that the intrinsic charge transport properties in organic thin-film transistors (OTFTs) depend strongly on the crystal structure of the organic semiconductor layer. Pentacene, showing one of the highest charge carrier mobilities among organic semiconductors, is known to crystallize in at least four polymorphs, which can be distinguished by their layer periodicity  $d(001)$ . Only two polymorphs grow as single crystals, and their detailed crystal structure has been solved. The substrate-induced 15.4 Å polymorph is the most relevant for OTFT applications; however, its crystal structure has remained incomplete as it only grows as a fiber structured thin film. Here we extend the crystal truncation rod X-ray scattering technique to fiber structured thin films. We determined the complete crystal structure of this polymorph grown on technologically relevant substrates. We found that the molecular arrangement within the unit cell is substrate dependent, which may lead to a controlled fine-tuning of intrinsic charge transport properties.

Permanent weblink:

<http://pubs.acs.org/doi/full/10.1021/ja0730516>

MH contribution:

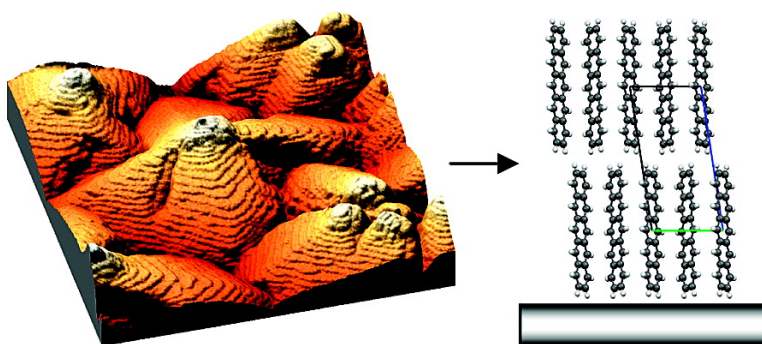
- x-ray sample fabrication.
- performed x-ray experiments at the synchrotron.
- discussions.

## Determination of the Crystal Structure of Substrate-Induced Pentacene Polymorphs in Fiber Structured Thin Films

Stefan Schiefer, Martin Huth, Alexander Dobrinevski, and Bert Nickel

*J. Am. Chem. Soc.*, 2007, 129 (34), 10316-10317 • DOI: 10.1021/ja0730516

Downloaded from <http://pubs.acs.org> on November 21, 2008



### More About This Article

Additional resources and features associated with this article are available within the HTML version:

- Supporting Information
- Links to the 12 articles that cite this article, as of the time of this article download
- Access to high resolution figures
- Links to articles and content related to this article
- Copyright permission to reproduce figures and/or text from this article

[View the Full Text HTML](#)

## Determination of the Crystal Structure of Substrate-Induced Pentacene Polymorphs in Fiber Structured Thin Films

Stefan Schiefer, Martin Huth, Alexander Dobrinevski, and Bert Nickel\*

Department für Physik and CeNS, Ludwig-Maximilians-Universität, Geschwister-Scholl-Platz 1, 80539 München, Germany

Received May 1, 2007; E-mail: nickel@lmu.de

The intrinsic charge transport properties in organic crystals as calculated by numerical methods depend strongly on the molecular packing and arrangement in the crystal.<sup>1–4</sup> Pentacene, showing one of the highest charge carrier mobilities among organic semiconductors,<sup>5,6</sup> is known to crystallize in at least four polymorphs, which can be distinguished by their layer periodicity<sup>7</sup>  $d_{(001)}$ . Only two polymorphs grow as single crystals, and their crystal structure has been solved.<sup>7,8</sup> The substrate-induced 15.4 Å polymorph is the most relevant for organic thin-film transistor (OTFT) applications; however, its crystal structure has remained incomplete<sup>7,9–13</sup> as it only grows as a fiber structured thin film. Here we extend the crystal truncation rod X-ray scattering technique to fiber structured thin films. We determine the complete crystal structure of this polymorph grown on various substrates and find that the molecular arrangement within the unit cell is substrate dependent.

Pentacene crystallizes in a layered structure with a herringbone arrangement and grows at room temperature in the so-called “thin-film” phase on amorphous silicon dioxide<sup>9</sup> (a-SiO<sub>2</sub>). Since X-ray reflectivity measurements only showed (00l) reflections associated with a spacing of  $d_{(001)} = 15.4$  Å, the crystallites are supposed to form a fiber structure with their  $a$ – $b$  plane oriented parallel to the substrate surface and the fiber axes parallel to the substrate normal<sup>9</sup> (Figure S1). The thin-film phase is a substrate-induced polymorph, as it is only observed near the substrate for film thicknesses of up to 50 nm at 300 K.<sup>7,14</sup> Hence, sample preparation for X-ray powder diffraction failed because insufficient sample could be produced,<sup>7</sup> and more importantly, it remains unclear if the thin-film phase can be removed from the substrate without changing its structure. The reciprocal unit cell parameters  $a^*$ ,  $b^*$ , and  $\gamma^*$  were obtained by electron diffraction experiments using electron transparent substrates such as thin copper grids coated with carbon.<sup>8,15</sup> Subsequent grazing incidence X-ray diffraction (GIXD) measurements on a-SiO<sub>2</sub> substrates revealed the in-plane unit cell parameters  $a$ ,  $b$  and their respective angle  $\gamma$ .<sup>10–13</sup> To solve the complete crystal structure, or the complete set of unit cell parameters and the molecular arrangement within the unit cell, a large reciprocal space section of Bragg peaks along with their intensities has to be measured and analyzed. Such a measurement has to overcome the inherently weak signal-to-noise ratio from the thin-film crystallites. Furthermore, a complex numerical analysis has to be developed to analyze the diffraction data of crystallites forming a fiber structure. Here we will employ a grazing incidence crystal truncation rod (GI-CTR)<sup>16</sup> geometry to cover the relevant section of reciprocal space for a substrate-supported thin film. Details of the experimental setup are given in the Supporting Information.

Here, we first focus on how to collect the relevant data set for pentacene thin films on technologically relevant substrates such as a-SiO<sub>2</sub>, octadecyltrichlorosilane-treated a-SiO<sub>2</sub> (OTS), and Topas.<sup>17</sup> As a first step, the in-plane Bragg peak positions are determined by a GIXD measurement as described elsewhere.<sup>10</sup> For each in-

plane Bragg peak, one GI-CTR scan is performed as follows: The incident X-ray beam is kept at a grazing angle  $\alpha_i = 0.15^\circ$  on the sample near the critical angle for total external reflection  $\alpha_c$ . The detector azimuth angle  $\delta$  is set to  $\delta'$ , an in-plane Bragg peak position of interest. A scan is performed by measuring the diffracted intensity while increasing the altitude angle  $\gamma$  and simultaneously adjusting  $\delta$  by

$$\delta = \arcsin\left(\frac{2 \cos(\delta') \cos(\alpha_i) + \cos^2(\gamma) - 1}{2 \cos(\gamma) \cos(\alpha_i)}\right) \quad (1)$$

This keeps the lateral momentum transfer  $q_{xy}$  constant while the perpendicular momentum transfer  $q_z$  is varied (Figure 1a). A highly collimated scintillating point detector is used for data collection, resulting in a Bragg signal with a signal-to-noise ratio of  $\sim 10^3$ . Background intensity is measured with an offset of  $\Delta\delta = 1^\circ$  and is subtracted.

Solving the crystal structure is achieved in a two-step procedure. First, the unit cell parameters are solved from those Bragg peak positions ( $q_{xy}$ ,  $q_z$ ) which can be assigned unambiguously to a Miller index.

After the unit cell parameters are determined, the molecular arrangement within the unit cell is inferred from the measured intensity distributions of all measured data points  $I(q_{xy}, q_z)$ . Technically, this is realized by simulating the sum of all individual intensities  $m$  superimposing due to the fiber structure (Figure 1b). For the simulation of the scattered GI-CTR intensity  $I(q_{xy}, q_z)$ , we use the semi-kinematical approximation:

$$I(q_{xy}, q_z) = C \cdot (A_0 N_A N_B)^2 \sum_m \left| e^{-B \cdot q_m^2} \cdot F(\vec{q}_m) \cdot \frac{e^{N_c(i \cdot \vec{q}_m \cdot \vec{c} - \sigma)} - 1}{e^{i \cdot \vec{q}_m \cdot \vec{c} - \sigma} - 1} \right|^2 \quad (2)$$

where  $A_0$  represents the incident intensity,  $C$  includes beam amplitude correction factors,<sup>18</sup>  $B$  is the B-factor of the Debye–Waller factor,  $N_A N_B$  are the number of unit cells of a crystallite in  $\vec{a}$  and  $\vec{b}$  direction,  $N_c$  is the film thickness in unit cells, and  $\sigma$  is the surface roughness, which describes the observed surface morphology of a pentacene thin-film crystallite.

The structure factor  $F(\vec{q}_m)$  is calculated from a unit cell consisting of two pentacene molecules arranged in a herringbone structure. The positions of the molecules are fixed with their center of mass at the unit-cell coordinates (0, 0, 0) for molecule A and (1/2, 1/2, 0) for molecule B. The structure of the pentacene molecule was taken from the 14.1 Å crystal structure,<sup>8</sup> and the Cromer–Mann scattering factor coefficients were used. The three angular degrees of freedom of each molecule were fitted independently. The angle between the two molecular planes is called the herringbone angle  $\theta_{\text{hrgb}}$  as illustrated in Figure 2a. The tilt angle of the long molecular axis (LMA, Figure 2b) with respect to the

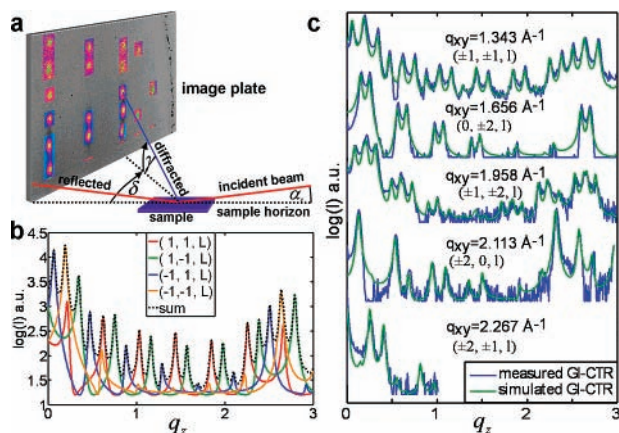


**Figure 1.** (a) GI-CTR geometry. Note that the sample does not move during a measurement. Here, the point detector is replaced by an image plate for better illustration. (b) Simulation of the  $h = k = \pm 1$  GI-CTR contributions and their superposition (dotted line). (c) Observed and best fit plots of GI-CTRs of the 15.4 Å pentacene thin-film phase on a-SiO<sub>2</sub>.

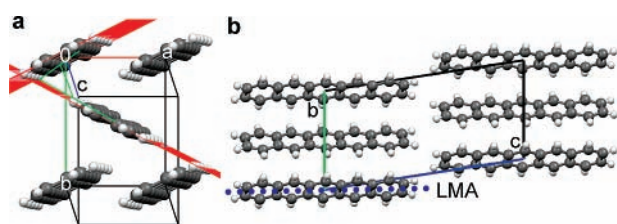


**Figure 2.** Three-dimensional view of 15.4 Å pentacene thin-film polymorph on SiO<sub>2</sub>. (a) Top view: the herringbone angle between the two red molecule planes is illustrated in green. (b) Side view: the LMA is illustrated as a dotted line.

substrate surface normal is called  $\varphi_A$  for molecule A and  $\varphi_B$  for molecule B. With model simulations using eq 2, we verified that GI-CTR measurements with a signal-to-noise ratio  $\geq 10^3$  are needed to detect the weak Bragg peaks which are most sensitive to the molecular arrangement, such as a variation of the herringbone angle. The measurements for the a-SiO<sub>2</sub> substrate and the best fits are plotted in Figure 1c. Notice that the used model reproduces the whole line shape of the measurements well. Forty-seven Bragg peak positions could be clearly assigned to a Miller index and were used to solve the unit cell parameters. We found that the unit cell parameters are identical within measurement precision on all measured substrates. The crystal structure was found to be triclinic with the following lattice parameters:  $a = 5.958 \pm 0.005$  Å,  $b = 7.596 \pm 0.008$  Å,  $c = 15.61 \pm 0.01$  Å,  $\alpha = 81.25 \pm 0.04^\circ$ ,  $\beta = 86.56 \pm 0.04^\circ$ , and  $\gamma = 89.80 \pm 0.10^\circ$ . The unit cell volume  $V = 697$  Å<sup>3</sup> is the largest of all pentacene polymorphs reported so far;  $a$ ,  $b$ , and  $\gamma$  differ only slightly from values reported from previous GIXD studies.<sup>10–13</sup> The unit cell angles  $\alpha$ ,  $\beta$ , and  $\gamma$  are in close correspondence to the values recently reported by Yoshida,<sup>19</sup> although the unit cell axes  $a$ ,  $b$ , and  $c$  differ slightly. Here, we find a herringbone angle  $\theta_{\text{hrbg}}$  of 54.3, 55.8, and 59.4° for a-SiO<sub>2</sub>, OTS, and Topas, respectively. The tilts of the two molecular axes ( $\varphi_A$ ,  $\varphi_B$ ) are (5.6°, 6.0°), (6.4°, 6.8°), and (5.6°, 6.3°) for a-SiO<sub>2</sub>, OTS, and Topas, respectively.

To conclude, we showed that the molecular orientation in the unit cell differs among different substrates while the unit cell dimensions of the 15.4 Å pentacene polymorph are identical. This indicates that substrate effects have to be included if one aims to understand the molecular structure of the thin-film phase<sup>19</sup> in detail.

The crystal structures reported here (atomic coordinates are given in the Supporting Information as cif files) provide a basis to apply techniques such as density functional methods to investigate intrinsic charge transport properties<sup>1,2</sup> and optical properties of organic thin-film devices on a molecular level. In previous studies, it was observed that different substrates vary the charge carrier mobility in OTFTs.<sup>20</sup> The substrate-dependent crystal structures observed here could be one reason for this variation. This topic may lead ultimately to a controlled fine-tuning of intrinsic charge transport properties.

The experimental approach to determine the crystal structure developed here can be easily applied to a wide range of organic thin-film systems used in organic electronic devices.

**Acknowledgment.** We acknowledge support and helpful discussions with O.H. Seeck, J. Pflaum, W. Schmahl, J.O. Rädler, M. Fiebig, S. Youssef, and N. Tsao, and financial support from HASYLab, Hamburg, DFG Schwerpunkt 1121 and CeNS. S.S. acknowledges a scholarship from the Elite Network of Bavaria.

**Supporting Information Available:** Sample preparation, AFM images, X-ray diffractometer setup, X-ray analysis, .cif files. This material is available free of charge via the Internet at <http://pubs.acs.org>.

## References

- (1) Troisi, A.; Orlandi, G. *J. Phys. Chem. B* **2005**, *109*, 1849–1856.
- (2) Troisi, A.; Orlandi, G. *Phys. Rev. Lett.* **2006**, *96*, 4.
- (3) Cornil, J.; Calbert, J. P.; Bredas, J. L. *J. Am. Chem. Soc.* **2001**, *123*, 1250–1251.
- (4) Cheng, Y. C.; Silbey, R. J.; da Silva, D. A.; Calbert, J. P.; Cornil, J.; Bredas, J. L. *J. Chem. Phys.* **2003**, *118*, 3764–3774.
- (5) Lin, Y. Y.; Gundlach, D. J.; Nelson, S. F.; Jackson, T. N. *IEEE Electron Device Lett.* **1997**, *18*, 606–608.
- (6) Kelley, T. W.; Baude, P. F.; Gerlach, C.; Ender, D. E.; Muysers, D.; Haase, M. A.; Vogel, D. E.; Theiss, S. D. *Chem. Mater.* **2004**, *16*, 4413–4422.
- (7) Mattheus, C. C.; Dros, A. B.; Baas, J.; Oostergetel, G. T.; Meetsma, A.; de Boer, J. L.; Palstra, T. T. M. *Synth. Met.* **2003**, *138*, 475–481.
- (8) Mattheus, C. C.; Dros, A. B.; Baas, J.; Meetsma, A.; de Boer, J. L.; Palstra, T. T. M. *Acta Crystallogr., Sect. C* **2001**, *57*, 939–941.
- (9) Dimitrakopoulos, C. D.; Brown, A. R.; Pomp, A. *J. Appl. Phys.* **1996**, *80*, 2501–2508.
- (10) Ruiz, R.; Mayer, A. C.; Malliaras, G. G.; Nickel, B.; Scoles, G.; Kazimirov, A.; Kim, H.; Headrick, R. L.; Islam, Z. *Appl. Phys. Lett.* **2004**, *85*, 4926–4928.
- (11) Fritz, S. E.; Martin, S. M.; Frisbie, C. D.; Ward, M. D.; Toney, M. F. *J. Am. Chem. Soc.* **2004**, *126*, 4084–4085.
- (12) Yang, H. C.; Shin, T. J.; Ling, M. M.; Cho, K.; Ryu, C. Y.; Bao, Z. N. *J. Am. Chem. Soc.* **2005**, *127*, 11542–11543.
- (13) Drummy, L. F.; Martin, D. C. *Adv. Mater.* **2005**, *17*, 903.
- (14) Mayer, A. C.; Kazimirov, A.; Malliaras, G. G. *Phys. Rev. Lett.* **2006**, *97*, 4.
- (15) Wu, J. S.; Spence, J. C. H. *J. Appl. Crystallogr.* **2004**, *37*, 78–81.
- (16) Feidenhansl, R. *Surf. Sci. Rep.* **1989**, *10*, 105–188.
- (17) Topas is the trade name for Ticona cyclo-olefin copolymers (COC), a flexible and optical transparent substrate.
- (18) Smilgies, D. M. *Rev. Sci. Instrum.* **2002**, *73*, 1706–1710.
- (19) Yoshida, H.; Katsuhiko, I.; Sato, N. *Appl. Phys. Lett.* **2007**, *90*, 181930.
- (20) Shtein, M.; Mapel, J.; Benziger, J. B.; Forrest, S. R. *Appl. Phys. Lett.* **2002**, *81*, 268–270.

JA0730516

# Appendix B

## Performing Reflectometry Experiments

This section summarizes some general remarks on how to perform reflectometry experiments, especially at synchrotron sources. Three main topics are covered:

- Preparing the sample
- Mounting the sample
- Possible sources of errors during alignment/measurement

### B.1 Preparing the sample

Some critical issues have to be taken into account when preparing a sample for reflectometry measurements. Depending on the size of the features that should be resolved from the measurement, the **surface roughness**  $\sigma$  should be less than half of the feature size, and always below  $10\text{\AA}$ . Also be aware of the increased roughness due to aggressive cleaning procedures like piranha (30%  $H_2SO_4$  in deionized water) or plasma ozone cleaning.

The **shape** of the sample should be rectangular with the opposing borders being parallel to each other and perpendicular to the beam (Fig. B.1a). Furthermore, the sample should have sharp edges (Fig. B.1b), to ensure that no reflected light from round shapes hits the detector at positions where no signal is expected. Additionally, the observed surface should be perfectly flat (Fig. B.1c), in order to get a distinct intensity maximum when performing a rocking scan. Please note that sometimes the outer pieces of a polished wafer are more curved than the inner pieces. Disregarding these basic rules leads to bad alignment properties.

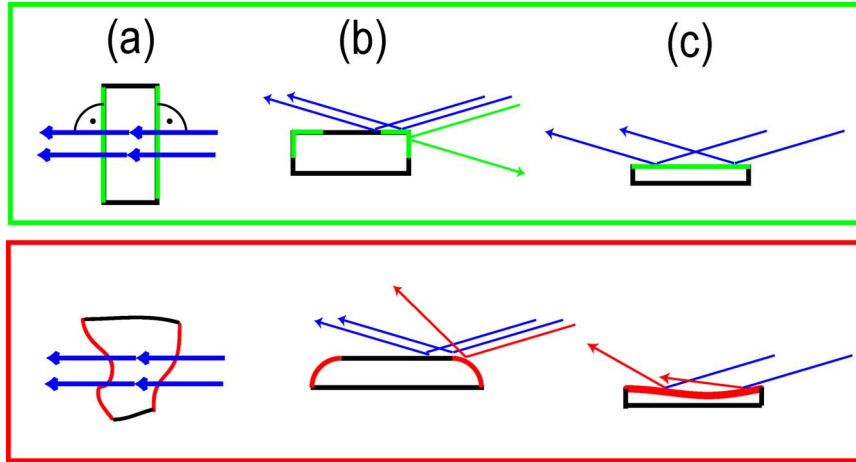


Figure B.1: Before preparing samples for reflectometry measurements one should pay attention that they are rectangular (a) with sharp edges (b) and have a flat surface (c).

## B.2 Mounting the sample

An important issue when mounting a reflectometry sample in a diffractometer is not to deform it due to the forces keeping it in place. If the sample is fixed with double sided scotch tape at both ends of the sample (Fig. B.2a), the weight of the sample could lead to a bending of the surface. This effect can also occur if the sample is fixed with a retainer clip (Fig. B.2b), or when underpressure is used to keep the sample in place. Samples which have been fixed (e.g. in a microfluidic chamber) with a strong glue have also been found to be bend during the curing process of the glue.

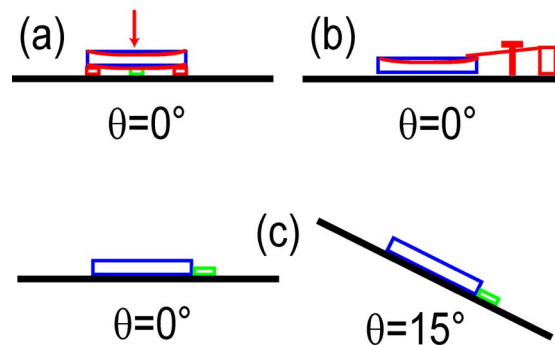


Figure B.2: (a) Avoid fixing the sample only at few positions or clamping the sample (b). (c) Best way to mount a sample.

The best solution is to put the sample on the sample stage without any tape or clamped attachment (Fig. B.2c). To prevent it from moving, a scotch tape is put next to the sample in the direction it would move when the sample is tilted during the measurement.

In situations where it is necessary to physically fix the sample, the applied force should be kept as small as possible.

### B.3 Possible errors during alignment/measurement

There are several ways to combine translation and rotation stages in order to setup a diffractometer. Sometimes larger translation stages are found at the bottom to be able to move heavy equipment (Fig. B.3a). If these motors are used to align the sample, the center of rotation (COR) of the uppermost  $\theta$  stage is changed, which could induce errors. In any case one should try to include translation stages (z and x direction) on top of the  $\theta$  stage (Fig. B.3b).

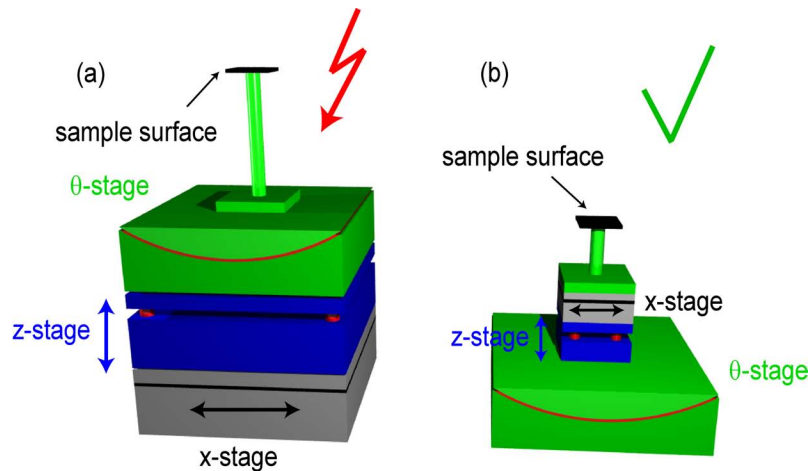


Figure B.3: (a) Translation stages (z, x) are mounted below the  $\theta$  stage. Moving the x or z stage also translates the center of rotation of the  $\theta$  stage. (b) Here, the translation stages can be moved without moving the COR of the  $\theta$  stage.

Thus, before using an already installed diffractometer, one should clarify which motors can be moved without moving a center of rotation at the same time. In general, three positions have to be spatially matched: The sample surface, the center of rotation and the beam position. In many setups, the beam position is fix (e.g. at the synchrotron). In that case, the center of rotation of the motors moving the detector ( $2\theta$ ) and the sample ( $\theta$ ) have to be aligned to match the beam position (Fig. B.4a). A separate sample movement stage, which can be moved without changing the center of rotation is best suited to avoid errors during alignment or measurement. If detector and sample slit systems (Fig. B.4) are used to suppress the background noise, the situation is even more challenging.

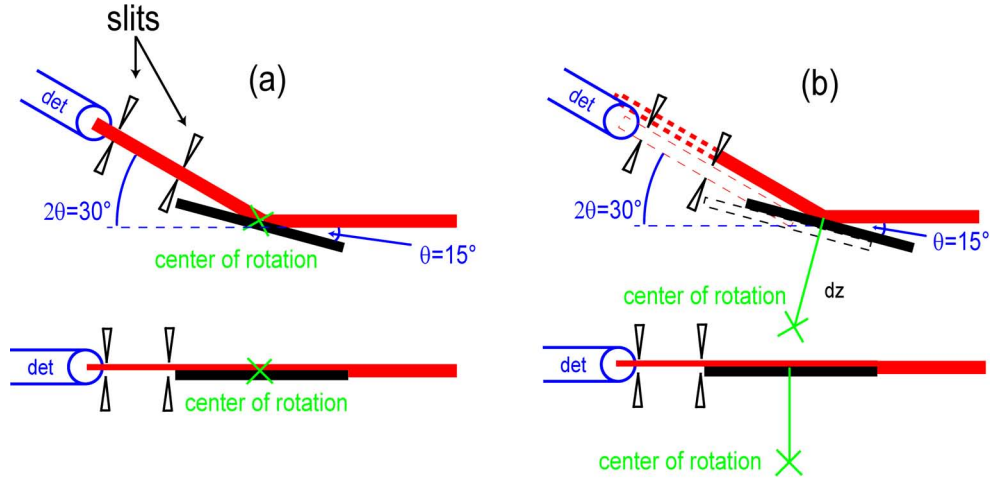


Figure B.4: (a) Center of rotation (shown as green cross) matches the sample surface and the beam position. At a tilted sample angle  $\theta$  the specular beam hits the detector at  $2\theta$ . (b) Illustration of the situation when the center of rotation is vertically misaligned. As a result, the specular beam misses the detector at high ( $\theta$ ) values, or shows a maximum at a  $\theta$ -position different from  $2\theta/2$ .

To quantify the errors involved, a misplaced center of rotation of the sample angle ( $\theta$ ) is assumed (Fig. B.4b). A close up of the geometry used to calculate the specular beam offset with respect to the position of a beam reflected from a perfectly aligned sample is depicted in Fig. B.5. The offset  $d$  (Fig. B.5b) as a function of vertical displacement  $a$  (of the center of rotation) and the sample angle ( $\theta$ ) is calculated.

First the length  $x$  (Fig. B.5a, red line) is calculated to  $x = \frac{b}{\sin(\theta)}$ . Using  $b = a(1 - \cos(\theta))$  we find

$$x = \frac{a \cdot (1 - \cos(\theta))}{\sin(\theta)} \quad (\text{B.1})$$

The offset  $d$  of the specular beam reflected from a misaligned sample (Fig. B.5, blue full line) with respect to the position of the beam assuming a perfectly aligned center of rotation (blue dashed line) is

$$d = c \cdot \sin(\theta) = 2 \cdot x \cdot \cos(\theta) \cdot \sin(\theta) = 2 \cdot a \cdot (\cos(\theta) - \cos^2(\theta)) \quad (\text{B.2})$$

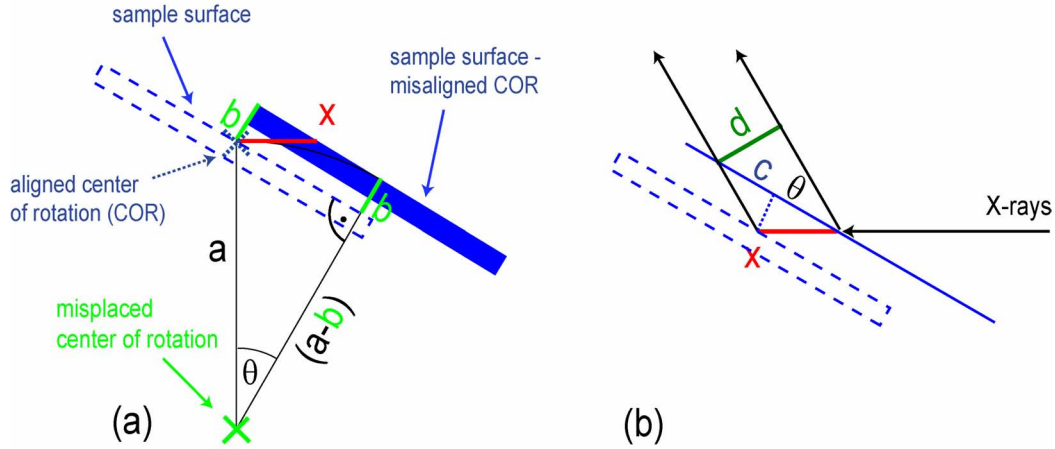


Figure B.5: (a) The center of rotation (COR, shown as green cross) of the sample angle  $\theta$  is vertically shifted about the length  $a$ . (b) Schematic illustrates the geometry used to determine the specular beam offset  $d$ . Dashed lines show the position of the sample if the COR is perfectly aligned. Full lines correspond to the misaligned situation. X-rays are shown as black arrows.

using equation B.1 (Fig. B.5b). The offset  $d$  is plotted in (Fig. B.6) for four different misplacements,  $1mm$ ,  $2mm$ ,  $3mm$  and  $4mm$ .

If a typical beam height (slit setting) in vertical direction of  $200\mu m$  (as e.g. used at beam-line W1, HASYLAB) and a misalignment of the center of rotation of  $3mm$  is assumed, the signal is completely lost when the sample is tilted by  $\theta \geq 7.5^\circ$  (see Fig. B.6, green curve). Please note that even a misalignment of only  $1mm$  leads to significant errors at high sample angles ( $\theta \geq 10^\circ$ ).

The alignment of the angle vertical to the beam direction in the sample surface plane at  $\theta = 0^\circ$  (often named  $\chi$ , see Fig. B.7a) is also depending on the height accuracy of the center of rotation (in direction of the surface normal). A misalignment in this direction would lead to a translation of the sample in a direction perpendicular to the beam. Because also the sample angle  $\theta$  is tilted when  $\chi$  is aligned, the specular beam position depends on both angles. The geometry used to determine the displacement errors is shown in Fig. B.7. At first, the translation  $x$  (Fig. B.7b) of the sample in direction perpendicular to the beam is determined to

$$x = \frac{a \cdot (1 - \cos(\chi))}{\sin(\chi)} \quad (\text{B.3})$$

At the position the beam would hit the perfectly aligned sample, the misaligned sample surface is now higher (or lower) by the distance  $h$ .  $h$  (Fig. B.7c) is calculated to

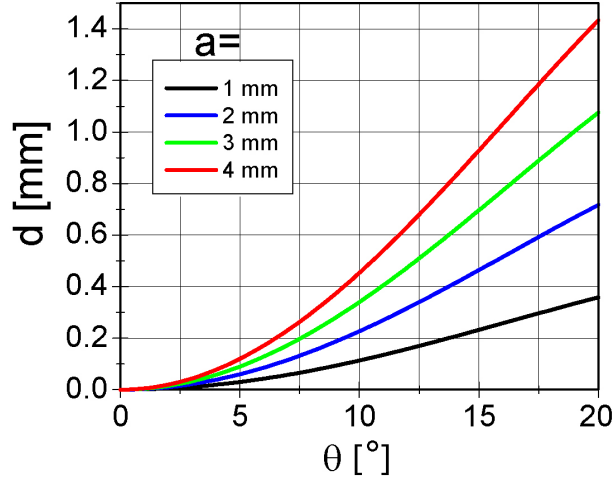


Figure B.6: The specular beam offset  $d$  due to a vertical misalignment of the center of rotation of  $\theta$  is plotted as a function of the sample angle  $\theta$ .

$$h = x \cdot \tan(\chi) = \frac{a \cdot (1 - \cos(\chi))}{\cos(\chi)} \quad (\text{B.4})$$

Now we calculate the offset  $y$  (black dashed line in (Fig. B.7d)) in direction along the beam, which is determined by the tilt of the angle  $\theta$  and the height  $h$  to

$$y = \frac{h}{\tan(\theta)} = \frac{a \cdot (1 - \cos(\chi))}{\cos(\chi) \cdot \tan(\theta)} \quad (\text{B.5})$$

The offset  $d$  of the specular beam is

$$d = c \cdot \sin(\theta) = 2 \cdot y \cdot \cos(\theta) \cdot \sin(\theta) = 2 \cdot \frac{a \cdot (1 - \cos(\chi))}{\cos(\chi)} \cdot \cos^2(\theta) \quad (\text{B.6})$$

Assuming that the sample angle is  $\theta = 1^\circ$ , the errors involved are plotted for misalignments of 1mm, 2mm, 3mm and 10mm as a function of  $\chi$  in Fig. B.8.

We find that a misalignment of the center of rotation of  $\chi$  in vertical direction (Fig. B.8b) is negligible. The offset  $d$  of the specular beam is in the order of some micrometers.

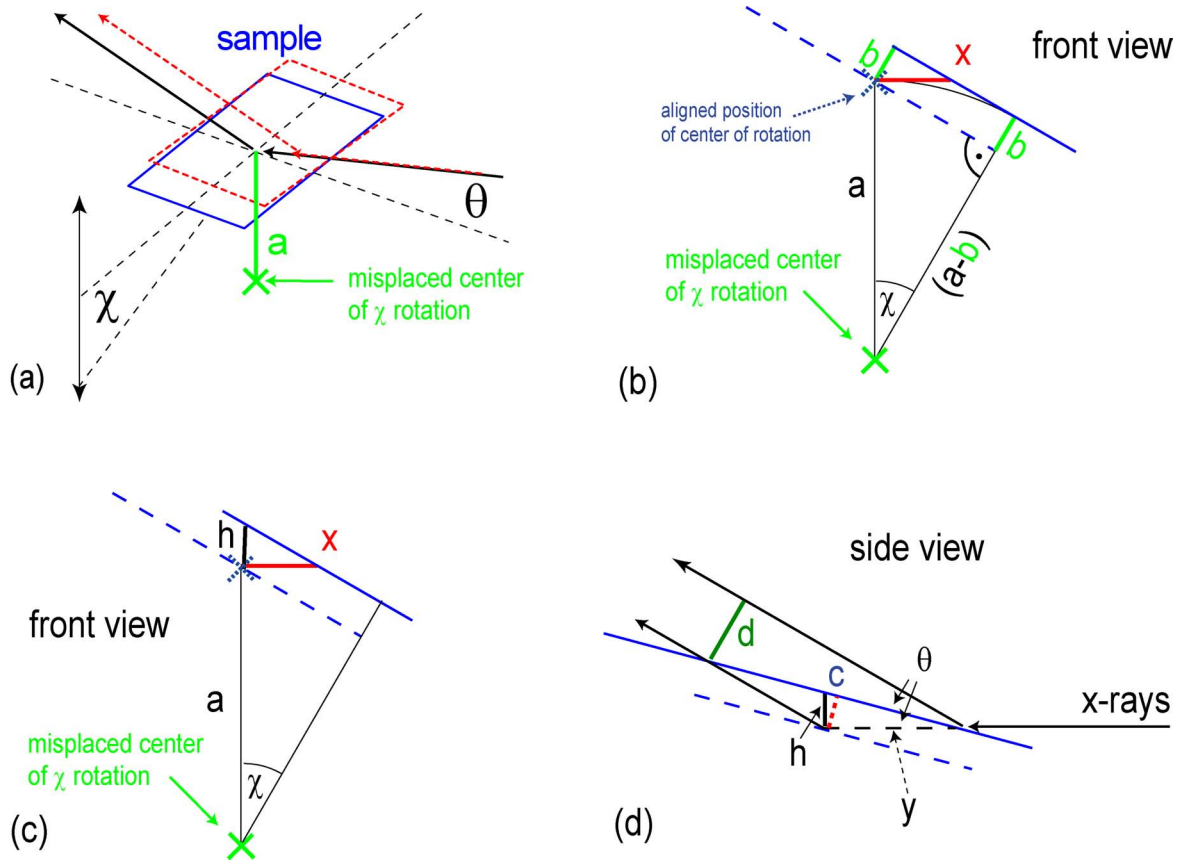


Figure B.7: (a) The center of rotation (shown as green cross) of the alignment angle  $\chi$  is vertically shifted by the length  $a$ . (b-d) illustrate the geometries used to determine the specular beam offset  $d$ . "Front view" means from the perspective of the X-ray beam.

More important is the horizontal alignment of the center of rotation of  $\chi$ . Depending on the geometry of the motors that move specific angles and directions, a lateral translation of the sample in order to measure different spots on a larger sample might also move the center of rotation of  $\chi$  (which is the case e.g. at beamline D4 at HASYLAB). The geometry to estimate the errors is shown in (Fig. B.9). Part (a) shows the sample in a front view (the beam entering the picture plane). The height offset of the sample  $x$  is determined to  $x = a \cdot \tan(\chi)$ . A side view of the situation is depicted in (Fig. B.9b). The length  $x' = x \cdot \cos(\theta) = a \cdot \tan(\chi) \cos(\theta)$  Here the beam offset  $d$  can be determined to

$$\begin{aligned}
 d &= c \cdot \sin(\theta) = 2 \cdot \frac{x'}{\tan(\theta)} \cdot \sin(\theta) = 2 \cdot \frac{a \cdot \tan(\chi) \cdot \cos(\theta)}{\tan(\theta)} \cdot \sin(\theta) \\
 &= 2 \cdot a \cdot \tan(\chi) \cdot \cos^2(\theta)
 \end{aligned} \tag{B.7}$$

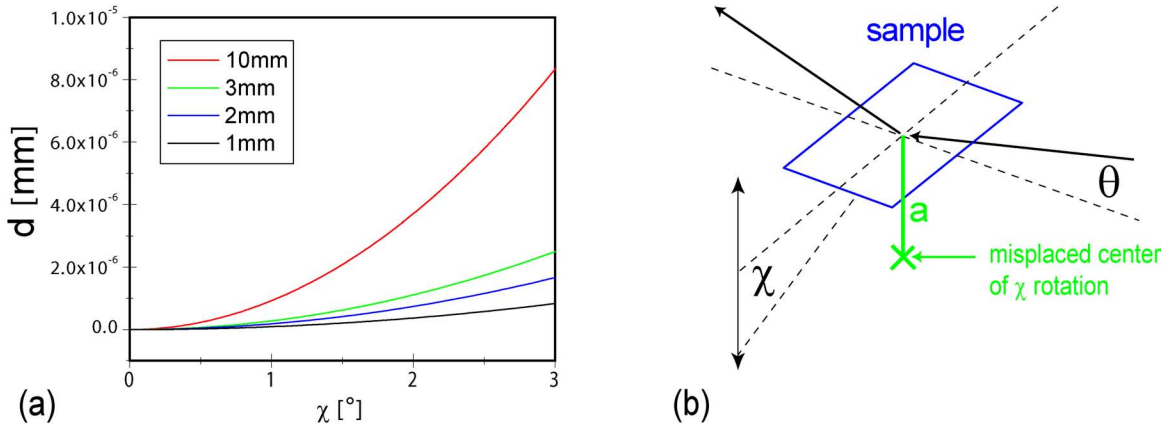


Figure B.8: (a) Plot of the specular beam offset when scanning  $\chi$  from  $0^\circ$  to  $3^\circ$  (b) The center of rotation (shown as green cross) of  $\chi$  is vertically shifted about the length  $a$ .

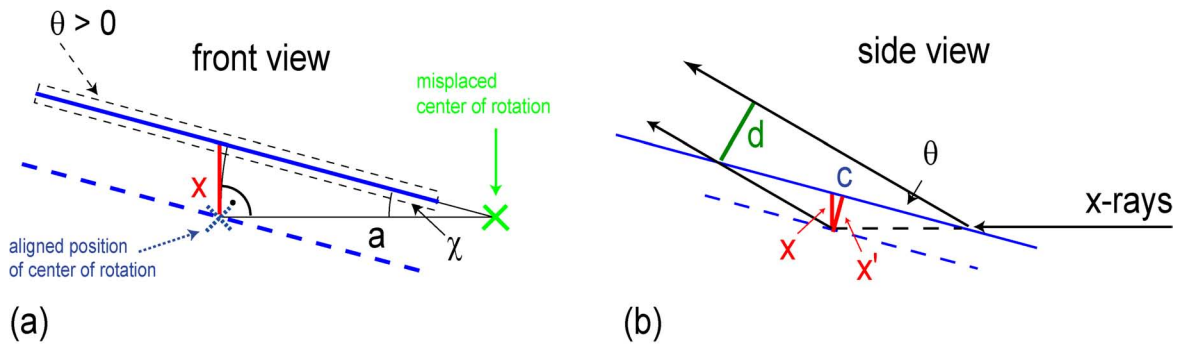


Figure B.9: (a) The center of rotation (shown as green cross) of the alignment angle  $\chi$  is horizontally shifted about the length  $a$ . (b) Schematic illustrates the geometry used to determine the specular beam offset  $d$ .

The calculated errors are plotted assuming  $\theta = 1^\circ$  (which is a reasonable value during alignment) for different degrees of misalignment ( $a = 1, 2, 3$  and  $10\text{mm}$ ) in the region  $0^\circ < \chi < 3^\circ$  (Fig. B.10a). The offset of the specular beam reaches critical values only for large misalignments of the center of rotation of  $\chi$ . When measuring different positions on large samples, a misalignment of  $10\text{mm}$  is realistic, assuming that the motors moving the horizontal sample position move the center of rotation at the same time. Please note that the error scales with  $\cos^2(\theta)$ . Aligning  $\chi$  at larger sample angles  $\theta$  leads to a decreased error.

The most important alignments has been identified to be the vertical position of the center of rotation of the sample angle  $\theta$ , and the horizontal alignment of the center of rotation of  $\chi$ . Thus, a height adjustment of the sample holder is highly recommended to be able

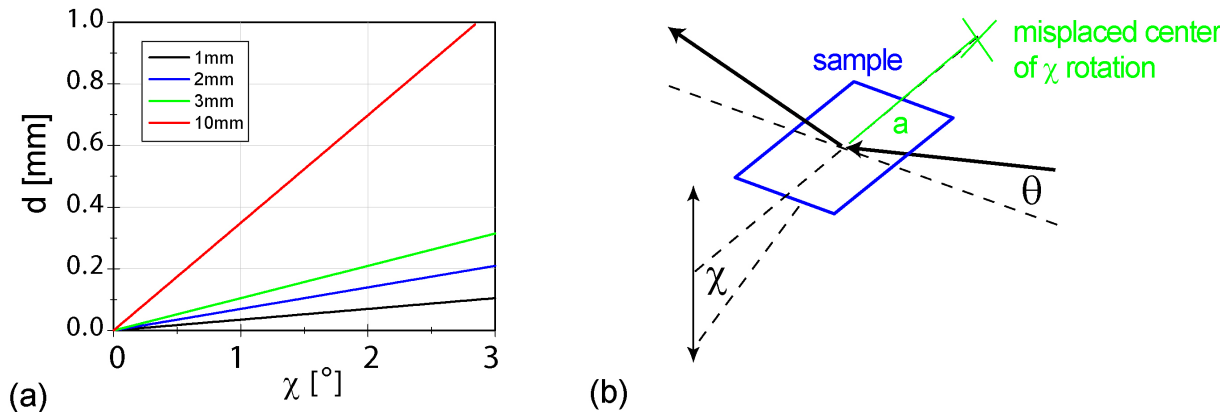


Figure B.10: (a) The specular beam offset  $d$  due to a horizontal misalignment of the center of rotation of  $\chi$  is plotted as a function of  $\chi$ . In the calculation,  $\theta$  is kept fix at  $1^\circ$ . (b) Clarifies the misalignment of the center of rotation of  $\chi$ .

to vary the sample height without moving the center of rotation of  $\theta$ . Additionally the sample holder should be able to move the sample horizontally if different sample positions should be measured.

Basic rules to consider when aligning samples for reflectometry measurements are summarized:

- control the setup and motor movements before starting the alignment. Print out the starting configuration.
- start with aligning the sample parallel to the beam (rocking scan in direct beam).
- when your sample is almost parallel, do a high resolution rocking scan in the direct beam.
- perform a high resolution height scan and position the sample surface in the middle of the beam. Take into account that some materials are transparent to certain wavelengths.
- do not change the  $z$  position any more.
- check  $\theta$  at small angles.
- check  $\chi$  at large angles.
- finally, check  $\theta$  at large angles.



# Appendix C

## MATLAB custom tools

Some useful tools have been implemented in Matlab during this thesis. Here, a brief overview over the main functions is given. M-files are available from MH.

The unit cell solver (C.1) can:

- calculate all possible q-positions of Bragg reflections from a given structure
- fit measured q-positions to structure using boundary conditions for start parameters
- assign measured peaks to certain planes
- save fit results to a text file

The file merger (C.2) handles the output files obtained with the line detector (MythenII) at HASYLAB, DESY beamline W1. Raw data are text files with only non-zero data points listed one below the other. Output is a matrix containing intensity information. Main functions are:

- complete raw data and convert it to matrices
- combine different datafiles belonging to one measurement, subtracting to overlap
- save final matrix as ascii text file

## C.1 Unit Cell Solver

This tool is developed to analyze X-ray powder diffraction measurements and find the unit cell dimensions of the investigated material (Fig. C.1). It is used in situations where organic molecules have been crystallized on a surface and a number of Bragg peaks have been identified, e.g. from reflectometry and crystal truncation rod measurements. The tool calculates all possible reflections from a given unit cell in q-space and compares the results to the measured values. The fit routine optionally uses a Levenberg-Marquardt non-linear least square fit to minimize the difference between theoretical and measured peak positions. To ensure global minimization, a Monte-Carlo method is applied to vary the start parameters in a given range.

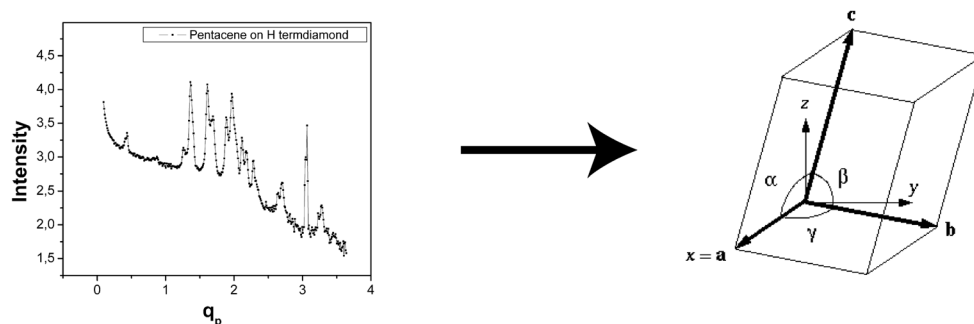


Figure C.1: The goal of the unit cell solver is to find a unit cell structure by fitting X-ray diffraction data.

The X-ray data is provided to the Matlab tool in Excel sheets. All the observed peak positions are put ascending in the first column (usually column A). If you want to assign a peak to a specific crystal plane you can enter the  $h, k$  and  $l$  values in columns B, C and D respectively. The fit quality is determined by calculating the sum of the the square of the deviation from the measured and the calculated peak positions. The results file saves the structural parameters of the best ten (can be chosen) hits.

The theoretical Bragg peak positions are determined by calculating the absolute value of all vectors  $\vec{Q}$  matching a reciprocal lattice vector  $\vec{G}$  of the assumed structure. The absolute value of  $\vec{Q}$  is given by

$$|\vec{Q}| = \sqrt{Q_x^2 + Q_y^2 + Q_z^2}$$

where

$$\vec{Q} = \vec{G} = h \cdot \vec{a}^* + k \cdot \vec{b}^* + l \cdot \vec{c}^*$$

The reciprocal lattice vectors  $\vec{a}^*$ ,  $\vec{b}^*$  and  $\vec{c}^*$  are defined by

$$\vec{a}^* = \frac{2\pi}{a} \cdot \begin{pmatrix} w \cdot u_1 \\ -\cot(\gamma) \\ 1 \end{pmatrix}; \quad \vec{b}^* = \frac{2\pi}{b} \cdot \begin{pmatrix} w \cdot u_2 \\ 1/\sin(\gamma) \\ 0 \end{pmatrix}; \quad \vec{c}^* = \frac{2\pi}{c} \cdot \begin{pmatrix} 1 \\ 0 \\ 0 \end{pmatrix} \quad (\text{C.1})$$

The following abbreviations have been used:

$$\begin{aligned} w &= [2\cos(\alpha)\cos(\beta)\cos(\gamma) - \cos^2(\alpha) + \sin^2(\gamma) - \cos^2(\beta)]^{-\frac{1}{2}} \\ u_1 &= \frac{\cos(\alpha)\cos(\beta) - \cos(\gamma)}{\sin(\gamma)} \\ u_2 &= \frac{\cos(\beta)\cos(\gamma) - \cos(\alpha)}{\sin(\gamma)} \end{aligned} \quad (\text{C.2})$$

Here, the  $a$ ,  $b$ ,  $c$ ,  $\alpha$ ,  $\beta$  and  $\gamma$  values are the structural parameters of the unit cell (Fig. C.1).

The work flow diagram of the program is shown in Fig. C.2. After reading the experimental data (I), the routine randomizes the start values (unit cell dimensions) within the allowed range (II). Next, the unit cell volume is calculated via

$$\text{Vol}_{\text{uc}} = a \cdot b \cdot c \cdot \sqrt{(1 - \cos^2(\alpha) - \cos^2(\beta) - \cos^2(\gamma)) + 2(\cos(\alpha)\cos(\beta)\cos(\gamma))}$$

using the randomized start values. Comparison to the user defined range (III) sorts out the randomized parameter sets with a unit cell volume which is too big or too small. If  $\text{Vol}_{\text{uc}}$  is outside the tolerated region, the program rolls new start parameters, and checks the volume of the new parameter set. If a parameter set has been found that matches the volume condition, the  $q$ -values of the randomized structure are calculated (IV). The fit quality  $res$  is determined by calculating the sum of the squared difference between the measured and the calculated  $q$ -value:

$$res = \sum_{peaks} (q_{measured} - q_{calc})^2$$

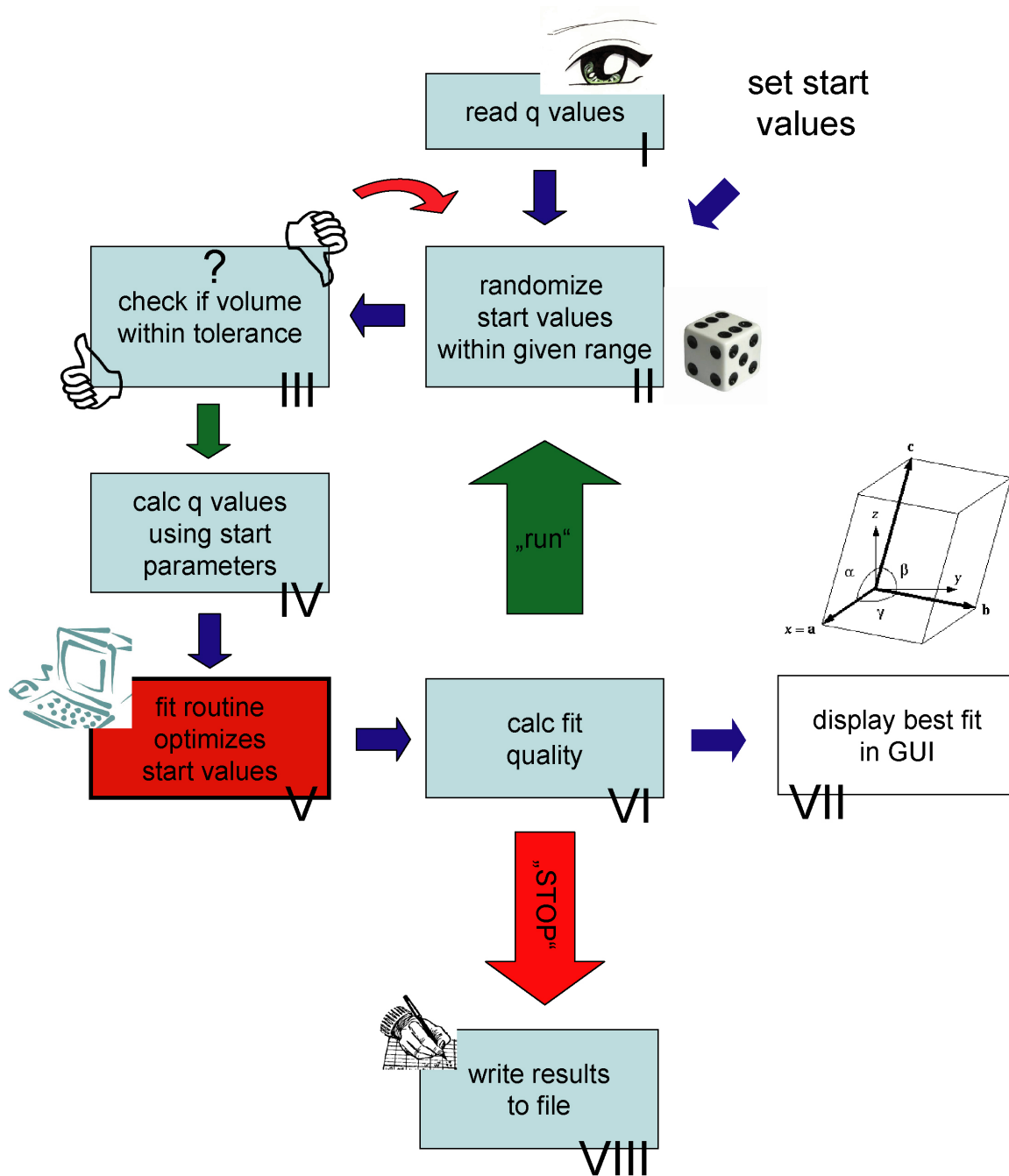


Figure C.2: Work flow diagram of the unit cell solver.

Then one can choose if a non-linear least-square fit (V) that automatically minimizes *res* using the randomized start parameters is used. This option is only reasonable if significantly more measured peak positions are available than parameters to fit (six in general). In case only a few peaks are available, the fit option can be turned off. The obtained results are then the randomized structures showing the lowest calculated *res*, without further variation of the start parameters.

Global minimization is ensured by iteratively varying the fitting start parameters within the given region. After each iteration, the calculated *res* is compared to the former results and the current best fit is displayed in the GUI (VII). If the "Stop" button is pressed, the results with the lowest values are saved in the results file (VIII).

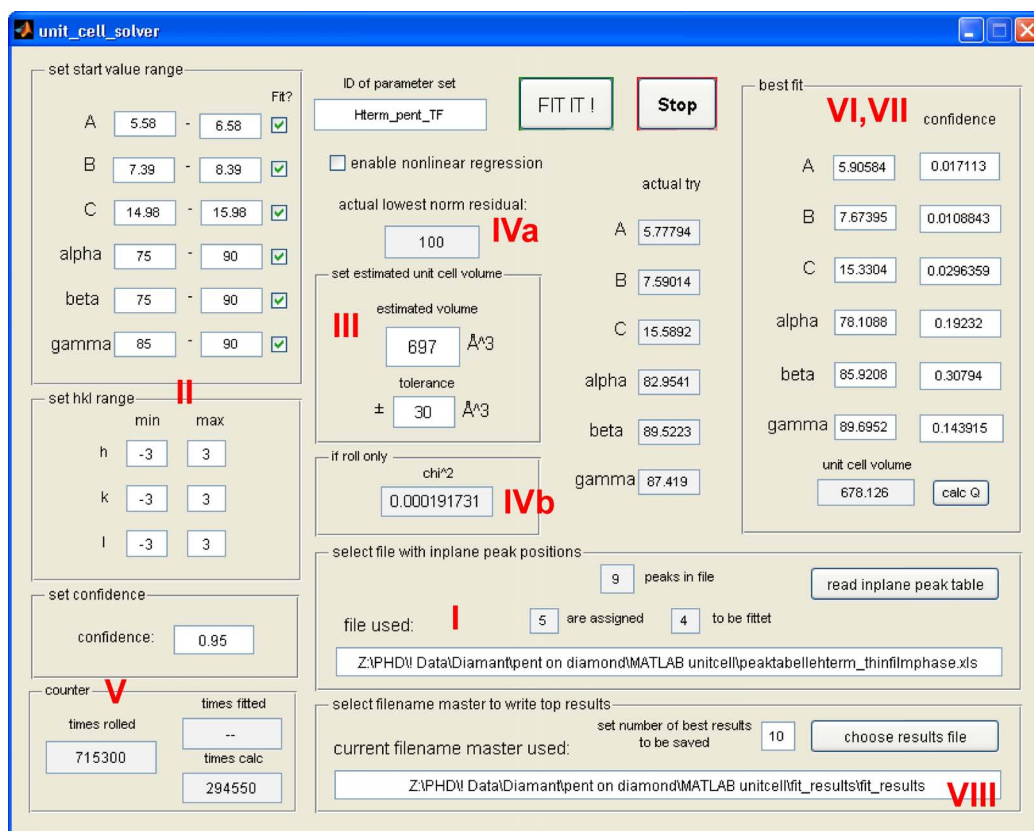


Figure C.3: Screen shot of the user interface. Red numbers are inserted to clarify the correlation to the work flow diagram (Fig. C.2) and the process description.

A screen shot of the user interface is given in Fig. C.3. A typical fitting process is described in the following. Choose a data file containing the measured *q*-positions (I) and a path where the results file should be saved (VIII). Set the range of the structural parameters in the graphical user interface (GUI) as well as the *hkl* range (II) and the unit cell volume range (III). To fix a specific structural parameter, deselect the fitting option, and enter the

fix value in the "best fit" panel to the right (VI). Select/unselect the "enable nonlinear regression" option. Enter a name in the field "ID of parameter set". Ensure that the stop button has not been pushed. Click on "FIT IT"! Calculation will continue until you hit the Stop button (when you hit it, the routine will stop after finishing the current calculation, this can take a few seconds). During operation, a counter (V) shows the statistic achieved so far, and the respective best fit is displayed (VI).

## C.2 File Merger

This tool helps to handle the data files obtained by using the line detector (MythenII) at the Hamburger Synchrotronstrahlungslabor (HASYLAB) at DESY, Germany, Hamburg, beamline W1. Raw data is provided as space limited text files with 6 columns, reading the motor position [ $^{\circ}$ ], the number of the measurement point [number], the detector channel [number], the signal [counts] and the number of absorption foils [number]. To measure large area reciprocal space maps, several subsequent measurements have to be taken from one sample (Fig. C.4), due to the limited length of the detector. The program converts the raw data into matrix format and merges the files belonging to one sample. In the process, a correction of the detector channel intensity is applied, and the measurement overlap is subtracted.

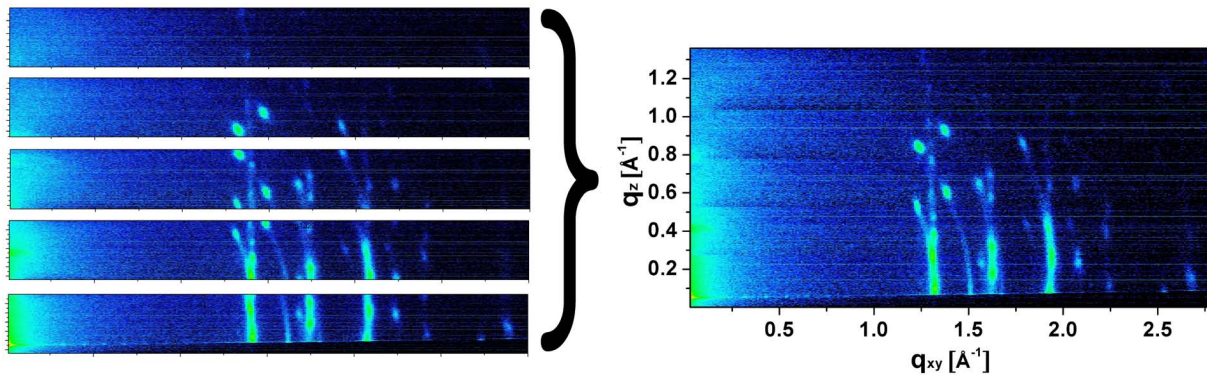


Figure C.4: Illustration of the function of the file merger tool. On the left, five subsequent inplane measurements are shown, each with increased detector angle. The combined data is plotted in the right graph after subtracting the measurement overlap.

Two additional routines are provided. The first checks if a column is missing in the respective data file, which is necessary because a signal of "0" counts is deleted from the raw data file. In the rare event when all 1280 detector channels read no counts, the matrix dimension is corrupted due to one missing measurement point. The "file\_check" routine reports to the Matlab command window if the file is corrupted and what datapoint is missing. If the file is corrupted, you have to open it manually with any text editor, and fill

in 1 dummy data point having the value of 1 count at the position the measurement point is missing.

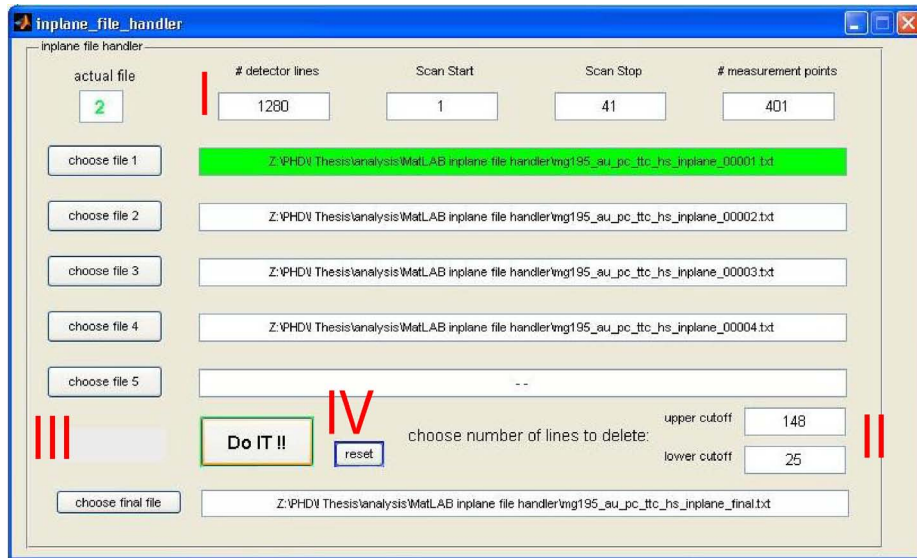


Figure C.5: Screen shot of the user interface. Red numbers are inserted to clarify the process description (see text).

The second routine modifies raw data files measured before summer 2009 in a way that they can be operated with the file merger tool. Files saved before than summer 2009 have one column less (column 2, the measurement point number, is missing). "Column\_inserter" creates a new ascii text file with the missing column inserted. As the entries of the inserted column are of no relevance for the file merging tool, the whole column has the value 1.

A screen shot of the user interface is shown in Fig. C.5. To use the tool, set the number of detector lines (I, default is 1280) and the number of detector lines you want to delete due to the measurement overlap (II). Hitting the "chosed file" buttons (III) opens a file finder panel. Do not forget to provide a name for the final file. When processing of a file is finished, the background color of the respective field turns green. In the upper left corner, a counter displays the number of the file which is currently processed. If all files are processed, "READY" appears in red letters in the lower left corner.



# Appendix D

## Photos

A collection of photographs related to the dissertation is shown on the following pages.

- Some impressions of the high vacuum coating equipment in the X-ray lab of the LMU department of physics are shown in Fig. D.1.
- Fig. D.2 shows a group picture and some scientific snapshots of the PHD student exchange program "Junior Nanotechnology Network" with McGill University in Montreal, Canada.
- Pictures of measurement visits at synchrotron sources ("beamtimes") are found in Fig. D.3.
- A short photo documentation of the EU-project "Biodot" is given in Fig. D.4.

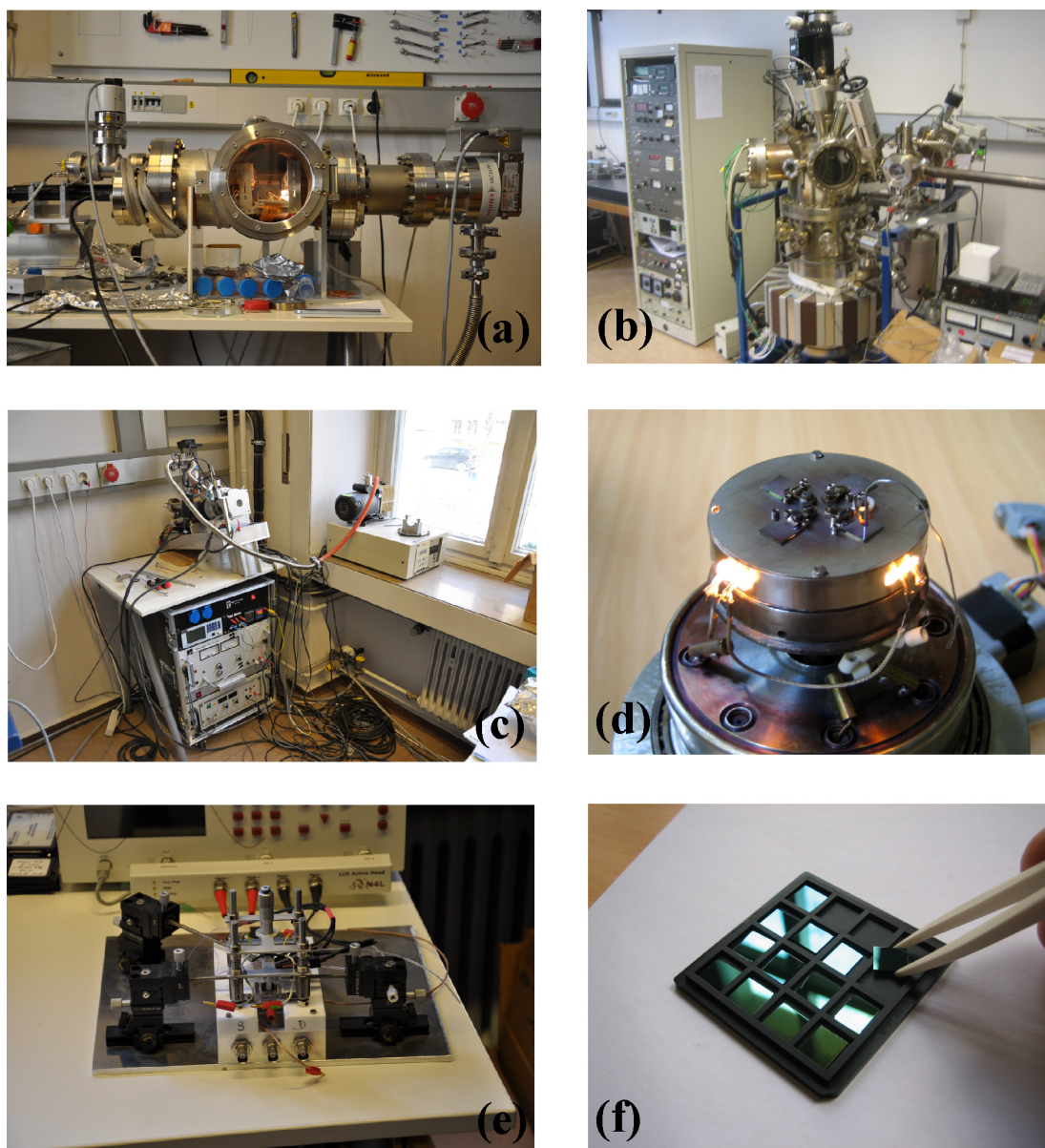


Figure D.1: The thin film laboratory at LMU. (a) - (c) shown the vacuum chambers used to fabricate the organic thin films with vacuum deposition. (d) sample holder used in the mobile UHV chamber (c). (e) electrical characterization setup. (f) sample storage.



Figure D.2: Pictures from the PHD student exchange with McGill University in Montreal (a) participants from Munich (b) Chemical realization of the german flag. (c) CdS nano particles produced during the lab courses. (d) watching the football world championship.

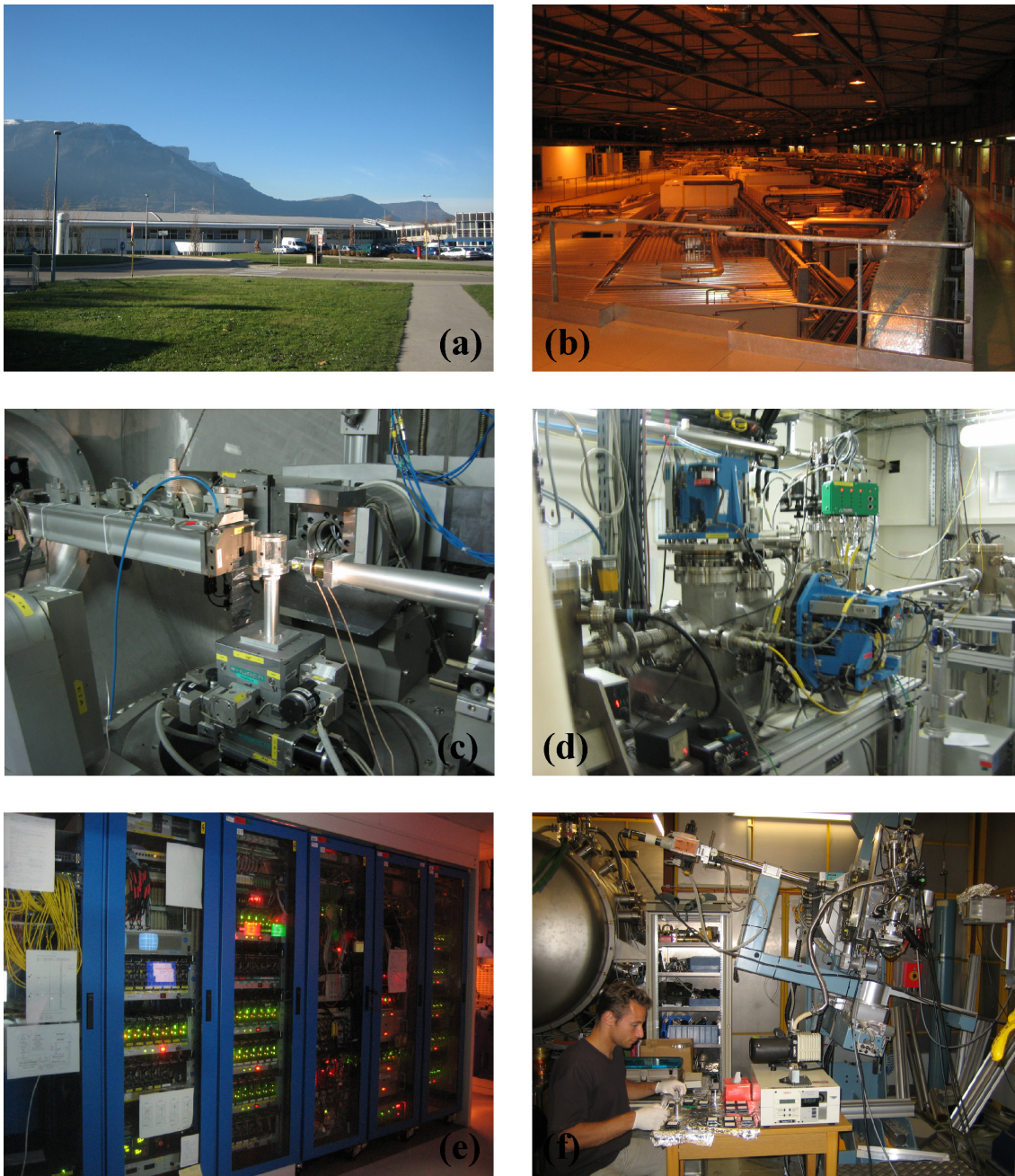


Figure D.3: Impressions from synchrotron sources. (a)-(e) European Synchrotron Radiation Facility (ESRF) in Grenoble. (a) outside and (b) inside the storage ring building. (c) sample environment at beamline ID01 and (d) optics hutch. (e) control electronics. (f) our mobile UHV chamber mounted in the diffractometer at HASYLAB, Hamburg, beamline W1.

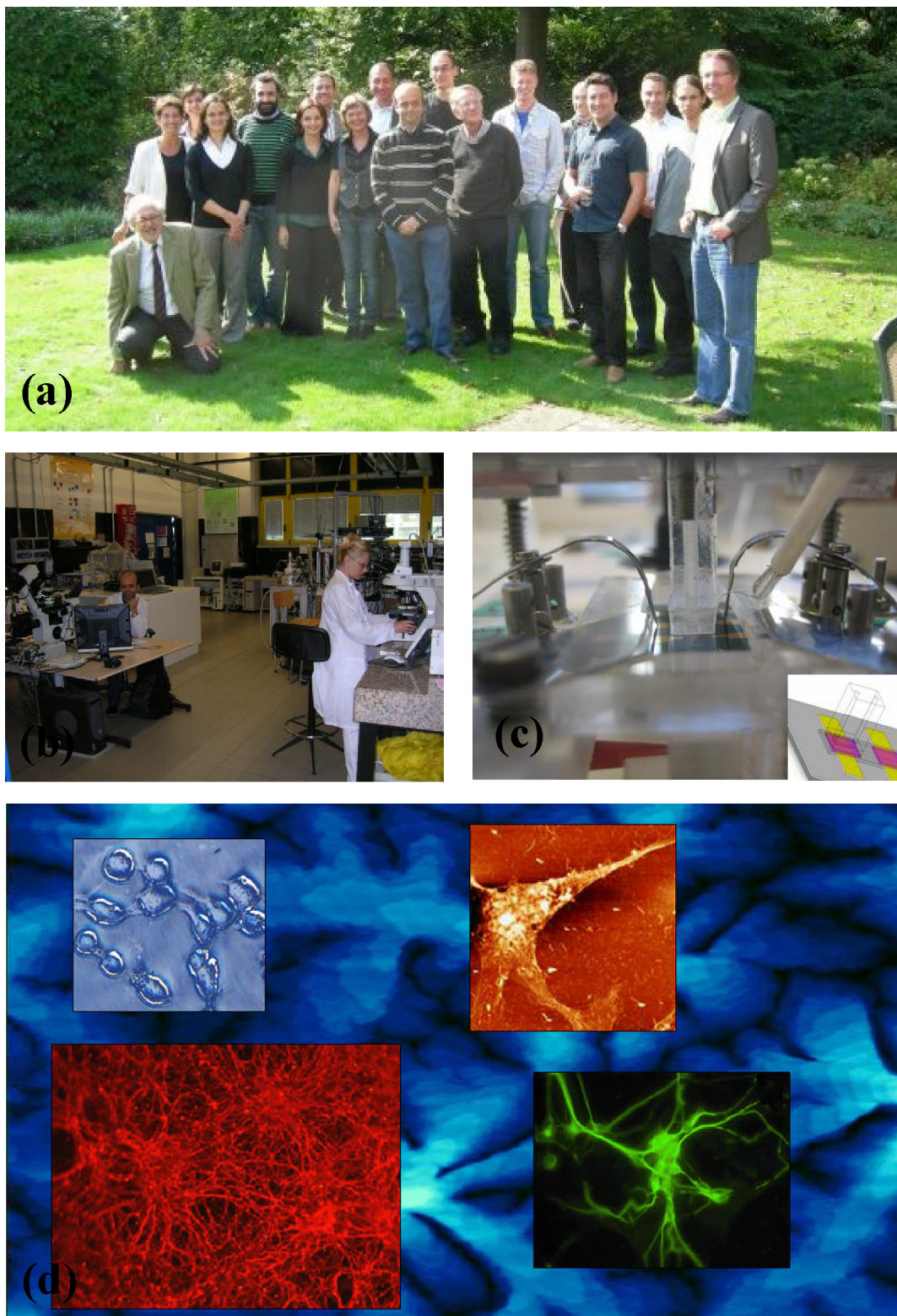


Figure D.4: Pictures related to the EU project BIODOT (**BIO**systems and their **D**ynamics in fluids with **O**rganic **T**ransistors). (a) group picture at the final meeting in Eindhoven. (b) thin film laboratory at CNR Bologna. (c) LMU device. (d) Neuronal networks grown on pentacene. Picture taken from <http://www.bo.ismn.cnr.it/biodot/>.



# List of Figures

1.1	Introduction - structure determination . . . . .	2
1.2	Introduction - supported lipid membrane formation . . . . .	3
1.3	Introduction - coating architecture . . . . .	4
2.1	Introduction - aggregation on surface . . . . .	5
2.2	Introduction - molecular models . . . . .	6
2.3	Summary of interaction geometries . . . . .	7
2.4	Van der Waals pair potential . . . . .	8
2.5	Van der Waals pair potential cylinder vs. surface . . . . .	9
2.6	Molecular beam particle density . . . . .	13
2.7	Dependency of cylinder geometry - ratio $R/L$ . . . . .	15
2.8	Plots of the forces . . . . .	16
2.9	Dependency of the cylinder length $L$ - interaction energy . . . . .	17
2.10	Dependency of the cylinder length $L$ - force . . . . .	18
2.11	Box shaped molecules close to a surface - interaction energy . . . . .	19
2.12	Box shaped molecules close to a surface - forces . . . . .	20
2.13	Cylinder simulates pentacene . . . . .	21
2.14	Estimation surface vs. thermal energy . . . . .	22
2.15	Integration schemes - box and disc shaped molecules . . . . .	23
2.16	Maple worksheet used for integration . . . . .	24
2.17	Forces on a particle close to disc with different radii . . . . .	25
2.18	Integration scheme particle in front of a disc . . . . .	26
2.19	Maple integration loop . . . . .	27
2.20	Force components on particle being asymmetric in front of a disc . . . . .	28
2.21	3D plot of the force on a particle asymmetric in front of a disc . . . . .	29
3.1	Knudsen cell installation . . . . .	31
3.2	Vacuum deposition chambers . . . . .	32
3.3	Screenshot LabView evaporation program . . . . .	33
3.4	Pentacene structure & AFM . . . . .	34
3.5	Polystyrene layer on silicon wafer - X-ray data . . . . .	35
3.6	1ML pentacene on SiO <sub>2</sub> : reflectometry and AFM . . . . .	36
3.7	Pentacene - sketch of the molecular orientation . . . . .	37

3.8	AFM graphs of 50nm pentacene on PS . . . . .	37
3.9	X-ray reflectivity curves of 50nm PC on various surfaces . . . . .	38
3.10	AFM graphs 1ML pentacene on diamond . . . . .	40
3.11	AFM graphs 8ML pentacene on diamond . . . . .	41
3.12	XRD pattern of pentacene on diamond . . . . .	42
3.13	Pentacene on H-terminated diamond: XRD and schematic . . . . .	43
3.14	Pentacene on single crystal diamond: GIXRD maps . . . . .	44
3.15	Pentacene on single crystal diamond: Reflectometry . . . . .	45
4.1	Spincoating . . . . .	48
4.2	X-ray setup . . . . .	49
4.3	Reflectometry curves after spincoating . . . . .	50
4.4	Reflectometry curves after spincoating . . . . .	51
4.5	Reflectometry curves after sputtering . . . . .	52
4.6	Photograph of sputter machine . . . . .	53
4.7	Short alkanes . . . . .	54
4.8	TTC structure . . . . .	54
4.9	AFM of 10nm TTC on SiO <sub>2</sub> . . . . .	55
4.10	AFM of pentacene and capped pentacene film . . . . .	56
4.11	Schematic sample layout . . . . .	56
4.12	Reflectometry capped pentacene . . . . .	57
4.13	Maps capped pentacene . . . . .	59
5.1	Microfluidic setup . . . . .	62
5.2	Lipid membrane on pentacene . . . . .	63
5.3	Lipid membrane on pentacene - X-ray reflectometry . . . . .	64
5.4	Lipid membrane on TTC - fluorescence microscopy . . . . .	65
5.5	Lipid membrane on Pc/TTC - continuous bleaching . . . . .	66
6.1	Schematic peptide synthesis . . . . .	70
6.2	Schematic supported lipid bilayer . . . . .	71
6.3	Sketch biomimetic surface . . . . .	71
6.4	Sketch biomimetic surface characterization . . . . .	72
6.5	Sketch measurement layout and AK-cyclo(RGDfC) dimensions . . . . .	73
6.6	Reflectometry curves, x-ray and neutron . . . . .	75
6.7	Hydration level and sld profiles . . . . .	76
6.8	Adhesion peptide on cell surface . . . . .	77
6.9	Cells on biomimetic surfaces . . . . .	78
B.1	Reflectometry XP - sample preparation . . . . .	154
B.2	How to mount a sample . . . . .	154
B.3	Illustration of different diffractometer setups . . . . .	155
B.4	Schematic of misalignment effect of the center of rotation of $\theta$ . . . . .	156
B.5	Illustration of vertical $\theta$ misalignment . . . . .	157

---

B.6	Effect if center of rotation of $\theta$ is misaligned vertically . . . . .	158
B.7	Illustration of vertical $\chi$ misalignment . . . . .	159
B.8	Effect if center of rotation of $\chi$ is misaligned vertically . . . . .	160
B.9	Illustration of horizontal $\chi$ misalignment . . . . .	160
B.10	Effect if center of rotation of $\theta$ is misaligned vertically . . . . .	161
C.1	Unit Cell Solver - goal . . . . .	164
C.2	Unit Cell Solver - work flow diagram . . . . .	166
C.3	Unit Cell Solver - screen shot user interface . . . . .	167
C.4	File Merger - combining measurements . . . . .	168
C.5	File Merger - screen shot user interface . . . . .	169
D.1	Photos - LMU lab . . . . .	172
D.2	Photos - JNN exchange McGill University Montreal . . . . .	173
D.3	Photos - synchrotron measurement times . . . . .	174
D.4	Photos - BIODOT . . . . .	175



# List of Tables

2.1	Summary of the interaction potentials and forces used in the simulations. .	12
4.1	Summary of the results of the spincoating experiments. . . . .	51
6.1	Summary of fit parameters . . . . .	74



# Vielen herzlichen Dank

**Prof. Dr. Joachim Rädler** und dem gesamten Lehrstuhl-Kollegium, die das Arbeiten in einem sehr angenehmen Klima ermöglicht haben.

**PD Dr. Bert Nickel** für die hervorragende Betreuung dieser Arbeit, die konstruktive und sachliche Art der Besprechungen und Diskussionen und viele aufregende Strahlzeiten und Meetings in ganz Europa. Du warst ein super Chef und ein Top-Kickerpartner.

**Dr. Stefan Schiefer** für die Einführung in Experimentier- und Analyse-Techniken, das exzellente Teamwork und die enge Freundschaft die daraus entstanden ist.

**Martin Göllner** für das ausgezeichnete Teamwork bei den zahlreichen BIODOT - Vorträgen und den zugrunde liegenden Experimenten.

**Matthias Fiebig** für erheiternd kritische Anregungen während der gesamten Doktorarbeit (den einen oder anderen "klassischen Fiebig") und die unkomplizierte Zusammenarbeit im gemeinsamen Labor.

**Dr. Susi Kempter** und **Gerlinde Schwake**, für die nette Zeit im gemeinsamen Büro und die optimale Fürsorge in allen Belangen des Biolabors.

**Samira Hertrich** für zahlreiche Neutronen-Messungen und erfolgreiche Strahlzeiten.

**Prof. Dr. Fabio Biscarini** und alle Mitwirkenden des **BIODOT Projektes**, die durch fachübergreifende Anregungen und Kritiken viel zur Entwicklung dieser Arbeit beigetragen haben.

**Kirstin Fritz, geb. Seidel** für die Unterstützung beim Erlernen der Membranherstellung und allem was dazu gehört.

**Dr. Jose Garrido, Wojciech Gajewski, Simon Lud** und **Felix Buth** vom Walther-Schottky Institut in Garching für die tolle Zusammenarbeit im Diamant-Projekt.

dem gesamten **Lehrstuhl Kotthaus**, insbesondere **Alex Paul, Stefan Schöffberger**,

**Philipp Altpeter** und **Bert Lorenz** für die umfangreiche Unterstützung und viel Geduld in allen Reinraum - Angelegenheiten.

**Simon Noever**, **Christian Westermeier**, **Christian Hundschell** und **Julia Schmidt** für die Zusammenarbeit und das gute Arbeitsklima in der "Nickel"-Gruppe.

**Simon Youssef** für inspirierende Gespräche und erholsame Ludwigs-Kaffees.

meiner Frau **Sherly** und meiner Familie für die Unterstützung und Motivation.

# Curriculum vitae

## Martin Huth

geboren am 21.09.1977 in München

### Schulbildung

---

9/1983 - 7/1987 Besuch der Grundschule an der Grandlstrasse in München

9/1987 - 7/1996 Besuch des Louise-Schröder Gymnasiums in München

### Wehrersatzdienst

---

2/1997 - 3/1998 Wehrersatzdienst an der Blindeninstituts-Stiftung in München

### Hochschulbildung

---

10/1998 - 12/2004 Physik-Studium an der Ludwig-Maximilians Universität München

2/2005 - 2/2006 Diplomarbeit am Lehrstuhl für Experimentalphysik  
der LMU München bei Prof. Dr. J.O.Rädler

5/2006 - 12/2010 Promotion am Lehrstuhl für Experimentalphysik der LMU München  
bei PD Dr. B.Nickel